

PONTIFÍCIA UNIVERSIDADE CATÓLICA
DO RIO DE JANEIRO



Gabriela de Castro Almeida

**Numerical prediction of hemodynamic patterns
during a cardiac cycle for one healthy and 30
aneurysmatic aortas**

Tese de Doutorado

Thesis presented to the Programa de Pós-graduação em Engenharia Mecânica of PUC-Rio in partial fulfillment of the requirements for the degree of Doutora em Engenharia Mecânica.

Advisor: Prof^a. Dra. Angela Ourivio Nieckele
Co-advisor: Dr. Bruno Alvares de Azevedo Gomes

Rio de Janeiro
April 2024



Gabriela de Castro Almeida

**Numerical prediction of hemodynamic patterns
during a cardiac cycle for one healthy and 30
aneurysmatic aortas**

Thesis presented to the Programa de Pós-graduação em Engenharia Mecânica of PUC-Rio in partial fulfillment of the requirements for the degree of Doutora em Engenharia Mecânica. Approved by the undersigned Examination Committee.

Prof^a. Dra. Angela Ourivio Nieckele

Advisor

Departamento de Engenharia Mecânica – PUC-Rio

Dr. Bruno Alvares de Azevedo Gomes

Co-Advisor

Departamento de Engenharia Mecânica – PUC-Rio

Dr. Gabriel Cordeiro Camargo

Instituto Nacional de Cardiologia - INC

Prof. Dr. Hugo Luiz Oliveira

Departamento de Estruturas – Unicamp

Dr. Igor Braga de Paula

Departamento de Engenharia Mecânica – PUC-Rio

Prof. Dr. Ilan Gottlieb

Fonte Imagem Medicina Diagnóstica - FMID

Rio de Janeiro, April 26th, 2024

All rights reserved.

Gabriela de Castro Almeida

Graduated in Mechanical Engineering from the Federal University of Juiz de Fora (2016). Postgraduate in Occupational Safety Engineering from the Federal University of São João del Rey (2020). Master in Mechanical Engineering from the Pontifical Catholic University of Rio de Janeiro (2019). Currently a full-time professor at the Federal Institute of Ceará. Expertise in computational fluid dynamics and bioengineering field.

Bibliographic data

Almeida, Gabriela de Castro

Numerical prediction of hemodynamic patterns during a cardiac cycle for one healthy and 30 aneurysmatic aortas / Gabriela de Castro Almeida ; advisor: Angela Ourivio Nieckele ; co-advisor: Bruno Alvares de Azevedo Gomes. – 2024.

172 f. : il. color. ; 30 cm

Tese (doutorado)–Pontifícia Universidade Católica do Rio de Janeiro, Departamento de Engenharia Mecânica, 2024.

Inclui bibliografia

1. Engenharia Mecânica – Teses. 2. Aorta. 3. CFD. 4. 4D Flow MRI. 5. Aneurisma de aorta ascendente. I. Nieckele, Angela Ourivio. II. Gomes, Bruno Alvares de Azevedo. III. Pontifícia Universidade Católica do Rio de Janeiro. Departamento de Engenharia Mecânica. IV. Título.

CDD: 621

Acknowledgements

I thank my parents, Marcelo and Márcia, my son João Vicente, and my brother Rafael for all the patience, strength and support they provided to me.

Thank you to all the professionals at PUC-Rio. Without the work of each one, this thesis would not be possible. I am very grateful to my mentors Angela and Bruno for all knowledge, suggestions and unrestricted assistance provided. You are inspiring.

To the Cardiovascular Engineering Team, for all the meetings, discussions and stimulation to improve my work.

This study was financed in part by the Coordenação de Aperfeiçoamento de Pessoal de Nível Superior - Brasil (CAPES) - Finance Code 001.

Abstract

Almeida, Gabriela C.; Nieckele, Angela O.; Gomes, Bruno A. A. **Numerical prediction of hemodynamic patterns during a cardiac cycle for one healthy and 30 aneurysmatic aortas**. Rio de Janeiro, 2024. 172p. Tese de Doutorado – Departamento de Engenharia Mecânica, Pontifícia Universidade Católica do Rio de Janeiro.

This study presents the validation of a physical/numerical model designed to predict the ascending aorta flow in a healthy patient, aiming to extend its application to analyze other patients, specifically, with ascending aortic aneurysm (AAoA). Applying the patient-specific model (PSM) concept, the results provided by the Four-dimensional Flow Magnetic Resonance Imaging (4D-Flow MRI) technique were used in the simulation employing the Computational Fluid Dynamics (CFD) approach, with a turbulence model capable of predicting laminar/turbulent regime transitions during the cardiac cycle. Boundary condition based on measured flow rate was imposed at the aorta's inlet. At the outlets, the physiological percentages of inlet flow rate corresponding to each output were considered, as well as the three-element Windkessel model to establish a more accurate approximation of the pressure-flow relationship. The favorable results obtained on pressure, flow rate and shear stress profiles at various positions along the aorta and throughout the cardiac cycle, validated the potential application of PSM to other patients, in particular patients with AAoA. AAoA is a silent disease with high mortality, and factors associated with a worse prognosis are not yet fully known. Aiming to relate flow dynamics characteristics with the disease, personalized anatomic models were obtained from angiotomography scans of 30 patients in two different years (with intervals of one to three years between them). Based on the volume difference of the ascending aorta from one year to another, two groups were defined: one with aneurysm growth and another without growth. The flow field during the cardiac cycle and the geometry corresponding to each group were compared to find patterns that may indicate the aneurysm growth from the first exam. Although there was no clear trend between the two patient groups, higher time-averaged pressure (*TAP*) values were observed in patients with aneurysm growth, as well as longer time periods during the cycle with the aorta subjected to high values of shear stress. The present study explored the

remodeling process of patients with aneurysm and how the geometry and flow pattern can impact its growth, contributing to a better understanding of aortic pathophysiology.

Keywords

Aorta, CFD, 4D Flow MRI, Ascending Aortic Aneurysm

Resumo

Almeida, Gabriela C.; Nieckele, Angela O.; Gomes, Bruno A. A. **Predição numérica de padrões hemodinâmicos durante um ciclo cardíaco para uma aorta saudável e 30 aortas aneurismáticas.** Rio de Janeiro, 2024. 172p. Tese de Doutorado – Departamento de Engenharia Mecânica, Pontifícia Universidade Católica do Rio de Janeiro

Este estudo apresenta a validação de um modelo físico/numérico para prever o escoamento na aorta ascendente de um paciente saudável, com o objetivo de estender sua aplicação para analisar outros pacientes, especificamente, com aneurisma da aorta ascendente (AAoA). Aplicando o conceito paciente-específico (PSM), os resultados fornecidos pela técnica de Ressonância Magnética Quadridimensional (4D-Flow MRI) foram utilizados na simulação empregando a abordagem de Dinâmica dos Fluidos Computacional (CFD) com um modelo de turbulência capaz de prever transições entre regimes laminar/turbulento durante o ciclo cardíaco. Condição de contorno baseada na vazão medida foi imposta na entrada da aorta. Nas saídas, foram considerados os percentuais da vazão de entrada correspondentes à cada saída, bem como o modelo Windkessel de três elementos para estabelecer uma aproximação mais precisa da relação pressão-vazão. Os resultados favoráveis obtidos dos perfis de pressão, vazão e tensão de cisalhamento em várias posições ao longo da aorta e ao longo do ciclo cardíaco validaram a aplicação potencial do PSM a outros pacientes, em particular, pacientes com AAoA. O AAoA é uma doença silenciosa com alta mortalidade, e os fatores associados ao pior prognóstico ainda não são totalmente conhecidos. Com o objetivo de relacionar características da dinâmica do escoamento com a doença, modelos anatômicos personalizados foram obtidos a partir de angiotomografias de 30 pacientes em dois anos diferentes (com intervalos de um a três anos entre eles). Com base na diferença de volume da aorta ascendente de um ano para outro, dois grupos foram definidos: um com crescimento do aneurisma e outro sem crescimento. O escoamento durante o ciclo cardíaco e a geometria correspondente a cada grupo foram comparados para encontrar padrões que possam indicar o crescimento do aneurisma a partir do primeiro exame. Embora não tenha havido uma tendência clara entre os dois grupos de pacientes, foram observados valores mais altos da pressão média-

temporal (*TAP*) em pacientes com crescimento do aneurisma, bem como períodos mais longos durante o ciclo com a aorta submetida a altos valores de tensão de cisalhamento. O presente estudo explorou o processo de remodelação de pacientes com aneurisma e como a geometria pode impactar em seu crescimento, contribuindo para uma melhor compreensão da fisiopatologia aórtica.

Palavras-chave

Aorta, CFD, 4D Flow MRI, Aneurisma de Aorta Ascendente.

Summary

1	Introduction	22
1.1	OBJECTIVES	25
1.2	RESEARCH ETHICS	25
1.3	THESIS OUTLINE	26
2	Fundamental Concepts	27
2.1	HEART STRUCTURE	27
2.2	CARDIAC CYCLE	28
2.3	HEART VALVES	29
2.4	THE WIGGERS DIAGRAM	29
2.5	AORTA	31
2.6	AORTIC VALVE	33
2.7	BLOOD RHEOLOGY	35
3	Literature Review	38
3.1	PHYSIOLOGIC ENVIRONMENT	38
3.2	PATHOLOGIES IN AORTIC VALVE	39
3.3	PATHOLOGIES IN AORTA	40
3.4	CFD MODELLING AND HEMODYNAMIC VARIABLES	41
3.5	4D-FLOW MRI	45
3.6	CFD X 4D-FLOW MRI	48
3.7	PATIENT-SPECIFIC SIMULATION	49
4	Mathematical Modeling	51
4.1	PROBLEM DEFINITION	51
4.2	CONSERVATION EQUATIONS	54
4.3	INTERMITTENCY TRANSITION $\kappa - \omega$ SST MODEL	56
4.4	BOUNDARY CONDITIONS	57
4.4.1	<i>Windkessel Model</i>	59
4.5	HEMODYNAMIC VARIABLES	64
4.5.1	<i>Strain Indices</i>	64
5	Numerical Modeling	66

5.1	PREPROCESSING	66
5.2	PROCESSING	70
5.2.1	<i>Coupling With Windkessel Model</i>	71
5.3	POST-PROCESSING	71
6	Healthy Patient	73
6.1	MEASURED 4D FLOW MRI VARIABLES	73
6.2	BOUNDARY CONDITION	74
6.3	POST-PROCESSING DEFINITIONS	78
6.4	MASS FLOW RATE	79
6.5	PRESSURE	83
6.5.1	<i>Approximated Pressure Difference</i>	86
6.6	WALL SHEAR STRESS	90
6.7	STREAMLINES	93
6.8	THREE-ELEMENT WINDKESSEL MODEL X PERCENTAGE OUTFLOW AS BOUNDARY CONDITION	97
7	Patients With Ascending Aortic Aneurysm	101
7.1	AORTIC GEOMETRY AND METHODOLOGY IN PATIENT CLASSIFICATION	101
7.2	BOUNDARY CONDITION	107
7.3	PRESSURE	109
7.3.1	<i>TAP</i>	112
7.4	WALL SHEAR STRESS	115
7.4.1	<i>TAWSS</i>	118
7.4.2	<i>OSI</i>	121
8	Final Coments	125
8.1	CONCLUSION	128
8.2	FUTURE DEVELOPMENTS	128
	References	130
	A1. Intermittency Transition Model	156
	A2. Grid Test	159
	A3. The Cardiac Cycle Periodicity	164
	A4. Inlet Flow Rate	167
	A5. Patients' Information	171

List of figures

Figure 1.1 – Progression of a normal cardiac valve to a severe aortic stenosis. Adapted from Otto (2008).	23
Figure 1.2 – Thesis workflow.	26
Figure 2.1 – Heart and its principals' parts (CC BY-SA 3.0, 2023).	27
Figure 2.2 – a) Valves during diastolic phase. b) Valves during systolic phase (Sun, 2014).	29
Figure 2.3 – Wiggers Diagram (Courneya & Parker, 2011).	30
Figure 2.4 – Aorta in a human body (CC BY-SA 3.0, 2023).	31
Figure 2.5 – Physiologic thoracic aorta (Criscione, 2013).	32
Figure 2.6 – Aortic root reconstructions: principal anatomic components of the aortic root (Morganti, 2011).	33
Figure 2.7 – Aortic valve during a) systole. b) diastole (Mendelson & Schoen, 2006).	33
Figure 2.8 – Aortic valve histology within the three layers and interstitial and endothelial cells (Mendelson & Schoen, 2006).	34
Figure 2.9 – Main blood composition (Sochi, 2013).	35
Figure 2.10 – Blood viscosity x Shear Rate for a range of hematocrit concentrations (Sochi, 2013).	36
Figure 2.11 – Dependence of blood viscosity on the internal diameter of a vessel (Mogensen, 2011).	37
Figure 2.12 – Viscosity profile of whole blood and plasma (Rosencranz & Bogen, 2006).	37
Figure 3.1 – A typical example of an ascending aortic aneurysm. Adapted from Criscione (2013).	41
Figure 3.2 – A) and B) Computed tomography determining the site of the rupture. C) WSS' mapping with the red circle delimitating the rupture region (Malvindi et al., 2016).	43
Figure 3.3 – Velocity field of an aorta captured by an CTA exam (Own Authorship).	46
Figure 3.4 - Flow streamlines during peak systole in (a) a patient with an AscAA and (b) and normal healthy volunteer (Biegging et al., 2011).	47

Figure 3.5 – Difference between 4D-Flow MRI and CFD simulation (Itatani et al., 2017).	48
Figure 4.1 – Illustration of a reconstructed 3D aortic model (Own Authorship).	51
Figure 4.2 – Turbulence resolution approaches. Adapted from Sporschill (2021).	53
Figure 4.3 - Fluctuation of a random variable in a turbulent flow depending on time (Own Authorship).	54
Figure 4.4 – Inlet and outlets in a 3D aorta (Own Authorship).	58
Figure 4.5 – Concept of Windkessel model (Westerhof et al., 2009).	60
Figure 4.6 – Two-element Windkessel model (Own Authorship).	61
Figure 4.7 - Three-element Windkessel model (Own Authorship).	62
Figure 4.8 Diagram of the flow rate (systole and diastole) and pressure inlet during a cardiac cycle. Adapted from Borazjani et al. (2008) and Ibanez (2019).	62
Figure 4.9 – Schematic representation of the inlet and boundary (Own Authorship).	63
Figure 5.1 – CTA slices views with Synedra View Personal (Own Authorship).	67
Figure 5.2 – Step to collect slice distance at Fiji Software (Own Authorship).	68
Figure 5.3 – (a) All images transferred to Fiji (b) Aortic region selected (c) Segmented aorta (Own Authorship).	68
Figure 5.4 – Reference system (Own Authorship).	69
Figure 5.5 – Aorta's grid and a perpendicular slice (Own Authorship).	70
Figure 5.6 – (a) Coupling of 3D geometry and the Windkessel RCR model. (b) Iterative update scheme for pressure and flow (Own Authorship).	71
Figure 6.1 – Volumetric flow rate in planes along the ascending aorta provided by cvi42 v5.14.2 4D-Flow MRI software.	74
Figure 6.2 – Volumetric flow rate curves of outlet planes provided by cvi42 v5.14.2 4D-Flow software.	75
Figure 6.3 – Mass flow rate input curve.	75
Figure 6.4 – Comparison between the mass flow inlet curve and sum of all mass outflow curve of the experimental results.	76
Figure 6.5 – Difference between inlet mass flow and the sum outflow of the experimental results.	77
Figure 6.6 – Inlet, outlets and selected planes along the aorta (Own Authorship).	78
Figure 6.7 –Region of interest (Own Authorship).	79
Figure 6.8 – Numerical-experimental comparison of mass flow rate at outputs	80

Figure 6.9 – Pressure drops of planes in ascending aorta provided by cvi42 v5.14.2 4D-Flow software	83
Figure 6.10 – Numerical-experimental pressure drops comparison of planes along the aorta using Eq. 6.9.	85
Figure 6.11 – Numerical-experimental pressure drops planes comparison.	89
Figure 6.12 - WSS curves of ‘asc1’, ‘asc2’, ‘asc3’, ‘desc1’ and ‘desc2’ planes provided by cvi42 v5.14.2 4D-Flow software.	91
Figure 6.13 – Numerical-experimental WSS in planes of the ascending aorta.	91
Figure 6.14 – Inlet Reynolds number.	92
Figure 6.15 – WSS Comparison.	93
Figure 6.16 – Numerical simulation streamlines over the cardiac cycle colored by velocity vector magnitude.	95
Figure 6.17 – 4D-Flow experimental streamlines over the cardiac cycle colored by velocity vector magnitude.	96
Figure 6.18 – <i>TAWSS</i> field using as BC (a) Percentage Outflow. (b) WK.	98
Figure 6.19 – <i>OSI</i> field using as BC: (a) Percentage Outflow. (b) WK.	99
Figure 6.20 – Pressure comparison considering the two different BC.	100
Figure 7.1 - Selection of patients with ascending aortic aneurysm (Azevedo et al., 2024).	102
Figure 7.2 – Region of interest colored in red (Own Authorship).	103
Figure 7.3– Same aorta overlapped in two different years with circles indicating the difference in the size of the of patient Y5: (a) View 1. (b) View 2 (Own Authorship).	104
Figure 7.4 - θ angle (Salmasi et al., 2021).	105
Figure 7.5 – Angles proposed by Almeida et al. (2022): (a) θI . (b) θII .	105
Figure 7.6 – Aorta’s geometric parameters as a function of volume ratio of second to first exam: (a) inlet diameter, (b) angle θ (c) angle θI (d) angle θII .	106
Figure 7.7 – Complete cardiac cycle for patient with aneurysm.	108
Figure 7.8 – Percentage of outflow distribution.	108
Figure 7.9 –Area average pressure above 100 Pa, $P > 100 Pa$, time evolution along the cardiac cycle: (a) patients with growth; (b) patients without growth.	110
Figure 7.10 - Dispersal of high pressure $P(> 100 Pa)$ values.	111
Figure 7.11 - Dispersal of time period with high pressure. $\Delta t_{pressure}$.	111
Figure 7.12 – Time and area average high pressure $P > 100 Pa$ dependence on aorta’s geometric parameters: (a) inlet diameter D , (b) angle θ (c) angle θI (d) angle θII .	112

Figure 7.13 - TAP for patients without and with aneurysm growth.	113
Figure 7.14 - Dispersal of TAP_{ave} values.	114
Figure 7.15 – TAP_{ave} dependence on aorta's geometric parameters: (a) inlet diameter, (b) angle θ (c) angle θI (d) angle θII .	115
Figure 7.16 – Average high WSS time evolution during the cardiac cycle, $WSS(> 7 Pa)$. (a) patients with growth; (b) patients without growth.	116
Figure 7.17 - Dispersion of $WSS(> 7 Pa)$ values.	117
Figure 7.18 - Dispersion of $\Delta tWSS$ values.	117
Figure 7.19 - $WSS > 7 Pa$ dependence on aorta's geometric parameters: (a) inlet diameter, (b) angle θ (c) angle θI (d) angle θII .	118
Figure 7.20 – $TAWSS$ of patients without and with aneurysm growth.	119
Figure 7.21 Dispersal of $TAWSS_{ave}$ values.	120
Figure 7.22 - $TAWSS_{ave}$ dependence on aorta's geometric parameters: (a) inlet diameter D , (b) angle θ (c) angle θI (d) angle θII .	121
Figure 7.23 – OSI for patients without and with aneurysm growth.	122
Figure 7.24 - Dispersal of OSI_{ave} values.	123
Figure 7.25 - OSI_{ave} dependence on aorta's geometric parameters: (a) inlet diameter, (b) angle θ (c) angle θI (d) angle θII .	124
Figure A2.1 – The complete cardiac cycle demarcated by the interval Δt_1 considered to analyze the hemodynamic variables.	160
Figure A2.2 – $TAWSS$ field for the three different meshes: (a) 1.87×10^6 cells. (b) 3.48×10^6 cells. (c) 7.31×10^6 cells.	161
Figure A2.3 - OSI field for the three different meshes: (a) 1.87×10^6 cells. (b) 3.48×10^6 cells. (c) 7.31×10^6 cells.	162
Figure A2.4 – Z-line.	162
Figure A3.1 – The average cycle variables fields on 4 different cycles: (a) TAP . (b) $TAWSS$. (c) OSI .	165

List of Tables

Table 5.1 – Example of slice distance and pixel size.	69
Table 6.1 – Flow percentage art each outlet.	77
Table 6.2 – Three-element Windkessel model parameters for each outlet.	78
Table 6.3 – Numerical-experimental comparison of inlet x outputs mass flow rate	81
Table 6.4 – Numerical-experimental comparison of velocity peaks and average mass flow rate at auxiliary planes	82
Table 6.5 – Numerical-experimental comparison of maximum and cycle time-average of the average-area pressure difference	84
Table 6.6 – Numerical-experimental comparison of maximum calculated pressure drops.	90
Table 6.7 – 3E WK x Outflow variables comparison.	97
Table 7.1 – Mean values and the standard deviation of analyzed variables. Adapted from Azevedo et al. (2024).	107
Table 7.2 – Quantitative analysis of patients: mean $P(> 100 Pa)$ and $\Delta t_{pressure}$.	110
Table 7.3 - Quantitative analysis of TAP_{min} , TAP_{ave} and TAP_{max} .	114
Table 7.4 - Quantitative analysis of $WSS(> 7 Pa)$ and $\Delta twss$.	116
Table 7.5 - Quantitative analysis of $TAWSS_{min}$, $TAWSS_{ave}$ and $TAWSS_{max}$.	120
Table 7.6 - Quantitative analysis of OSI_{min} , OSI_{ave} and OSI_{max} .	123
Table A2.1 – Variables in the region of interest.	161
Table A3.1 – Comparison of the cardiac cycles	161
Table A4.1 – Mass flow rate input data for healthy patient.	167
Table A5.1 – Time between exams, inlet diameter and volume of patients with aneurysm.	171
Table A5.2 – Geometric parameters of patients with aneurysm.	172

List of Symbols and Abbreviations

A	Cross-Sectional Area
asc	Ascending
$asc1, asc2, asc3$	Ascending 1, Ascending 2 and Ascending 3
C	Capacitance
C_μ	Empirical Constant
c	Pulse Wave Velocity
\mathcal{D}	Maximum Aneurysm Diameter
D	Inlet Valve Diameter
D_κ	Destruction of Turbulent Kinetic Energy
D_ω	Destruction of Specific Dissipation
$desc$	Descending
$desc1, desc2$	Descending 1 and Descending 2
F_1, F_2	Damping Factors
f	Friction Factor
G_κ	Generation of Turbulent Kinetic Energy
G_ω	Generation of Specific Dissipation
I_κ	Turbulent Intensity
L_i	Length of the Vessel Segment
m	Mass
\dot{m}	Mass Flow Rate
N	No, Patients Without Growth
out	Outlet
$out1, out2$	Outlet 1 and Outlet 2
$out3, out4$	Outlet 3 and Outlet 4
p_i^0	Initial Pressure
p^*	Instantaneous Pressure
p	Time Average Pressure
\hat{p}	Modified Pressure
R_d	Distal Resistance
R_{ef}	Effective Radius
Re	Reynolds number

$Re_\beta, Re_\kappa, Re_\omega$	Empirical turbulent Reynolds parameters
R_p	Proximal Resistance
$Re_{\theta C}$	Critical Reynolds Number
R_{tot}	Total Resistance
S	Magnitude of the Time Average Strain Rate Tensor
S_{ij}	Time Average Strain Rate Tensor
T	Period
T_I	Time Interval of Interest
Tu_l	Turbulent Intensity
t	Time
u, v, w	Velocities Components in the x, y and z directions
u_j	Time Average Velocity Vector Component j
u_j^*	Instantaneous Velocity Vector Component j
u_t	Tangential Velocity
u_τ	Friction Velocity
V	Average Plane Velocity
\mathbf{V}	Velocity Vector
x, y, z	Spatial Coordinate Components
x_j	Coordinate Axes
Y	YES, Patients With Growth
y	Wall Distance
y^+	Dimensionless Wall Distance
$year1, year2$	Year 1, Year 2
W_{in}	Inlet Normal Velocity in the z direction

Greek Symbols

α^*	Empirical Function
$\alpha_\infty^*, \alpha_0, a_1$	Empirical Constants
$\beta_{i,1}, \beta_{i,2}, \beta_\infty^*$	Empirical Constants
δ_{ij}	Kronecker Delta
ε	Dissipation Rate
ϵ	Difference Variable
ϵ_{ijk}	Levi-Civita Symbol
ξ_i	Vorticity

ξ	Blending Factor
γ	Turbulent Intermittency
$\theta, \theta_I, \theta_{II}$	Heart-Aortic Angles
k	von Kármán constant
κ	Turbulent Kinetic Energy
$\lambda_{\theta l}$	Non-Dimensional Pressure Gradient Parameter
μ	Molecular Viscosity
μ_t	Turbulent Viscosity
ν	Kinematic Viscosity
ρ	Density
$\sigma_\kappa, \sigma_{\kappa,1}, \sigma_{\kappa,2}$	Empirical turbulent kinetic energy Prandtl numbers
$\sigma_\omega, \sigma_{\omega,1}, \sigma_{\omega,2}$	Empirical turbulent dissipation Prandtl numbers
τ_{ij}	Viscous Stress Tensor
τ_w	Wall Shear Stress
ϕ	Generic Variable
$-\rho \overline{u'_j u'_i}$	Turbulent Tensor
ω	Specific Dissipation
Ω	Vorticity Magnitude
Ω_{ij}	Vorticity Tensor
\forall	Volume
$\dot{\forall}$	Volumetric Rate

Subscripts

<i>avg</i>	Average
<i>conv</i>	Convective Inertia
<i>diastole</i>	Diastole
<i>exp</i>	Experimental
<i>i</i>	Selected Plane
<i>in</i>	Inlet
<i>lam</i>	Laminar
<i>max</i>	Maximum
<i>min</i>	Minimum
<i>n</i>	Normal Component
<i>num</i>	Numerical
<i>peak</i>	Peak

<i>per</i>	Percentage
<i>pressure</i>	Pressure
<i>ref</i>	Reference
<i>scan</i>	Scan
<i>systole</i>	Systole
<i>tran</i>	Transient Inertia
<i>tr_B</i>	Convective and Transient Contribution
<i>turb</i>	Turbulent
<i>w</i>	Wall

Acronym

AAoA	Ascending Aortic Aneurysm
AAV	Ascending Aortic Volume
AP	Aortic Pressure
AS	Aortic Stenosis
AscAD	Ascending Aortic Dilatation
ATAA	Ascending Thoracic Aortic Aneurysm
AV	Atrioventricular valves
AVS	Aortic Valvular Stenosis
AVJ	Aorto-Ventricular Junction
BAV	Bicuspid Aortic Valve
BC	Boundary Conditions
bpm	Beats per minute
CAVD	Calcific Aortic Valve Disease
CFD	Computational Fluid Dynamics
CMR	Cardiovascular Magnetic Resonance
CT	Computed Tomography
CTA	Computed Tomography Angiography
CVD	Cardiovascular Disease
DDES	Delayed Detached Eddy Simulation
DES	Detached Eddy Simulation
DNS	Direct Numerical Simulation
ECG	Electrocardiogram
ECM	Extra Cellular Matrix
EOA	Effective Orifice Area
FSI	Fluid-Structure Interaction

GBD	Global Burden of Disease Study
IQR	Interquartile Range
LAP	Left Atrial Pressure
LVOT	Left Ventricular Outflow Tract
LVP	Left Ventricular Pressure
LVV	Left Ventricular Volume
MRI	Magnetic Resonance Imaging
NS	Navier-Stokes
OSI	Oscillatory Shear Stress Index
PSM	Patient-Specific Modeling
RANS	Reynolds-Averaged Navier Stokes
RBC	Red Blood Cells
RCR WK	Resistance -Capacitance_Resistance Windkessel
SD	Standard Deviation
STJ	Sinotubular Junction
TAA	Thoracic Aortic Aneurysm
TAP	Time Average Pressure
TAWSS	Time-Averaged Wall Shear Stress
TTE	Transthoracic Echocardiography
URANS	Unsteady Reynolds-Averaged Navier-Stokes
WK	Windkessel
WSS	Wall Shear Stress
1D	One-Dimensional
2D	Two-Dimensional
2E WK	2-Element Windkessel Model
3D	Three-Dimensional
3E WM	3-Element Windkessel Model
4D-Flow	Four-Dimensional Flow

You can't connect the dots looking forward; you can only connect them looking backwards.

Steve Jobs

1 INTRODUCTION

Cardiovascular diseases (CVDs) are the principal cause of global mortality (Roth et al., 2020) as well in Brazil (Oliveira et al., 2022). The Global Burden of Disease Study (GBD) is a systematic, multinational collaborative and scientific effort research used to quantify the magnitude of diseases and risk factors burden for every country and region in the world. The GBD 2019 (Roth et al., 2020; Abbafati et al., 2020) reveals that, in Brazil, CVDs are estimated in 6,1% of the population and has grown from 1990 to 2019.

The heart valve diseases increased 50% from 1990 to 2019 in Brazil (Roth et al., 2020). Focusing on pathologies in the aortas, the aortic aneurysm, which consists of dilatation of the artery, in 2019 reached 3.32 million years of life lost (YLLs) (it was 2 million in 1990) and 172,000 deaths (in 1990 was 100,000) (Roth et al., 2020). In Brazil, the aortic aneurysm is the 7th cause of death when is considered the deaths by CVDs in 2019 (Oliveira et al., 2022).

An aneurysm is a localized widening or ballooning of a portion of an artery, when its diameter exceeds 1.5 times the normal calibre, usually due to the weakness of the wall of the blood vessel (Marinov et al., 2013). It can occur in any part of the body, being very dangerous since its rupture or dissection causes massive internal bleeding.

Ascending thoracic aortic aneurysms (ATAAs) are the most common (Bicer et al., 2020) and frequently, an asymptomatic disease. In so many cases, it is discovered by accident when a chest X-ray or other screening exam is required for different reasons (Aggarwal et al., 2011).

This condition can be associated to the population growth and population aging (Roth et al., 2020; Oliveira et al., 2022). Besides that, factors risks such as sex (more incidence in men over women) (Lederle et al., 2000), arteriosclerosis (Messika-Zeitoun et al., 2007), hypertension (Kato et al., 2008), smoking (Pendergraft, 2016; Landenhed et al., 2015), obesity (Eckstein & Maegdefessel, 2020) and inflammatory or autoimmune diseases (Chen et al., 2006) can affect the aorta, which may lead to the development of an aneurysm.

ATAA is usually associated with aortic valve diseases, especially aortic stenosis (AS) (Silva et al., 2019). AS is the obstruction of blood flow across the

aortic valve, that occurs with a narrowing of the patient's aortic valve opening. Etiologies include congenital (bicuspid/unicuspid), rheumatic disease and calcification (Pujari & Agasthi, 2023).

The Calcific Aortic Valve Disease (CAVD) is a condition that calcium deposits form on the aortic valve and in atherosclerotic vascular lesions. The CAVD is a slow and progressive disorder, that ranges from mild valve thickening without obstruction of blood flow, until severe calcification with impaired leaflet motion, as showed in Figure 1.1. The thick increment at aortic valve leaflets and the progressive narrowing of aortic annulus leads to increase mechanical stress on the left ventricle and reduces cardiac output, ensuing further complications (Lerman et al., 2015).

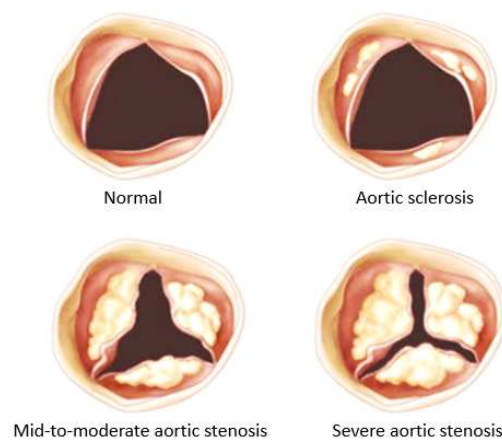


Figure 1.1 – Progression of a normal cardiac valve to a severe aortic stenosis. Adapted from Otto (2008).

The treatment for patients with significant aortic valve insufficiency includes repair or replacement of the aortic valve. The election is made considering factors as age, type of the valve disease and the mechanisms that causes the regurgitation (Ramlawi et al., 2014).

If the timing for valve replacement is not clearly determined, a typical consequence from either reduced valve area or atherosclerosis is the dilation of the ascending aorta (Otto & Prendergast, 2014). This dilatation can evolve to an aneurysm or even an aortic dissection (rupture).

For an aneurysm larger than 5.5 cm of diameter, a replacement surgery is indicated, since if an ATAA ruptures, the mortality is nearly 100% (He et al., 2021). Nonetheless, when it is not recommended, the patient must be followed up in order to avoid rupture or dissection.

Notwithstanding, some aneurysms smaller than threshold of 5.5 cm have ruptured while some larger aneurysms do not (Coady et al., 1999; Bürk et al., 2012). Thus, this simple geometrical criterion is controversial since it may

underestimate the rupture risks of small aneurysms as well overestimated the risk of large aneurysms (He et al., 2021). In the same way, for some patients, the aneurysm does not grow, therefore, remaining with the same diameter in years of follow-up, while others present a significant growth. The mechanisms for the different behaviors are not well known (Kuzmik et al., 2012; Weininger et al., 2022).

Researchers point out that changes of flow patterns can influence the disease (Almeida et al., 2022; Hope et al., 2007; Weigang et al., 2008). Vessel morphology with an associated aneurysm repair show changes in local vortical, helical flow formations and flow acceleration (Frydrychowicz et al., 2007) as well, in the increase of wall shear stress (Salmasi et al., 2021).

In order to understand the impact of blood flow behavior inside arteries and vessels, Computational Fluid Dynamics (CFD) is emerging as an excellent mechanical engineering tool to figure out the pathophysiology of the development and progression of cardiovascular diseases, as well to establish and refine the individually assessment of adequate treatment of patients (Lee B-K., 2011; Randles et al., 2017). Combining CFD parameters with proper and consistent validation, it may be possible to revolutionize aortic treatment decisions, helping to decide how, when and where to intervene (Ong et al., 2020).

The Four-dimensional Flow Magnetic Resonance Imaging (4D-Flow MRI) is a technique that combines Magnetic Resonance Imaging with specialized software to capture a detailed picture of blood flow patterns throughout the body. Integrating both techniques (CFD and 4D-Flow MRI), Patient-Specific Modeling is used to perform patient-specific simulations, employing the geometry and boundary conditions determined from 4D-Flow MRI data. It is gaining interest due to the potential to improve diagnosis and optimize clinical treatment by predicting outcomes of therapies and surgical interventions.

From this analysis, it was observed a gap in the literature related to the relationship between flow patterns and tensions in the aortic wall and aneurysm. Furthermore, since the flow depends directly on the geometry and the aortas' geometries vary significantly, it is imperative to analyze a large number of patients.

Therefore, this work aims to contribute in this field by analyzing the complete cardiac cycle of a large number of patients with indications of the growth or not of the aneurysm, providing information of which parameters may in the future lead to greater dilation of the aneurysm. Furthermore, the correlation analysis of hemodynamic variables and geometry, delving into the remodeling process, helps to improve the understanding of aortic pathophysiology and contributes to the advancement of knowledge in this area.

In the modelling process, several hypotheses are necessary. To assist in this evaluation, this thesis presents a comparison between a CFD simulation and 4D-Flow MRI data of a healthy patient, to verify the performance of the methodology.

1.1 Objectives

This doctoral thesis aims to achieve two main objectives:

- Propose a fluid-flow model to numerically analyze the blood flow in the ascending aorta.
 - The methodology is evaluated by comparing the CFD predictions of a healthy specific-patient with an *in vivo* measurements.
 - In addition, it is performed an investigation of the impact of different models for the outlet boundary conditions on flow results.
- Anatomic-specific analysis to identify flow variables correlation with aneurysm growth. More specifically:
 - Selection of the volume as a criterion to classify patients into two groups: with and without growth of the ascending aortic aneurysm.
 - Analysis and evaluation of hemodynamic variables of the complete cardiac cycle of 30 patients with ascending aortic aneurysm with non-surgical indication, based on their anatomy.
 - Identification of hemodynamic variables that indicate progression of the ascending aortic aneurysm.

1.2 Research Ethics

Research involving human beings, individually or collectively, directly or indirectly, including the management of their data, information or biological materials must be submitted to a Research Ethics Committee, which is coordinated by the National Council of Ethics in Research, that is one of the commissions of National Health Council of the Ministry of Health, that analyses, decides and becomes co-responsible for ensuring the protection of participants.

As this research uses images and data from real patients, it was necessary to have the assessment by an ethics committee. In this way, the research project was subjected by the approval of the Research Ethics Committee of the National Institute of Cardiology with the register number CAAE 86716318.3.0000.5272.

1.3 Thesis outline

The thesis contains 8 chapters including this introduction. Since this is a multidisciplinary study, to aid the engineer reader, in the next chapter, fundamental concepts related to the heart are presented. In the sequence, a literature review is presented in Chapter 3. Chapter 4 shows the mathematical model employed in the present analysis. The numerical modeling is in Chapter 5, explaining the preprocessing, processing and post-processing steps. Chapter 6 presents the validation of the methodology through a healthy patient-specific analysis. The results of the numerical simulation of the 30 patients are analyzed in Chapter 7. Finally, in Chapter 8 the final comments and suggestions for future work are given.

Figure 1.2. presents the thesis workflow, i.e., a step by step of how the research was developed. First, a healthy patient volunteered for the study. Then it was necessary the selection of ATAA patients, who underwent Computed Tomography Angiography (CTA) scanning and the healthy patient recruitment, that underwent a Four-Dimensional Flow Magnetic Resonance Imaging technique or 4D-Flow MRI. After that, procedures of preprocessing, processing and post-processing of data were done aiming to validate the methodology, to understand the impact of different boundary conditions imposed, as well, the comparison between the results of patients with and without aneurysm growth.

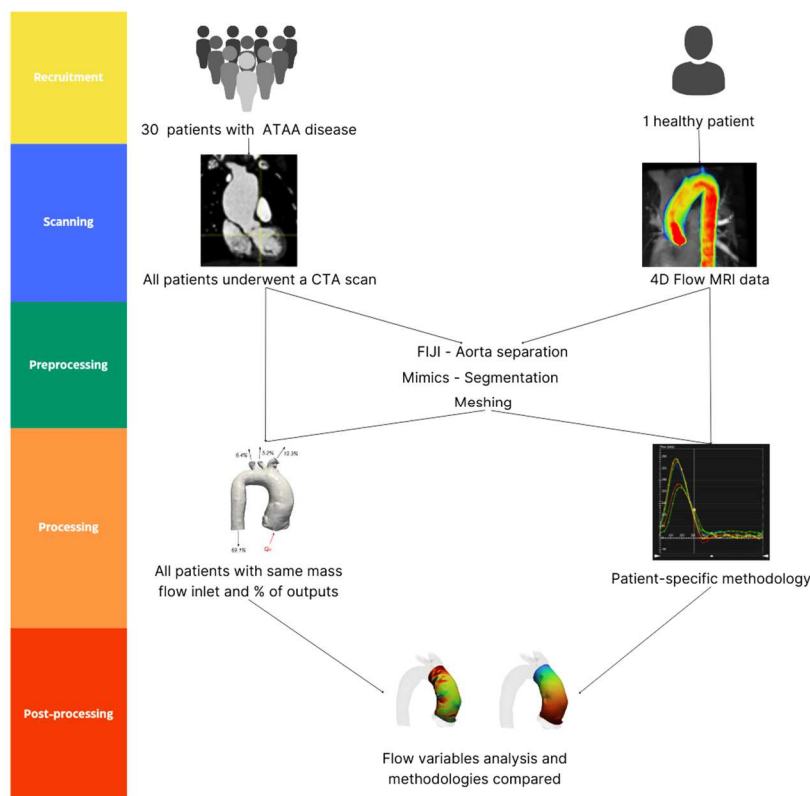


Figure 1.2 – Thesis workflow.

2 FUNDAMENTAL CONCEPTS

In this chapter, some fundamental concepts of the circulatory system are described, such as the heart structure, cardiac cycle, aorta, aortic valve, and heart diseases.

2.1 Heart Structure

The central part of the circulatory system is the heart, which is a muscular organ, with the function of pumping the blood to provide oxygen and nutrients to body, as well as to withdraw metabolic waste as dioxide carbon from the human tissues.

Figure 2.1 shows a heart with its principal parts. It is divided into four different chambers; the two upper are called atria, and the two lower are known as ventricles. The blood travels unidirectionally, due to the presence of valves inside the cardiac cavities. The opening and closing of the valves are controlled by difference of pressure.

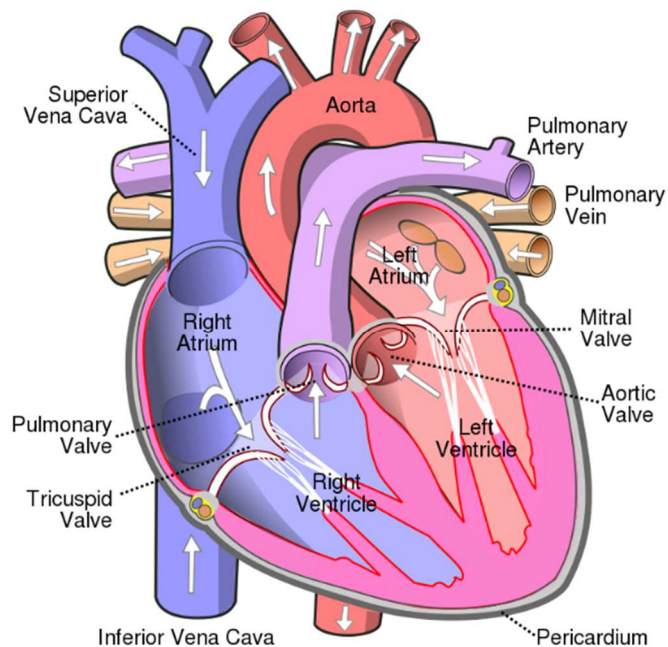


Figure 2.1 – Heart and its principals' parts (CC BY-SA 3.0, 2023).

The chambers located at the right part receive deoxygenated blood from the body and forward to the lung. The right atrium, located at the upper part, receives

blood from the inferior vena cava (blood from legs and lower torso) and superior vena cava (blood from head and upper body). The left atrium is located at upper left chamber of the heart. During the cardiac cycle, it receives oxygenated blood from the lungs through the pulmonary vein. Once both atria are full, they contract. The deoxygenated blood in the right atrium flows into the right ventricle through the open tricuspid valve and the oxygenated blood from the left atrium flows into the left ventricle through the open mitral valve.

The ventricles pump blood away from the heart, its walls known as pericardium, are fibrous and thicker than the wall of atria to resist the high pressures at these chambers. When the ventricles contract, there is a pressure gain and at the right side, the tricuspid valve opens while at the left side, the aortic valve opens. The right ventricle pumps venous blood toward the pulmonary artery that is connected to the lungs and, and on the other side, the left ventricle pumps rich oxygen blood to the aorta, that sends it to the rest of the body.

2.2 Cardiac Cycle

The cardiac cycle begins when venous blood from the body flows into the right atrium. After the chamber is full, blood flows to the right ventricle and then goes to the lungs, through the pulmonary artery, which is split into smaller arteries that are progressively subdivided, becoming arterioles. The gas exchange occurs by capillary microcirculation. During this trajectory, blood releases the waste gases, becomes rich in oxygen, and returns through the pulmonary vein, flowing to the left atrium. After the chamber is completely full, the blood flows into the left ventricle. Finally, the left ventricle pumps it to the aorta that carries blood to all parts of the body, and one cycle is completed.

The cardiac output, i.e., the volume of blood pumped out of the heart, is for an average person at rest, about 5 l/min (normal range 4-8 l/min) (Bacon, 2013). To enable this pumping, the sinoatrial node located at the posterior wall of the right atrium generates a powerful periodical heartbeat, at constant frequencies. The interval between the start of one heartbeat until the beginning of the next is known as cardiac cycle, i.e., from relaxation through contraction and back to relaxation again.

The average rate of the pulse for a healthy adult is 72 beats per minute (bpm) (Sharma, 2015), meaning that the cardiac cycle happens 72 times in a minute. However, the American Heart Association accepts as a normal beat range between 60 and 100 bpm (American Heart Association, n.d.).

The maximum pressure experienced when heart contracts and ejects blood into the aorta from the left ventricle (approximately 120 mmHg) is defined as the systolic blood pressure. In contrast, the minimum pressure occurs when the heart is relaxing before ejecting blood into the aorta from the left ventricle (approximately 80 mmHg) (Homan et al., 2012).

2.3 Heart Valves

During the cardiac cycle, the blood flows through the system of chambers, valves, and vessels. The valves open due to the pressure differential between chambers or chamber/vessel, and the flow through them is unidirectional. The valves are formed by endothelial and connective tissue, forming flaps (termed leaflets or cusps) that separates two chambers (the atrium and the ventricle – atrioventricular valves (AV), that is the mitral and tricuspid valve) or a chamber of a great vessel (the semilunar valves, that isolates right ventricle and pulmonary artery – the pulmonary valve –, and left ventricle and aorta – the aortic valve).

Figure 2.2 shows AV and semilunar valves in two different time instants on the cardiac cycle. Figure 2.2a displays diastolic period, when semilunar valves are closed to prevent backward flow, and AV valves are open due the pressure difference present between atria and ventricles. Figure 2.2b corresponds to systolic time instant, when the maximum pressure occurs, forcing the opening of the aortic and pulmonary valves, while AV valves are closed.

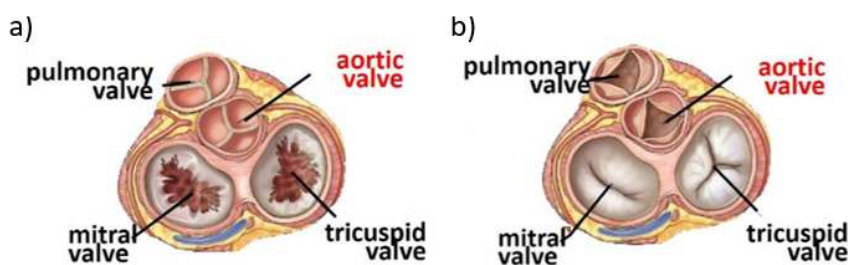


Figure 2.2 – a) Valves during diastolic phase. b) Valves during systolic phase (Sun, 2014).

2.4 The Wiggers Diagram

The Wiggers Diagram shown at Figure 2.3 is a graphical representation of the cardiac cycle. It is separated into cardiac events through diastole, systole and back to diastole.

As described by Courneya & Parker (2011), the diagram illustrates pressures and volumes in the left heart. The top panel Y-axis corresponds to pressure (in

mmHg) and shows: aortic pressure (AP), left atrial pressure (LAP) and left ventricular pressure (LVP). The middle panel Y-axis indicates the left ventricular volume (LVV), in mL. Electrocardiogram (ECG) waveforms shown at bottom panel (P, QRS and T waves) are associated with changes in voltage as a result of electrical conduction through the heart muscle and finally, the curve of the four heart sounds (S1, S2, S3 and S4) are illustrated.

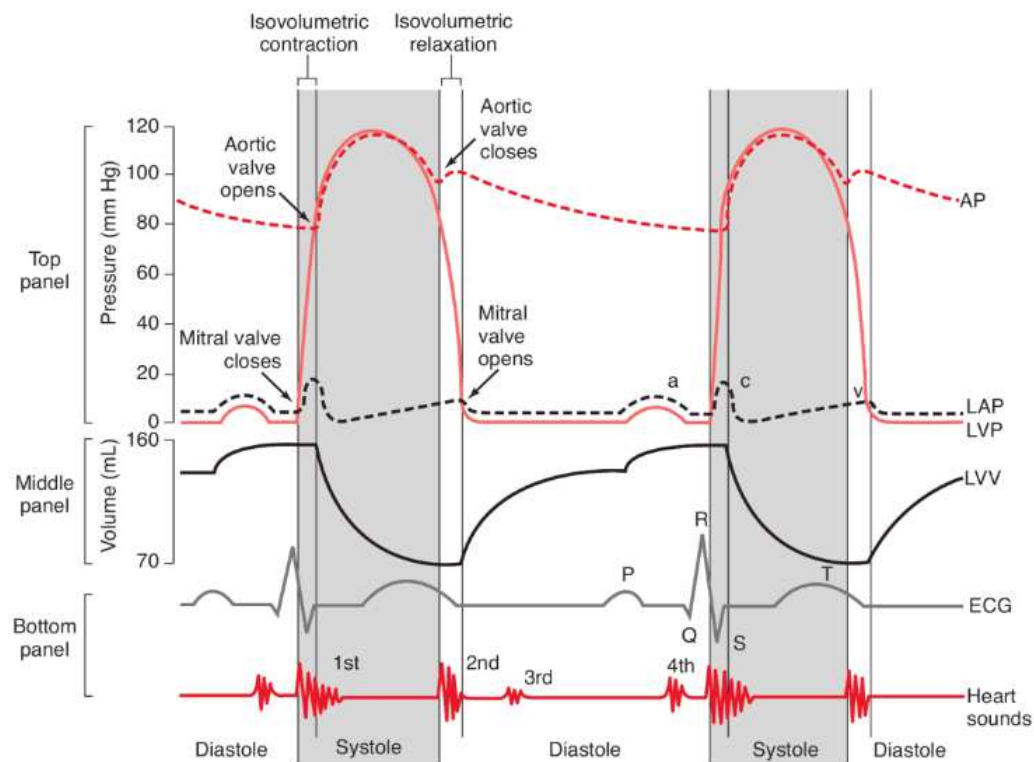


Figure 2.3 – Wiggers Diagram (Courneya & Parker, 2011).

Observing the left side of the graphic, it is seen the diastole, when left atrium and ventricle are fully relaxed, so the pressure is low. Note that aortic pressure is considerably higher than left ventricular pressure, during the relaxation period, but there is not backward because the aortic valve is closed. In the end of ventricular filling, there is a point when the left ventricular volume is expected to rise. The pressure of the left ventricle is slightly lower than left atrial pressure, so the mitral valve is opened, and left ventricle continues to fill passively with blood.

The sinoatrial node located at the posterior wall of the right atrium sends a potential impulse in a cluster of cells and begins to excite the atria. Atrial depolarization generates de “P wave” on ECG, what makes atrial contracts and fills the ventricle with the rest of blood present in this chamber.

After that, the ventricles begin to depolarize (“QRS wave” in the ECG), they contract and systole initiates. The mitral valve closes and for a briefly moment while

the aortic valve is still closed, there is no change in left ventricular volume, but there is an increase in left ventricular pressure, being this part of cardiac cycle called as isovolumetric contraction.

When aortic valve opens, blood is injected into aorta, causing a rise in the aortic pressure, as well a rapid reduction of the left ventricular volume. After reaching the aortic pressure peak, ventricles begin to repolarize and a “T wave” can be seen on ECG; indicating that contraction of the ventricle has ended. As a result, the pressure begins to fall, eliminating the injection of blood into the aorta. During a moment when the left ventricular pressure is below the aortic pressure, the aortic valve leaflets are still opened, due the inertia of the blood flowing through the valve, but the mitral valve has not opened. This period is called isovolumetric relaxation and pressure falls. When mitral valve reopens, diastole starts and cardiac cycle initiates again.

2.5 Aorta

Aorta is the major artery in the human body. Figure 2.4 shows an aorta, where it is possible to visualize the connection with the heart and its principals' parts. The physiological normal diameter in adults is established as 33.4 mm, with interquartile range (IQR) around 30.7-36.7 mm (Eliathamby et al., 2021; Rahmani et al., 2016). Its length from the aortic valve to the iliac bifurcation measures a median of 83.2mm, with IQR 74.5-90.7 mm (Eliathamby et al., 2021).

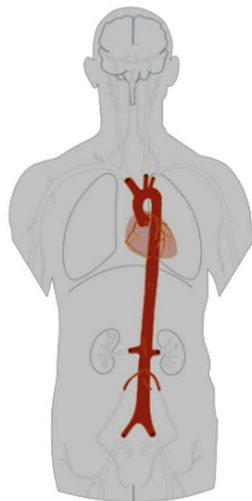


Figure 2.4 – Aorta in a human body (CC BY-SA 3.0, 2023).

Human aorta is classified in two differed ways (Criscione, 2013). The first one is according to the anatomical region. The thoracic aorta extends from the aortic annulus to the diaphragm. After that, there is the abdominal aorta, which

runs up to the aortic bifurcations. The other classification is based on the pathway of blood flow ejected from the aortic valve. First, there is the ascending aorta, which is turned into the aortic arch, being responsible to distribute blood to the upper limbs and head, continuing the blood trajectory, it becomes the descending aorta that presenting a vertical downward trajectory until its bifurcation into two iliac arteries.

A thoracic aorta is presented in Figure 2.5. The aortic root is a bulb-shaped fibrous structure situated between the left ventricle outflow and ascending aorta, which supports the aortic valve leaflets and where is located the origin of the coronary arteries (right and left coronaries) (Saremi et al., 2010). The coronaries are responsible for supplying blood that recoils during diastole to the heart.

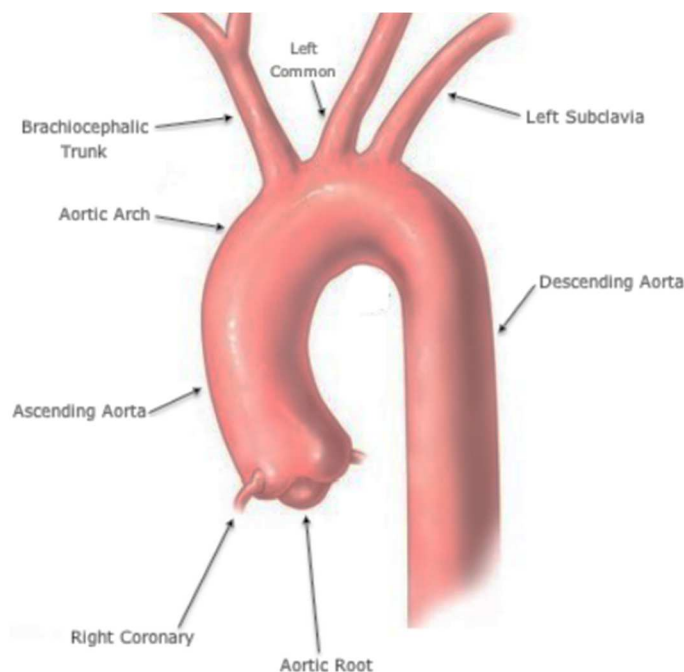


Figure 2.5 – Physiologic thoracic aorta (Criscione, 2013).

Figure 2.6 shows an external view of the reconstructed aortic root with the different anatomic entities that compose it: aorto-ventricular junction (AVJ); leaflets; interleaflet triangles; right coronary; left coronary; valsalva sinus and sinotubular junction (STJ).

After the ascending aorta, the aortic arch starts at the brachiocephalic trunk and ends at the origin of the left subclavian artery. Three branches arise from the aortic arch: the brachiocephalic trunk (that is divided into the right common carotid artery and the right subclavian artery) the left common carotid artery, and the left subclavian artery. These arteries are responsible for distributing blood to the head and upper limbs. After the ends of the aortic arch, there is the descending aorta.

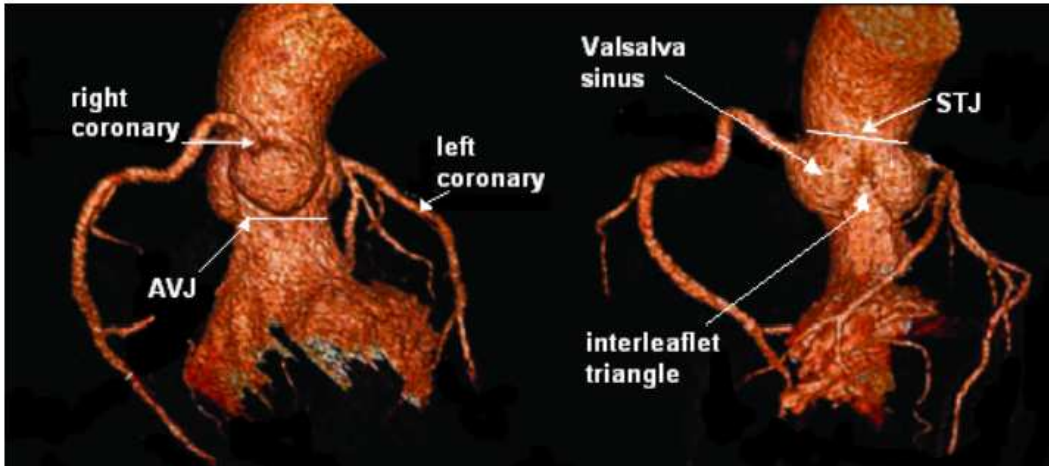


Figure 2.6 – Aortic root reconstructions: principal anatomic components of the aortic root (Morganti, 2011).

The aortic tissue is compounded by three distinct layers: outer adventitia, middle media, and inner intima. The outer adventitia is formed of irregularly arranged collagen bundles, providing support and structure to the artery, with the greatest tensile strength of the three aortic wall layers (Augoustides & Cheung, 2014). The middle layer, media, is thicker and contains arranged elastic fibers, connective tissue, and smooth muscle cells. The inner layer, intima, is the surface where blood flows. The media layer accomplishes the compliant function being the largest thickness at the ascending aorta wall, which are the most requested of the entire aorta (Marieb & Hoehn, 2018).

2.6 Aortic Valve

Normal aortic valves are composed of three flexible semilunar leaflets (or cusps). As already described, during systole, they open and close in an efficient way and during diastole they remain closed throughout final stage of the cardiac cycle, as shown in Figure 2.7.

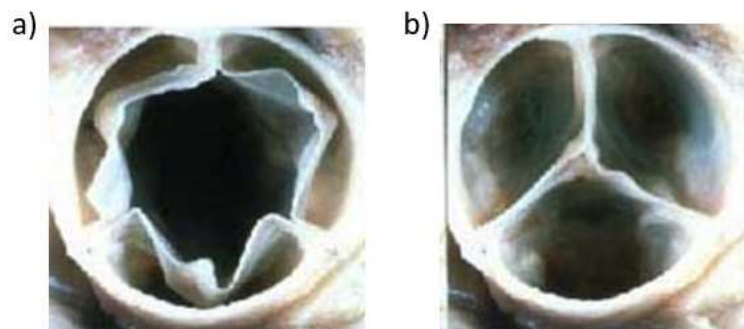


Figure 2.7 – Aortic valve during a) systole. b) diastole (Mendelson & Schoen, 2006).

By virtue of the significant number of deformations and coaptation cycles, the layers which compose the valve need to have properties that make possible the rearrangements, being known as Extra Cellular Matrix (ECM) (Mendelson & Schoen, 2006).

Microscopically, an aortic valve is composed of three layers: ventricularis, spongiosa and fibrosa. Together, these layers, composed respectively by elastin fibers, glycosaminoglycans and collagen fibers, comprise the valve ECM (Figure 2.8). A large proportion of interstitial cells are on the matrix of the heart valve, communicating to smooth muscle cells. The function of the elastin fibers that are on the structure of the ventricularis is to aid the leaflets to reduce the surface area when the valve is fully open and expand when blood pressure is increased (Thubrikar, 2011). The spongiosa facilitates the interchange between interstitial and endothelial cells, and serves as a shock and shear absorber, protecting the leaflets from stress-related damage and structural deterioration (Saremi et al., 2010). Lastly, fibrosa within endothelial cells covers the surface within an arrangement of aligned collagen fibers, maintaining a nonthrombogenic blood-tissue interface and regulating immune and inflammatory reactions (Mendelson & Schoen, 2006).

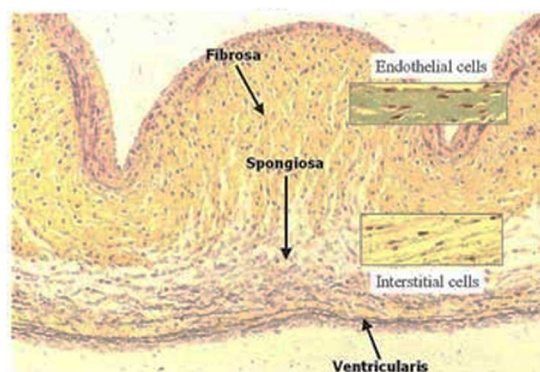


Figure 2.8 – Aortic valve histology within the three layers and interstitial and endothelial cells (Mendelson & Schoen, 2006).

Sripathi et al. (2004) showed that the aortic annulus approaches to a circular shape during the systolic period. In Bertaso et al. (2012) study, it is discussed that although there is a difference in aortic annular diameter measurement during systole and diastole, it is small.

Nonetheless, since the complex shape of the aortic valve, for numerical simulation, several authors simplify the aortic root inlet as a circular-shaped hole as an approximation of the aortic valve area (Ibanez et al., 2021; Al-Jumaily et al., 2023). The diameter used is determined using the effective orifice area (EOA). EOA is the minimal cross-sectional area of the flow jet, that corresponds of the

cross-sectional area of the vena contracta, downstream of an aortic heart valve (Garcia et al., 2004).

Cosentino et al. (2020) studied patients with ascending aortic aneurysm and employed the largest orifice area captured by CTA scan in the reconstruction of the orifice valve. The same approach were followed by Brown et al. (2012) Ha et al. (2016), Pirola et al. (2018), Salmasi et al. (2021) and Cherry et al. (2022).

2.7 Blood Rheology

Blood is a multi-phase heterogeneous mixture of solids bodies (red blood cells or erythrocytes (RBC), white blood cells and platelets) dispersed in a plasma fluid (an aqueous solution of proteins, organic molecules and minerals) (Figure 2.9 with rheological characteristics and properties affected by intake of fluids, nutrients and medication (Sochi, 2013).

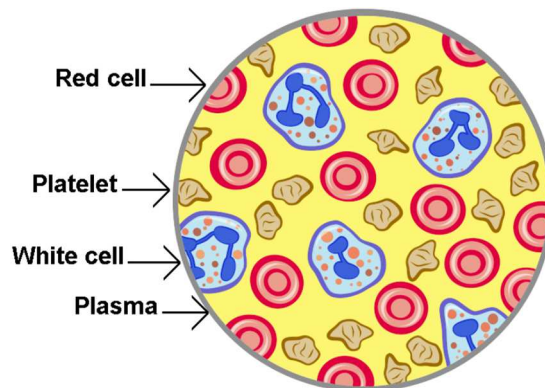


Figure 2.9 – Main blood composition (Sochi, 2013).

While the plasma is essentially a Newtonian fluid, i.e., the viscous stress tensor is directly proportional to the rate of deformation tensor, the blood behaves as a non-Newtonian fluid, which includes in its rheology: deformation rate dependency, viscoelasticity, yield stress and thixotropy.

Blood viscosity is determined by several factors such as the viscosity of plasma, hematocrit level, blood cell distribution and the mechanical properties of blood cells (Sochi, 2013b). The viscoelasticity is an important rheological property of blood that is associated with the pronounced elastic deformability of the red blood cells, which can aggregate forming three-dimensional structure known as rouleaux (Stoltz, 1985). Rouleaux is the aggregation of blood red cells and is most common at low shear rates, i.e., low flow rate. It makes that viscosity becomes more pronounced at regimes of low deformation and decreases as the fluid is subjected to a higher shear rate (Figure 2.10). This rheological property of blood is time independent and is known as shear thinning.

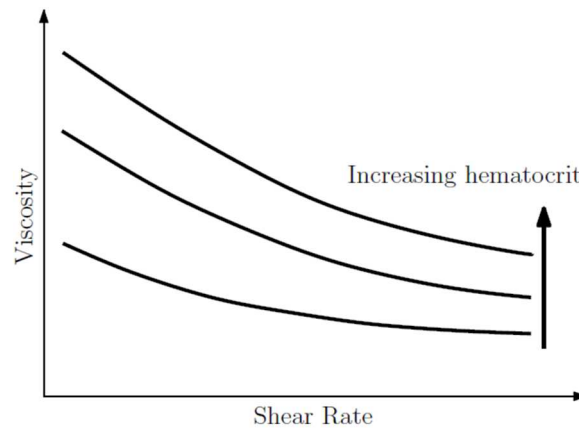


Figure 2.10 – Blood viscosity x Shear Rate for a range of hematocrit concentrations (Sochi, 2013).

Chien et al. (1970) initiated the studies to understand the impact of shear-thinning on blood. For small diameter vessels, it is recommended suitable models that include non-Newtonian properties of blood (Criscione, 2013). However, for large arteries, it does not appear to be a consensus in the literature the importance of non-Newtonian effects on unsteady flows (Johnston et al., 2006).

Since there is no full consensus of a homogenized model of non-Newtonian fluid that can predict the viscoelastic response of blood (Bodnár et al., 2011), several models were developed by parameters fitting with experimental viscosity data obtained at certain deformation rates under steady-state conditions (Walburn & Schneck, 1976; Ballyk et al., 1994; Cho & Kensey, 1991).

Carreau model is one of the generalized Newtonian fluid models which is also considered as a viscosity model since it is a mixture of power-law and Newtonian fluid models and is widely applied on the study of blood vessel fields (Ahmad et al., 2021). Firstly proposed by Carreau (1972), it models the fluid flow in high shear regions and at narrow arteries with low shear rates.

Almeida et al. (2021) investigated the influence of viscosity in the flow pattern and tension distribution on patients with ascending aorta aneurysm. The blood was modelled as a Newtonian fluid, with two different viscosities values, and as a non-Newtonian fluid described within Carreau model. It was shown that all cases presented very similar results, showing the small impact of viscoelasticity in large diameter vessels.

Fåhræus & Lindqvist (1931) found that blood viscosity changes with the vessel diameter. The responsible for this variation are the erythrocytes that can be rearranged depending on the vessel diameter. They are highly deformable biconcave disks which transport oxygen in the blood. As presented in Figure 2.11, in capillaries smaller than $10 \mu\text{m}$, erythrocytes develop into a unique profile which

raises the shear force to its maximal. For vessel diameters below $5 \mu m$, the viscosity increases dizzily due the narrowing of the tube, making it difficult for the erythrocytes to slip. An increase in the vessel's diameter causes the concentration to decrease at the boundaries, and the viscosity decreases drastically. For wider vessels, this effect is not presented, due to the low shear rate since erythrocytes do not have difficulty to flow.

According to Long et al. (2004) for deformation rates below $50 s^{-1}$, blood cannot be modeled as a Newtonian fluid, since in that range, the viscosity increases exponentially due the formation of large aggregates of RBC, Figure 2.12. However, when shear rate increases, the blood cells start to disaggregate, they disperse and align in the flow direction, behaving as Newtonian fluid, as observed by several authors (Rosencranz & Bogen, 2006; Stuart & Kenny, 1980).

Since aortas are characterized by high shear rate (Deutsch et al., 2006; Simão et al., 2017), and as defined by Gy et al. (2016) having a value of $150 s^{-1}$, the hypothesis that the blood behaves as a Newtonian fluid is acceptable.

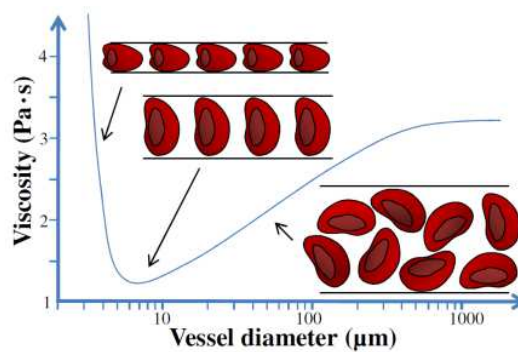


Figure 2.11 – Dependence of blood viscosity on the internal diameter of a vessel (Mogensen, 2011).

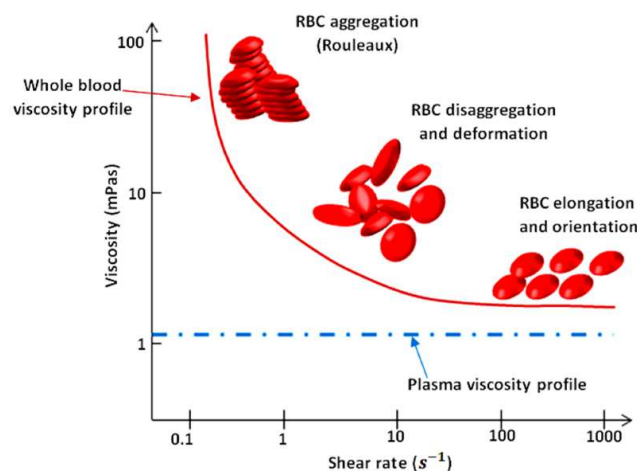


Figure 2.12 – Viscosity profile of whole blood and plasma (Rosencranz & Bogen, 2006).

3 LITERATURE REVIEW

In this chapter, a review of hemodynamic studies involving the physiologic environment of aortic valve is presented, including the pathologies focus of this study. The use of techniques to assess the flow field using Computational Fluid Dynamics and Four-Dimensional Flow Magnetic Resonance Imaging technique and the concept of patient-specific simulation are presented.

3.1 Physiologic Environment

Blood is a heterogeneous multi-phase mixture that transports oxygen and nutrients to cells and carries away waste products. It is a complex fluid formed by a liquid matrix called plasma, which is an aqueous solution with dissolved proteins, organic molecules, and minerals, besides erythrocytes, leukocytes (white blood cells) and platelets (thrombocytes). RBC typically comprise ~40% of blood by volume (Wootton & Ku, 1999).

Viscosity of blood may vary depending of: viscosity of plasma; hematocrit level; blood cell distribution; mechanical properties of blood cells; deformability of erythrocytes; aggregation ability; deformation forces, which can be extensional as well as shearing and the ambient physical conditions (Sochi, 2013; Gy et al., 2016). Plasma behaves as a Newtonian fluid, although blood is a non-Newtonian fluid, with variable rheological aspects such as deformation rate dependency, viscoelasticity, yield stress and thixotropy (Sochi, 2013; Fajelson & Jakobsons, 2003; Rodkiewicz, 1983).

In healthy blood, the erythrocytes are grouped into aggregates, i.e., "rouleaux". This phenomenon tends to increase especially due to the low flow in smaller vessels (Bishop et al., 2001).

Furthermore, due to the pulsatile nature of cardiac cycle induced by pressure changes, which causes acceleration and deceleration of flow that stabilizes and destabilizes the flow field (Yoganathan et al., 1988), formation of rouleaux may occur.

It has been observed that endothelial surface exposed to a high rate of shearing stress by the acceleration of the blood flow presents cell deformation, disintegration and finally dissolution and erosion of cell substance (Fry, 1968).

In a pulsatile flow, the spatiotemporal variation in shear rate has a crucial role in the aggregate formation, with some studies demonstrating an inverse relationship between them, i.e., when shear rate fluctuates more significantly, it may lead to less aggregation or clot formation (Cloutier & Shung, 1993; Lee & Paeng, 2021; Snabre et al., 1987; Lei et al., 2013).

Alteration of endothelial cells play a central role in various human diseases such as atherosclerosis (Rajendran et al., 2013) and aneurysms (Spartalis et al., 2020).

3.2 Pathologies in Aortic Valve

Atherosclerosis is a multifactorial pathology that occurs when protein, cholesterol crystals and/or calcium deposit under the endothelium and above the elastic lamina causing chronic inflammation in the vessel wall (Kuusisto et al., 2005).

According with Otto and colleagues (1994), aortic valvular stenosis (AVS) indicates an active inflammatory disease process with some similarities to atherosclerosis. Aortic stenosis is characterized by severe valvular calcification, impaired leaflet motion and outflow obstruction. Researches point out oscillatory shear stress can induce endothelial dysfunction and be initiating factor in both atherosclerosis and aortic stenosis pathologies (Glagov et al., 1988; Yearwood et al., 1989; Goody et al., 2020)

The established risks factors for AVS as well as for atherosclerosis (Otto et al., 1994) are few (Larsson et al., 2019), but evidences indicate that cardiometabolic risk factors as age (Mohler et al., 1991; Hoagland et al., 1985), obesity (Eveborn et al., 2014), hypertension, diabetes, dyslipdemia (Yan et al., 2017) and smoking (Yamaura et al., 2023) can influence the increase of these diseases.

Valvular aortic stenosis is a progressive disease which can completely obstruct the left ventricular outflow, resulting in inadequate cardiac output, decreasing exercise capacity, causing heart failure and death (Otto & Prendergast, 2014).

There are three factors which are considered when examining a patient to help the decision of the aortic-valve replacement: severity of the valve obstruction, clinical symptoms, and the left ventricular pressure overload.

As a result of the valve area reduction, an increase in velocity is induced in the valve accompanied by a decrease in pressure. In this way, aortic stenosis is

not a pathology that is limited to the valve leaflets, affecting the entire cardiovascular system, such as the upstream left ventricle and downstream systemic vasculature, besides the valve itself (Lindman et al., 2013). The dilatation of the ascending aorta is a common consequence of the valve obstruction, and the time of valve replacement must be well indicated in order to prevent the occurrence of an aortic dissection (Otto & Prendergast, 2014).

3.3 Pathologies in Aorta

Aneurysm is an abnormal permanent localized (i.e., focal) dilatation or bulging of a blood vessel or artery in any part of the human body, involving the three layers of the wall. It is considered when the diameter is at least 50% greater than the normal size of the vessel (Hallett, 2009).

This pathology is frequently asymptomatic and, in many cases, detected as an incidental finding on ultrasonography, abdominal computed tomography (CT) or magnetic resonance imaging (MRI) performed for other purposes (Aggarwal et al., 2011).

Aortic aneurysm is correlated with aortic wall deformities and injury, because of inflammation, matrix metalloproteinases activation, oxidative stress, and apoptosis of vascular smooth muscle cells. The endothelial wall has a critical part in the inflammation of the aorta and endothelial heterogeneity has proven to be significant for modeling aneurysm formation (Spartalis et al., 2020)

Considering the segment where the dilatation occurs in an aorta, a possible classification refers to the thoracic part. Thoracic aortic aneurysms (TAAs) can be classified considering the segment where the dilatation occurs, which can be the aortic root and/or ascending aorta, aortic arch, or descending aorta.

ATAAs are the most common subtype of thoracic aortic aneurysms (Figure 3.1, comprising 60% of cases of TAAs occurrence (Bicer et al., 2020). Established risk factors associated within the aneurysm growth rate include the presence of aortic valve disease (stenosis), congenital abnormalities (bicuspid aortic valve), or connective tissue disorders (Bürk et al., 2012). For elderly people, the major cause is due to atherosclerosis (Lavall et al., 2012), which leads to weakening of the aortic wall (Kharawala et al., 2023).

The guideline to determine when the intervention should be performed is given by maximum-diameter criterion greater than 5.5 cm or when the aorta diameter increases rapidly (Coady et al., 1997; Isselbacher et al., 2022). An intervention is also performed, in the presence of symptoms or for diameter greater

than 5.0 cm, if a tricuspid aortic valve is being replaced (Isselbacher et al., 2022).

Once an aneurysm reaches a maximum diameter of 5.5 cm, the annual probability of rupture, dissection, or death is 14.1% (Elefteriades, 2002). Approximately 50% of patients with acute untreated ascending aortic dissection die within 48 hours, and those undergoing emergency surgery have 15-26% mortality (Hagan et al., 2000; Ehrlich et al., 2000).

Thus, the treatment decisions should be very carefully analysed, due to the increased risk of dissection or rupture with aneurysm enhancement (Coady et al., 1997). Rupture rates in patients not treated surgically are high and the risk of operation is about 5% to 9% in elective operation and emergency operation is higher than 57% (Davies et al., 2002; Isselbacher, 2005)

When the surgery is not indicated, an option of treatment of the ascending aortic aneurysm consists of a careful monitoring and referral for surgical consultation to avoid rupture or dissection of the aneurysm, reducing the morbidity and mortality associated with this pathophysiology (Saliba et al., 2015).

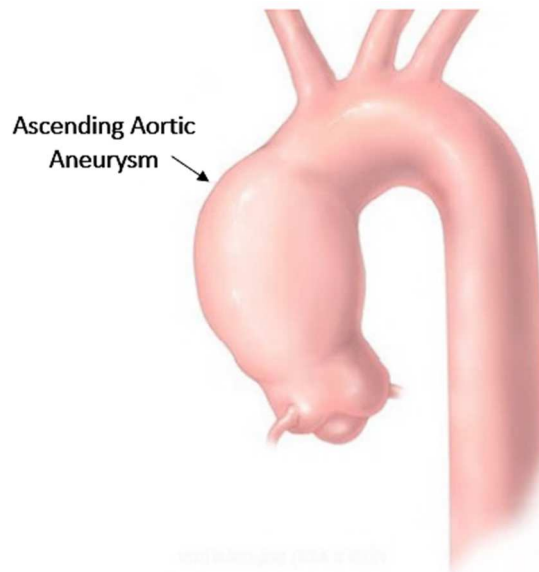


Figure 3.1 – A typical example of an ascending aortic aneurysm. Adapted from Criscione (2013).

3.4 CFD Modelling and Hemodynamic Variables

Cardiovascular CFD modeling is nothing more than combining physical models to predict blood flow in vessels of the circulatory system, with numerical methods to solve the resulting conservation equations, followed by the interpretation of the results for a particular application. Therefore, the first step to

analyze the flow is to define appropriate hypothesis to create a physical model, followed by different techniques to solve the equations.

As pointed out by Yoganathan et al. (1988), to examine patient results based on imaging modalities such as Doppler ultrasound and nuclear magnetic resonance imaging, cardiologists need to apply basic fluid flow concepts to analyze the flow. The authors adapted the conservation equations derived for confined jets to predict the cardiac blood flow. De Leval et al. (1988) have also performed simulation of some basic hydrodynamic flows, to aid the interpretation of the blood flow. Years later, de Leval et al. (1996) numerically evaluated the flow in cavopulmonary connections, indicating the use of CFD as an important tool in the design of surgical procedures.

The most common medical application of CFD in biomedical engineering and medicine is in the cardiovascular system (Bluestein, 2017; Ueda et al., 2018).

Nonetheless CFD shows up as a powerful tool, some cares need to be taken in order to accurately represent the actual flow in a patient. Taylor & Figueroa (2009) reviewed methods to create anatomic and physiologic models, to obtain properties, to assign boundary conditions (BCs) and solve the equations governing blood flow and vessel wall dynamics. As emphasized by Bluestein (2017), several conditions and steps need to be followed at preprocessing stage. Appropriate boundary conditions are extremely necessary to achieve high fidelity and accurate physiological flow scenarios.

After attaining a successful converged solution, a postprocessing stage comprehends the tools for visualizing, quantification and interpretation of the results. In CFD, these tools commonly encompass the velocity flow field and profiles within the flow domain, pressure distribution and parameters as Wall Shear Stress (WSS), Time-Averaged Wall Shear Stress (*TAWSS*) and the Oscillatory Shear Stress Index (OSI; Ku et al., 1985; Bluestein, 2017). OSI gives the shear stress direction preferential direction, being 0 for uniaxial flows and 0.5 when there is no preferential direction (Alimohammadi et al., 2017).

In the aortic dilation line, several authors regard the WSS distribution as an important hemodynamic variable in the development of the atherosclerotic lesion (Caro et al., 1971; Friedman et al., 1981; Ku et al., 1985).

Six patients with abdominal aortic aneurysm and a control patient without aneurysm were computational evaluated by Raghavan et al. (2000). It was noticed that the wall shear distribution was complexly distributed with large regional variations while the control patient presented a relatively low and uniformly distribution.

Malvindi et al. (2016) performed a pre-dissection computational fluid analysis at peak systole of an ascending aortic aneurysm associated with unicuspidal aortic valve of a patient that refused an elective operation. Then, he developed a type A aortic dissection and underwent emergency surgical repair. The researchers were able to compare the location of the aneurysm rupture with the hemodynamic variable's distribution in that area. Figure 3.2 (A) and (B) show the computed tomography image determining the site of the rupture. The circle in Figure 3.2(C) represents that region in the aorta WSS' mapping, showing an area with high shear stress.

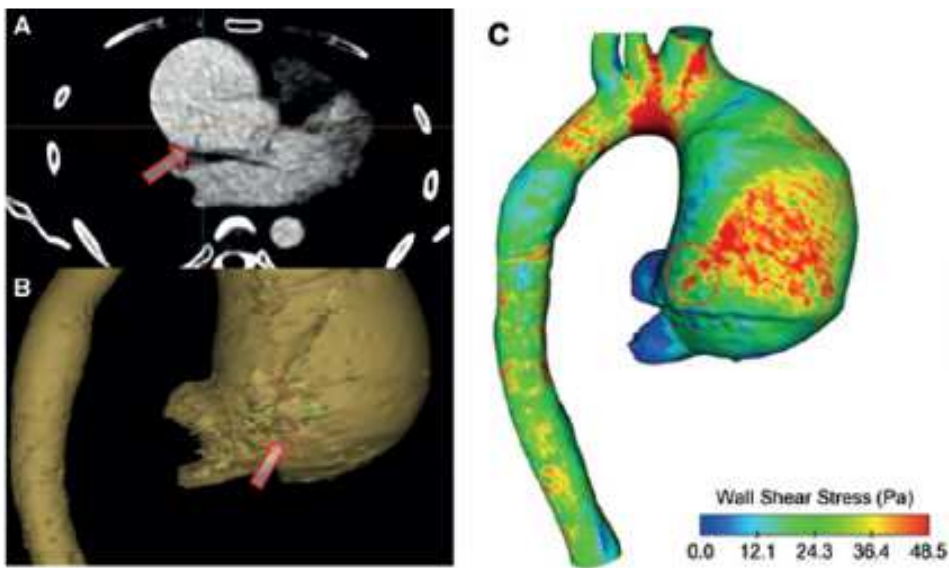


Figure 3.2 – A) and B) Computed tomography determining the site of the rupture. C) WSS' mapping with the red circle delimitating the rupture region (Malvindi et al., 2016).

Boyd et al. (2016) studied three-dimensional geometries generated from CTA images of ruptured abdominal aortic aneurysms. It was observed that the rupture location coincided with regions of reduced flow velocity and in most cases, in recirculation zones, where low WSS happened. The authors discuss that the WSS was significantly lower, and the thrombus deposition was abundant at the site of rupture.

Nonetheless, there is no consensus in the literature about the influence of WSS on the growth of an aneurysm, whether this occurs due to high or low WSS values. Thus, this variable is still not included as a clinical management (Rodríguez-Palomares et al., 2018).

Some authors have found that regions with low average shear stress combined with high oscillatory shear stress can influence the increase risk of the

development of the atherosclerotic lesions (Cecchi et al., 2011; Meng et al., 2014; Alimohammadi et al., 2016).

Gülan and colleagues (2018) observed that in the systolic phase, for healthy cases, counterclockwise helical flow patterns develop towards the aortic arch, while for aneurysmatic cases, large rotational regions, as noticed by Weigang et al. (2008).

The abrupt enlargement of the aorta's diameter causes the separation of the boundary layer, leading to the formation of a separation bubble. Gülan et al. (2018) emphasizes the analogy between the separation, the associated turbulence and pressure loss to the aneurysm growth.

Ibanez et al. (2021) investigated the influence of the prosthetic valve inclination angle in the mechanical stresses acting in the ascending aortic wall. For the inclination of 4° directed to the left main coronary artery, the area with high values of WSS and pressure decrease. The authors indicate that these changes may be important to reduce the aortic remodelling process.

Duronio & Di Mascio (2023) aimed to understand the thoracic aortic flow characteristics. Applying CFD simulation, it is seen that the aneurysm onset causes instability to the flow field, recirculation zones grow in the enlargement section with the consequent deposition or aneurysm formation. Besides that, it was identified regions with WSS levels that may be more prone to dilatation or aneurysm formation. The magnitude of the WSS reaches the maximum values in the enlarged zone.

In Ascending Aortic Aneurysm (AAoA) field, Almeida et al. (2022) conducted an analytical and observational study aiming to analyze velocity fields and coherent structures to correlate with the presence or absence of aneurysm growth to compare within the clinical data. Nine patients were simulated, and the results revealed that when it was evaluated the systolic peak, the incident jet in the aortic wall created recirculation areas in the posterior region, resulting in the formation of complex vortices in the group with aneurysm growth. Furthermore, it impacted to an average increase in pressure in the ascending aortic wall, while the group without aneurysm growth decreased the average pressure. In Azevedo et al. (2024), thirty patient-specific models with and without aneurysm growth were investigated also during peak systole to observe any pattern that would indicate the dilation of the vessel. The authors concluded that the association of high-pressure region and high WSS in the ascending aortic wall can indicate a growth of ATAA.

Xiao et al. (2023) performed the simulation on one-hundred ATAA patients

to examine the relationship between hemodynamic conditions, ascending aortic volume (AAV), ascending aortic curvature and aortic ratios. It was separated groups of ATAA geometries based on AAV. Comparing the results, the authors founded that ATAAs with enlarged AAV showed significantly higher maximum OSI and WSS, suggesting that the volume might be a feasible risk identifier for ATAAs.

Researchers are still seeking the best way to compare numerical simulation to reality, either by obtaining more reliable boundary conditions or validating simulations. Comparison approaches used can come from *In Vivo* measurements as the noninvasive methodology, 4D-Flow MRI.

3.5 4D-Flow MRI

In Vivo refers to measurements or experiments directly in an artery or organ, which is crucial to the development of medical devices, procedures, or novel therapies. It can use invasive or noninvasive approach.

Invasive strategy is conducted inside of a living organism, during a surgery procedure. Cousins et al. (2019) proposed a universal definition for invasive procedures with key components aimed to facilitate the selection of relevant methods for study design, streamline evidence synthesis and improvement of research tracking.

Noninvasive methodology is based in images acquisition tools, as ultrasound, MRI or CTA. In this context, it is possible to obtain the aorta morphology and dimensions, as well as information about biological processes and physiological functions. Thus, the aortic diameter root and data as pressure and velocity can be measured.

Blood flow variables has been determined with one-dimensional (1D) formulation (Mynard & Nithiarasu, 2008; Epstein et al., 2015). Two-dimensional (2D) formulation is a well-established technique (Lotz et al., 2002) that utilizes 2D slice planes positioned during scanning, but it requires a high degree of operator skill (Brix et al., 2009). Three-dimensional (3D) formulation are based on phase contrast technique, where the entire 3D volume is imaged (Pelc et al., 1991; Wigström et al., 1996).

The 3D technique helps the understanding of measurements as material properties and boundary conditions. Alastruey et al. (2016) implemented an in vivo non-invasive strategy to simulate the upper aorta of a young healthy volunteer. They demonstrated that this kind of modelling can minimize the number of arbitrary modelling decisions, improving the assumptions about pressure and blood flow.

The technique that allows the measurement and visualization of blood flow in a 3D volume over time (the fourth dimension) is the Four-Dimensional Flow Magnetic Resonance Imaging or 4D-Flow MRI. 4D-Flow combines MRI with specialized software to capture a detailed picture of blood flow patterns throughout the body. From the 2D images by MRI over time, a software processes and analyzes the motion of the blood in each voxel (3D pixel) within the image. By tracking the motion of the blood in each voxel over time, the software can create a blood flow four-dimensional map.

Hemodynamics studies can help to understand the circulation patterns through arteries. Pressure and velocity fields are provided, as well the information about the WSS, granting valuable information to researchers and physicians. Figure 3.3 shows an example of the velocity field in an aorta captured by 4D-Flow MRI technique.

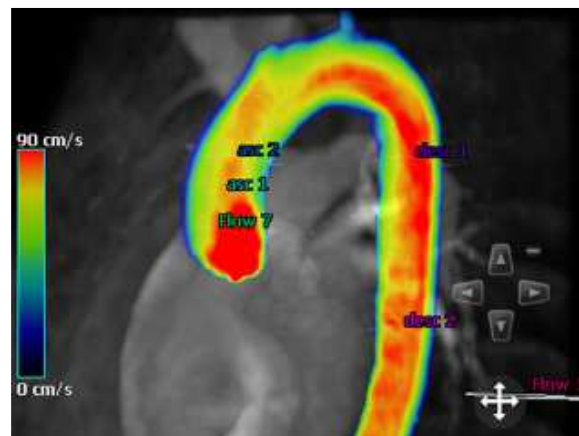


Figure 3.3 – Velocity field of an aorta captured by an MRI exam (Own Authorship).

Biegging et al. (2011) compared 11 patients with ascending aortic dilatation (AscAD) with 10 healthy volunteers using 4D-Flow MRI. It was demonstrated a delayed onset of peak systolic WSS of patients with AscAD in relation to the healthy ones. These finds are in convergence with the reported of Hope et al. (2007), that found a delay in peak flow velocity in patients with ascending aortic dilatation. The authors assign this delay through the increased volume of patients with ascending aorta and the dissipation of kinetic energy during systole. Besides that, it was observed changes in WSS associated with alterations in flow patterns. Figure 3.4 shows the difference between the flow streamlines during the peak systole with a patient with an AscAA in relation to a normal healthy volunteer. For the patient with an AscAA (a), vortical flow (arrowheads) with higher velocities are

present along the anterior surface of the aneurysm (arrow), corresponding to areas of highest WSS. For the healthy volunteer (b), the flow is laminar (arrows), without vortices and with relatively uniform velocity distribution around the aorta surface, corresponding to observed uniform distribution of wall shear stress values.

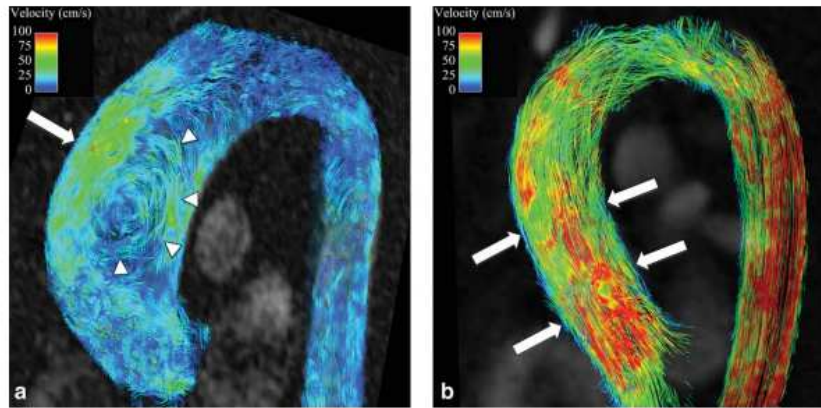


Figure 3.4 - Flow streamlines during peak systole in (a) a patient with an AscAA and (b) and normal healthy volunteer (Biegging et al., 2011).

Burris & Hope (2015) discussed 4D-Flow MRI in the aortic research field by highlighting that aortic quantitative hemodynamic markers are the relation of the flow field and WSS. The authors suggest how this technique can be beneficial to predict aortic valve and aortic wall diseases.

Takehara (2022) showed the application of 4D-Flow MRI for abnormalities detection in WSS non-invasively, stating that this technique is an important tool to predict future vascular lesions on abdominal aorta.

Takahashi et al. (2022) reviewed the use of 4D-Flow MRI in thoracic aortic diseases. The clinical advances are shown, as also, a systematic overview of key evidence regarding normal thoracic aortas, thoracic aortic aneurysms, aortic dissections and thoracic aortas with prosthetic graft replacement. The authors listed the benefits of 4D-Flow MRI, stressing that the assessment of thoracic aortic diseases in vivo has been significantly enhanced. It is described in their work that 4D-Flow MRI depicts flow alterations, which may cause aneurysm formation, particularly in Bicuspid Aortic Valve (BAV) patients. In dissected aortas, the accurate assessment of flow alteration are potential predictive factors for delayed complications. Furthermore, the technique provides detailed hemodynamic information of surgically replaced. Nonetheless, the clinical predictive relevance of the 4D-Flow MRI analysis remains a matter of speculation, since all research involves cross-sectional observational studies based on evaluations in advanced aortic diseases. To understand the causal relationship between flow dynamics and

clinical prognoses, prospective data in a large cohort are essential; therefore, 4D-Flow MRI application is expected to become widely used.

3.6 CFD x 4D-Flow MRI

Although both 4D-Flow MRI and CFD simulation enable 3D blood flow visualization during the cardiac cycle, there are substantial differences in the techniques. As discussed by Itatani et al. (2017), while 4D-Flow MRI enables the acquisition of data on the actual measurement, CFD simulation is the creation of a model with computer technology. Since it captures the measurement of the streamline, MRI can detect the actual flow even when the accurate geometry of the artery is not well known but has a poor spatial and temporal resolution. In the other hand, CFD simulation model needs, besides a physical model and a mathematical model (which can be solved with numerical approximations), the geometry creation, the mesh and boundary conditions establishment. The resolution can be increased depending on available computer memory. A mesh refinement study should be performed before model creation considering the importance between mesh size and time step when a pulsatile flow is being simulated. Figure 3.5 presents the difference between 4D-Flow MRI and CFD simulation from the perspective of temporal and spatial resolution.

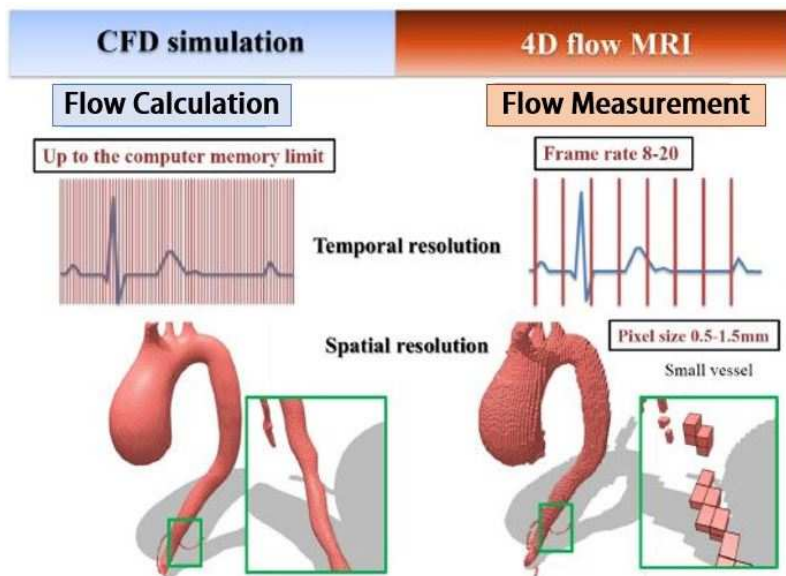


Figure 3.5 – Difference between 4D-Flow MRI and CFD simulation (Itatani et al., 2017).

Soudah et al. (2017) evaluated the WSS distribution of aortic a blood flow using the combination of 4D-Flow MRI and CFD technique considering a healthy

aorta at the peak of systole. The main goal of the study was to investigate the differences between the resolution of the models (computational mesh). The 4D-Flow MRI was used to obtain the spatial domain and boundary conditions. Similar WSS fields were found for the cases simulated.

Cherry et al. (2022) discussed how 4D-Flow MRI provided a robust, accurate and reliable method to determine the flow field and reproduce repetitive results in studies involving diagnosis of the impact a diagnosis of BAV had on the WSS in the thoracic aorta (Barker et al., 2010; Hope et al., 2011; Barker et al., 2012) as well the assessment of the flow field in patients with aortopathy (Rose et al., 2016; de Beaufort et al., 2019). However, despite proving to be a method with many advantages, it is necessary to understand the impact of accuracy dependence on the spatial and temporal resolution. In this way, the authors compare different spatial resolution mesh distributions of a patient-specific CFD simulation aiming to establish the minimum spatial resolution requirement needed to produce reliable patient-specific CFD simulations. It is suggested that a minimum spatial resolution of 1.5 mm x 1.5 mm x 1.5 mm should be used to avoid inaccurate data.

Besides that, Aycaan et al. (2023) discuss the importance of the mesh type in the accuracy and computational cost of simulations. According to the findings, the polyhedral mesh type is clearly demonstrated as superior over other mesh types.

3.7 Patient-Specific Simulation

Patient-specific simulation is possible when 4D-Flow MRI and CFD techniques are combined, i.e., the CFD simulation is done employing the geometry and boundary conditions determined from 4D-Flow MRI data.

The concepts of Patient-Specific Modeling (PSM) began to appear in the 1990's, when researchers (Krams et al., 1997; Milner et al., 1998) performing image processing in consonance of CFD, considered all geometric characteristics of a patient for its simulation. Taylor et al. (1999) proposed the utilization of computational tools by physicians to construct and evaluate a combined anatomic/physiologic model to predict the outcome of alternative treatment plans for an individual patient. In 2009, Neal & Kerckhoffs reported that PSM was gaining more attention because of its potential to improve diagnosis, optimize clinical treatment by predicting outcomes of therapies and surgical interventions besides inform the design of surgical training platforms.

Since the boundary conditions can strongly influence the results, the combination of CFD Modeling with 4D-Flow MRI to perform patient-specific

simulations has emerged as widely accepted method as shown in studies as Miyazaki et al. (2017), Kimura et al. (2017), Bakhshinejad et al. (2017), Pirola et al. (2018), Hellmeier et al. (2018), Nannini et al. (2021) and Stokes et al. (2021).

Pirola et al. (2019) have combined 4D-Flow MRI and CFD, and presented a comparison between both methodologies. They used the data from 4D-Flow MRI to obtain the BCs. The measured flow rate was adopted as the inlet boundary condition and for the outlets, the 3-Element Windkessel Model (3E WM) was imposed, based on pressure measurements. The hemodynamic flow distribution of the arterial system was determined, and resistance and compliance of the aortic wall was discussed. The comparison of CFD results and in vivo measurements showed good qualitative agreement between the flow patterns, however for low velocities – the visualization is difficult for 4D-Flow MRI. Quantitative comparison revealed maximum higher velocity peaks of 4D-Flow MRI than CFD simulation. Systolic and diastolic pressure presented the same levels, with the largest difference (11 mmHg) found in peak systolic pressure in the descending aorta region.

Focusing in ascending aortic aneurysm, Jayendiran et al. (2020) integrated Computational Fluid Dynamics and 4D-Flow MRI to anticipate the progressive changes in hemodynamics induced by morphological changes in the ATAAs of patients. An analytical equation has been devised to project aneurysm progression based on age, sex, and body surface area. Various parameters, including helicity, WSS), *TAWSS* and *OSI*, were assessed for two patients at distinct stages of aneurysm growth and compared with age- and sex-matched healthy subjects. The findings indicate that despite the gradual nature of hemodynamic changes in ATAAs, they are significantly influenced by morphological alterations, potentially affecting biomechanical factors and aortic mechanobiology.

Salmasi et al. (2021) corroborate this finding with the investigation of WSS' mapping using CFD simulation of eleven patients with aortic aneurysm that have underwent pre-operative 4D-Flow MRI scanning. Velocity profiles generated by CFD simulation were quantitatively and qualitatively analyzed. The numerical model employed data coming from 4D-Flow MRI to provide the patient-specific simulation. The study points out that geometry parameters as tortuosity, curvature and aortic length can be important influence roles in the pathogenesis of ATAAs. Moreover, the authors conclude that abnormal flow patterns, including accelerated velocity and higher WSS, may provide predictors of aneurysm prognosis.

4 MATHEMATICAL MODELING

The mathematical model to evaluate the hemodynamic characteristic of the blood flow during a cardiac cycle is presented in this chapter. First, the problem definition is presented. In the sequence, the conservation equations and the turbulence model are defined. Then, the boundary conditions are discussed, and the Windkessel model is described.

4.1 Problem Definition

As already described in Chapter 1, this research aims to numerically analyze and evaluate the hemodynamic variables of a complete cardiac cycle in the ascending aorta of specific patients, based on their actual anatomy. To this end, it is necessary to determine the blood flow behavior during two sequential heartbeats, after the blood is ejected by the heart and enters the aorta artery.

Figure 4.1 illustrates a reconstructed 3D aortic model. The oxygenated blood, after being pumped by the heart, enters through the aortic valve, develops in the ascending part and then, part of the blood is ejected on the three great vessels of the aortic arch. The brachiocephalic artery, the left common carotid artery, and the left subclavian artery, are the arteries which provide blood to the head, neck and upper extremities. Most of the remaining blood flow goes into the descending aorta to be distributed to the lower parts of the body.

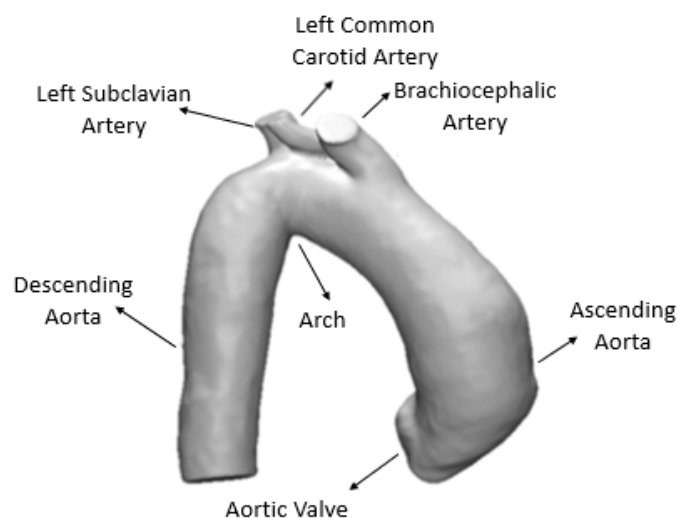


Figure 4.1 – Illustration of a reconstructed 3D aortic model (Own Authorship).

To model the flow, the first step is to define the aorta domain. All patients' aortas were obtained from their CTA images. Due to the high number of patients and the lack of detailed images of each patient's valves, the aorta flow entrance was modelled as a circular orifice, adopting the measured effective diameter of the valve for each patient as utilized by Al-Jumaly et al (2023).

Another simplification employed related with the aortas' geometry, was to neglect vascular compliance, since the use of rigid wall simulations have been reported to produce comparable hemodynamic variable distribution (Stokes et al., 2023; Jayendiran et al., 2020; Ibanez et al., 2020; Alimohammadi et al., 2016).

The blood flow through the aorta is evaluated by examining the distribution of the pressure and velocity field, and all correlated variables, such as, the shear stress. To obtain these variables, a model must be created based on hypothesis applied to the problem of interest, and the first issue to address is the nature of the flow, i.e., laminar or turbulent.

The nature of a flow can be determined by the predominance of the inertia forces or the viscous forces. If the viscous forces are dominant, the flow is known as laminar, with particles moving in parallel layers, or sheets, with small variations.

However, when the inertia forces dominate, perturbations are amplified, inducing the formation of vortices with a large variety of sizes, presenting a 3D and transient behavior. The flow becomes turbulent.

To evaluate the nature of the flow the ratio between these two forces can be estimated with the Reynolds number (Re) as

$$Re = \frac{\rho W_{in} D}{\mu} = \frac{4 \rho \dot{V}_{in}}{\pi D \mu} \quad (4.1)$$

where ρ is the density, μ is the molecular viscosity, D is the inlet valve diameter, which is the effective valve diameter (Flachskampf et al., 1990), W_{in} is the inlet normal velocity and \dot{V}_{in} is the inlet volumetric flow rate.

The transition between laminar and turbulent depends on several parameters like geometry, boundary conditions, perturbations, etc. For the particular case of an aorta, at the systolic peak the flow is turbulent (Celis et al., 2020; Davies et al., 1986; Gomes et al., 2017), as well as at the valve region, due to jet expansion after leaving the valve (Sallam & Hwang, 1984; Yoganathan et al., 1988). However, along the remaining of the cardiac cycle, transition to laminar flow develops, due to the low flow rate during diastolic phase.

Since turbulent flow is intrinsically three-dimensional and unsteady, with vortex structures with different orders of magnitude of time and length scales, the

analysis of turbulent flow is computationally very costly, since a very small-time step and mesh size must be employed to capture the phenomena at Kolmogorov scales. Thus, there are several approaches with different levels of accuracy and computational effort to simulate turbulent flows (Pope, 2000), as illustrated in Figure 4.2.

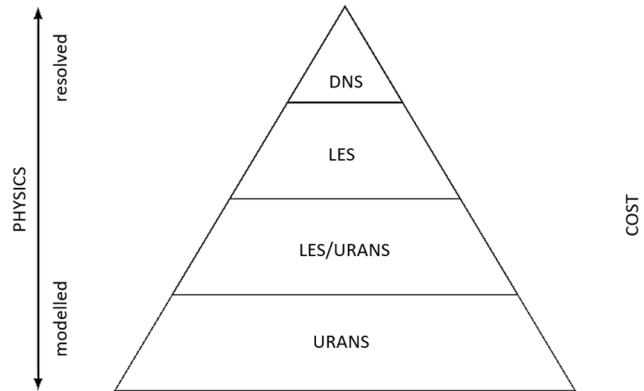


Figure 4.2 – Turbulence resolution approaches. Adapted from Sporschill (2021).

The Direct Numerical Simulation (DNS) solves the full Navier-Stokes equation without any turbulence model. The high computational demand results in the high cost of this methodology.

The Large Eddy Simulation (LES) directly simulates large turbulent structure while smaller scales are filtered out and modelled. In comparison to DNS is more computationally economic, but still considered with high cost.

Hybrid methods combine LES with Unsteady Reynolds-Averaged Navier-Stokes (URANS), that is an approach where all the scales are modelled statistically. The hybrid methods have been developed to retain the accuracy and time-dependence of LES on regions away from the walls and using URANS close to walls, where scales are very small.

At the base of pyramid presented in Figure 4.2, is the URANS methodology, which was originally proposed for statistically steady state situation, called Reynolds-Averaged Navier-Stokes (RANS) methodology (Pope, 2000).

The URANS methodology uses a time filter that removes out high-frequencies based on the Reynolds average definition. Any generic variable ϕ^* (like pressure or velocity) varies in a random form around a mean value $\bar{\phi}$, and only the mean value is determined and is defined as

$$\phi^* = \phi + \phi'; \quad \phi = \frac{1}{\Delta t} \int_{\Delta t} \phi^* dt \quad (4.2)$$

Figure 4.3 shows the fluctuation of a random variable in a turbulent flow depending on time.

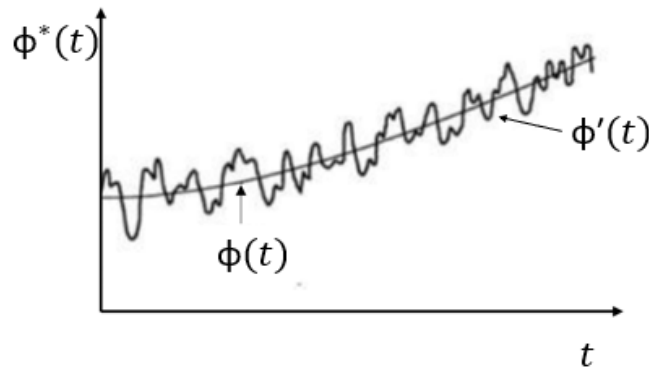


Figure 4.3 - Fluctuation of a random variable in a turbulent flow depending on time (Own Authorship).

In this case, all scales are modelled, and the time average conservation equations are solved to determine the mean flow field. Therefore, URANS allows coarser spatial discretization and time step than LES or DNS, resulting in computational economy. Aiming to capture the transition from laminar to turbulent flow, turbulence intermittency has been added in the formulation, acting on the production and destruction of turbulent quantities (Menter et al., 2004). Despite involving a higher level of modeling, it is cheaper to compute, and it has been shown to predict good results for similar application (Celis et al., 2020). Due to the high number of cases to be analyzed, computing effort is a critical parameter, thus this approach was selected in this work.

4.2 Conservation Equations

In the present work, the following hypotheses were made to model blood flow in arteries:

- i. Isothermal flow, as the temperature gradient is small inside the human body (Hao, 2010);
- ii. Negligible gravitational effects regarding the pressure variations that are dominant inside the artery;
- iii. Incompressible fluid ($\rho = 1054 \text{ kg/m}^3$), due to its very small pressure dependence (Feijoo & Zouain, 1988; Li, 2000);
- iv. Blood is modeled as a Newtonian fluid (Crowley & Pizziconi, 2005; Almeida et al., 2021), due to large shear rate present along most of the cardiac cycle, with constant viscosity ($\mu = 3.5 \text{ cP}$);

- v. Rigid wall (Stokes et al., 2023);
- vi. Valve represented by an orifice (Cherry et al., 2022);
- vii. Transitional flow.

Based on these hypotheses, the physical laws describing the instantaneous blood flow in arteries are the conservation of mass and momentum:

$$\frac{\partial u_j^*}{\partial x_j} = 0 \quad (4.3)$$

$$\frac{\partial \rho u_i^*}{\partial t} + \frac{\partial \rho u_i^* u_j^*}{\partial x_j} = -\frac{\partial p^*}{\partial x_i} + \mu \frac{\partial^2 u_i^*}{\partial x_j^2} \quad (4.4)$$

where x_j corresponds to coordinate axes, t is time, u_j^* is the velocity vector components, p^* is the pressure, ρ and μ are the density and molecular viscosity, respectively.

In accordance with the URANS approach, all variables are decomposed by the sum of a time average variable with its fluctuation, as defined by Eq. 4.2. To obtain the time average variables, the time averaging procedure is applied to the conservation equations, resulting in following time average continuity equation

$$\frac{\partial u_j}{\partial x_j} = 0 \quad (4.5)$$

being u_j the components of the time average velocity vector. The time average linear momentum conservation equation is

$$\frac{\partial \rho u_i}{\partial t} + \frac{\partial \rho u_j u_i}{\partial x_j} = -\frac{\partial p}{\partial x_i} + \mu \frac{\partial \tau_{ij}}{\partial x_j} - \frac{\partial \overline{\rho u_j' u_i'}}{\partial x_j} \quad (4.6)$$

where the viscous stress tensor τ_{ij} , for an incompressible Newtonian fluid is

$$\tau_{ij} = \mu \ 2 \ S_{ij} \quad (4.7)$$

and S_{ij} is the time average strain rate tensor, corresponding to the symmetric part of the time average velocity gradient tensor,

$$S_{ij} = \frac{1}{2} \left(\frac{\partial u_i}{\partial x_j} + \frac{\partial u_j}{\partial x_i} \right) \quad (4.8)$$

$-\rho \overline{u'_j u'_i}$ is a new variable, called turbulent tensor or Reynolds stress tensor, which needs closure. Utilizing the Boussinesq approximation, the deviatoric part of the Reynolds tensor (trace-free) can be modeled through an analogy with the viscous stress. In this way, the traceless Reynolds stress tensor is defined as

$$-\rho \overline{u'_j u'_i} + \frac{2}{3} \rho \kappa \delta_{ij} = \mu_t 2 S_{ij} \quad (4.9)$$

where μ_t is the turbulent viscosity and κ is the turbulent kinetic energy, defined as

$$\kappa = \frac{1}{2} \overline{u'_i u'_i} \quad (4.10)$$

The second term in the Eq. 4.9 can be interpreted as turbulent dynamic pressure, where δ_{ij} is the Kronecker delta.

Substituting the Reynolds stress tensor in the time average momentum equation, we obtain

$$\frac{\partial \rho u_i}{\partial t} + \frac{\partial \rho u_j u_i}{\partial x_j} = -\frac{\partial \hat{p}}{\partial x_i} + \frac{\partial}{\partial x_j} \left[(\mu + \mu_t) \left(\frac{\partial u_i}{\partial x_j} + \frac{\partial u_j}{\partial x_i} \right) \right] \quad (4.11)$$

where \hat{p} is a modified pressure, which includes the turbulent dynamic pressure

$$\hat{p} = p + \frac{2}{3} \rho \kappa \quad (4.12)$$

To close the modeling, the turbulent viscosity needs be defined, and it is presented in the next section.

To solve the conservation equations, appropriate boundary and initial conditions must be defined. Boundary conditions are presented in Section 4.4. However, since we are interested in the periodic regime, the initial condition is only relevant to initiate the numerical solution, and further details will be presented in Chapter 5 (Numerical Modeling).

4.2.1 Turbulent viscosity

To determine the flow inside an aorta, Celis Torres (2017) recommended to employ the $\kappa - \omega$ SST model (Menter et al., 2004) to define the turbulent viscosity. This recommendation was based on a comparison of the velocity field obtained at steady state, considering the flow rate at systole peak inside an aorta, with experimental data of Gomes (2017).

The model was developed by Menter (1994), where SST stands for shear-stress-transport, κ is the turbulent kinetic energy and ω is the specific dissipation. This model is based on a blending of the $\kappa - \omega$ model (Wilcox, 1988) and the $\kappa - \varepsilon$ model (Harlow & Nakayama, 1968; Jones & Launder, 1972), where ε is the dissipation rate, $\omega = \varepsilon/\kappa$. It takes advantage of accurate formulation of the $\kappa - \omega$ model in the near-wall region and of the $\kappa - \varepsilon$ model in the far field. The characteristic length of the $\kappa - \omega$ is $L_c \approx \omega/\kappa^{1/2}$ while the characteristic length of the $\kappa - \varepsilon$ model is $L_c \approx \varepsilon/\kappa^{3/2}$. The turbulent eddy viscosity is given by

$$\mu_t = \frac{\rho \kappa}{\omega} \xi \quad (4.13)$$

where ξ is the blending factor between $\kappa - \varepsilon$ and $\kappa - \omega$ models. This model requires the solution of conservation equations for the turbulent kinetic energy κ and specific dissipation ω , which are presented in Appendix A1.

Due to the periodic nature of the physiological flow, the ascending aortic flow is indicated as disturbed (Nerem & Seed, 1972). Several authors point out the importance of a transition model application, a suitable approach which consider the potential transition from laminar to turbulent flow (Sengupta et al., 2023; Kousera et al., 2013; Tan et al., 2009a; Tan et al., 2009b).

In order to capture the regime transition, the Intermittency Transition $\kappa - \omega$ SST model was selected (Menter et al., 2004). The flow intermittency γ , refers to the percentage of time that the flow is turbulent (0 = fully laminar, 1 = fully turbulent) and acts on the production of the turbulent kinetic energy transport equation in the SST model, its conservation equation is also presented in Appendix A1.

4.3 Boundary Conditions

To define the boundary conditions, it is necessary to establish the flow inlet, outlet, and wall regions. For an aorta, the inlet plane is the plane where the aortic valve is located and the outlets planes, namely 'out1', 'out2', 'out3' and 'out4', correspond to the brachiocephalic artery; the left common carotid artery; the left subclavian artery; and the descending aorta, respectively, as shown in Figure 4.4. The wall is the aorta surface.

Inlet

During the cardiac cycle, it is possible to impose as input the time variation of mass flow rate or pressure. In this study, the mass flow rate (\dot{m}) was imposed

since the simulation presented more stability. Therefore, the velocity profile is uniform. It was assumed that the flow is perpendicular to the plane.

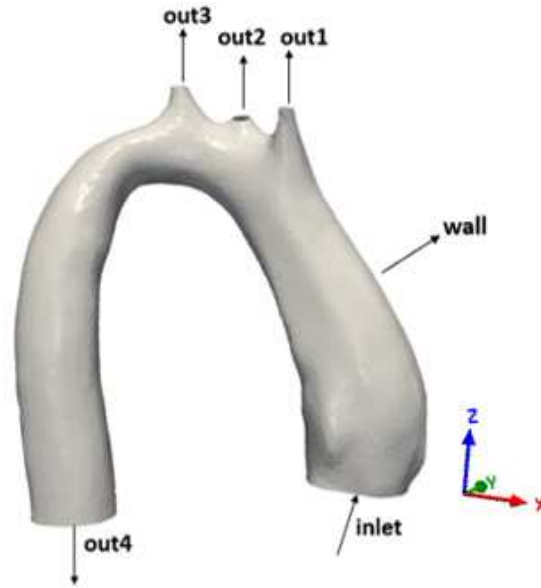


Figure 4.4 – Inlet and outlets in a 3D aorta (Own Authorship).

The system of coordinates is defined at the inlet plane, with the z direction perpendicular to the plane and the x direction aligned the left coronary close to the valve (Figure 4.4). Thus, the normal velocity component of the inlet plane, which is intrinsically the average inflow velocity, is in the z direction and it is defined as

$$W_{in} = \frac{4 \dot{m}}{\rho \pi D^2} \quad (4.14)$$

Both x and y velocities components are null at the inlet.

At the inlet, the turbulent quantities κ_{in} and ω_{in} are also considered uniform. The turbulent kinetic energy, κ_{in} , is based on the inlet velocity and the turbulent intensity I_κ .

$$\kappa_{in} = \frac{3}{2} (W_{in} I_\kappa)^2 \quad (4.15)$$

The turbulence intensity was defined as 10% based on Celis Torres (2017) recommendation for the inlet aorta flow, in accordance with the experimental work of Gomes et al. (2017).

The specific dissipation, ω_{in} , is based on the empirical constant $C_\mu = 0.09$, and on a length scale, which was defined equal to the inlet diameter D , as

$$\omega_{in} = \frac{\sqrt{\kappa_{in}}}{C_\mu^{1/4} D} \quad (4.16)$$

Outlet

At each outlet, is possible to impose the flow rate percentage or the Windkessel model, described in the next subsection. Independently of the modelling, at all output regions, a null diffusive flow condition was applied.

$$\frac{\partial}{\partial x_n} = 0 \quad (4.17)$$

being n the direction normal to the outflow plane.

Wall

At the aorta's surface, a non-slip condition was specified as a boundary condition for the velocity's components

$$u = v = w = 0 \quad (4.18)$$

The boundary condition of κ at the solid surface is also zero. Nonetheless, the boundary condition for the specific dissipation in the walls is given, according to Menter (1994), as a function of its dimensionless value, and considers the thickness of the molecular sub layer

$$\omega^+ = \frac{\omega_w \mu}{\rho u_\tau} = \min\left(2500, \frac{6}{\beta_\infty^* (y^+)^2}\right) \quad (4.19)$$

where y^+ is the dimensionless wall distance of the first internal node

$$y^+ = \frac{\rho u_\tau y}{\mu} \quad , \quad u_\tau = \sqrt{\frac{\tau_w}{\rho}} \quad (4.20)$$

and $\beta_\infty^* = 0.09$ is an empirical constant, and u_τ is the friction velocity, where τ_w is wall shear stress,

$$\tau_w = \mu \left. \frac{\partial u_t}{\partial x_n} \right|_w \quad (4.21)$$

based on the normal gradient to the wall of the tangential velocity, u_t .

Since the fluid was considered incompressible, the pressure level is not relevant. The solution was obtained as a function of a reference pressure defined at the inlet, p_{in} , at the center of the aortic valve, which in turn is the geometric origin of the inlet plane.

4.3.1 Windkessel model

To better represent the boundary condition at the outlet, Frank (1899)

formulated a simplified mechanical model used to describe the behavior of the arterial system, being called Windkessel (WK) model. The term ‘Windkessel’ is German and it is translated as ‘air chamber’ or ‘air vessel’, which refers to the model’s analogy with an ‘elastic reservoir’.

This model aims to consider the interaction between the heart’s pumping action and the compliance (elasticity) and peripheral resistance of the arterial wall. Large arteries such as the aorta can distend and store larger amount of blood, which is afterward distributed in diastolic phase. This leads to a pulsatile pressure waveform, which can induce wave propagation and reflection throughout the vessel. The peripheral resistance is present in small vessels. That resistance can be referred to Poiseuille’s law, which defines that for laminar flow inside tube, the flow resistance is inversely proportional to the fourth power of the tube diameter.

Figure 4.5 shows the concept of the Windkessel. The air reservoir is the actual Windkessel and the large arteries act as the Windkessel. The combination of compliance, together with aortic valves and peripheral resistance, results in a rather constant peripheral flow.

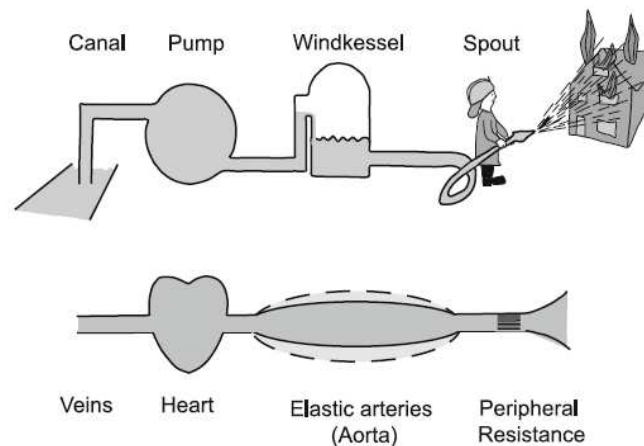


Figure 4.5 – Concept of Windkessel model (Westerhof et al., 2009).

WK model is widely used as the outlet boundary condition in cardiovascular modelling field. Blood pressure is correlated with the blood flow rate, considering compliance, peripheral resistance, impedance and blood flow inertia.

The basic WK model is the two-element Windkessel. One evolution is the Three-element Windkessel, which was selected to be employed in this work, following the works of Deyranlou (2021). These models are described next.

Two-element Windkessel (2E WK)

The simplest WK model considers the arterial compliance and peripheral

resistance to correlate pressure and blood flow rate. This is made through an analogy with electrical circuit with two components: a capacitor and a resistor. The capacitor represents the elasticity of the arteries and the resistor reflects the peripheral arteries effects. Therefore, employing Kirchhoff's law for the current and voltage in an electrical circuit, the theoretical model can be formulated as

$$\dot{V}(t) = \frac{p(t)}{R_d} + C \frac{dp(t)}{dt} \quad (4.22)$$

where $\dot{V}(t)$ is the volumetric rate, $p(t)$ the pressure, R_d the distal resistance (or peripheral resistance), t time and C the capacitance (wall compliance). The circuit representing the two-element Windkessel model is shown in Figure 4.6.

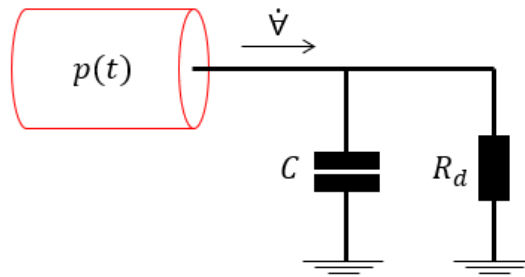


Figure 4.6 – Two-element Windkessel model (Own Authorship).

Three-element Windkessel (3E WK)

The three-element Windkessel model is an improvement on the classical two-element Windkessel and was introduced by Westerhof et al. (1969). While 2E WK poorly predicts the pressure waveform at high frequencies, since the resulting waveform is significantly different from the realistic measured pressure data (Deyranlou, 2021), 3E WK considers the wave effects through a characteristic impedance for the proximal region.

The characteristic impedance can be defined as $R_p = \rho c/A$, where c is the pulse wave velocity, ρ the density and A the cross-sectional area. It represents the overall resistance of a system or element and it has a similar unit to resistance. If impedance is included in addition to the resistance, the compliance and capacitance of the system or element will be considered. The 3E WK is also referred to as RCR WK (Resistance–Capacitance–Resistance Windkessel). However, if it is considered as another resistance in 3E WK model, it induces small error at low frequency region. In this way, R_p is introduced as the proximal resistance (Figure 4.7). Note that the two-element Windkessel is obtained if R_p is null (2E WK).

$$\left(1 + \frac{R_p}{R_d}\right) \dot{V}(t) + R_p C \frac{d\dot{V}(t)}{dt} = \frac{p(t)}{R_d} + C \frac{dp(t)}{dt} \quad (4.23)$$

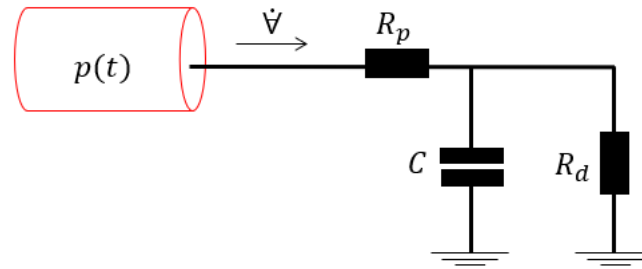


Figure 4.7 - Three-element Windkessel model (Own Authorship).

WK parameters

The WK resistances and capacitance must be defined based on the pressure, and volume flow rate. Thus, to apply the WK model to an aorta, it is convenient to visualize how the pressure and flow rate vary during the cycle, as well as a schematic of the aorta.

Figure 4.8 illustrates a typical mass flow rate and pressure at the aorta inlet during the cycle. The mass flow, \dot{m}_{in} entering the aorta increases until it reaches a maximum value, when the pressure in the heart drops, due to its emptying and the valve is closed, resulting in a drop in flow. This initial period of the cycle is called systole and lasts approximately 1/3 s. The final period of the cycle, called diastole, lasts 2/3 s, and corresponds to the heart's relaxation period, when the valve is closed and almost no flow enters the aorta.

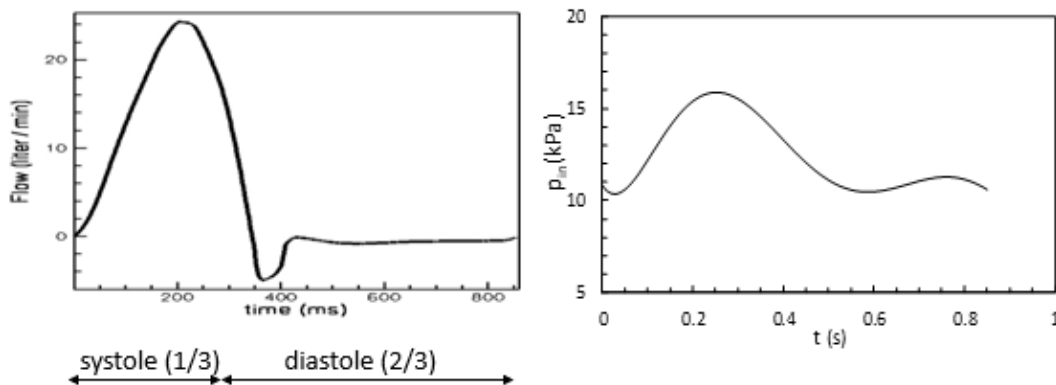


Figure 4.8 Diagram of the flow rate (systole and diastole) and pressure inlet during a cardiac cycle. Adapted from Borazjani et al. (2008) and Ibanez (2019).

Figure 4.9 shows the schematic representation of an aorta, with one inlet and four outlets as already shown in Figure 4.4. For each outlet the WK model can be applied.

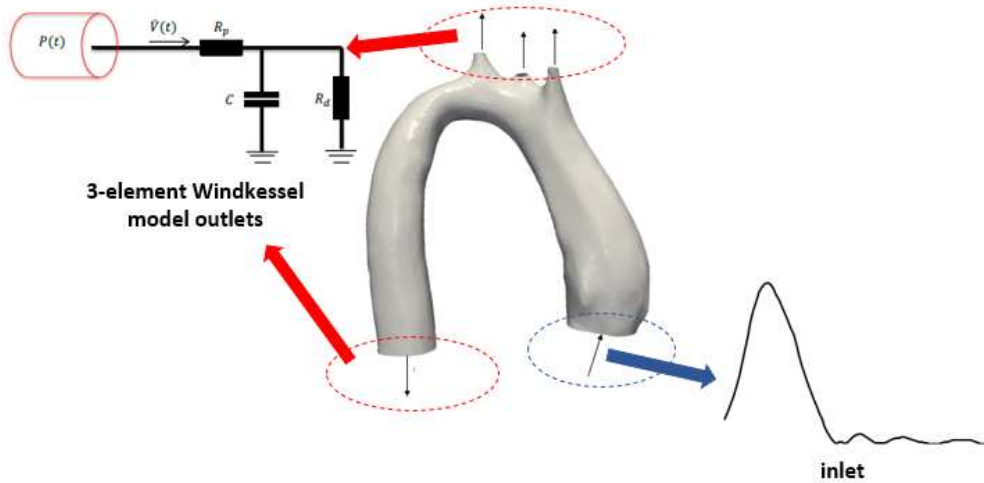


Figure 4.9 – Schematic representation of the inlet and boundary (Own Authorship).

According to Deyranlou (2021), the proximal resistance (R_p) and the distal resistance (R_d) for each outlet are a percentage fraction of the total resistance, equal to 9% and 91% respectively.

$$R_p = 0.09 R_{tot}; \quad R_d = 0.91 R_{tot} \quad (4.24)$$

The total resistance, R_{tot} , is determined by the ratio of the available potential (average pressure) over the available current (flow rate at each outlet, which is a fraction of the average flow rate) (Deyranlou, 2021)

$$R_{tot} = \frac{p_{avg}}{\xi \dot{V}_{avg}} \quad (4.25)$$

The average arterial pressure p_{avg} , and average volumetric flow rate \dot{V}_{avg} during the cycle are (Deyranlou, 2021)

$$p_{avg} = \frac{p_{systole} + 2 p_{diastole}}{3} \quad (4.26)$$

$$\dot{V}_{avg} = \frac{1}{T} \int_0^T \dot{V}(t) dt \quad (4.27)$$

where $p_{systole}$ is the peak pressure during systole, and $p_{diastole}$ the average pressure during diastole. The fraction of the flow rate of each outlet (\dot{V}_{out}) in relation to the inlet flow rate (\dot{V}_{in}) is (Deyranlou, 2021)

$$\xi = \frac{\dot{V}_{out}}{\dot{V}_{in}} \quad (4.28)$$

The total capacitance is defined as (Deyranlou, 2021)

$$C = \frac{2T}{3 R_{tot} \ln\left(\frac{P_{systole}}{P_{diastole}}\right)} \quad (4.29)$$

where T is the period of the cardiac cycle.

4.4 Hemodynamic Variables

The hemodynamic variables are an important tool to evaluate the flow inside the aortas and are defined below.

- Wall Shear Stress

The WSS, τ_w , is defined as

$$\tau_w = \mu \left. \frac{\partial u_t}{\partial x_n} \right|_w \quad (4.30)$$

where u_t is the tangential velocity component to the wall and x_n the coordinate normal to the wall.

4.4.1 Strain Indices

The shear indices are time average values along the period:

- Time Average Pressure (*TAP*)

The *TAP* variable evaluates the average pressure over the cardiac cycle as (Ibanez, 2019)

$$TAP = \frac{1}{T} \int_0^T p \, dt \quad (4.31)$$

- Time-averaged wall shear stress (*TAWSS*)

The time-averaged wall shear stress describes the average magnitude of the shear stress and can be written as (Black et al., 2023)

$$TAWSS = \frac{1}{T} \int_0^T |\tau_w| \, dt \quad (4.32)$$

where τ_w is the wall shear stress on the wall.

- Oscillatory Shear Index (*OSI*)

Another mechanical factor related to flow oscillation is the OSI, representing

the change of direction of the WSS vector from a predominant blood flow direction during the cardiac cycle. OSI is calculated by (Ku et al., 1985)

$$OSI = 0.5 \left(1 - \frac{\left| \frac{1}{T} \int_0^T \tau_w dt \right|}{\frac{1}{T} \int_0^T |\tau_w| dt} \right) \quad (4.33)$$

The OSI value can vary from 0.0, for no-cyclic variation of WSS vector, when the direction of $\vec{t} = \boldsymbol{\tau} \cdot \vec{n}$ does not change during the cardiac cycle, to 0.5 when the vector \vec{t} changes its direction in 180°, which is related to low values of WSS.

5 NUMERICAL MODELING

To analyze the blood flow, it must be determined the velocity field coupled with the pressure field. Ansys Fluent software 2021vR1 (Ansys, 2021) were used to perform the CFD analysis. Three steps are essential and must be followed: pre-processing, processing itself and post-processing.

In the pre-processing step, initially the aorta geometry must be defined. Thereunto, medical images were used for the geometrical extraction which defines the physical boundaries of simulated geometry. Several medical imaging techniques can be applied for this purpose, including CTA or MRI exams (Ueda et al., 2018), as they guarantee sufficient anatomical resolution to enable subsequent segmentation and data extraction. In this research, CTA and MRI images were employed. Once the object of interest was generated, spatial discretization, or meshing, was performed with Meshing from Ansys Inc. (2021), which consists into the division of the geometry in a number of discrete volumetric elements or cells that are linked to the resolution of solution.

The processing step consists in the solution of the discretized form of the flow governing equation of mass and momentum, coupled with the relevant boundary conditions. The discretized conservation equations were solved with the software Fluent (Ansys, 2021), which is based on the finite volume numerical method.

Finally, at the post-processing step, several auxiliary variables are determined to allow the analysis of the flow, such as: shear rate, pressure, maximum and mean quantities. At this stage, different types of graphs are also created to analyze the flow in a qualitative form with 3D contours, and in a quantitative form, with the spatial and temporal variation of selected variables in x-y plots.

In the next sections, the systematic methodology created and followed to evaluate the flow during a cardiac cycle of different patients' aortas are described.

5.1 Preprocessing

The image exams of patients with aneurysm were provided by the National Institute of Cardiology, from a CTA scan in DICOM format, in a 64-slice scanner

SOMATOM Sensation 64 (Siemens, Germany). It was excluded patients with a history of cardiac surgery, percutaneous intervention of the aortic valve or ascending aorta, aortic coarctation, ascending aortic dissection, collagen disease or Marfan syndrome. Patients with unavailable CTA images or inadequate radiological techniques (*e.g.*, artefacts or no use of contrast agent) were also excluded. All CTA exams were performed as recommended by the attending medical team.

The image exams of the healthy patient were collected by MRI scanner MAGNETOM Prisma 3 Tesla (Siemens, Germany). All the slices were spanned from the aortic annulus to the thoracic aorta and were first evaluated by Synedra View Personal software (Synedra, Austria) (Figure 5.1).

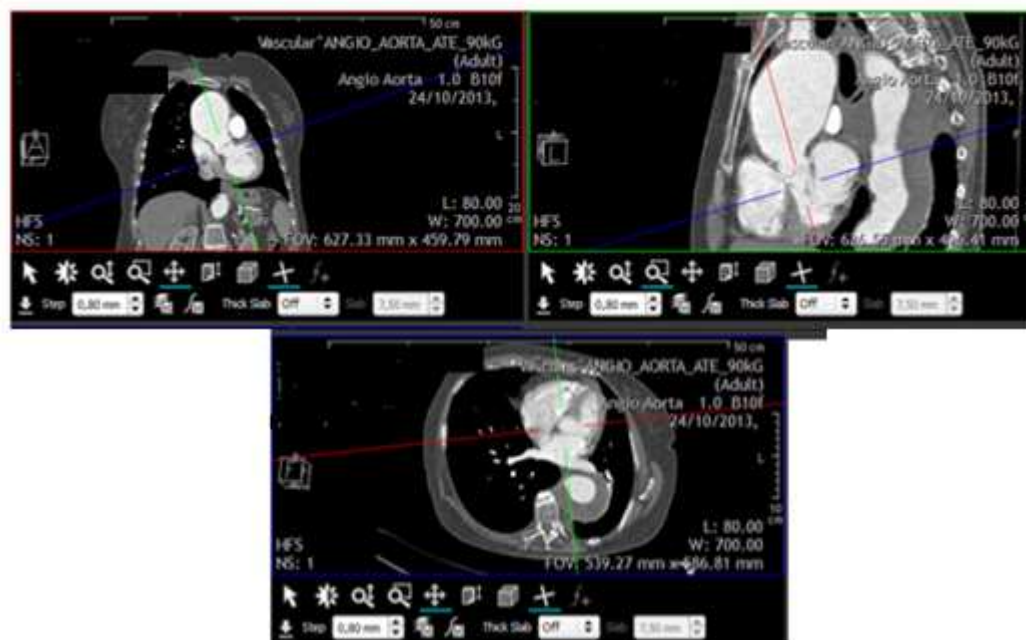


Figure 5.1 – CTA slices views with Synedra View Personal (Own Authorship).

In order to guarantee the real size of the 3D geometry, the DICOM images were transferred to FIJI (Fiji is Just ImageJ) software, which is distributor of the popular open-source software ImageJ, focused on biological-image analysis (Schindelin et al., 2012) (Figure 5.2).

Pixels, that means “picture elements,” are the smallest units of information in a digital image or display. Each pixel contains color and brightness information and for same geometry proximal values are found. It enables the usage of filters image which separates pixels in a range, selecting what is inside this cutting and removing pixels outside of it.

Aiming to obtain the 3D geometry of the aorta, a large area of the exam containing the object of interest of this study was demarcated in all slices transferred to FIJI software, as shown in the yellow square line in Figure 5.3(a). The biggest circle corresponds to ascending aorta while the smallest circle the descending aorta. A semi-automatic approach was used. After that, just the demarcation was considered [Figure 5.3(b)], and then the pixels corresponding to the aorta was isolated through a series of filters, to finally obtain only the aortic geometry at slices, Figure 5.3(c).

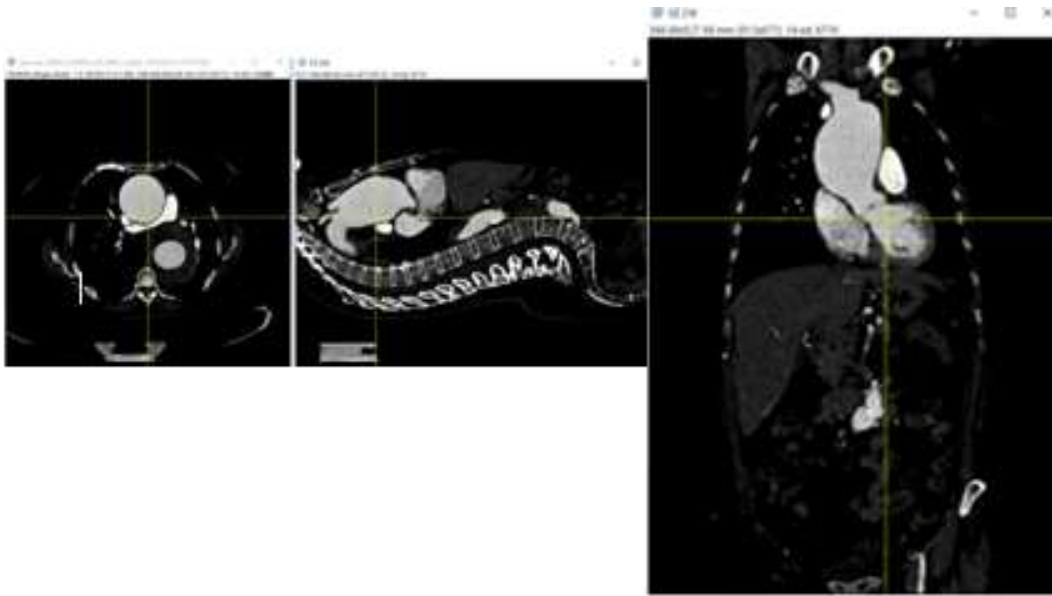


Figure 5.2 – Step to collect slice distance at Fiji Software (Own Authorship).

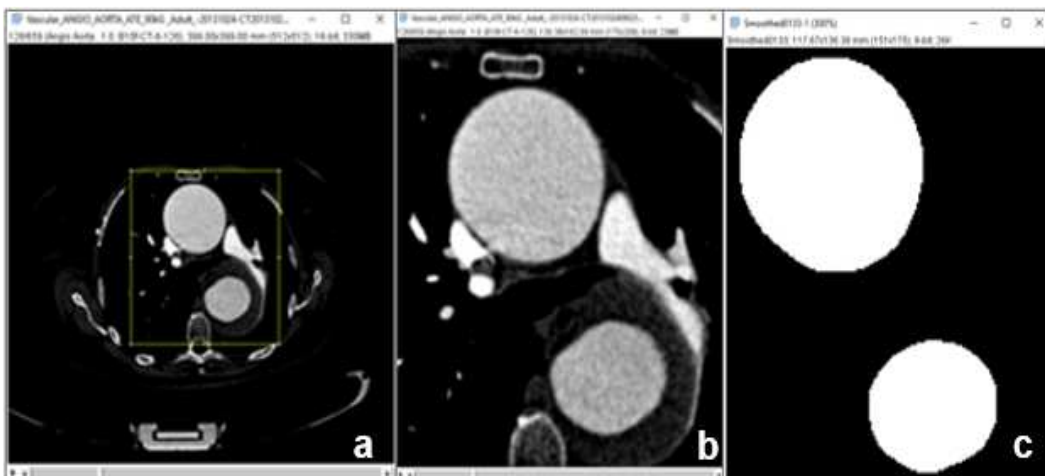


Figure 5.3 – (a) All images transferred to Fiji (b) Aortic region selected (c) Segmented aorta (Own Authorship).

After that, the slices were transferred Mimics software (Materialise, Belgium)

to segment the aorta, i.e., transforming into a 3D object. The data contained in Table 5.1. such as pixel size and slice distance, besides aorta orientation, were given to the software aiming to adjust the object into its real size (Figure 5.4).

Table 5.1 – Example of slice distance and pixel size.

Slice	Scale [pixels/mm]	z [mm]	Slice Distance [mm/slice]	Pixel Size [mm/pixel]
659	1.28	527.58	0.80	0.78

Therefore, the methodology discussed above was applied to all patients analyzed. After these steps, the geometry was transferred to Design Modeler, where the orientation of the object was done, i.e., the definition of the reference system. Figure 5.5. shows two views of the geometry detailing the axes of reference system used, where the z-axis is positioned perpendicularly at the entrance and y-axis pointed to the left coronary, defining the inlet plane. The outlets planes are defined as showed in Figure 4.4.

The subsequent step was the grid creation, i.e., the computational domain, using the Meshing Tool from Ansys Inc. (2021). It was defined with tetrahedral elements and five prism layers near the wall, to guarantee the proper refinement of this region. In Figure 5.6 an aorta's grid and a perpendicular slice is shown.

To define the mesh to be used, a grid test was performed, and its results is presented in Appendix A2. It was obtained that a domain of 3.5×10^6 cells can be used without compromising the results of the simulations.

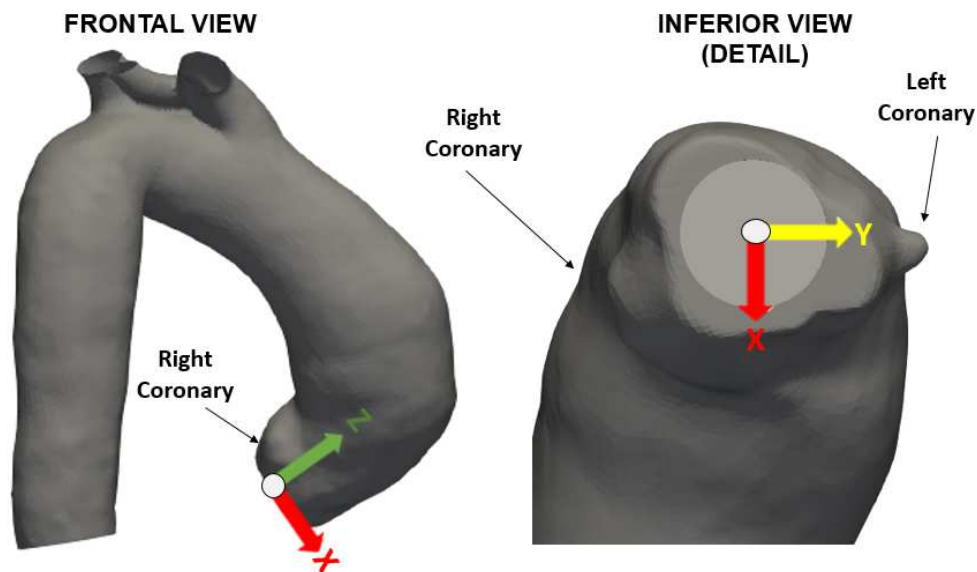


Figure 5.4 – Reference system (Own Authorship).

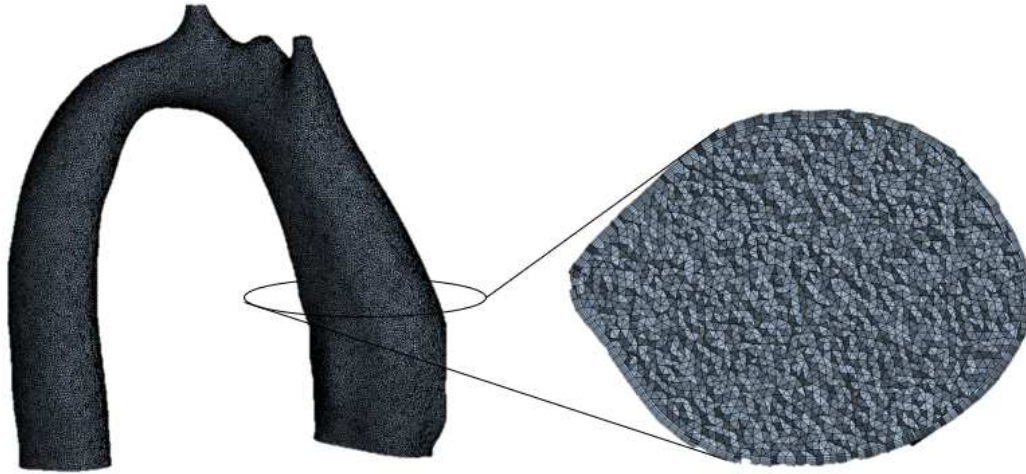


Figure 5.5 – Aorta's grid and a perpendicular slice (Own Authorship).

5.2 Processing

The Finite Volume Method, as introduced by Patankar (1980) stands as a discretization technique that ensures the global conservation of the variables of interest. This method is highly recommended to solve fluid flow problems. It involves the subdivision of the computational domain into small control volumes, each possessing a central node. The discretized equations are derived by integrating the differential equations over each control volume. Additionally, various schemes are applied to estimate the convective and diffusive fluxes across the faces of these control volumes, as well as source terms of the resulting balance equation (Tanyi & Thatcher, 1996)

The conservation of mass, conservation of momentum and turbulence equations that delineate the study were solved using the finite volume method provided by the ANSYS Fluent software v2021R1 (Ansys Inc.,2021).

The liquid flux through each control volume face has a convective and diffusive contribution. In order to estimate the flux, the Second Order Upwind was the approach selected.

The Pressure-Velocity Coupling, that solves all momentum and turbulent quantities equations in a sequential form, and the pressure field is obtained to enforce mass conservation, was solved using the Coupled scheme.

The system of algebraic conservation equation of each variable was solved with the Green Gauss-Seidel Cell Based.

Due the fact that conservation equations are non-linear, sub-relaxation was employed. Appropriate sub-relaxation factors decrease the oscillations of the variables. The sub-relaxation parameters were defined as: 0.5 for the momentum

and pressure, 0.3 of intermittency, 0.5 for the Turbulent Kinetic Energy (κ), 0.5 for Specific Dissipation Rate (ω) and 0.3 for the Turbulent Viscosity. The system was considered converged when the residual of all differential equations were inferior to 10^{-6} .

5.2.1 Coupling with Windkessel model

When adopting the Windkessel model at the boundaries, the solution of the 3E WK model for each outlet must be coupled with the flow solution. The approach employed was developed by Deyranlou (2021). It is a regression method, where the WK equation is rewritten for each outlet i as

$$\dot{V}_i = C \frac{d}{dt} (p_i - \dot{V}_i R_p) + \frac{p_i - \dot{V}_i R_p}{R_d} \quad (5.1)$$

The flowchart of the employed algorithm with the coupling between the Fluent 3D-domain and the Windkessel model is present in Figure 5.6. The area-averaged volumetric flow \dot{V}_i at the boundary of the 3D-Domain is computed and used by RCR model to compute the correspondingly static pressure p_i at this boundary for the next iteration step. The initial condition for this process is an initial pressure p_i^0 at $t = 0$.

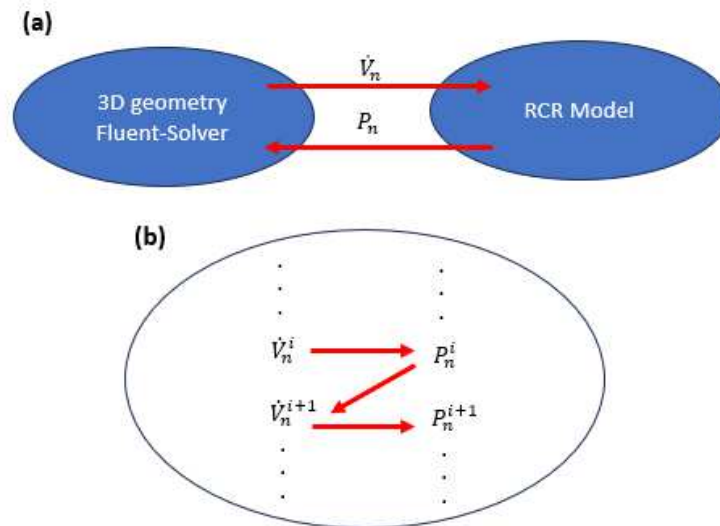


Figure 5.6 – (a) Coupling of 3D geometry and the Windkessel RCR model. (b) Iterative update scheme for pressure and flow (Own Authorship).

5.3 Post-processing

The present numerical study concerns an entire cardiac cycle, which is

periodic. Thus, the initial numerical condition does not affect the overall results after a stable periodic solution is reached. To obtain the periodic solution, the initial values for pressure, velocity components, turbulent kinetic energy and specific dissipation were computed based on the inlet plane values. The intermittency was set as zero. Five cycles were solved and, each cycle was compared with the previous one. In Appendix A3, it is shown that the solution of the 4th cycle presented is equivalent to the fifth cycle, therefore, all post-processing were performed with the data of the last cycle.

There are several types of post-processing that were used: iso-surfaces of selected variables, streamlines, profiles along a line for a particular time instant, or along time for a particular position, etc. Due to the huge volume of data in transient 3D problems, area-average values and average in the period (a complete cardiac cycle) are important measures to be evaluated, as well as maximum and minimum values.

Considering ϕ as any variable of interest, to determine an area-average, first the area of interest A_I must be selected. The area-average is defined as,

$$\bar{\phi} = \frac{1}{A_I} \int_{A_I} \phi dA_I \quad (5.2)$$

The average on a desired time interval of interest, T_I , can be written as

$$\langle \phi \rangle = \frac{1}{T_I} \int_{T_I} \phi dt \quad (5.3)$$

where t is time.

To compare the variables between the two groups (with and without growth), the relative difference variable ε was calculated as

$$\varepsilon = \frac{|\phi_{growth} - \phi_{without\ growth}|}{\phi_{growth}} = \left| 1 - \frac{\phi_{growth}}{\phi_{without\ growth}} \right| \quad (5.4)$$

6 HEALTHY PATIENT

To approximate the methodology described in the previous chapters, a simulation of the blood flow along the aorta of a healthy specific patient was performed. The volunteered patient, that is the author of this thesis, underwent an CT exam, which allowed the definition of the 3D aorta's model. The input flow data to perform the simulations were obtained from measurements of the 4D-Flow MRI technique.

The simulations were performed specifying the measured mass flow rate at the inlet. With respect to the boundary conditions at the four outlets, two types of conditions were imposed: the WK and a simpler and faster approach, based only on the mass flow rate percentage at each outlet. In both cases, the data needed for the simulations were determined from the measured values.

In this way, a thorough study was established with the comparison between the results of CFD simulations and the measured quantities provided by 4D-Flow MRI.

6.1 Measured 4D Flow MRI Variables

The 4D-Flow MRI software provides graphs of the volumetric flow rate, pressure, WSS at several planes along the aorta, as well as streamlines colored by velocity.

The pressure and WSS data made available by the 4D-Flow MRI software, are in fact determined indirectly from the velocity. Further, it is not clearly presented by the software documentation how these quantities are obtained. This issue will be better discussed when presenting the data related with these two variables.

The volumetric flow rate (\dot{V}) was converted to mass flow rate (\dot{m}) considering the blood density equal to 1054 kg/m^3 (Vitello et al., 2015), as employed here.

$$\dot{m} = \rho \dot{V} \quad (6.1)$$

The standard clinical reading was performed using cvi42 v5.14.2 4D-Flow (Circle Cardiovascular Imaging Inc., Calgary, AB, Canada). The software provides the 3D aorta visualization, as shown on the left side of Figure 6.1, and allows the placement of planes which are used to obtain the hemodynamic variables based

on the collected data from the CT scan. The plans are freehand placed by the operator, which may cause inaccuracy of results from 4D-Flow MRI.

Since all experimental data were provided only by the image, as presented in Figure 6.1, it was necessary to extract the data with the Engauge software, to allow comparison with the simulation, which results in an additional data uncertainty.

For the analyzed patient, it was considered the measured pressure values at the exam's day, which was $P_{systole} = 100 \text{ mmHg}$ and $P_{diastole} = 60 \text{ mmHg}$.

6.2 Boundary Condition

Figure 6.1 and Figure 6.2 illustrate the measured volumetric flow rate variation during the cycle, at the different selected planes. From the image shown, the cycle period T was defined as 0.96 s.

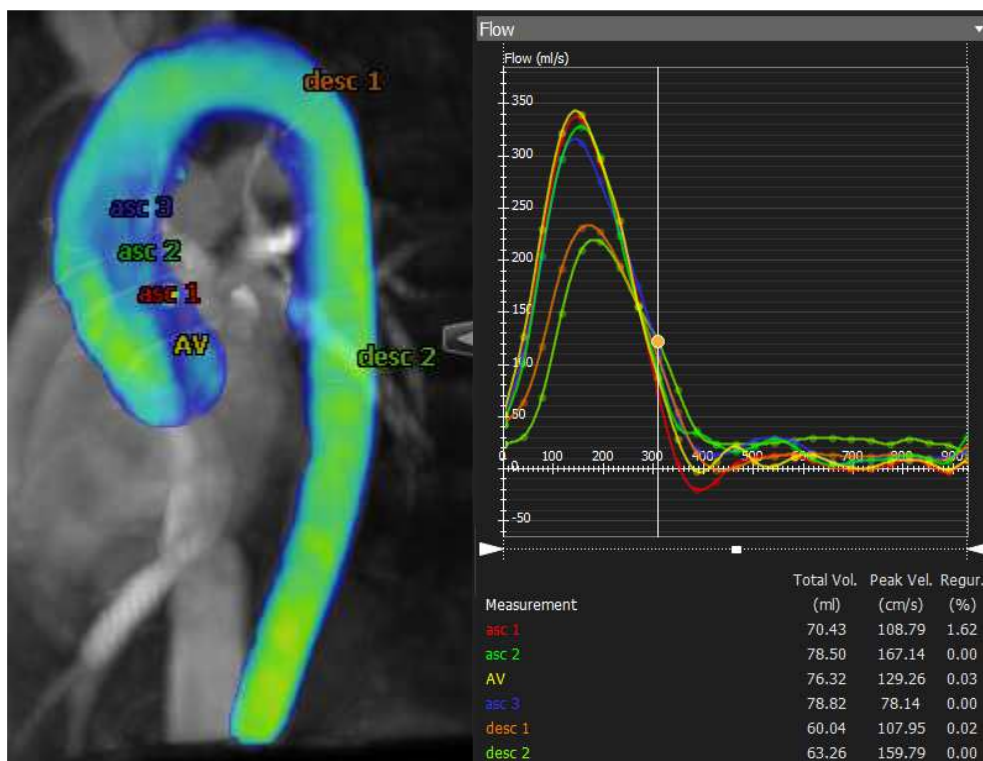


Figure 6.1 – Volumetric flow rate in planes along the ascending aorta provided by cvi42 v5.14.2 4D-Flow MRI software.

The curve 'AV' colored in yellow, illustrated in Figure 6.1, corresponds to the volumetric flow rate of the inlet plane. For the abdominal aorta volumetric flow, it is used the curve 'desc2' from Figure 6.1, which corresponds to 'out4'. Besides that, the planes namely 'asc1', 'asc2' and 'asc3' are located in the ascending aorta,

while 'desc1' and 'desc2' in the descending aorta.

Figure 6.2 presents the volumetric flow for the exits in the aortic arch, where the curves 'TBC' refers to the brachiocephalic trunk ('out1'), 'Carotida esq' to the left subclavian ('out2') and 'Subclavia esq' to left common ('out3').

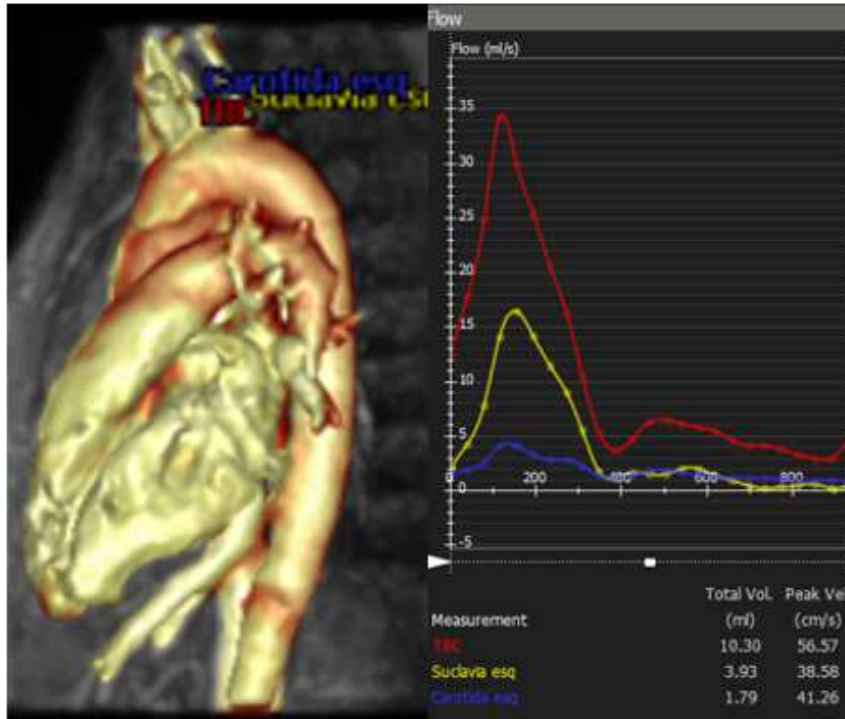


Figure 6.2 – Volumetric flow rate curves of outlet planes provided by cvi42 v5.14.2 4D-Flow software.

The data 'AV' of Figure 6.1 was extracted as the inlet boundary condition for the simulation and it is shown in Figure 6.3 (the curve data is presented in Appendix A4).

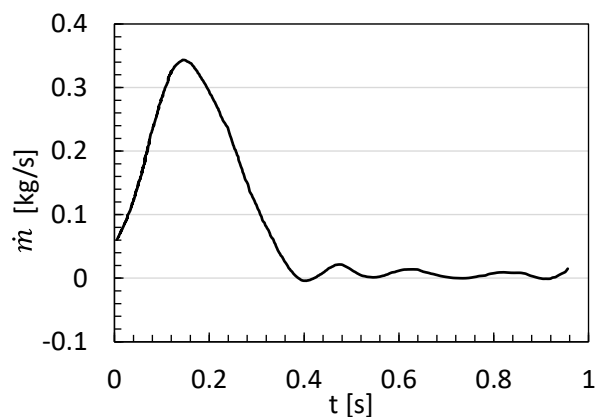


Figure 6.3 – Mass flow rate input curve.

In the absence of detailed velocity field at the aorta inlet, a uniform velocity profile normal to the inlet plane was imposed. Although Pirola et al. (2019) argues

that the blood flow in the aorta is helical, according to Morbiducci et al. (2013) findings, this approximation could serve as a suitable inlet BC, allowing the accurate representation of wall shear distributions in normal aortas. Further, for individuals with good health, valvular velocity profiles typically exhibit symmetry, featuring a predominant axial component.

As mentioned, two types of outflow boundary conditions were imposed for the numerical simulation. As shown in Figure 2.5, the aorta presents four outlets, corresponding to the brachiocephalic trunk, left subclavian, left common and the abdominal aorta. For both types of boundary conditions, it is necessary to know the flow rate percentage in relation to the inflow rate, at each outlet.

The present model considers the fluid as incompressible, flowing through a rigid aorta, therefore, due to uncertainties in the measurements, the mass conservation is never experimentally conserved. However, the mathematical model employed requires mass conservation, thus, it is important to verify if the same mass enters and leaves the domain. The total mass conservation of blood inside the aorta is

$$\frac{d \rho \forall}{d t} = \dot{m}_{in} - \dot{m}_{out} \quad (6.2)$$

where the mass inside of the aorta is $m = \rho \forall$, with ρ as the blood density, and \forall the volume inside the aorta, \dot{m}_{in} is the mass flow rate entering the aorta, and \dot{m}_{out} the total mass flow rate leaving the aorta.

Figure 6.4 shows a comparison between the mass flow inlet curve and the total mass outflow (sum of the 4 outflow planes). As it is possible to notice, for each instant of time, the mass flux that enters in the aorta does not correspond to what comes out.

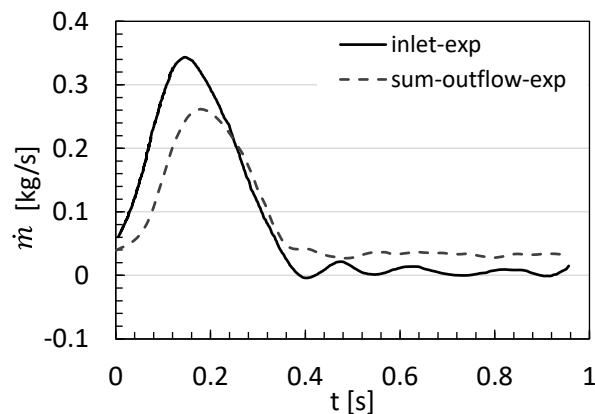


Figure 6.4 – Comparison between the mass flow inlet curve and sum of all mass outflow curve of the experimental results.

Figure 6.5 presents the difference between the mass flow inlet and the sum outflow. The biggest difference occurs at the systolic peak and this may have occurred due the vessel's dilation (Ibanez, 2019) and also due to a possible compressibility of the blood flow, but more likely due to uncertainties on the measurements. However, considering the overall balance of the cycle, the continuity equation is preserved, with an error of less than 0.03%.

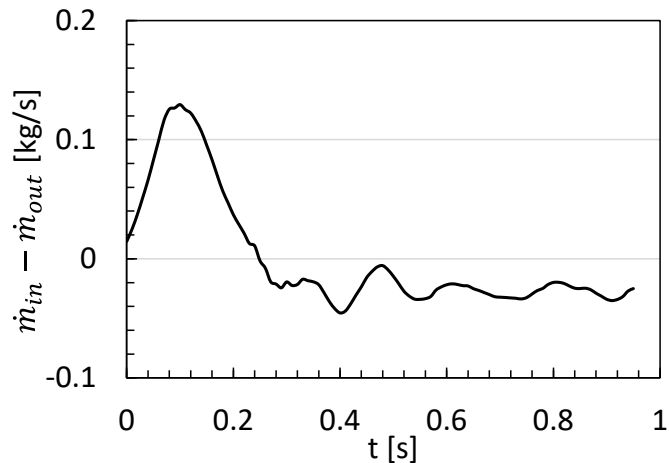


Figure 6.5 – Difference between inlet mass flow and the sum outflow of the experimental results.

For the present model (incompressible and rigid aorta), an adjustment of the outflow rate percentages was performed, so that the mass balance was guaranteed at each time instant. Therefore, to determine the outflow percentage, the mass flow rate over the complete cycle of each outlet was calculated in relation to the total inflow, and the time percentages are shown in Table 6.1.

Table 6.1 – Flow percentage at each outlet.

Plane	Flow percentage [%]
<i>out1</i>	13.1
<i>out2</i>	4.9
<i>out3</i>	2.2
<i>out4</i>	79.8

For the case based on the RCR WK model, the resistances and capacitance at each outlet must also be determined, as boundary conditions. Considering the analyzed patient, the pressure values at exam's day ($p_{systole} = 100 \text{ mmHg}$; $p_{diastole} = 60 \text{ mmHg}$) were imposed, resulting in an average pressure equal to $p_{avg} = 73.3 \text{ mmHg}$. The average flow rate was calculated based

on the input curve shown in Figure 6.3 as $\dot{V}_{avg} = 80.40 \text{ ml/s}$. The calculated parameters for each outlet are shown in Table 6.2.

Table 6.2 – Three-element Windkessel model parameters for each outlet.

Plane	$R_p \times 10^7$ [$\text{kg m}^{-4} \text{s}^{-1}$]	$R_d \times 10^8$ [$\text{kg m}^{-4} \text{s}^{-1}$]	$C \times 10^{-9}$ [$\text{kg m}^4 \text{s}^2$]
<i>out1</i>	8.35	8.45	1.35
<i>out2</i>	22.30	22.60	50.50
<i>out3</i>	49.70	50.30	22.70
<i>out4</i>	1.37	1.39	8.22

6.3 Post-processing definitions

To compare the results numerically obtained with the measured experimental data, five planes were created in the aorta geometry, based on the locations of the measured data during the exam. Figure 6.6 shows these planes. There is one at the entrance, the ‘inlet’ plane, and four at the outputs: ‘out1’, ‘out2’, ‘out3’ and ‘out4’. Further, four planes were created at the ascending aorta, namely ‘asc1’, ‘asc2’ and ‘asc3’ and two at the descendent aorta, ‘desc1’ and ‘desc2’. These planes were defined such that they are perpendicular to the aorta’s wall, aiming to obtain reproducibility of the data.

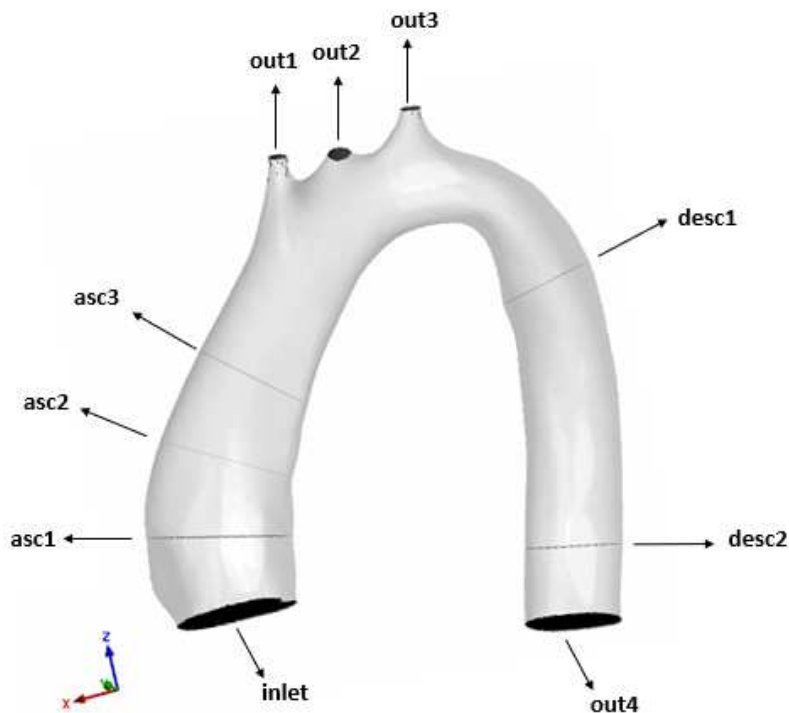


Figure 6.6 – Inlet, outlets and selected planes along the aorta (Own Authorship).

To aid the understanding of the graphs, the experimental results are represented by 'exp' and the numerical results by 'num'.

The ascending aorta was defined as the region of interest of the study and is shown in Figure 6.7. The region was limited between the entrance and the beginning of the brachiocephalic trunk.



Figure 6.7 –Region of interest (Own Authorship).

Initially, the results obtained with the Windkessel model are compared with the experimental data. In the sequence, the impact of employing the simple outflow percentage boundary condition is addressed. All results considered are from the 4th cycle, since according on the test presented in Appendix A3, the periodicity is achieved.

6.4 Mass Flow Rate

To evaluate the numerical model, a comparison of the predicted mass flow rate over one period for each output with the experimental data is shown in Figure 6.8. It is possible to visualize a qualitative agreement between the experimental and numerical results at all outlets.

To carry out a quantitative analysis, the average mass flow rate along the cycle at each outlet i , was determined as

$$\langle \dot{m}_i \rangle = \frac{1}{T} \int_0^T \dot{m}_i dt \quad (6.3)$$

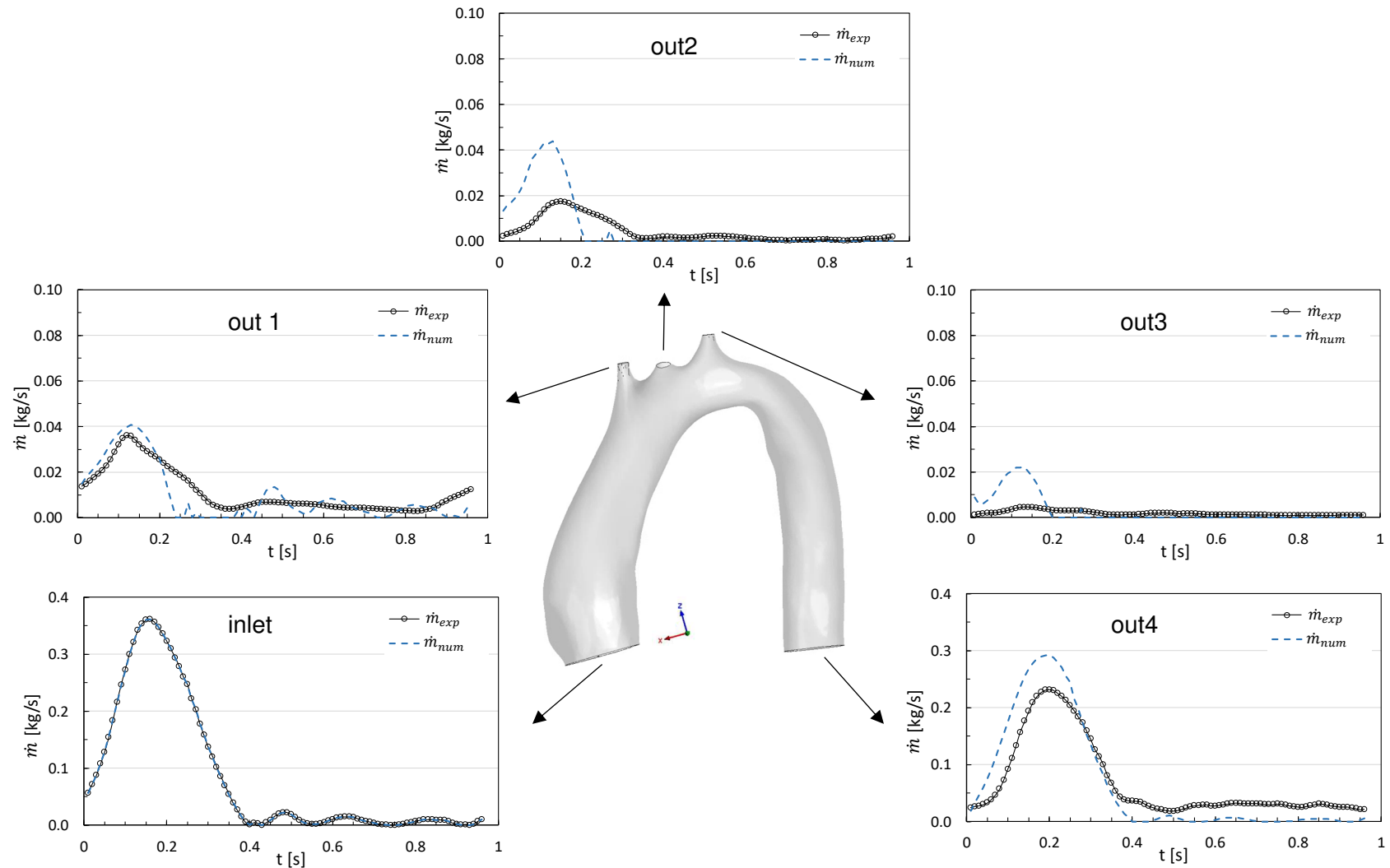


Figure 6.8 – Numerical-experimental comparison of mass flow rate at outputs

The percentage ratio of each average outflow in relation to the average inflow was determined and shown in Table 6.3. In the same table, it is shown the error ϵ between the experimental and numerical results, expressed as

$$\epsilon = \frac{|\phi_{exp} - \phi_{num}|}{\phi_{exp}} = \left| 1 - \frac{\phi_{num}}{\phi_{exp}} \right| \quad (6.4)$$

Table 6.3 – Numerical-experimental comparison of inlet x outputs mass flow rate

Plane	Experimental		Numerical		Error ϵ [%]
	$\langle \dot{m} \rangle$ [kg/s]	$\frac{\dot{m}_{out}}{\dot{m}_{in}}$ [%]	$\langle \dot{m} \rangle$ [kg/s]	$\frac{\dot{m}_{out}}{\dot{m}_{in}}$ [%]	
<i>inlet</i>	8.47		8.47		
<i>out1</i>	1.11	13.1	0.96	11.28	13.96
<i>out2</i>	0.42	4.9	0.59	6.94	43.33
<i>out3</i>	0.19	2.2	0.28	3.27	48.33
<i>out4</i>	6.75	79.8	6.62	78.15	1.86
<i>Total</i>	8.47	100.0	8.44	99.65	0.35

Analysing Table 6.3, it is possible to observe that the agreement between numerical and experimental data with the last output, ‘out4’, is very good. Due to large number of uncertainties, the agreement with ‘out1’ can be considered acceptable. Examining the agreement between the data for ‘out2’ and ‘out3’, a large percentage error is seen. However, at these two outflow regions, the mass flow measured is very small, leading to large uncertainties.

To better analyse the results, Figure 6.8 illustrates the time mass flow evolution at the four-outflow region during the cardiac cycle. ‘out1’ presents after the systolic period, an oscillation around the experimental data which may be explained by the pressure waves not captured by the experimental device, leading to an error of 13.96%. An overprediction is observed during the systole at ‘out4’, while there is practically null flow rate during the diastole (underprediction), ensuring overall mass balance. Considering the entire cycle, the error is calculated as 1.86%, indicating that the percentage of output flow matches by the captured in 4D-Flow MRI.

As mentioned, the second and third outputs, ‘out2’ and ‘out3’, exhibit the highest error due to their low flow rate and the overprediction of the mass flow rate during the systole. This discrepancy might be a consequence of the imbalance in mass flow rate rates observed in the experimental data during the systole, as illustrated in Figure 6.5. Notably, practically no outflow was predicted at outlets 2 and 3 during diastole, aligning with the experimental findings.

To aid in the evaluation of the mass flow rate through the aorta, Table 6.4 shows the numerical-experimental comparison of the average mass flow rate along the cycle at each selected plane, indicated in Figure 6.6. The average plane velocity, corresponding to the maximum flow rate, V_{peak} , at each plane is also included in Table 6.4, since this information was experimentally measured (Figure 6.1).

The mass flow rate at each time instant, at the planes in the interior of the domain and the peak velocities were numerically determined by

$$\dot{m}_i = \sum_j \rho (u_x n_x + u_y n_y + u_z n_z) dA_j \quad ; \quad V_{peak} = \frac{\max \dot{m}_i}{\rho \sum_j dA_j} \quad (6.5)$$

where j corresponds to each cell in the plane.

As already shown at the boundary planes, there is a discrepancy at the maximum flow rate during the cycle, as a consequence, V_{peak} errors are higher than the average mass flow rate. However, we believe that V_{peak} errors at the planes closer to the curvature are high, also due to the lack of accuracy of 4D-Flow software to capture the turbulence flow and recirculation in this region, as discussed in the literature Kalpakli Vester et al. (2016). The average mass flow rate during the cycle at each plane presents similar value, with equivalent error as the ones obtained at the boundaries. These results indicate the mass balance throughout the complete cycle and a reasonable agreement between numerical and experimental results.

Table 6.4 – Numerical-experimental comparison of velocity peaks and average mass flow rate at auxiliary planes

Plane	Experimental		Numerical		ϵ [%]	
	V_{peak} [m/s]	$\langle \dot{m} \rangle$ [kg/s]	V_{peak} [m/s]	$\langle \dot{m} \rangle$ [kg/s]	V_{peak} [m/s]	$\langle \dot{m} \rangle$ [kg/s]
<i>asc1</i>	1.09	74.23	0.86	81.09	21.10	9.24
<i>asc2</i>	1.67	82.74	0.95	80.97	43.11	2.14
<i>asc3</i>	0.78	83.08	1.19	66.51	52.56	19.94
<i>desc1</i>	1.08	63.28	1.55	63.19	43.52	0.15
<i>desc2</i>	1.60	66.68	1.54	63.58	3.75	4.65

A final important comment related to the flow comparison is related to the definition of the blood density, which was not measured, and as it is well known influences the flow. Thus, in spite of this additional uncertainty, reasonable results were obtained.

6.5 Pressure

The cvi42 v5.14.2 4D-Flow software calculates the pressure difference between a particular position, chosen by the operator, in relation to a reference location, all placed freehand. Here, it was assumed that the displayed values along the cycle, obtained by the images, represent average values at the plane containing the selected position, since full velocity and pressure field were not provided.

On the left side of Figure 6.9, the selected planes along the aorta geometry are shown, and on the right side, the graph with the experimental pressure differences, $\Delta\bar{P}_{exp} = \bar{P} - \bar{P}_{ref}$, between the defined planes and the reference plane. The plane namely 'asc' refers to 'asc1'. The reference plane was defined by the operator as the inlet plane.

The numerical pressure difference $\Delta\bar{P}_{num}$ was calculated employing the pressure field obtained by the solution of the conservation equations. It is based on the area average pressure of the selected plane \bar{P}_i and the reference plane \bar{P}_{ref}

$$\Delta\bar{P}_{num} = \bar{P}_i - \bar{P}_{ref} \quad (6.6)$$

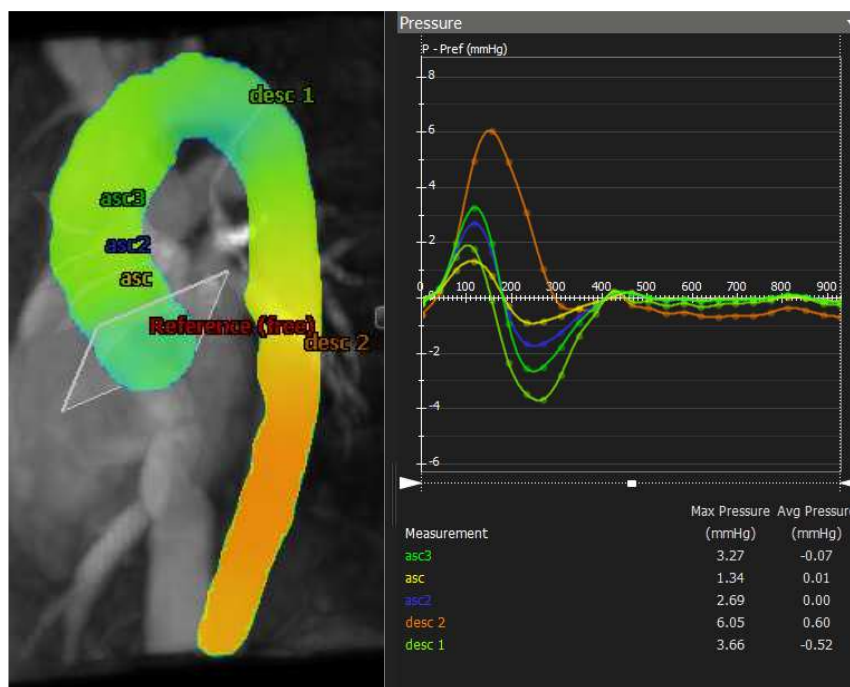


Figure 6.9 – Pressure drops of planes in ascending aorta provided by cvi42 v5.14.2 4D-Flow software

The maximum and cycle time-average of the average-area pressure difference at the five selected planes (Figure 6.6) are shown in Table 6.5. Table 6.5 reveals that the error of $\Delta\bar{P}_{max}$ is smaller at the planes in the ascending aorta,

showing agreement between numerical and experimental results. Conversely, the planes at the descending part exhibit considerable error, indicating substantial divergence between the results. Similarly, $\langle \Delta \bar{P} \rangle$ shows elevated error values, likely attributed to the influence of the diastolic phase during the cardiac cycle.

Table 6.5 –Numerical-experimental comparison of maximum and cycle time-average of the average-area pressure difference

Plane	Experimental		Numerical		ϵ	
	$\Delta \bar{P}_{exp_{max}}$ [mmHg]	$\langle \Delta \bar{P}_{exp} \rangle$ [mmHg]	$\Delta \bar{P}_{num_{max}}$ [mmHg]	$\langle \Delta \bar{P}_{num} \rangle$ [mmHg]	$\Delta \bar{P}_{max}$ [%]	$\langle \Delta \bar{P} \rangle$ [%]
<i>asc1</i>	1.34	0.01	1.18	-0.02	11.9	300.0
<i>asc2</i>	2.69	0.00	2.49	-0.07	7.4	NA
<i>asc3</i>	3.27	-0.07	4.25	-0.26	30.0	271.4
<i>desc1</i>	3.66	0.52	117.00	-3.18	3096.7	711.5
<i>desc2</i>	6.05	0.60	200.81	-4.74	3219.2	890.0

To elucidate the aforementioned high error, Figure 6.10 illustrates a comparison of area-average pressure difference along the cycle at the selected planes. To reduce the numerical oscillations captured in the planes, the 8th order Fourier series was used in the data. Planes ‘asc1’, ‘asc2’ and ‘asc3’, present a good agreement between the results, approximating the model developed. However, the same conclusion is not obtained in the descending part, where the experimental data is significantly smaller than the numerical results. Nevertheless, the predicted numerical results seem more realistic than the displayed values obtained from the exam.

Kalpakli Vester et al. (2016) presented an extended review regarding the effect of curvature on transition to turbulence, pressure losses, swirling and pulsating flow. They have indicated that recirculation’s arise due to the secondary flow of the fluid due to the irreversibility’s associated with the geometry, leading to a high pressure drop. The effect of load loss caused by mass outflow from the aortic arch was investigated, but no significant results were found, suggesting the great contribution of the curvature effects.

It should be mentioned that the cardiovascular pressure fields are not a trivial task to measure. Usually, it is determined indirectly from the velocity field. The result obtained may indicate that 4D-Flow software does not consider the real pressure that occurs in the evaluated plane when the pressure drop is calculated from the velocity profile.

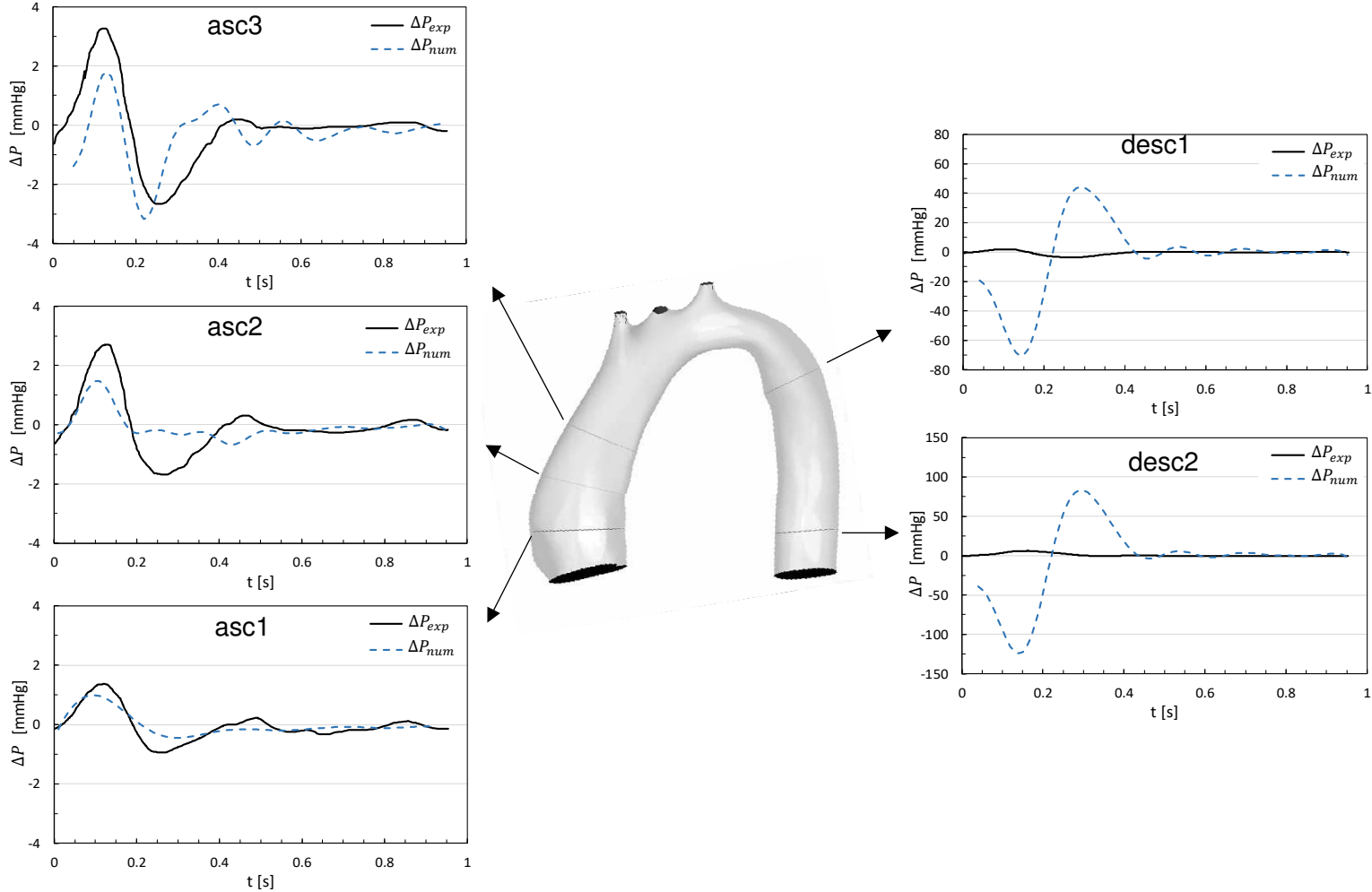


Figure 6.10 – Numerical-experimental pressure drops comparison of planes along the aorta using Eq. 6.9.

Several researchers (Ebbers & Farnebäck, 2009; Bouaou et al., 2019; Nolte et al., 2021, Rengier et al. (2014), Krittian et al. (2012), Saitta et al. (2019) and Nolte et al. (2021)) have determined the pressure gradients from the 3D time resolved velocity MRI measurements using the full velocity field, $\mathbf{V} = (u, v, w)$, provided.

However, these procedures require the complete velocity field (in time and space), which rarely are available. Thus, simplified approaches are applied to estimate the pressure. Ramaekers et al. (2023) in its clinician's guide investigated the aortic 4D-Flow MRI data, and they pointed out that compared to other flow related variables, the acquired pressure field accuracy, reproducibility, and clinical applicability using this technique are still relatively unknown.

The cvi42 v5.14.2 4D-Flow software manual is not clear exactly which approximation is employed to present the pressure evolution with time at the selected planes. A few approximations are found in the literature and are discussed in the sequence.

6.5.1 Approximated pressure difference

The simplest approximation to estimate the pressure difference is to neglect all pressure losses, and to estimate the pressure applying steady state Bernoulli's equation (Shi et al., 2019),

$$\Delta P_{conv} = (\bar{P}_i - \bar{P}_{ref}) = \frac{\rho}{2} (\bar{V}_{ref}^2 - \bar{V}_i^2) = \frac{\rho}{2} \bar{V}_i^2 \left[\left(\frac{\bar{V}_{ref}}{\bar{V}_i} \right)^2 - 1 \right] \quad (6.7)$$

where $\bar{V}_i = \dot{V}/A_i$ is the average velocity at plane i , and \dot{V} is the volumetric flow rate. This pressure difference is named as "convective pressure" since it is due to the variation of the velocity, because of the plane transversal area change.

This approximation depends strongly on the definition of the reference velocity, requiring the definition of the plane cross-section area. Note that, since the plane is defined manually with the indication of a point in the interior of the aorta, and if there is a small difference in the plane inclination, the resulting area is completely different.

To simplify even further this estimation, Hatle et al. (1978) approximated the steady state Bernoulli equation, by considering the blood density equal to 1060 kg/m^3 , and maximum velocity module (V_{max}), as

$$\Delta P_{SB} = \frac{\rho}{2} V_i^2 \left[\left(\frac{V_{ref}}{V_i} \right)^2 - 1 \right] [Pa] \approx 4 V_{max}^2 [mmHg] \quad (6.8)$$

This last approximation is widely applied in techniques such as catheterization and Doppler, being considered the 'gold standard' when the pressure drop across a stenotic valve is considered (Heys et al., 2010).

The simplified Bernoulli approximation ΔP_{SB} was also employed by Archer and colleagues (2020), that performed a comparison of four-dimensional flow technique, considering the peak pressure drop in the aorta during systole. This was the first study to compare the peak pressure gradient across the aortic valve by 4D-Flow Cardiovascular Magnetic Resonance (CMR) against Transthoracic Echocardiography (TTE) and the gold standard invasive method. They point out that previous studies have demonstrated a discordance between the invasive and Doppler TTE peak pressure gradient assessment and that Doppler methods overestimate the peak pressure drop. The authors found out that 4D-Flow CMR described in their study also relies on the maximum instantaneous pressure gradient but did not result in any overestimation. Reduction in overestimation could be because the peak velocity plane was spatially identified by velocity vector visualization. This technique is not routinely applied in Doppler TTE as peak velocity assessment is made by continuous-wave Doppler, which summates all velocities in one direction. In this way, despite the requirement of a significant acquisition data and post-processing competence, the 4D-Flow offers an alternative method for non-invasive assessment of aortic stenosis in relation to invasive methods, agreeing with Saitta et al. (2019).

Donati et al. (2017) argue that these formulations neglect the unsteady term and suggested to include the transient contribution to the Bernoulli equation. Thus, the pressure loss due to the transient inertia portion, called by the authors as blood inertia, ΔP_{tran} , is added

$$\Delta P_{tran} = \int_i^{ref} \rho \frac{\partial \bar{v}}{\partial t} ds \quad (6.9)$$

So, the pressure difference is represented by two contributions, the traditional convective contribution and the transient one, as described by Shi et al. (2019).

$$\Delta P_{trB} = (\bar{P}_i - \bar{P}_{ref}) = \Delta P_{conv} + \Delta P_{tran} \quad (6.10)$$

The transient contribution depends not only on the distance ΔL between plane i and the reference plane, ref , but on the time variation of the velocity between planes. It can be approximated, assuming constant area between sections, corresponding to velocity \bar{v}_i as

$$\Delta P_{tran} = \sum_i \rho L_i \frac{d\bar{V}_i}{dt} \quad ; \quad \Delta L = \sum_i L_i \quad (6.11)$$

where L_i is the length of the vessel segment, i.e., the distance between sections. Further, to calculate the pressure drop at the descending planes, it is necessary to consider the difference of mass flow rate from the ascending part (subscript 'asc') and the descending part (subscript 'desc') due to outflow in the arteries of the aortic arch.

As outlined by Shi et al. (2019), since inertial effect is determined by the density of the blood, length and sectional area of the vessel segment, as the length of the vessel segment increases, so does the magnitude of the inertial effect. Analyzing the results, it seems that only the convective inertia pressure loss, ΔP_{conv} , is being considered to calculate the pressure of 'desc2'. However, it is important to emphasize that the pressure captured by the numerical simulation considers the transient contribution, as well as the pressure loss associated with friction and geometry curvature. As it is possible to notice, Eq. 6.10 described above does not contemplate viscous pressure losses and pressure loss related with the vessel geometry and the aortic arch outflow.

Patankar et al. (1975) has shown that the head loss associated with friction depends strongly on the difference between the curvature radius and the vessel radius. The aorta analyzed has a low ratio of radial curvature and the radius of the vessel (≈ 1.25), what suggests that the friction factor is highly relevant and cannot be ignored.

Since it is not known how the 4D-Flow software determines the pressure, an investigation of the different propositions of the literature is carried on. Figure 6.11 shows the comparison between ΔP_{exp} , ΔP_{trB} , ΔP_{tran} and ΔP_{conv} of each plane through the cardiac cycle. In the ascending planes ('asc1', 'asc2' and 'asc3'), the blood inertia curve, ΔP_{tran} , which is dominant, presents a similar behavior to the experimental pressure drop curve, ΔP_{exp} . The combined ΔP_{trB} curve does not present as good adherence with the data, what can be explained by the significant uncertainty in the determination of ΔP_{conv} , regarding the chosen reference velocity. In the descending planes ('desc1' and 'desc2'), ΔP_{tran} overestimates the pressure in comparison with the experimental data (consequently also ΔP_{trB}), what can be explained by the fact that this term is estimated considering a straight pipe with constant area, neglecting the head loss associated with the curvature, which induces strong recirculation just after the curve. The most similar curve of plane 'desc2' refers to the convective inertia pressure loss curve, ΔP_{conv} .

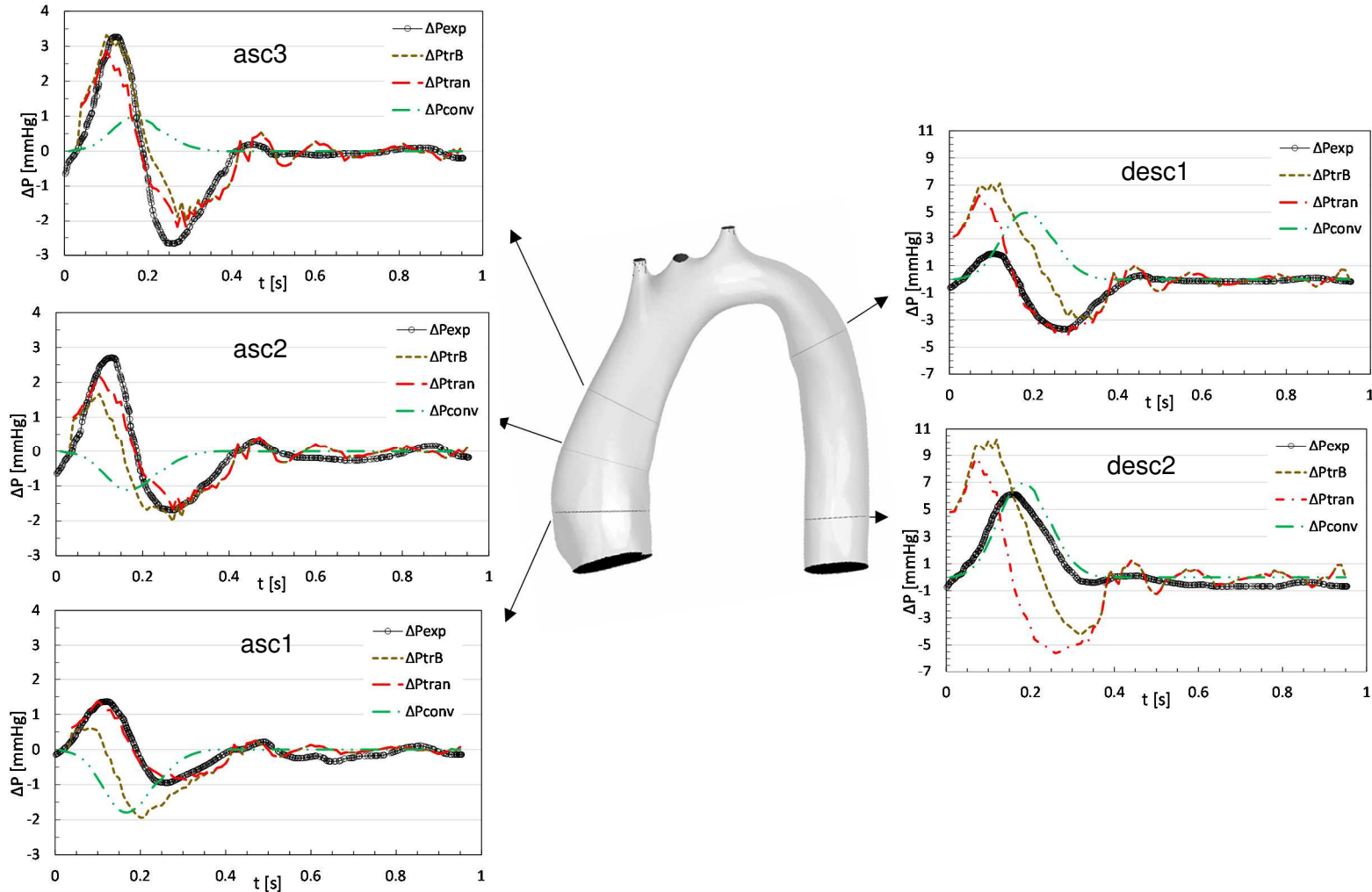


Figure 6.11 – Numerical-experimental pressure drops planes comparison.

To complete this analysis, Table 6.6 presents quantitatively the maximum pressure drop through the cycle, related with the different contributions. As it is possible to visualize in Table 6.6, the minimum error (that was calculated in relation to ΔP_{exp}) for ‘asc1’ and ‘asc2’ refers to $\Delta P_{tran_{max}}$, while for ‘asc3’ is $\Delta P_{tr_{B_{max}}}$, agreeing with what was perceived in Figure 6.11. For ‘desc1’ and ‘desc2’, the minimum error is for $\Delta P_{conv_{max}}$.

Table 6.6 –Numerical-experimental comparison of maximum pressure drops.

Plane	Experimental		Numerical				ϵ [%]	
	$\Delta P_{exp_{max}}$ [mmHg]	$\Delta P_{tr_{B_{max}}}$ [mmHg]	$\Delta P_{tran_{max}}$ [mmHg]	$\Delta P_{conv_{max}}$ [mmHg]	$\Delta P_{tr_{B_{max}}}$ [%]	$\Delta P_{tran_{max}}$ [%]	$\Delta P_{conv_{max}}$ [%]	
<i>asc1</i>	1.34	0.61	1.38	0.00	54.48	2.99	100.00	
<i>asc2</i>	2.69	1.67	2.19	0.00	37.92	18.59	100.00	
<i>asc3</i>	3.27	3.32	2.87	0.98	1.53	12.33	70.03	
<i>desc1</i>	3.66	7.13	6.25	4.97	94.81	70.77	35.79	
<i>desc2</i>	6.05	10.20	8.80	6.93	68.60	45.45	14.55	

Analyzing Figure 6.11, it is clear that the transient behavior is dominant at the ascending aorta and should be considered as stated by Shi et al. (2019), when the focus of the research is the ascending aorta to study aorta aneurysm, for example. At the descending aorta, approximated estimations of the pressure with simplified models are not adequate due to the high-pressure loss related with the curvature of the aortas arch.

6.6 Wall Shear Stress

The 4D-Flow software presents a variable named “WSS” at each selected plane, as shown in Figure 6.12. Once again, what exactly the software is determining is not known. It should represent the average WSS along the perimeter of the selected plane but there is no certainty as to how this is done.

As previously discussed, due to the uncertainty of the descending part results, the ascending part will be the focus of this analysis. Therefore, Figure 6.13 shows a comparison of the CFD WSS (τ_w) and the experimental WSS data ($\tau_{w_{exp}}$) extracted from Figure 6.12, at the three selected planes of the ascending aorta. In the CFD analysis, τ_w is the average value along the perimeter of the aortic wall of the selected planes. Due to the significant difference between the two sets of data,

logarithmic scale was employed, to allow visualization of the data. The only agreement between the results, is the fact that it has the same behavior but at different scales. There is an increase of the values close to the systolic peak and then a decrease during diastole. Higher WSS can also be observed in planes further away from the inlet plane.

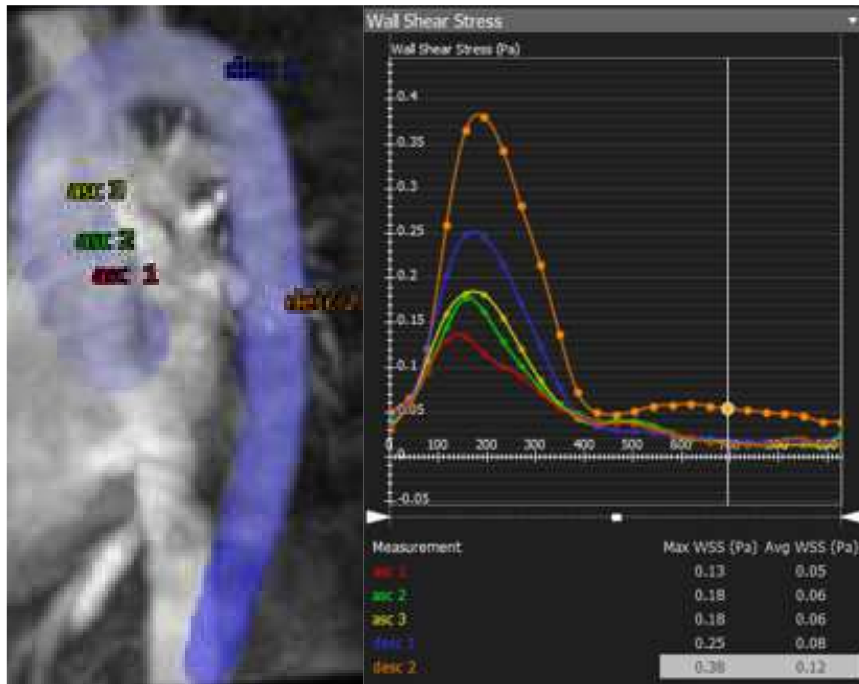


Figure 6.12 - WSS curves of ‘asc1’, ‘asc2’, ‘asc3’, ‘desc1’ and ‘desc2’ planes provided by cvi42 v5.14.2 4D-Flow software.

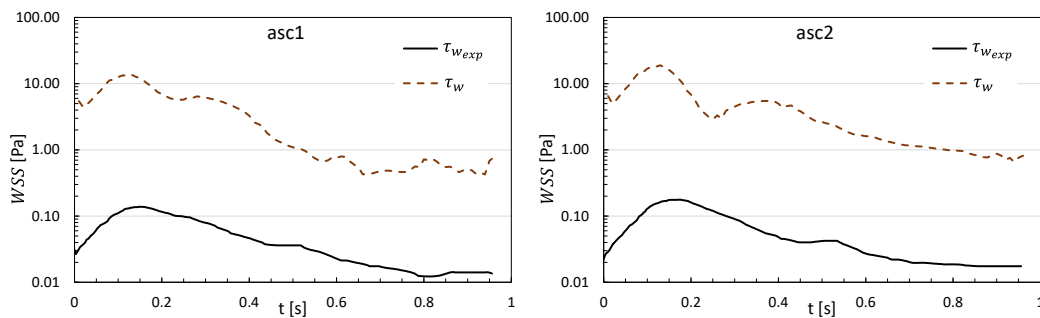


Figure 6.13 – Numerical-experimental WSS in planes of the ascending aorta.

At plane ‘asc3’, that is close to the brachiocephalic trunk, values of up to 30

Pa were obtained, as reported by several authors as Rinaudo & Pasta (2014), Celis Torres et. al. (2017), Kimura et al. (2017), Youssefi et al. (2017) and Ibanez et al. (2021).

Hence, realizing the discrepancy between the 4D-Flow and CFD simulation findings, it was decided to plot the WSS field based on velocity field, since there is also a discussion in the literature speculating which methodology employed by the 4D-Flow software to determined WSS.

According to Stalder et al. (2008), the WSS calculated by 4D-Flow software is based on the measured volume flow rate, assuming that the aorta can be represented by a circular pipe with a constant diameter, with the blood flowing in laminar regime, steady-state and fully developed. With these assumptions, the WSS, denoted as $\tau_{w_{lam}}$ is

$$\tau_{w_{lam}} = \frac{4 \mu \dot{V}}{\pi R_{ef}^3} ; \dot{V} = \bar{V} A \quad (6.12)$$

where \dot{V} is the volumetric flow rate, $R_{ef} = (4 A / \pi)^{0.5}$ is the effective radius of the plane. A and \bar{V} are the plane area and average velocity in the plane. The previous equation can also be written as

$$\tau_{w_{lam}} = \frac{f_{lam}}{8} \rho \bar{V}^2 ; f_{lam} = \frac{64}{Re} ; Re = \frac{\rho \bar{V} 2 R_{ef}}{\mu} \quad (6.13)$$

where Re is the Reynolds number evaluated at the selected plane. Since the mass flow rate varies during the cardiac cycle, as also the Reynolds number Re and the flow regime. Figure 6.14 illustrates the inlet Reynolds number variation during the cycle, where it can be seen that during almost the whole systole period, the flow is turbulent. However, it is true that, the time interval that the flow is turbulent is smaller than the time period with low Reynolds number, enforcing the need of employing a turbulent model capable of predicting the transition, as it was done here.

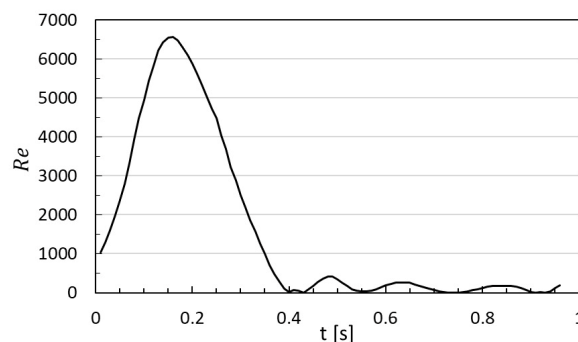


Figure 6.14 – Inlet Reynolds number.

To consider the variation of the flow regime during the cardiac cycle, a similar approximate estimation of the WSS as proposed by Stalder et al. (2008) was determined here, also assuming a straight circular pipe, steady state, fully developed, but considering laminar and turbulent regime during the cycle, determined based on a friction factor as

$$\tau_w = \frac{f}{8} \rho \bar{V}^2 \quad (6.14)$$

where the friction factor f was assessed using the following correlation (Swamee, 1993), which can be employed for both laminar and turbulent regimes.

$$f = \left\{ \left(\frac{64}{Re} \right)^8 + 9.5 \left[\log \left(\frac{\varepsilon/D}{3.7} + \frac{5.74}{Re^{0.9}} \right) - \left(\frac{2500}{Re} \right)^6 \right]^{-16} \right\}^{0.125} \quad (6.15)$$

being ε/D the relative roughness, which was neglected.

Figure 6.15 shows the comparison of the WSS provided by 4D-Flow software, $\tau_{w_{exp}}$, with $\tau_{w_{lam}}$ (Eq. 6.13) and $\tau_{w_{turb}}$ (laminar and turbulent, Eq. 6.14 and 6.15). The CFD data was not included, since it is two orders of magnitude higher.

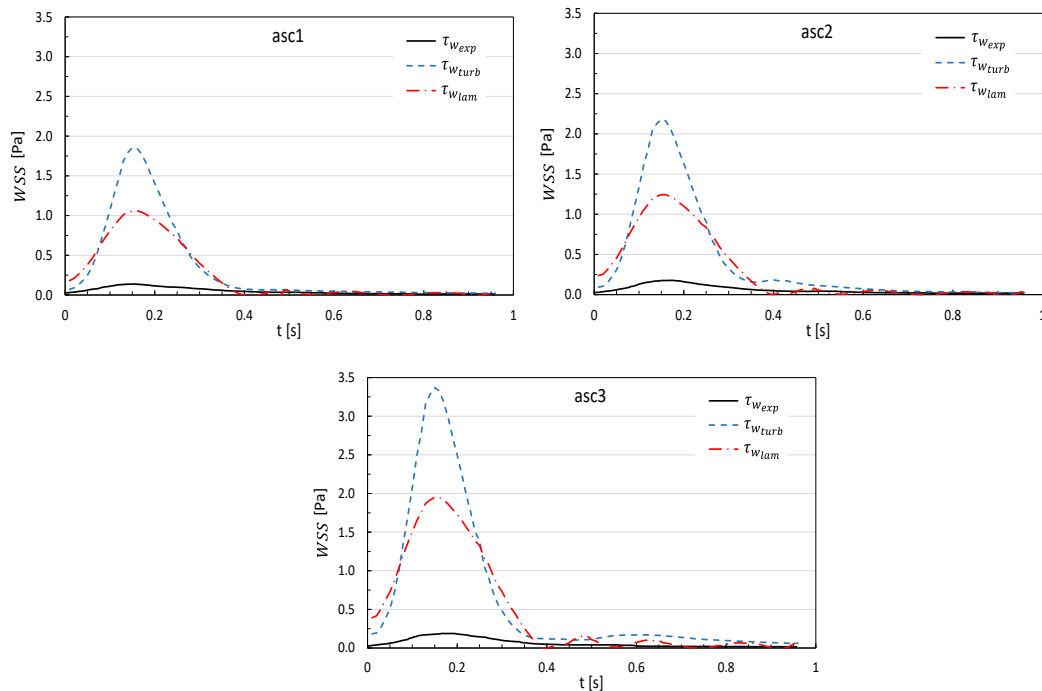


Figure 6.15 – WSS Comparison.

Analyzing Figure 6.15, one can observe the same behavior mentioned previously, regarding the increase of the shear stress as the flow rate increases, however, shear rate with one order of magnitude higher than the 4D-Flow software data was obtained with both approximations. The consideration of the turbulent

regimes when the Reynolds number is above a threshold, results as expected as in higher shear.

The smaller order of magnitude of WSS measured here by 4D-Flow software agrees with Callaghan & Grieve (2018) measurements, who employed 4D-flow MRI to examine thoracic aorta of healthy patients, reporting values in the order of 0.5–1.0 Pa. Salmasi et al. (2021) point out that the restricted temporal and spatial resolution and the uncertainties involved in velocity encoding, may lead to a considerable underestimation of WSS values. In contrast, CFD studies consistently report WSS in a range of 2.0–30.0 Pa (Biasseti et al., 2011; Celis Torres et al., 2017; Ibanez et al., 2021), which is more realistic if one considers that curvature and recirculation increase the shear stress.

6.7 Streamlines

Numerical streamlines coloured by velocity module are presented in Figure 6.16, at four-time instants, while the experimental data are shown in Figure 6.17. For each case, the time instant corresponding to the image is illustrated as a red dot in the graph of the inlet mass flow rate profile, in the bottom part of the figure, to relate with the time instant during the cycle. The first sub-figure corresponds to the systole peak and the second with the end of the systole, while the last two figures are associated with the diastole period. The same scale was employed for both data, with very similar colour palette, since exactly the same was not possible. The same point of view of the aorta was selected, to aid in the comparison of numerical results with the experimental data. However, the numerical streamlines present more information than the image with the experimental data.

At the systole peak ($\approx 0.16s$), high velocities can be seen both numerically and experimentally, Figs. (a), especially at the descending aorta. Numerically [(a)] although no recirculation can be clearly observed at this time instant, smaller velocities (yellow) can be seen around the inlet jet, near the aorta valve, indicating a possible recirculation in that region. Experimentally [Figure 6.17 (a)], a high velocity jet can be seen at the aorta valve, with smaller velocities around it, clearly indicating the presence of a recirculating flow.

After the systolic peak (b), a significant drop at the velocity level is observed in both data set. In both cases, it can be seen a recirculation near the inlet jet followed by a strong recirculation right after the aorta's arch, with higher velocities at the descending aorta. Qualitatively, the flow is similar, although, as mentioned, there are more information when examining the numerical image at the descending.

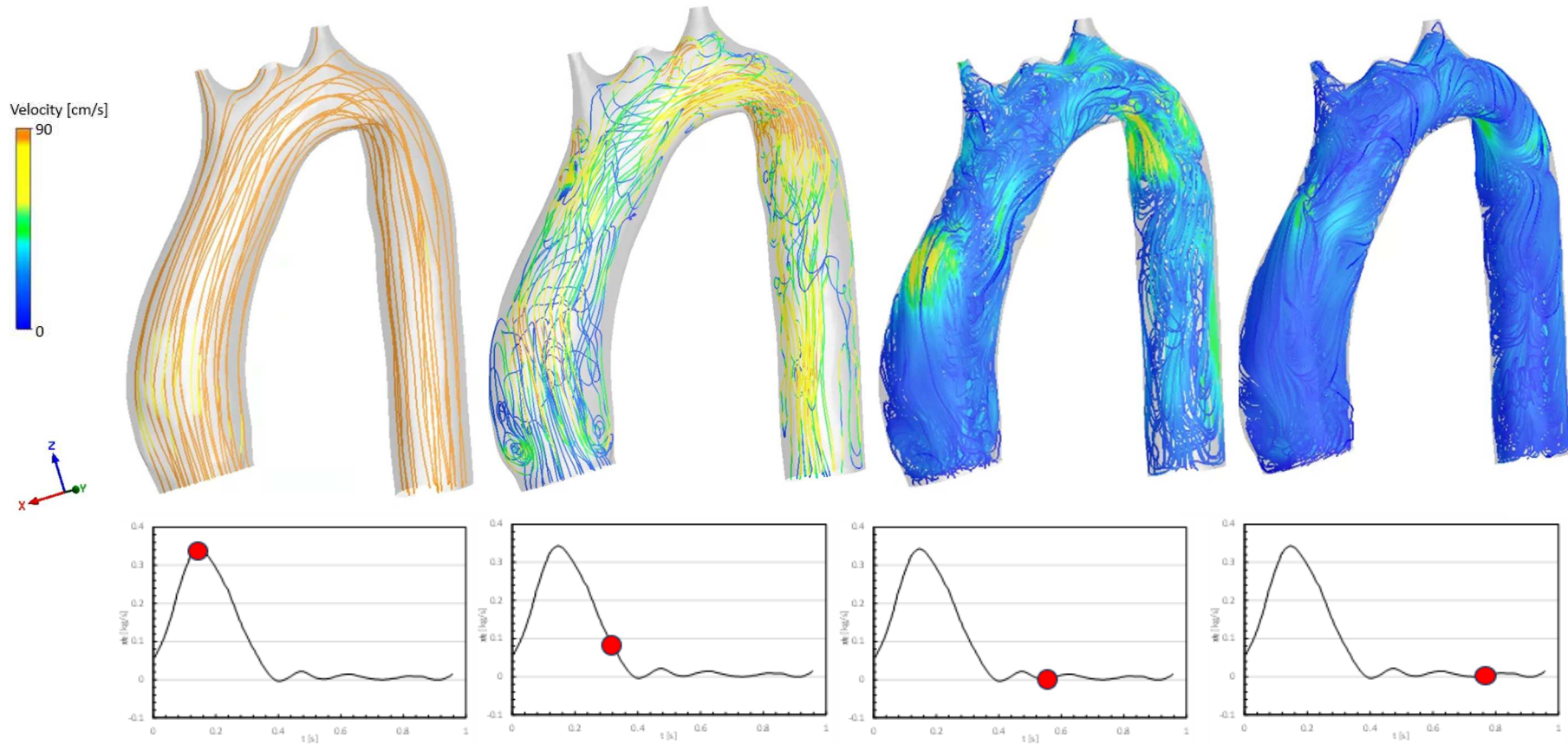


Figure 6.16 – Numerical simulation streamlines over the cardiac cycle colored by velocity vector magnitude.

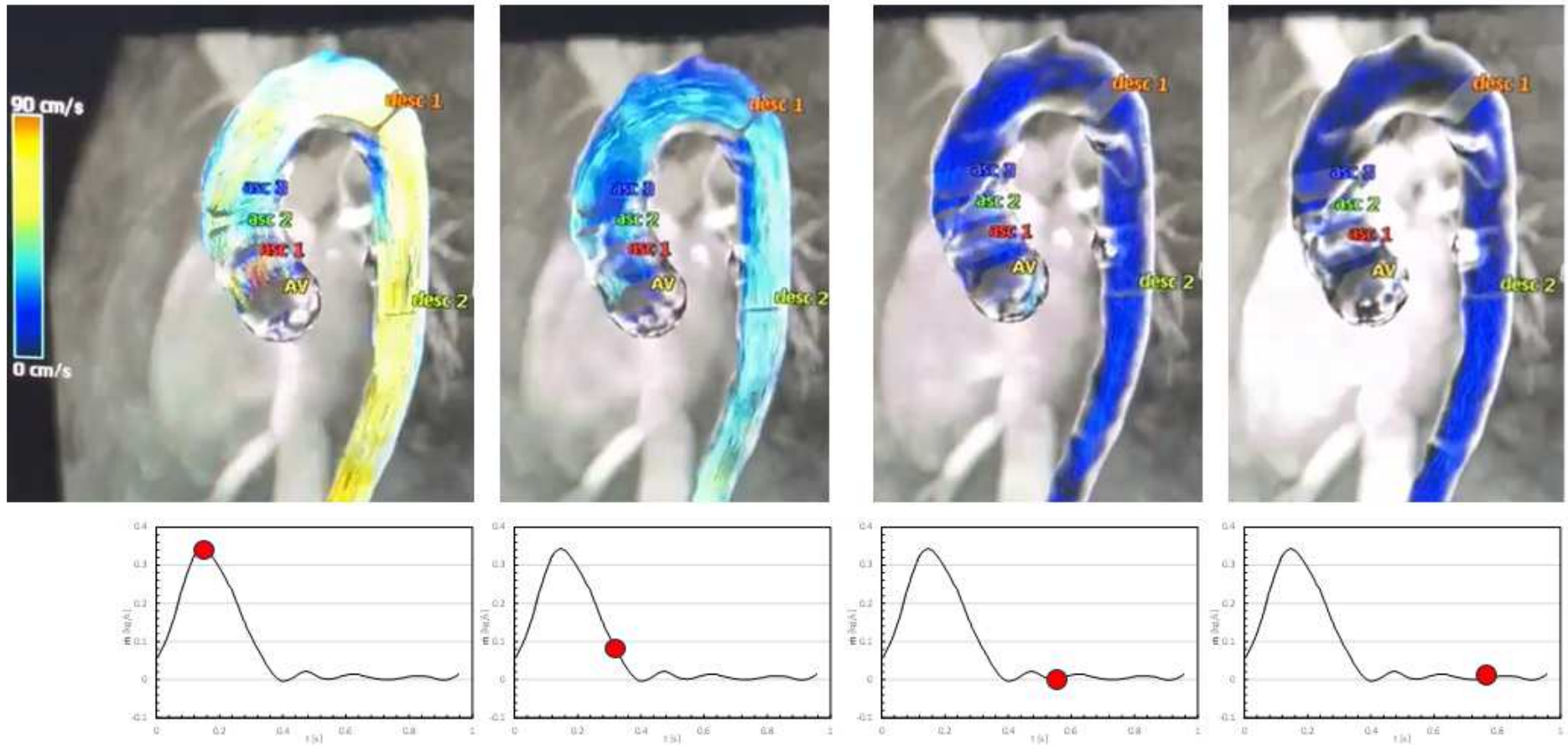


Figure 6.17 – 4D-Flow experimental streamlines over the cardiac cycle colored by velocity vector magnitude.

aorta. Qualitatively, the flow is similar, although, as mentioned, there are more information when examining the numeral image.

During the diastole period, low velocity and great recirculation are captured in the numerical results [Figure 6.16(c) and Figure 6.16 (d)], with very similar flow field. Experimental results in Figure 6.17 (c) and Figure 6.17 (d), also show very similar flow field at the two-time instants of the diastole period, the recirculation near the aortic valve and after the aorta's arch, although with significant less details.

The streamlines results corroborate the analysis of the pressure distribution, i.e., an increase in the pressure loss due to the large recirculation in the beginning of the descending part of the aorta. This head loss was not capture by the 4D-Flow, probably due to the indirect way to estimate the pressure.

6.8 Three-element Windkessel model x Percentage Outflow as Boundary Condition

To verify the influence of the BC on the results, a comparative analysis between the three-element Windkessel model and the percentage outflow model was performed. The flow percentage BC considers the percentage described in Table 6.1 for each outlet.

Table 6.7 presents the strain indices for the area of interest (ascending aorta) of the healthy patient analysed using these two different BC. The error was computed in function of 3E WK, with the subscript 'WK' representing the Windkessel results and 'per' the percentage outflow results.

Analyzing Table 6.7, it becomes apparent the low error values associated with the analysed strain indices. This result is very positive, as it shows the small variation in the wall when the simpler BC model is employed.

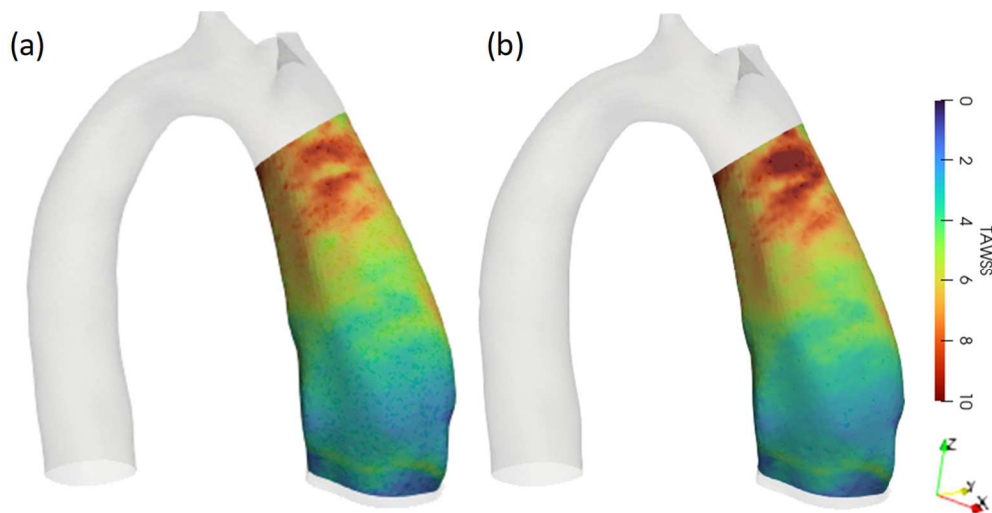
Figure 6.18 and Figure 6.19 show the *TAWSS* and *OSI* fields for the percentage outflow and 3E WK BC, respectively. Examining the figures, a great similarity is seen for the different BC of each image, reinforcing the result shown in Table 6.7.

Figure 6.20 presents the pressure field for each plane, as done in the analysis of Figure 6.10 and Figure 6.11. It was decided to analyse the pressure field using the planes since this variable was extensively explored in subchapter 6.5.

In this way, the experimental pressure drop data, ΔP_{exp} , was compared with the results obtained for the 3E WK BC, ΔP_{WK} (that was previously called by ΔP_{num}), and percentage outflow BC, ΔP_{per} .

Table 6.7 – 3E WK x Outflow variables comparison.

Variable	Three-element Windkessel [mean ± SD]	Percentage outflow [mean ± SD]	$ \epsilon = \left 1 - \frac{\phi_{per}}{\phi_{WK}} \right \times 100$ [%]
TAP_{max} [Pa]	0.57±0.21	-0.56±0.35	1.61
$TAWSS_{max}$ [Pa]	19.88±0.08	19.89±0.06	0.06
$TAWSS_{ave}$ [Pa]	5.14±0.20	5.05±0.09	1.65
$TAWSS_{min}$ [Pa]	1.30±0.20	1.27±0.09	2.15
OSI_{max}	4.97e-1±0.20	4.99e-1±0.09	0.28
OSI_{ave}	2.48e-1±0.20	2.41e-1±0.09	2.72
OSI_{min}	4.02e-3±0.20	4.14e-3±0.09	2.82

Figure 6.18 – $TAWSS$ field using as BC (a) Percentage Outflow. (b) WK.

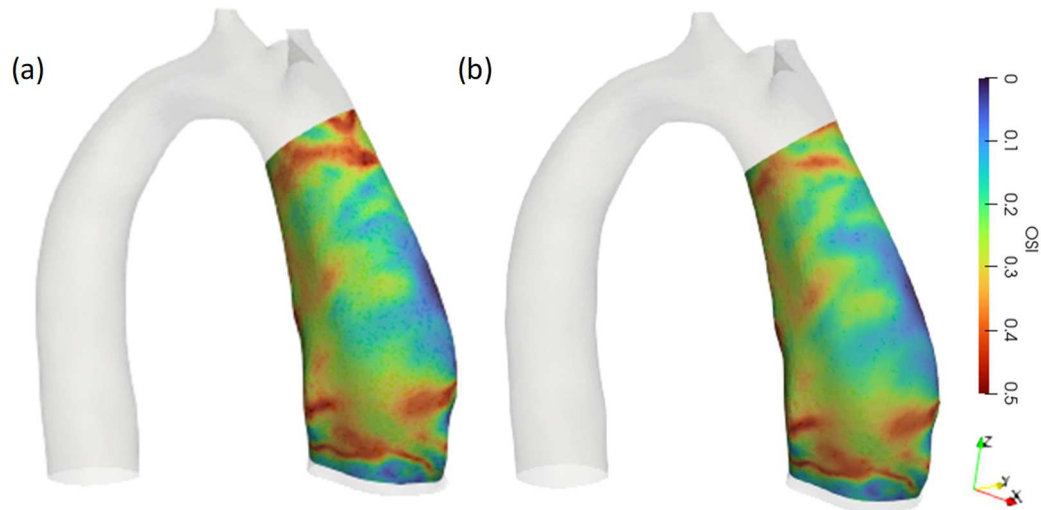


Figure 6.19 – *OSI* field using as BC: (a) Percentage Outflow. (b) WK.

Evaluating Figure 6.20, a good correspondence is perceived between the ΔP_{WK} and ΔP_{per} showing, therefore, the possibility of imposing the simplified percentage mass flow model boundary condition without loss of analysis.

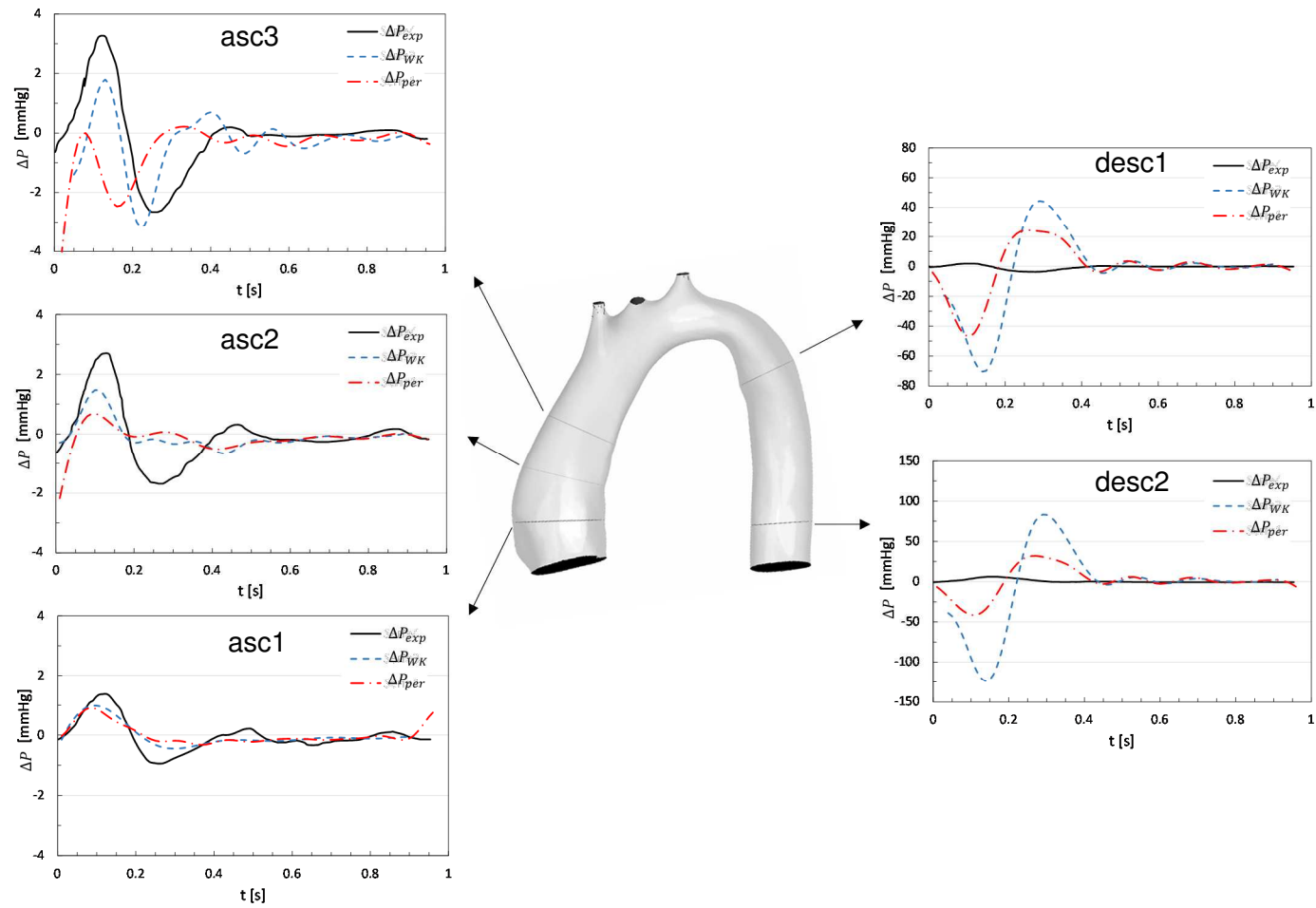


Figure 6.20 – Pressure comparison considering the two different BC.

7 PATIENTS WITH ASCENDING AORTIC ANEURYSM

In this chapter, the flow field along the aorta during the cardiac cycle of 30 patients with ascending aortic aneurysm with non-surgical indication are examined. Based on the volume difference of the ascending aorta within a specific time interval, two groups were defined: one with aneurysm growth and another without growth. The flow field corresponding to both groups was compared, with the objective of finding patterns that may indicate the aneurysm growth. The focus is to assess whether from the first exam there would be signs that the aneurysm would grow. Therefore, the information about the second-year exam was used only to classify the patients into two groups: with and without aneurysm growth.

This investigation expands the conclusions of the study of Azevedo et al. (2024) that evaluated the same geometries by modeling the flow on steady state, considering the flow rate critical condition, i.e., the systolic peak phase.

To compare the solution between the two groups of patients, time average and area average, as defined in Chapter 5, were employed. Further combination of the two types of average were also considered.

To visualize the results, contours of selected variables were used, as well as time variation during the cardiac cycle. The main variables examined here were pressure and WSS.

7.1 Aortic Geometry and Methodology in Patient Classification

As described by Azevedo et al. (2024), the study included a convenience sample of patients with AAoA who were examined at an outpatient clinic specialized in aortic diseases (Instituto Nacional de Cardiologia, Rio de Janeiro, RJ, Brazil) between April 2019 and August 2020.

Exclusions comprised patients with a history of cardiac surgery, percutaneous intervention on the aortic valve or ascending aorta, aortic coarctation, ascending aortic dissection, collagen diseases, or Marfan syndrome. Additionally, individuals lacking CTA images or those subjected to inadequate radiological techniques (e.g., artifacts or absence of contrast agent) were excluded. All CTA examinations adhered to the guidelines provided by the

attending medical team. The flowchart in Figure 7.1 shows the procedure used that 30 patients were selected among 389 patients with AAoA.

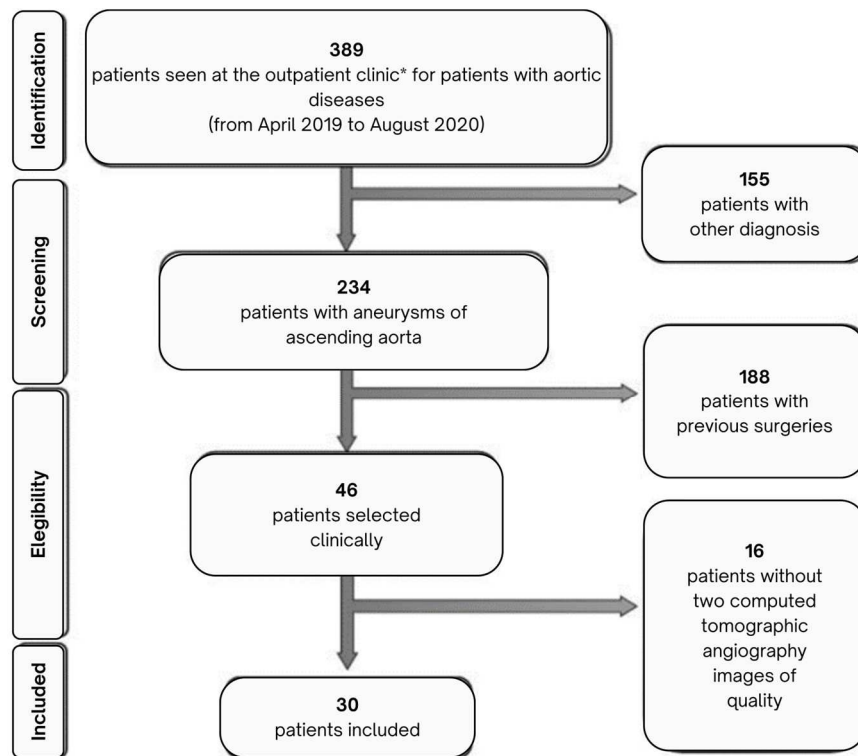


Figure 7.1 - Selection of patients with ascending aortic aneurysm (Azevedo et al., 2024).

From the group of patients selected, it was noticed that while some had increased dilatation, others had approximately the same dimensions. Thus, it was necessary to establish a standard to evaluate and separate the patients into two different groups: with aneurysm growth and without aneurysm growth.

To achieve this purpose, the parameter selected to aid this classification was the ascending aortic volume. According to Raghavan et al. (2000) and Xiao et al. (2023), the volume is more sensitive and can capture any change in the entire 3D geometry. As pointed out by Renapurkar et al. (2012), the aneurysm may potentially undergo remodeling without experiencing alterations in their maximum diameter. Aneurysm growth was considered when the difference in volume of the ascending aorta (region of interest) was superior than 5% between exams (Azevedo et al., 2024).

The region of interest of the ascending aorta is shown colored in red in Figure 7.2. Detailed methodology description used to delimit this region is presented in Almeida et al. (2022). To define this region, allowing a comparison of the volume, the entry flow plane was positioned in the centroid of the aortic annulus, with the

x-axis crosses the centroid of the left coronary artery, pointing towards the anterior aortic wall and the y-axis pointing to the right coronary artery. Then, the 3D aortic models for each patient corresponding to two different years were super-imposed, aiming to overlap the beginning of the brachiocephalic trunk and the right coronary artery. Once the arteries were overlapping, the aortic valve and the descending part were sliced, ensuring that the inflow and outflow sections had the same spatial reference.



Figure 7.2 – Region of interest colored in red (Own Authorship).

Appendix A5 presents the collected information of each patient. The subscript ‘year1’ and ‘year2’ refer to the first and second years that the exams were taken.

Time between scans, Δt_{scan} , the maximum aneurysm diameter measured by the doctor on the day of the exam, \mathcal{D} , the volume measured in the ascending aorta from the 3D geometry, and \forall are shown in Table A5.1. As it is possible to visualize, some patients presented a reduction in volume growth from the first year to the second one, which can be explained by measurement uncertainty during the scans.

Note also, in Table A5.1, that during the scans, the physician measured the same diameter for Patient Y5. Nonetheless, a volume increase can be observed in Figure 7.3. Figure 7.3 (a) and (b) depict distinct perspective of patient Y5’s aorta overlapped in two different years. The first year is colored in pink and the second one in gray. As it can be seen by the indicated circles in the figure, the gray image (2nd year) is larger indicating an increase in the size of the aneurysm in relation to the size of the first year (pink). Therefore, comparison based only in the diameter size to assess if the aneurysm has growth or not, can generate conclusions not well founded and create the false impression that there was no dilatation of the

vessel. This observation demonstrates the significance of selecting volume instead of diameter, as a superior indicator of aneurysm growth.

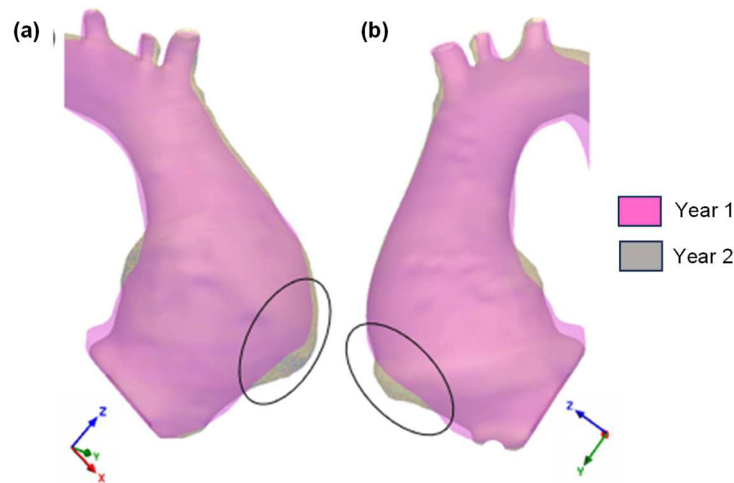


Figure 7.3– Same aorta overlapped in two different years with circles indicating the difference in the size of the of patient Y5: (a) View 1. (b) View 2 (Own Authorship).

Additionally, geometrical biomarkers are important studies subjects, since its association with other hemodynamics variables and flow patterns can provide better prognosis in association with mechanical variables, as discussed by Kauhanen et al. (2020) and Salmasi et al. (2021).

Kauhanen et al. (2020) studied the computed tomography angiograms of a large group of subjects ($n=1000$) and identified that aortas more angulated (or less aligned to the axis of the heart) were associated with dilatation of the aortic root.

Salmasi et al. (2021) defined the left ventricular outflow tract (LVOT) aortic angle. The LVOT is linked with a ‘heart-aortic angle’, θ , and is measured from the center line, as shown in Figure 7.4. The authors suggest that higher LVOT-angle is associated with larger aneurysm diameter, accelerated velocity on outer curve and increased WSS, being a predictor of disease severity in AAoA.

To characterize the aorta’s shape, Almeida et al. (2022) proposed the angle θ_I [Figure 7.5 (a)] to be measured between the line connecting the brachiocephalic trunk centroid with the left main coronary artery centroid and the x-axis centered in the inflow plane and θ_{II} [Figure 7.5 (b)], formed by the angle between the line that connects the brachiocephalic trunk centroid with a point on the extreme position on the x-axis of the inflow plane, and the line connecting this point with the extreme position on the y-axis of the inflow plane. Here, these geometrical parameters were measured for all patients, and it was examined their relationship with aneurysm growth.

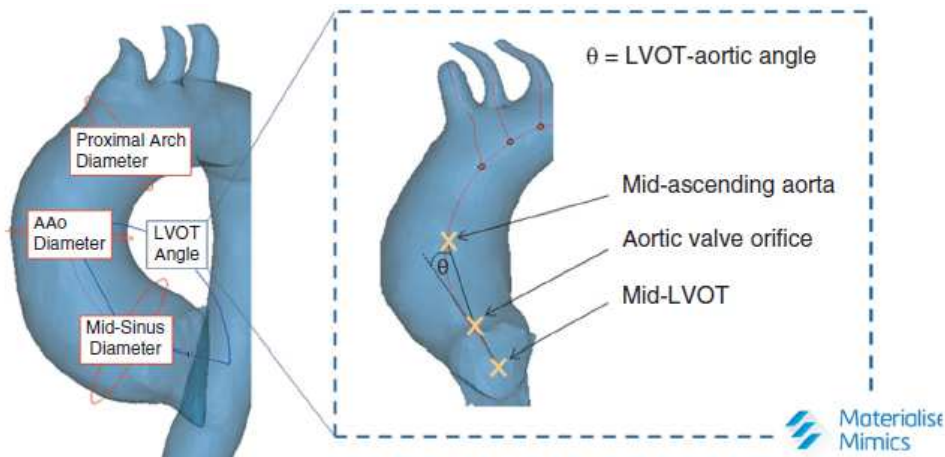


Figure 7.4 - θ angle (Salmasi et al., 2021).

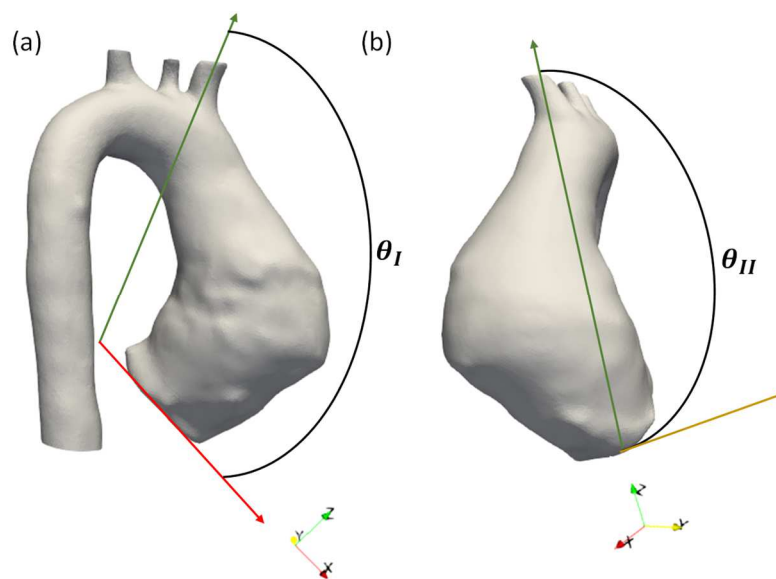


Figure 7.5 – Angles proposed by Almeida et al. (2022): (a) θ_I . (b) θ_{II} .

Believing in the importance of aorta' angulation, Table A5.2 in Appendix A5 presents the angle θ proposed by Salmasi et al. (2021) and the angles θ_I and θ_{II} proposed by Almeida et al. (2022). Table A5.2 also shows the effective inlet diameter, D . The patients are separated into two groups: with aneurysm growth and without aneurysm growth. The label 'N' refers to patients without aneurysm growth and 'Y', patients with growth. The relation of these geometric parameters with the volume ratio of the 2nd year exam to 1st year exam are also shown graphically in Figure 7.6. A trend line was added to enhance the analysis of the data pattern.

The relation of the inlet effective diameter, D , and the ascending aorta volume variation can be seen in Figure 7.6 (a). The trend behavior for all patients indicates that the volume ratio increases (indicating aneurysm growth) as the effective inlet diameter decreases. This behavior is expected, since smaller inlet diameter, leads

to higher velocities, consequently higher impinging pressure, which can impact on the growth.

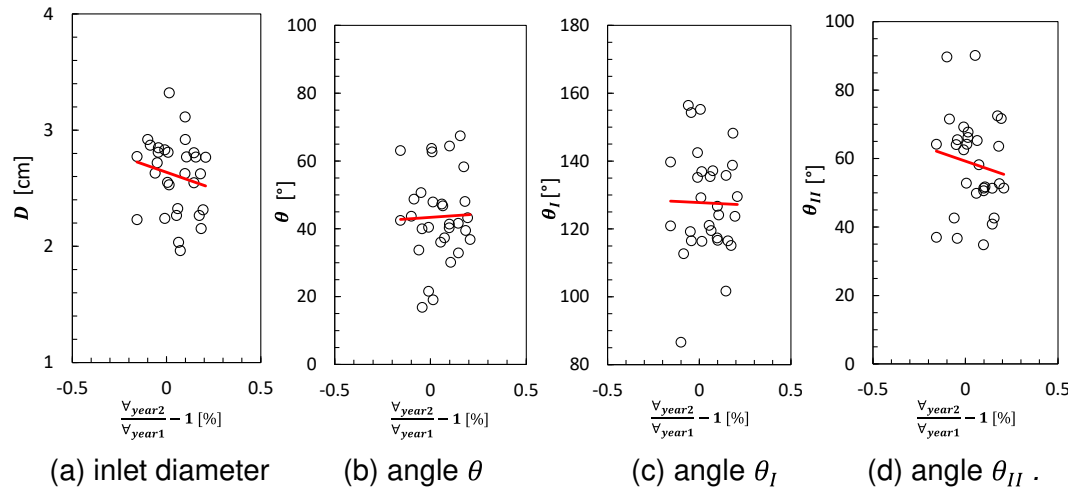


Figure 7.6 – Aorta's geometric parameters as a function of volume ratio of second to first exam: (a) inlet diameter, (b) angle θ (c) angle θ_I (d) angle θ_{II} .

Figure 7.6 (b) shows a significant dispersion of θ data in relation to the volume ratio, with a trend line practically constant, not indicating a clear relation with the volume variation. The same is true with respect to the angle angulation θ_I , Figure 7.6 (c), with no clear difference between the groups. However, as shown in Figure 7.6 (d), there is a clear volume ratio increase from year 1 to year 2 and a decrease of θ_{II} .

Finally, to compile the variables featured in Table A4.1 and Table A4.2, Table 7.1 gives a summary displaying both the average geometric parameters and standard deviation (SD), allowing an analysis of the behavior of the two groups of patients.

Table 7.1 indicates smaller average effective inlet diameter for patients with aneurysm growth, which is expected due to the higher inlet velocity. Note also higher average values of θ for patients with aneurysm growth. A hypothesis to be raised is that stronger curvature (due to higher θ) implies in higher angulation between the aortic orifice and the middle of the ascending aorta, what will direct the flow to the anterior aorta's wall, instead of the along the artery (Figure 7.4). This interpretation agrees with Salmasi et al. (2021) analysis, who concluded that more angulated orientation is associated with larger aortic diameters.

Contrasting the observed θ relation with volume variation, Table 7.1 shows that lower θ_I and θ_{II} contribute to the growth of the aneurysm. As shown in Figure 7.5, θ_I is an angle that explores the length extension of the aorta, whereas θ_{II} its inclination considering y -axis in relation of z -axis. Therefore, patients with

aneurysm growth, present lower mean values, indicating more tortuous aortas, leading to more complex flow structures, with more intense recirculation, resulting in higher stress at the aorta's wall.

Table 7.1 – Mean values and the standard deviation of analyzed variables.

Adapted from Azevedo et al. (2024).

Variables	30 patients [mean ± SD]	Patients Without Growth [mean ± SD]	Patients With Growth [mean ± SD]
$\forall_{year1} [cm^3]$	150.00± 38.98	152.87± 45.35	147.49± 33.78
$\forall_{year2} [cm^3]$	156.48± 41.94	145.92± 45.68	165.73± 37.37
$\frac{\forall_{year2}}{\forall_{year1}} - 1 [\%]$	4.53±10.42	-4.83± 5.86	12.71± 5.20
$D_{year1} [cm]$	5.04±0.35	4.97±0.39	5.11±0.31
$D_{year2} [cm]$	5.23±0.52	4.97±0.44	5.46±0.47
$\frac{D_{year2}}{D_{year1}} - 1 [\%]$	3.77±7.57	-0.02±4.30	7.07±8.35
$D [cm]$	2.61±0.32	2.72±0.28	2.52±0.34
$\theta [^\circ]$	43.56± 13.01	42.49± 15.57	44.49±10.72
$\theta_I [^\circ]$	127.64± 15.73	130.13± 19.61	125.46±11.59
$\theta_{II} [^\circ]$	58.40± 14.04	60.98± 14.40	56.14±13.78

Analyzing the Table 7.1 and Figure 7.6, we note that patients with aneurysm growth presented an increase of the aorta diameter and a more significative increase of the ascending aorta volume. This group has smaller inlet diameter; larger θ angle and smaller angles θ_I and θ_{II} .

7.2 Boundary Condition

As already shown in Figure 4.4, to define the boundary condition for the aorta, one must define one inlet condition and four outflow conditions.

In the absence of information regarding the boundary conditions of each patient, and following the procedures of Xiao et al. (2023), it was presupposed that all patients had similar stroke volume and cardiac output to focus in the impact of

the geometry in the aneurysm growth. Thus, to examine the complete cardiac cycle, a generic inlet mass flow rate curve as shown in Figure 7.7 (Lo et al., 2019) was employed to all patients and has its profile code shown in Appendix A4. The maximum volumetric flow rate, \dot{V} , was adjusted to 25 l/min aligning with Borazjani et al. (2008). This decision was made to allow the comparison between the transient and the permanent analysis evaluated in the research of Azevedo et al. (2024), who studied the same 30 patients.

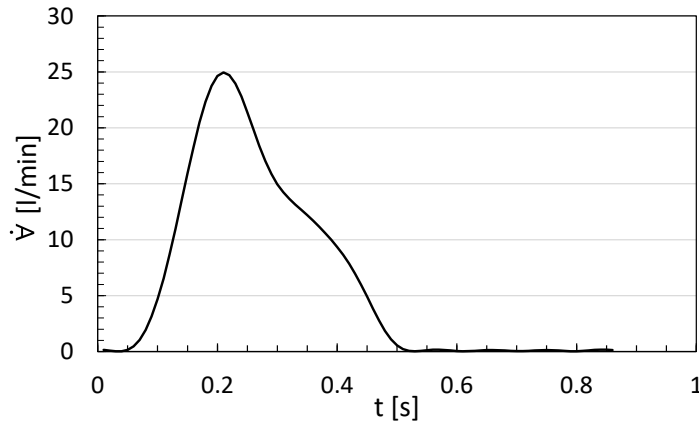


Figure 7.7 – Complete cardiac cycle for patient with aneurysm.

With respect to the four outflow conditions, the simplified boundary condition of neglecting diffusion, and imposing a percentage of inlet flow rate was defined at each outlet. For all cases, the same outlet flow rate distribution was imposed based on average values in the human body (Alastruey et al., 2016), as shown in Figure 7.8:

- Descending aorta: 69.1%
- Brachiocephalic artery: 19.3%
- Left carotid artery: 5.2%
- Left subclavian artery: 6.4%

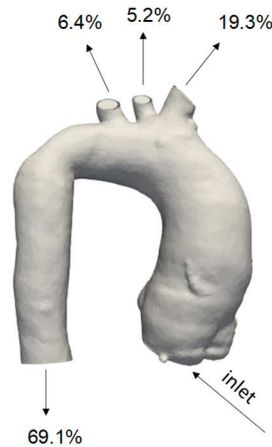


Figure 7.8 – Percentage of outflow distribution.

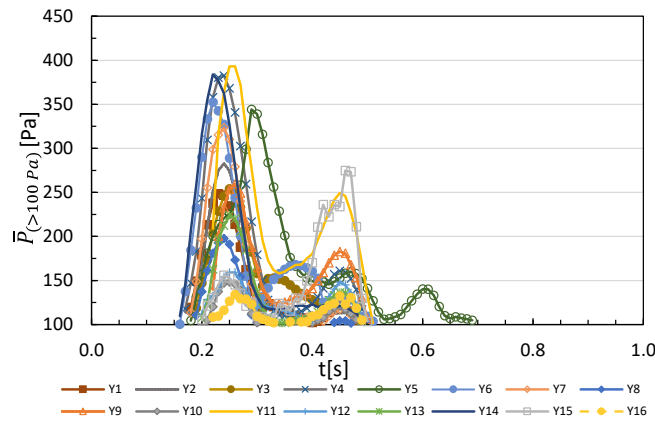
This simplified boundary condition was imposed, once the number of cases to be analyzed was high and the approach was significantly faster. As presented in the previous chapter, very similar predictions were obtained when the results obtained with this approximation were compared with the predictions obtained by imposing the Windkessel model at each outlet.

7.3 Pressure

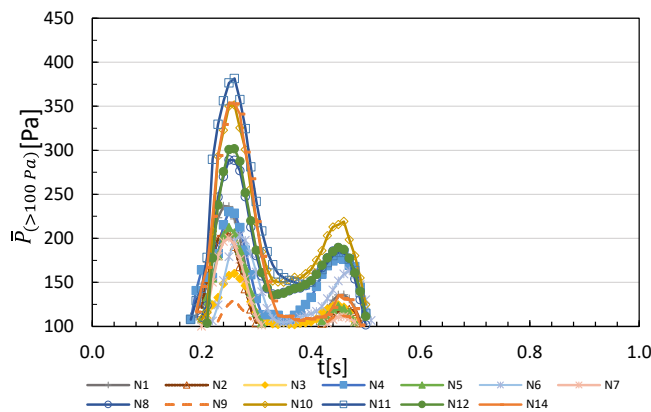
Following the approach of Almeida et al. (2022) and Azevedo et al. (2024) to correlate the pressure data between the two groups of patients (with and without aneurysm growth), a region of interest was defined, where the pressure was above a threshold of 100 Pa. This is a conservative threshold, selected based on the results of healthy patients as shown on the previous chapter and by Ibanez et al. (2021), who found a pressure difference between the aortic valve and the ascending aortic wall of approximately 1 mmHg (133 Pa).

Figure 7.9 (a) and Figure 7.9 (b) present the area average pressure in the region of interest with pressure above 100 Pa ($\bar{P}_{(>100 Pa)}$) as a function of time, for patients with and without aneurysm growth. For both groups, a similar trend is found, with a first higher peak, followed by a smaller peak right after. Further the pressure level is also similar. The time interval during the cycle with pressure above the threshold of 100 Pa, was defined as $\Delta t_{pressure}$. Analyzing the figures, it is noticeable that the high-pressure field occurs for a shorter time period, $\Delta t_{pressure}$, for the no growth group, indicating the aorta is subjected to high pressure for a smaller time.

Table 7.2 shows a quantitative comparison between the two groups, presenting the mean average within the patients' groups, regarding the time average of the area average pressure in the region with pressure above 100 Pa, $\langle \bar{P} \rangle_{(>100 Pa)}$. The difference between predictions of the two assemblies is very small, indicated by a difference ϵ of 1.31%. However, considering the meantime interval of the patient's group, that the aorta is under higher pressure, $\Delta t_{pressure}$, a greater difference is noticed when the two groups are compared (17.80%). This larger time interval with high pressure was already discussed in the analysis of Figure 7.9 leading to aneurysm increase.



(a) patients with growth



(b) patients without growth

Figure 7.9 –Area average pressure above 100 Pa, $\bar{P}_{(>100 Pa)}$, time evolution along the cardiac cycle: (a) patients with growth; (b) patients without growth.

Table 7.2 – Quantitative analysis of patients: mean $\langle \bar{P} \rangle_{(>100 Pa)}$ and $\Delta t_{pressure}$.

Variable	30 patients [mean ± SD]	Patients		ϵ [%]
		Without Growth [mean ± SD]	With Growth [mean ± SD]	
$\langle \bar{P} \rangle_{(>100 Pa)}$ [Pa]	157.51±27.91	158.65±27.50	156.58±29.13	1.31
$\Delta t_{pressure}$ [s]	0.28±0.08	0.25±0.07	0.30±0.08	17.80

In Figure 7.10, all patients belonging to the same group were gathered (“N” for no growth and “Y” for growth) and the dispersion of $\bar{P}_{(>100 Pa)}$ between the groups data was assessed. The limits of the bars indicate the standard deviation and the horizontal line, the median. Note that the dispersions data are equivalent for both groups, with a higher standard deviation for the growth group. The median

value of $\langle \bar{P} \rangle_{(>100 Pa)}$ for the no growth group is slightly lower when compared to the patients with aneurysm growth.

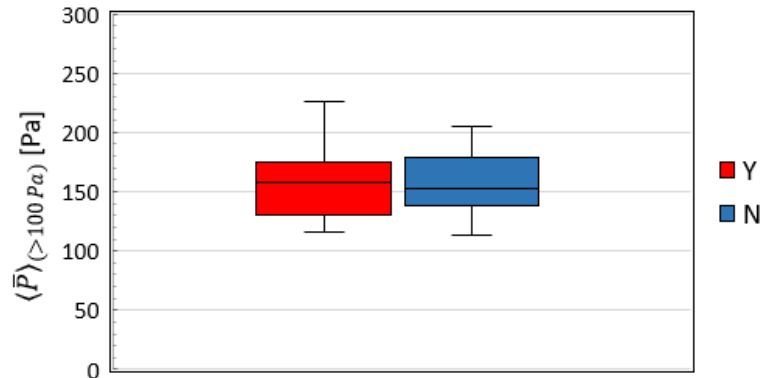


Figure 7.10 - Dispersal of high pressure $\langle \bar{P} \rangle_{(>100 Pa)}$ values.

Unlike what was observed by Azevedo et al. (2024), when analyzing the same group of patients, at the systolic peak, the small difference between the data of both groups does not allow inferring a relationship between this variable and the aneurysm growth.

An analysis of the dispersion, standard deviation and median of the period with high pressure, $\Delta t_{pressure}$, can be examined in Figure 7.11. Once again, despite longer average time period with high pressure, similar medians were obtained, with a significant larger dispersion for the non-growth group.

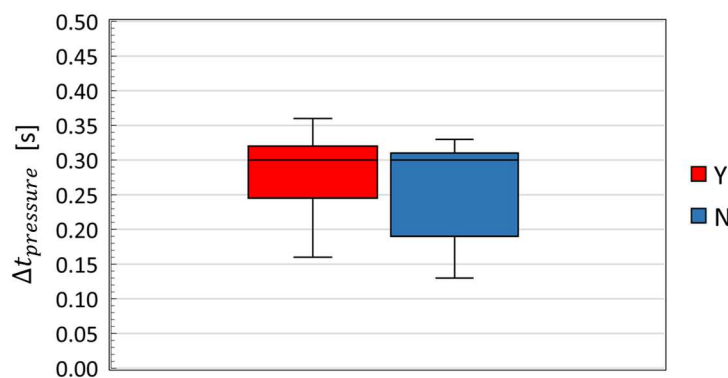


Figure 7.11 - Dispersal of time period with high pressure. $\Delta t_{pressure}$.

To evaluate the relation of the geometry with the pressure level, Figure 7.12 presents the association of $\langle \bar{P} \rangle_{(>100 Pa)}$ with the inlet diameter D and angles θ , θ_I and θ_{II} . The larger pressure associated with the smaller diameter is clearly seen, due to the resulting higher velocity, as mentioned, leading to an increase of the aorta's volume, as shown in Figure 7.6. The correspondence of the geometric

angles θ with the average high pressure also follows the same relation as observed with the volume increase. One unexpected result was obtained with the relation of angle θ_I and θ_{II} with the average high pressure $\langle \bar{P} \rangle_{(>100 Pa)}$. Completely different trend of the pressure with these geometric parameters and their relationship with the volume growth. Perhaps indicating, contrary to the first expectation, that these variables might not be directly related to the aneurysm growth.

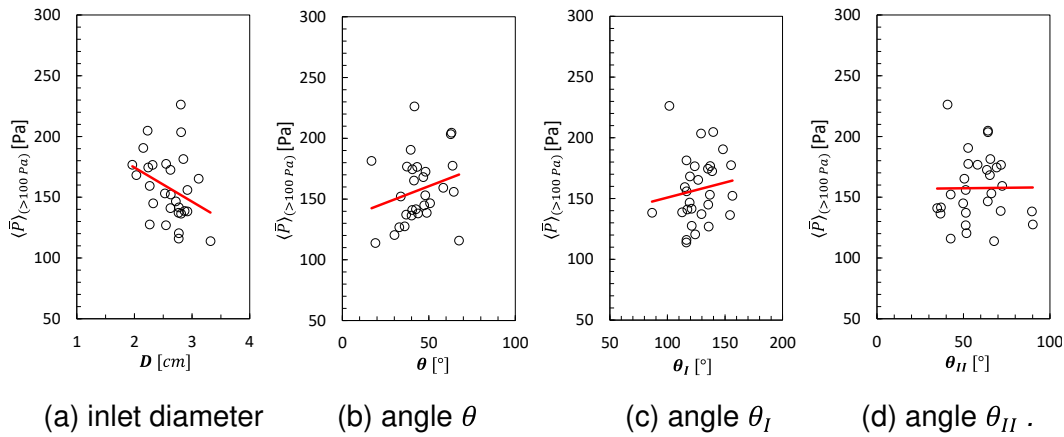


Figure 7.12 – Time and area average high pressure $\langle \bar{P} \rangle_{(>100 Pa)}$ dependence on aorta's geometric parameters: (a) inlet diameter D , (b) angle θ (c) angle θ_I (d) angle θ_{II} .

7.3.1 TAP

The time average pressure over the cycle, TAP , was evaluated for all patients and the isolines of TAP over the aorta surface are shown in Figure 7.13. Most patients of the growth group presented a well-defined and large area of high pressure, while for the patients without growth, lower TAP values are seen, with a few exceptions that also presented a large area of high pressure.

To attempt to find a quantitative differentiation between the two groups, Table 7.3 shows for the region of interest indicated in Figure 7.2: the minimum (TAP_{min}), area average (TAP_{ave}) and maximum (TAP_{max}) TAP values of each group.

The minimum TAP is similar for both groups, however, the maximum TAP value is larger for the group that presented aneurysm growth, as well as the area average TAP value, which presents a significant difference (127.98%). Such a difference indicates the average TAP value as an important variable to be monitored to control the disease.

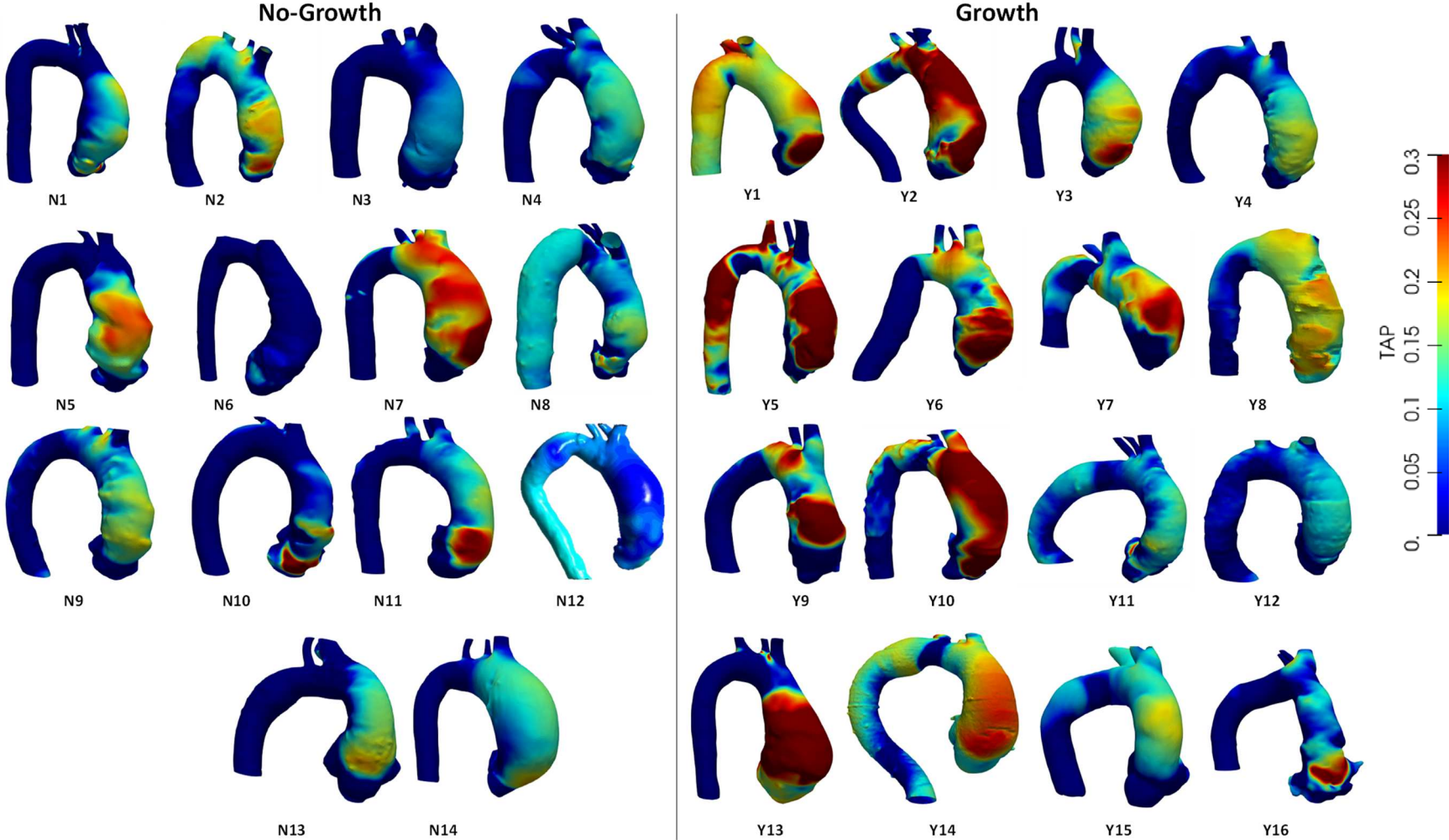
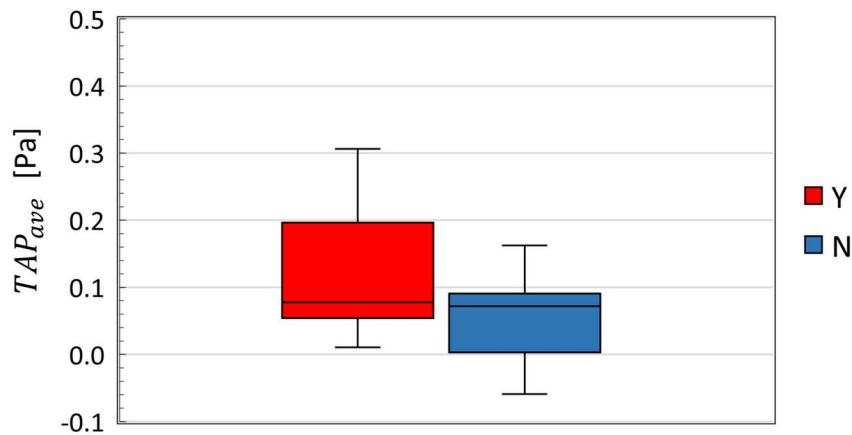


Figure 7.13 - *TAP* for patients without and with aneurysm growth.

Table 7.3 - Quantitative analysis of TAP_{min} , TAP_{ave} and TAP_{max} .

Variable	30 patients [mean \pm SD]	Patients Without Growth [mean \pm SD]	Patients With Growth [mean \pm SD]	$ \epsilon [\%]$
TAP_{min}	-0.261 \pm 0.16	-0.298 \pm 0.23	-0.232 \pm 0.07	22.16
TAP_{ave}	0.085 \pm 0.08	0.050 \pm 0.06	0.113 \pm 0.09	127.98
TAP_{max}	0.329 \pm 0.20	0.238 \pm 0.09	0.404 \pm 0.24	69.85

To further exam the average TAP of each group, TAP_{ave} , it is presented in Figure 7.14, its dispersion values, median and standard deviation corresponding to each group. For this variable, the growth group shows a larger dispersion, as well as standard deviation, resulting in similar median. Although both groups present almost the same median, the results clearly indicate different behaviors for each group, with a higher average value for the growth group, as discussed.

Figure 7.14 - Dispersal of TAP_{ave} values.

Like the analysis conducted for pressure exceeding 100 Pa, the TAP_{ave} was evaluated in relation to geometric parameters and the results are illustrated in. The same trend was obtained as with high average pressure, corroborating the notion that smaller inlet diameter and higher the θ angulation led to greater pressure, which can increase the size of the aneurysm. The relation between the TAP_{ave} and angles θ_I and θ_{II} , is equivalent with what was discussed in relation to $\langle \bar{P} \rangle_{(>100 Pa)}$.

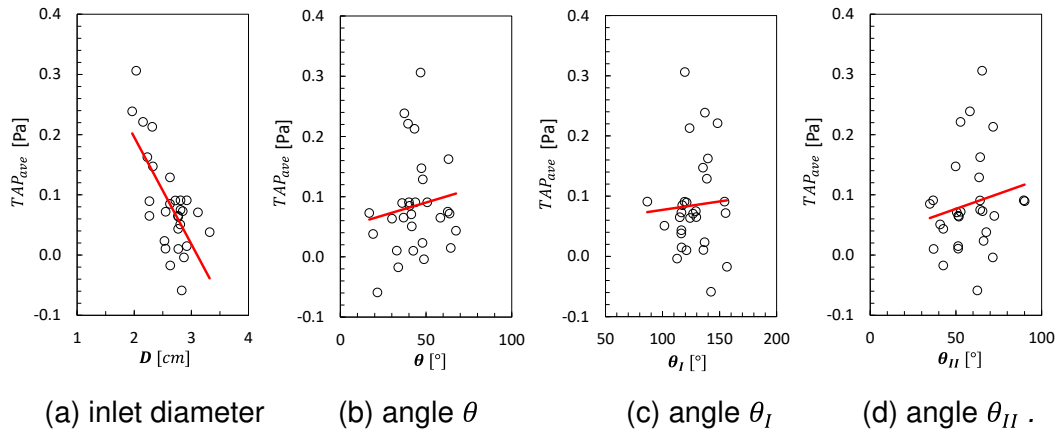


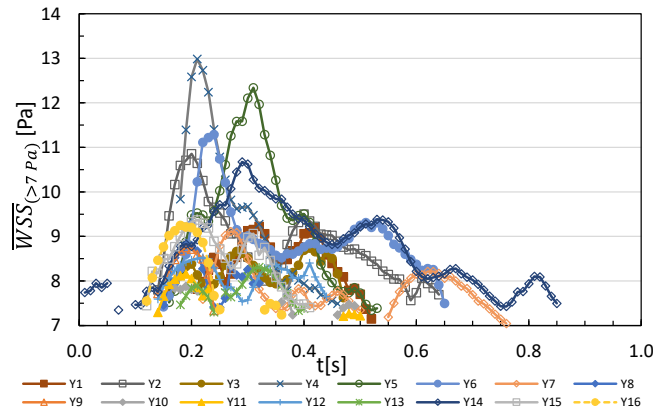
Figure 7.15 – TAP_{ave} dependence on aorta's geometric parameters: (a) inlet diameter, (b) angle θ (c) angle θ_I (d) angle θ_{II} .

7.4 Wall Shear Stress

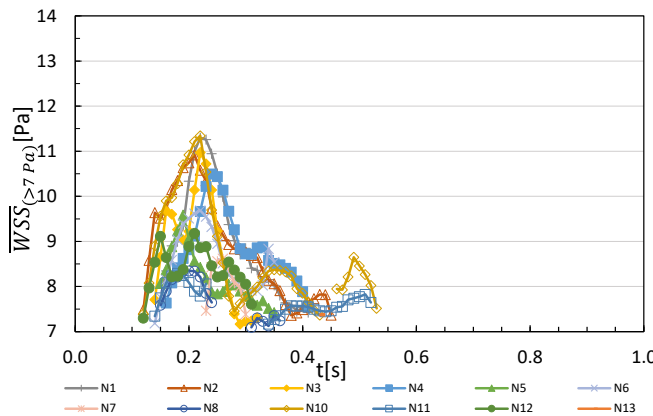
According to Simão et al. (2017), the critical WSS is 5 Pa, whereas Etili et al. (2021) propose 9 Pa as the critical threshold. In this study it was adopted an intermediate value for the threshold of the average WSS, i.e., above 7 Pa, denoted by $\overline{WSS}_{(>7 Pa)}$ (Almeida et al., 2022; Azevedo et al., 2024).

Figure 7.16 (a) displays the time variation of $\overline{WSS}_{(>7 Pa)}$ for patients with aneurysm growth during the cycle, and Figure 7.16 (b) for patients without aneurysm growth. Both groups present a peak in wall shear stress close to the systolic peak and then decline throughout the cycle. With similar behavior as seen for the pressure, patients who did have aneurysm growth also suffered high values of shear stress for a longer period of time.

Table 7.4 displays the quantitative analysis of the average values of WSS above 7 Pa and the time period during the cardiac cycle with high shear stress, Δt_{WSS} . The patients without growth present higher values of $\langle \overline{WSS} \rangle_{(>7 Pa)}$ in comparison of the other group. Nonetheless, the average period that it remains through the high value of 7 Pa, Δt_{WSS} , is smaller and the difference between the groups is high (40.74%).



(a) patients with growth



(b) patients without growth

Figure 7.16 – Average high WSS time evolution during the cardiac cycle, $\overline{WSS}_{(>7 Pa)}$. (a) patients with growth; (b) patients without growth.

Table 7.4 - Quantitative analysis of $\langle \overline{WSS} \rangle_{(>7 Pa)}$ and Δt_{WSS} .

Variable	30 patients [mean ± SD]	Patients Without Growth [mean ± SD]	Patients	ε [%]
			With Growth [mean ± SD]	
$\langle \overline{WSS} \rangle_{(>7 Pa)}$ [Pa]	8.38±0.52	8.43±0.43	8.34±0.58	1.15
Δt_{WSS} [s]	0.29±0.16	0.23±0.09	0.33±0.19	40.74

An analysis of the dispersion of $\langle \overline{WSS} \rangle_{(>7 Pa)}$, with median and standard deviation is provided in Figure 7.17 for both groups, while Figure 7.18 presents the dispersion of the time period with high shear stress, Δt_{WSS} . As shown visually in

Figure 7.17 patients with aneurysm growth have a larger dispersion and standard deviation of $\langle \overline{WSS} \rangle_{(>7 Pa)}$, resulting in a lower median. The dispersion of the time interval with high shear Δt_{WSS} is also higher for the growth group, and despite the also higher standard deviation of this group, the median is significantly higher.

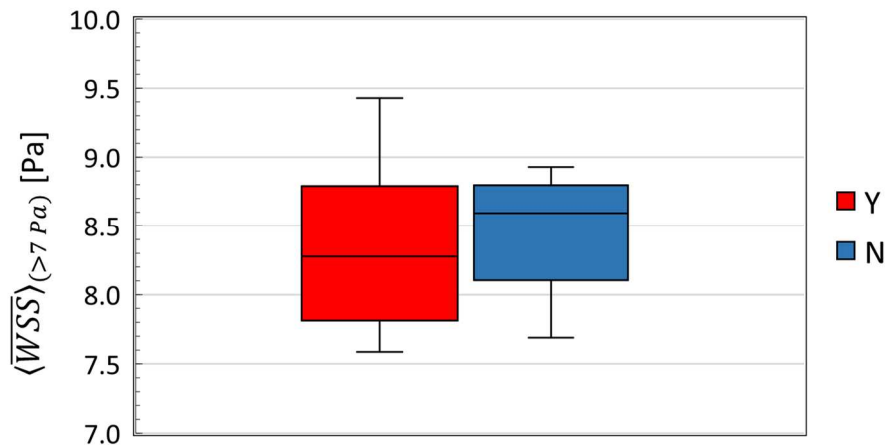


Figure 7.17 - Dispersion of $\langle \overline{WSS} \rangle_{(>7 Pa)}$ values.

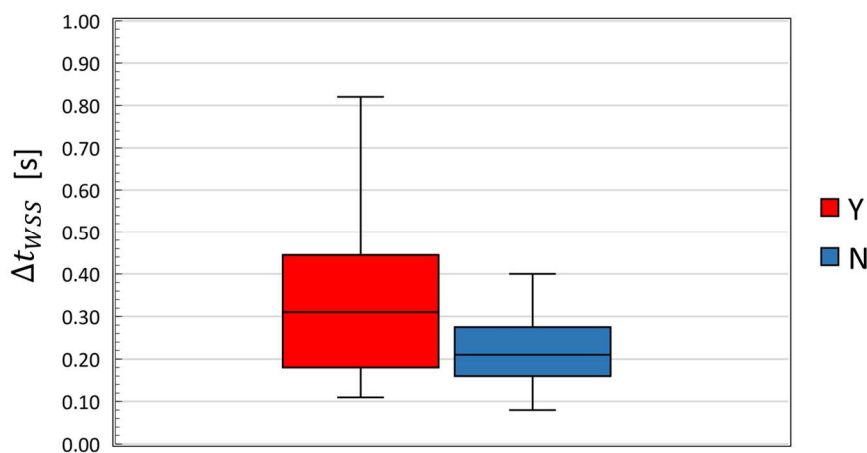


Figure 7.18 - Dispersion of Δt_{WSS} values.

The analysis of the average $\overline{WSS}_{(>7 Pa)}$ during the cycle $\langle \overline{WSS} \rangle_{(>7 Pa)}$ may be misleading, because, it is clearly seen that higher $\overline{WSS}_{(>7 Pa)}$ are present during not only the systolic period, but also during the diastolic period for the aneurysm growth group. Due to the longer time period of high shear, the resulting time average is lower. On the other hand, exposing the patient to higher shear for a longer time clearly contributes to the aneurysm growth.

To finalize the analysis of the WSS, the impact of the geometric parameters on the $\langle \overline{WSS} \rangle_{(>7 Pa)}$ is investigated in Figure 7.19. A prominent drop in WSS values

is noticeable with increase effective inlet diameter, as depicted in Figure 7.18 (a), due to the smaller inlet velocity.

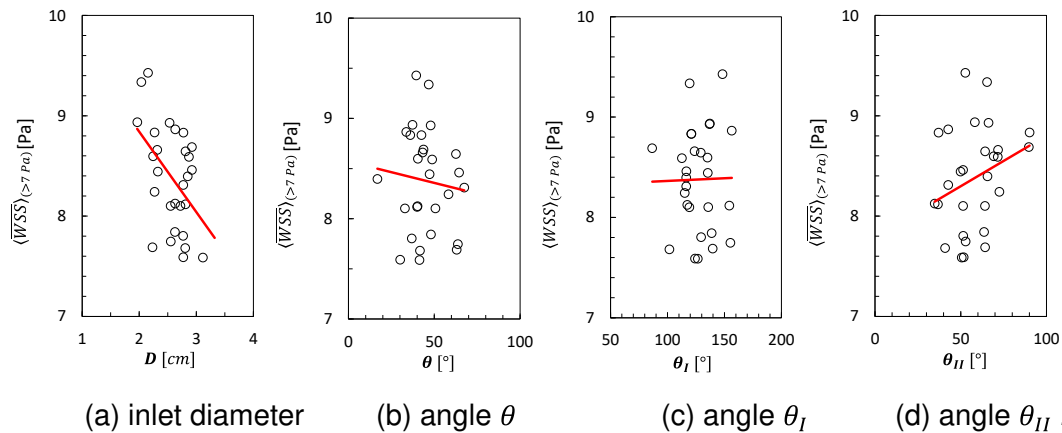


Figure 7.19 - $\langle WSS \rangle_{(>7 Pa)}$ dependence on aorta's geometric parameters: (a) inlet diameter, (b) angle θ (c) angle θ_I (d) angle θ_{II} .

Previously, it was shown that a stronger curvature (big θ angle) is related with larger pressure (Figure 7.12). Here, the opposite tendency is shown with respect to $\langle WSS \rangle_{(>7 Pa)}$ (Figure 7.19). Perhaps, these opposite behaviors, explain why the impact of this angle in the volume variation is small (Figure 7.6).

The impact of the curvature measured by the angles θ_I and θ_{II} in $\langle WSS \rangle_{(>7 Pa)}$, shown in Figure 7.19 (c) and Figure 7.19 (d) are also reversed in relation to what was shown for $\langle \bar{P} \rangle_{(>100 Pa)}$ (Figure 7.12), i.e., no impact of θ_I , and increased WSS with an increase of θ_{II} .

7.4.1 TAWSS

The TAWSS, that refers to the time average stress on the wall of a vessel over the cycle, is shown for all patients in Figure 7.20. Patients without growth appear to have smaller area of high WSS values, while in the growth group, patients with large areas of high wall shear stress values during the cycle are observed.

Table 7.5 presents the quantitative analysis of the minimum ($TAWSS_{min}$), the average ($TAWSS_{ave}$) and the maximum ($TAWSS_{max}$) values in the region of interest (Figure 7.2).

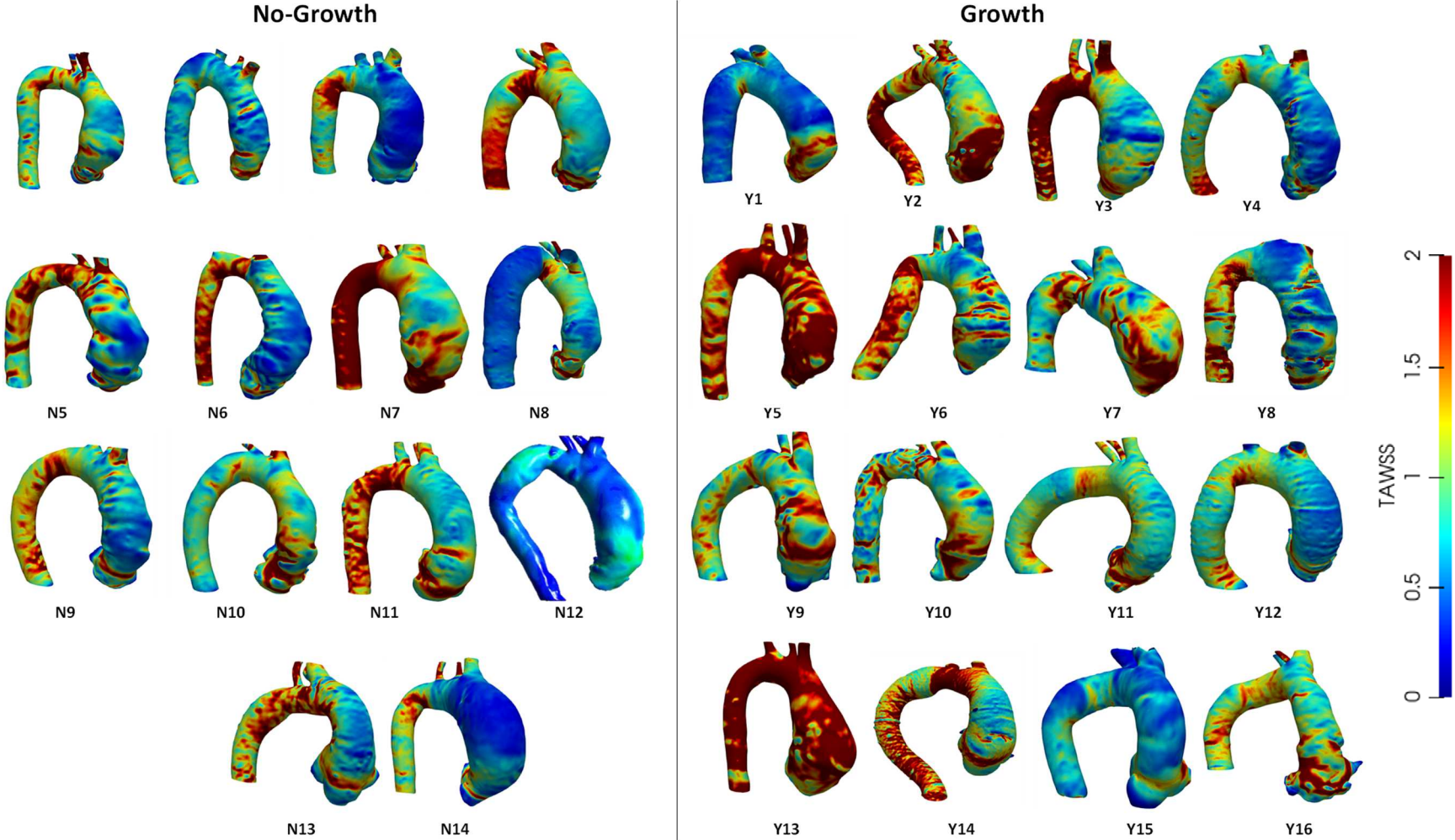


Figure 7.20 – TAWSS of patients without and with aneurysm growth.

Table 7.5 - Quantitative analysis of $TAWSS_{min}$, $TAWSS_{ave}$ and $TAWSS_{max}$.

Variable	30 patients [mean \pm SD]	Patients		ϵ [%]
		Without Growth [mean \pm SD]	With Growth [mean \pm SD]	
$TAWSS_{min}$	0.24 \pm 0.16	0.22 \pm 0.13	0.25 \pm 0.19	11.69
$TAWSS_{ave}$	1.11 \pm 0.37	0.97 \pm 0.28	1.22 \pm 0.41	26.17
$TAWSS_{max}$	4.18 \pm 1.19	3.69 \pm 1.31	4.58 \pm 0.95	24.08

As observed in Figure 7.20, patients who presented aneurysm growth exhibit a notably higher mean value in comparison with the patients without aneurysm growth, with a difference of 26.17%. The limiting values of $TAWSS$, $TAWSS_{min}$ and $TAWSS_{max}$, are also higher for the group with aneurysm growth.

Figure 7.21 shows equivalent dispersion of $TAWSS_{ave}$ for both groups, but with smaller standard deviation and higher median for the patients with increase of the aneurysm. For this variable, both mean and median are higher for the growth group, indicating a possible correlation of $TAWSS_{ave}$ with the progression of the disease.

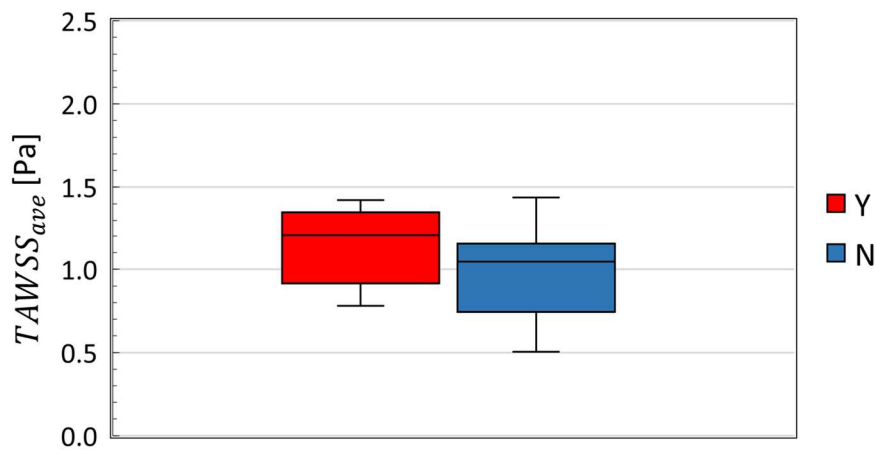
Figure 7.21 Dispersal of $TAWSS_{ave}$ values.

Figure 7.22 depicts the relation of the aorta's geometric parameters (D , θ , θ_I , θ_{II}) with $TAWSS_{ave}$. As seen previously, in relation to their impact to TAP_{ave} (Figure 7.15), the same tendency with respect to $TAWSS_{ave}$ is seen here. Higher $TAWSS_{ave}$ with smaller inlet effective diameter D and larger angle θ corresponding

to larger volume increase. The correlation of the angle θ with a deterioration of the disease was speculated by Salmasi et al. (2021), who suggested that aortas exposed to abnormal WSS over time may have accelerated wall degeneration, what can result in rupture or dissection. This hypothesis is being confirmed with the present work. The correlation of the other two angles θ_I and θ_{II} (proposed by Almeida et al., 2022) with higher strain (pressure and shear) and volume increase, is different for each variable, and cannot be considered as valid variables to analyze the disease.

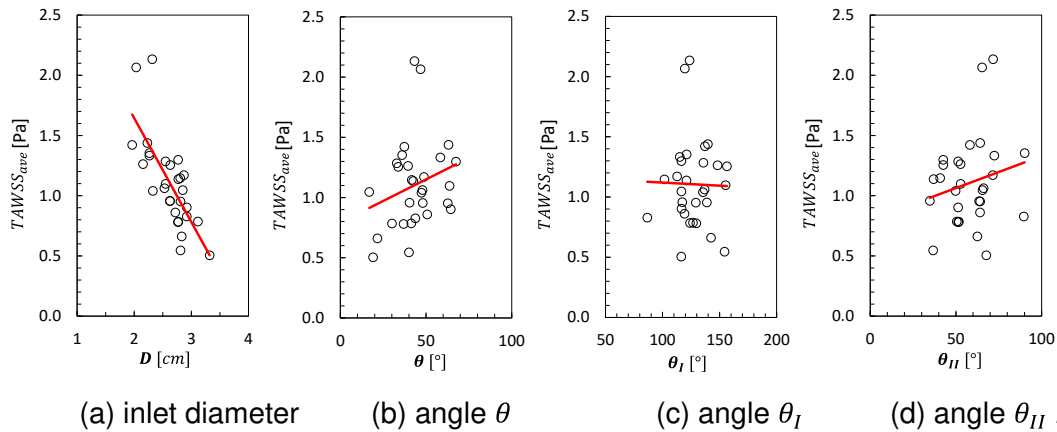


Figure 7.22 - $TAWSS_{ave}$ dependence on aorta's geometric parameters: (a) inlet diameter D , (b) angle θ (c) angle θ_I (d) angle θ_{II} .

7.4.2 OSI

The variable to characterize the degree of shear reversal in a pulsatile flow, OSI , is shown for all patients in Figure 7.23. Note that most of the patients of the aneurysm growth group present lower values of OSI at the impinging jet flow region at the anterior aorta's wall, indicating the shear vector does not change direction in that region during the cardiac cycle. Except for patient Y12, who shows high level of OSI all over the ascending aorta, with only a small region with slightly lower values. Actually, the no-growth group also shows smaller levels of OSI at the anterior aorta's wall, but not as defined as the other group.

Table 7.6 presents the minimum (OSI_{min}), average (OSI_{ave}) and maximum (OSI_{max}) values for each group and the percentual difference of these quantities among the groups. No significant difference between the groups is perceived, although, 13.03% was observed for the minimum OSI , indicating as mentioned in the previous paragraph, that the growth group, presents the flow slightly more aligned than the no-growth group.

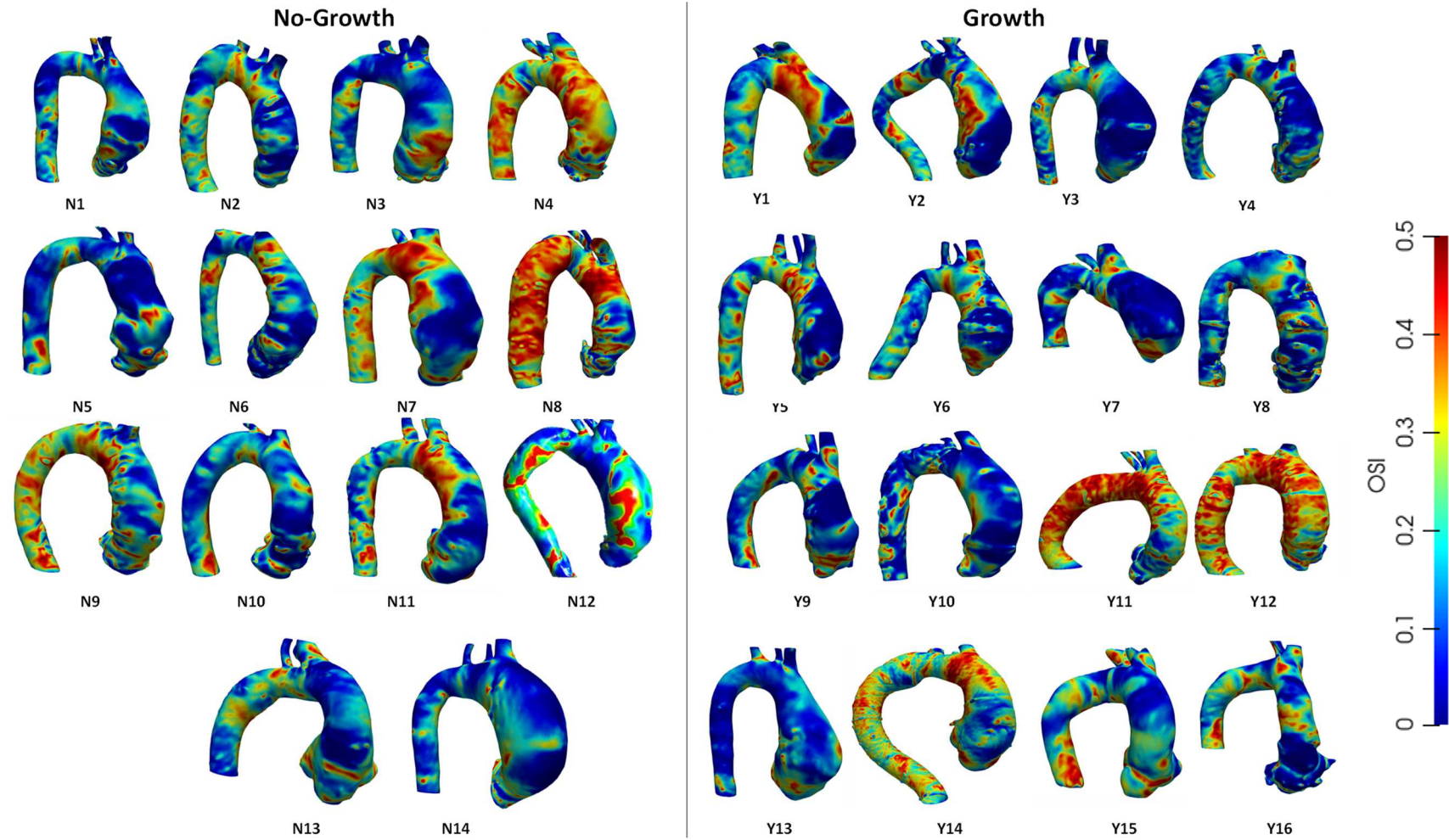


Figure 7.23 – *OSI* for patients without and with aneurysm growth.

Table 7.6 - Quantitative analysis of OSI_{min} , OSI_{ave} and OSI_{max} .

Variable	30 patients	Patients		ϵ [%]
	[mean \pm SD]	Without Growth [mean \pm SD]	With Growth [mean \pm SD]	
OSI_{min}	5.80×10^{-3} ± 0.01	6.25×10^{-3} ± 0.01	5.43×10^{-3} ± 0.01	13.03
OSI_{ave}	0.212 ± 0.06	0.213 ± 0.06	0.211 ± 0.05	1.07
OSI_{max}	0.497 ± 0.00	0.496 ± 0.00	0.497 ± 0.00	0.05

Figure 7.24 explores the dispersal of OSI_{ave} , standard deviation and median of the two groups. A greater dispersion in the values of OSI_{ave} for patients without aneurysm growth is seen, and a larger standard deviation, and equivalent medians. The smaller dispersion of OSI_{ave} may suggest that for the patients that presented aneurysm growth, the shear stresses were more aligned with the flow throughout the cycle.

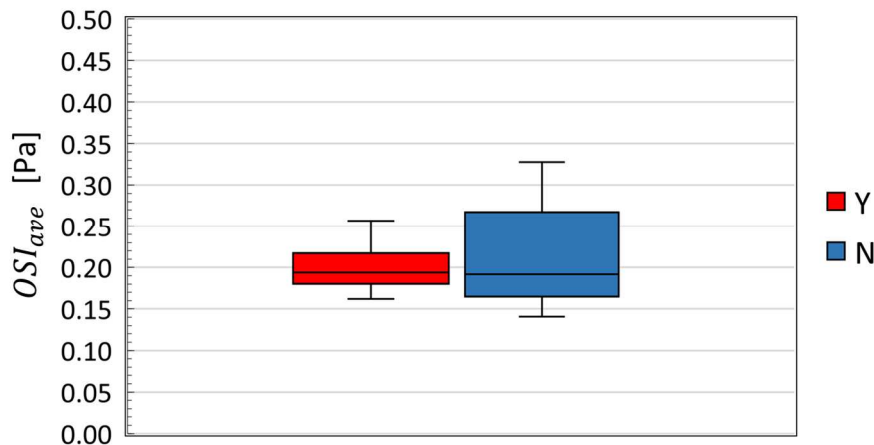


Figure 7.24 - Dispersal of OSI_{ave} values.

In Figure 7.25 the correlation between the geometric parameters D , θ , θ_I and θ_{II} with OSI_{ave} is presented. As seen in all previous analyses, a smaller effective inlet diameter D , leads to a higher velocity, higher pressure and WSS levels, and volume increase. It is also related with smaller OSI_{ave} , agreeing with the results of Figure 7.23 and Figure 7.24. The correlation of θ with OSI_{ave} is very small, with an almost horizontal trend. The angles θ_I and θ_{II} have opposite impact in OSI_{ave} , and as already mentioned, these angles do not present a consistent dependence with

the significant flow variables, that we believe are related with the growth of an aneurysm.

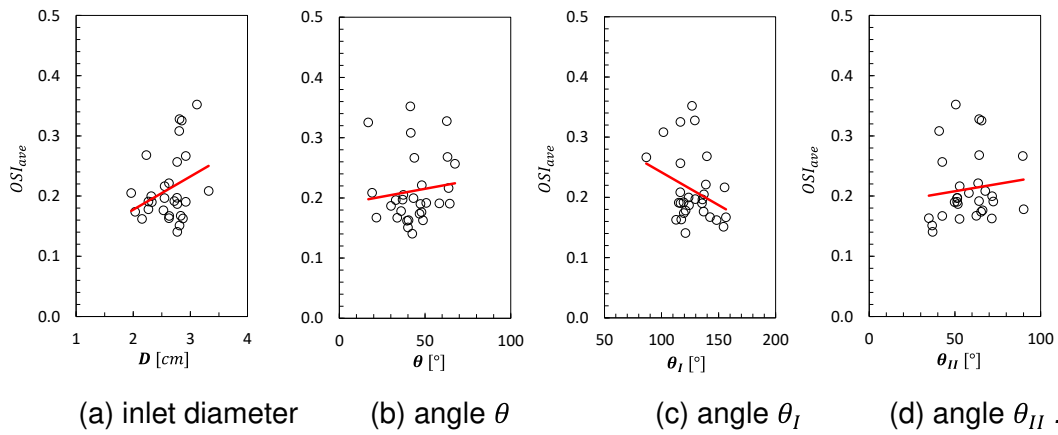


Figure 7.25 - OSI_{ave} dependence on aorta's geometric parameters: (a) inlet diameter, (b) angle θ (c) angle θ_I (d) angle θ_{II} .

8 FINAL COMENTS

This thesis aimed to understand the aortic remodeling of 30 patients with AAoA using CFD simulation. The investigation covered the entire cardiac cycle, employing the same boundary conditions to all patients. A physiological mass flow rate temporal curve was imposed at the inlet of the aorta, with identical mass flow rate percentages at each outflow, also based on physiological values. This approach was adopted due to the unavailability of all the necessary information required for a PSM simulation. It was prioritized the evaluation of the hemodynamic variables focusing on the geometric influences on disease progression.

To compare this methodology, a healthy patient with 4D-Flow MRI data was compared with the prediction obtained employing a CFD simulation. This approximation relied on data collected from the 4D-Flow MRI exam, which contained the patient's flow curve, in addition to systolic and diastolic pressure measurements taken on the day of the exam. This information is extremely relevant as a requirement for a PSM simulation.

The software 4D-Flow software provided volume flow rate temporal profiles at hand defined planes, during the exam. Pressure and WSS results were also graphically presented. Good mass flow rate agreement between the numerical and experimental data, despite the large number of uncertainties to numerically represent the actual fluid and planes definitions. Very similar streamlines distributions were also captured by the numerical simulation. The comparison of pressure and WSS were not satisfactory, since it was not available the methodology employed by the 4D-Flow software to measure these quantities.

4D-Flow MRI is a powerful tool to help in defining boundary conditions for numerical simulation, especially to be used in PSM methodology. Although promising, 4D-Flow MRI has limited spatial and temporal resolutions, compromising the accuracy of parameters derived from spatial gradients of measured velocities (Manchester et al., 2021), particularly in the descending part of the aorta. The lack of information related with the measurement technique is a major drawback to use this tool to compare with a numerical simulation. Nevertheless, the tool has potential to become a useful engineering/medical instrument, aiding treatment planning, disease progression, hemodynamics

predictive and surgery indication, if solving the limitations mentioned.

After performing the numerical-experimental comparison, simulations with different boundary conditions models at the outputs were performed, considering the 3E-WK versus the percentage outflow models. As discussed, the evaluated error was very low between the solutions, proving that percentage outflow rate methodology can be used for the numerical simulation of the 30 patients with AAOA, due to a significantly smaller computing effort.

Using the volume variance of the ascending aorta over a defined time span, two distinct groups were delineated: those exhibiting aneurysm growth and those without growth. A comparative analysis between the two groups of pressure and shear stress at the ascending aorta wall was conducted to identify potential quantities indicative of aneurysm progression.

Aiming to correlate the patient's geometry with the flow variables and consequently the growth of the aneurysm, the impact of geometric parameters in the flow field were examined. The inlet effective diameter was selected, and it was observed that as it decreases, the volume ratio of the ascending aorta increases, indicating aneurysm growth. This correlation was expected since the same mass flow rate was imposed at the inlet, and smaller inlet diameters result in higher velocities and subsequently elevated impinging pressure and shear stress, potentially influencing growth.

Believing in the significance of aortic angulation in the disease progression, the angles θ proposed by Salmasi et al. (2021) and the angles θ_I and θ_{II} proposed by Almeida et al. (2022) were selected to evaluate the impact of the aorta's shape in the volume ratio between the 2nd and 1st year of the exams, as well as in the pressure and shear stress at the ascending aorta's wall.

The angle θ is defined as the angle between the aortic orifice and the midpoint of the ascending aorta. High θ indicates greater curvature, redirecting the flow towards the anterior wall of the aorta, rather than along the artery. Salmasi et al. (2021) examined a set of patients, without the knowledge of the disease stage, and showed that more angulated orientation correlates with larger aortic diameters, and speculated that it might induce an increase of the aneurysm. This assumption was confirmed at the present work.

Although the angles θ_I and θ_{II} proposed by Almeida et al. (2022) seem to be also promising variables to correlate the aorta's shape with the aneurysm progression, the results obtained were not conclusive.

Based on previous works of Almeida et al. (2022) and Azevedo et al. (2024), pressure above the threshold of 100 Pa at the ascending aorta's wall was examined.

Azevedo et al. (2024) examined the flow for the same 30 patients, but employed a steady state analysis, considering the critical flow rate at the systolic peak and found a statistical correlation between the average pressure at a region with pressure above 100 Pa, $\bar{P}_{(>100 Pa)}$, with the aneurysm growth. Here, the complete cardiac cycle was examined. It was shown equivalent time evolution of $\bar{P}_{(>100 Pa)}$ during the cycle, with similar pressure levels for both groups. Equivalent time average during the time period with high pressure, with similar median. However, it is observed that the patient group with aneurysm group is exposed to higher pressure for a longer time period ($\Delta t_{pressure}$), implying that the patient is under stress for a longer period, which can induce the aneurysm growth. Furthermore, it was concluded that the average values during the time interval of high pressure are not adequate, as longer exposure time masks the results. Thus, to better evaluate the pressure along the cycle, the time average along the whole cycle TAP was analyzed. The area-averaged TAP value exhibits a notable difference between the groups. This substantial variance underscores the significance of monitoring the TAP_{ave} value as a crucial variable for disease management and control.

The time behavior of the average high WSS $\overline{WSS}_{(>7 Pa)}$ along the cycle, indicates elevated $\overline{WSS}_{(>7 Pa)}$ values are present not only during the systolic phase but also persist throughout the diastolic phase for the group with aneurysm growth, corresponding to a significant longer time interval Δt_{WSS} for the group with aneurysm growth. Due to the longer time interval of exposition to high shear Δt_{WSS} , the mean during this interval is misleading, as discussed for the pressure, and the time average during the total cycle $TAWSS$ is more adequate. It's evident that subjecting patients to higher shear stress for an extended duration significantly contributes to aneurysm growth.

Examining the mean value among the patients of the cycle time average stress, $TAWSS_{ave}$, patients displaying aneurysm growth demonstrate a significantly higher mean value compared to those without aneurysm growth, showing a notable difference. These results also validate the speculation of Samalsi et al. (2021), who suggested that aortas exposed to abnormal wall shear stress (WSS) over time may experience accelerated wall degeneration, potentially leading to rupture or dissection.

Finally, the narrower dispersion of OSI_{ave} suggests that in patients with aneurysm growth, shear stresses were more consistently aligned with the flow throughout the cardiac cycle.

To conclude, the most relevant variables found in patients with aneurysm growth and that may indicate the growth of the ascending aortic aneurysm, are:

- *Longer time interval with high strain:*
 - Pressure: $\Delta t_{pressure}$.
 - Shear Stress: Δt_{WSS} .
- *High values of:*
 - Curvature: θ .
 - Period Time Average, and Area Average Pressure: TAP_{ave} .
 - Period Time Average, and Area Average Shear Stress: $TAWSS_{ave}$.

8.1 Conclusion

This present thesis serves as a valuable contribution to cardiovascular research. Whether through comparing results between 4D-Flow MRI and CFD simulations in a healthy aorta, investigating the impact of employing different BC, or conducting CFD simulations on patients with ascending aortic aneurysm throughout a cardiac cycle.

Considering AAoA research field, this thesis fills a gap in the literature by analyzing a great number of patients with indicative of the grow or not of the aneurysm in the transient regime, providing information on whether patients experienced greater dilation of the aneurysm in the future. Furthermore, the correlation analysis of hemodynamic variables and geometry, delving into the remodeling process, helping to improve the understanding of aortic pathophysiology and contributes to the advancement of knowledge in this field.

Therefore, this study can potentially aid the development of more accurate diagnostic tools and treatment strategies. By bridging the gap between theoretical understanding and clinical practice, this research paves the way for more effective identification and management of aortic pathologies, ultimately leading to improved patient outcomes.

8.2 Future developments

Future developments and improvements of this work may include:

- *Aortic Valve:* consideration the aortic valve is an important step to more accurately represent the flow at the inlet of the aorta.
- *Fluid Structure Interaction (FSI):* incorporating FSI into aortic simulations enables a more realistic representations of its behavior and provides

insights about wall motion, elasticity and compliance.

- *3E-WK model for all 30 AAoA patients as outflow boundary condition:* although the solution obtained with the WK model and the flow percentages were close, the WK models depends on the pressure level during the cycle, resulting in a more faithfully representation of the patient condition.
- *Personalized boundary condition:*
 - Inflow: each patient presents a slightly different inlet mass flow rate, which has a significant impact in the flow velocity, acting on the pressure and WSS distribution. However, this condition is very difficult to be available.
 - Outflow: to improve the outflow boundary condition, the measured systolic and diastolic pressures of each patient to determine the coefficients of the WK model.
- *Statistical Analysis:* correlation coefficient of the analyzed variables and evaluation of covariance matrix.
- *Artificial Intelligence Models:* clusterization technique for Artificial Intelligence training as well the increase of patient data can enable the integration of aneurysm growth prediction with artificial intelligence based in machine learning and deep learning, offering better predictive analyses and optimizing treatment strategies.

References

- Abbatfati, C., Abbas, K. M., Abbasi-Kangevari, M., Abd-Allah, F., Abdelalim, A., Abdollahi, M., Abdollahpour, I., Abegaz, K. H., Abolhassani, H., Aboyans, V., Abreu, L. G., Abrigo, M. R. M., Abualhasan, A., Abu-Raddad, L. J., Abushouk, A. I., Adabi, M., Adekanmbi, V., Adeoye, A. M., Adetokunboh, O. O., ... Amini, S. (2020). Global burden of 369 diseases and injuries in 204 countries and territories, 1990–2019: a systematic analysis for the Global Burden of Disease Study 2019. *The Lancet*, *396*(10258), 1204–1222. [https://doi.org/10.1016/S0140-6736\(20\)30925-9](https://doi.org/10.1016/S0140-6736(20)30925-9)
- Aggarwal, S., Qamar, A., Sharma, V., & Sharma, A. (2011). Abdominal aortic aneurysm: A comprehensive review. *Experimental and Clinical Cardiology*, *16*(1), 11–15.
- Ahmad, R., Farooqi, A., Farooqi, R., Hamadneh, N. N., Fayz-Al-Asad, M., Khan, I., Sajid, M., Bary, G., & Saleem Khan, M. F. (2021). An Analytical Approach to Study the Blood Flow over a Nonlinear Tapering Stenosed Artery in Flow of Carreau Fluid Model. *Complexity*, *2021*, 9921642. <https://doi.org/10.1155/2021/9921642>
- Al-Jumaily, A. M., Embong, A. H. Bin, AL-Rawi, M., Mahadevan, G., & Sugita, S. (2023). Aneurysm Rupture Prediction Based on Strain Energy-CFD Modelling. *Bioengineering*, *10*(10). <https://doi.org/10.3390/bioengineering10101231>
- Alastruey, J., Xiao, N., Fok, H., Schaeffter, T., & Figueroa, C. A. (2016). On the impact of modelling assumptions in multi-scale, subject-specific models of aortic haemodynamics. *Journal of The Royal Society Interface*, *13*(119), 20160073.
- Alimohammadi, M., Pichardo-Almarza, C., Agu, O., & Díaz-Zuccarini, V. (2016). Development of a Patient-Specific Multi-Scale Model to Understand Atherosclerosis and Calcification Locations: Comparison with In vivo Data in an Aortic Dissection. *Frontiers in Physiology*, *7*. <https://doi.org/10.3389/fphys.2016.00238>
- Alimohammadi, M., Pichardo-Almarza, C., Agu, O., & Díaz-Zuccarini, V. (2017). A multiscale modelling approach to understand atherosclerosis formation: A

- patient-specific case study in the aortic bifurcation. *Proceedings of the Institution of Mechanical Engineers. Part H, Journal of Engineering in Medicine*, 231(5), 378–390. <https://doi.org/10.1177/0954411917697356>
- Almeida, G. D. C., Silva, J. D. A., & Nieckele, A. O. (2021). *Impact of Viscosity on Blood Flow in Ascending Aortic*. 1(2020), 1–7.
- Almeida, G. de C., Goms, B. A. de A., Azevedo, F. S. de, Kalaun, K., Ibanez, I., Teixeira, P. S., Gottlieb, I., Melo, M. M., Oliveira, G. M. M. de, & Nieckele, A. O. (2022). Computational Fluid Dynamics to Assess the Future Risk of Ascending Aortic Aneurysms. *Arquivos Brasileiros de Cardiologia*, 118(2), 448–460. <https://doi.org/10.36660/abc.20200926>
- American Heart Association. (n.d.). *All About Heart Rate (Pulse)*. Retrieved December 28, 2022, from <https://www.heart.org/en/health-topics/high-blood-pressure/the-facts-about-high-blood-pressure/all-about-heart-rate-pulse>
- Ansys. (2021). *Ansys Fluent Theory Guide*.
- Archer, G. T., Elhawaz, A., Barker, N., Fidock, B., Rothman, A., van der Geest, R. J., Hose, R., Briffa, N., Hall, I. R., Grech, E., Bissell, M., Al-Mohammad, A., Treibel, T. A., Swift, A. J., Wild, J. M., & Garg, P. (2020). Validation of four-dimensional flow cardiovascular magnetic resonance for aortic stenosis assessment. *Scientific Reports*, 10(1), 10569. <https://doi.org/10.1038/s41598-020-66659-6>
- Augoustides, J. G., & Cheung, A. T. (2014). 19 - *Aneurysms and Dissections* (D. L. Reich & G. W. B. T.-P. T. E. Fischer (eds.); pp. 191–217). W.B. Saunders. <https://doi.org/https://doi.org/10.1016/B978-1-4557-0761-4.00019-0>
- Aycan, O., Topuz, A., & Kadem, L. (2023). Evaluating uncertainties in CFD simulations of patient-specific aorta models using Grid Convergence Index method. *Mechanics Research Communications*, 133, 104188. <https://doi.org/https://doi.org/10.1016/j.mechrescom.2023.104188>
- Azevedo, F. S. de;, Almeida, G. de C., Gomes, B. A. de A., Ibanez, I. F., Azevedo, B. N., Camargo, G. C., Correa, M. G., Nieckele, A. O., & Oliveira, G. M. M. (2024). Stress Load and Ascending Aortic Aneurysms: An Observational, Longitudinal, Single-Center Study Using Computational Fluid Dynamics. *Bioengineering*, 11(204), 1–16. <https://doi.org/10.3390/bioengineering11030204>
- Bacon, S. (2013). *Cardiac Output BT - Encyclopedia of Behavioral Medicine* (M. D. Gellman & J. R. Turner (eds.); pp. 332–333). Springer New York. https://doi.org/10.1007/978-1-4419-1005-9_235
- Bakhshinejad, A., Baghaie, A., Vali, A., Saloner, D., Rayz, V. L., & D'Souza, R. M.

- (2017). Merging computational fluid dynamics and 4D Flow MRI using proper orthogonal decomposition and ridge regression. *Journal of Biomechanics*, *58*, 162–173. <https://doi.org/https://doi.org/10.1016/j.jbiomech.2017.05.004>
- Ballyk, P. D., Steinman, D. A., & Ethier, C. R. (1994). Simulation of non-Newtonian blood flow in an end-to-side anastomosis. *Biorheology*, *31*(5), 565–586. <https://doi.org/10.3233/bir-1994-31505>
- Barker, A. J., Lanning, C., & Shandas, R. (2010). Quantification of hemodynamic wall shear stress in patients with bicuspid aortic valve using phase-contrast MRI. *Annals of Biomedical Engineering*, *38*(3), 788–800. <https://doi.org/10.1007/s10439-009-9854-3>
- Barker, A. J., Markl, M., Bürk, J., Lorenz, R., Bock, J., Bauer, S., Schulz-Menger, J., & von Knobelsdorff-Brenkenhoff, F. (2012). Bicuspid aortic valve is associated with altered wall shear stress in the ascending aorta. *Circulation Cardiovascular Imaging*, *5*(4), 457–466. <https://doi.org/10.1161/CIRCIMAGING.112.973370>
- Bertaso, A. G., Wong, D. T. L., Liew, G. Y. H., Cunningham, M. S., Richardson, J. D., Thomson, V. S., Lorraine, B., Kourlis, G., Leech, D., Worthley, M. I., & Worthley, S. G. (2012). Aortic annulus dimension assessment by computed tomography for transcatheter aortic valve implantation: differences between systole and diastole. *The International Journal of Cardiovascular Imaging*, *28*(8), 2091–2098. <https://doi.org/10.1007/s10554-012-0018-4>
- Biasseti, J., Hussain, F., & Gasser, T. C. (2011). Blood flow and coherent vortices in the normal and aneurysmatic aortas: a fluid dynamical approach to intraluminal thrombus formation. *Journal of the Royal Society, Interface*, *8*(63), 1449–1461. <https://doi.org/10.1098/rsif.2011.0041>
- Bicer, M., Yuksel, A., & Kan, I. I. (2020). The Largest Reported Giant Ascending Aortic Aneurysm Presented with Superior Vena Cava Syndrome. *Brazilian Journal of Cardiovascular Surgery*, *35*(Braz. J. Cardiovasc. Surg., 2020 35(5)). <https://doi.org/10.21470/1678-9741-2019-0151>
- Bieging, E. T., Frydrychowicz, A., Wentland, A., Landgraf, B. R., Johnson, K. M., Wieben, O., & François, C. J. (2011). In vivo three-dimensional MR wall shear stress estimation in ascending aortic dilatation. *Journal of Magnetic Resonance Imaging: JMRI*, *33*(3), 589–597. <https://doi.org/10.1002/jmri.22485>
- Bishop, J. J., Popel, A. S., Intaglietta, M., & Johnson, P. C. (2001). Rheological effects of red blood cell aggregation in the venous network: a review of recent studies. *Biorheology*, *38*(2–3), 263–274.

- Black, S. M., Maclean, C., Hall Barrientos, P., Ritos, K., McQueen, A., & Kazakidi, A. (2023). Calibration of patient-specific boundary conditions for coupled CFD models of the aorta derived from 4D Flow-MRI. *Frontiers in Bioengineering and Biotechnology*, *11*. <https://doi.org/10.3389/fbioe.2023.1178483>
- Bluestein, D. (2017). Utilizing Computational Fluid Dynamics in Cardiovascular Engineering and Medicine-What You Need to Know. Its Translation to the Clinic/Bedside. In *Artificial organs* (Vol. 41, Issue 2, pp. 117–121). <https://doi.org/10.1111/aor.12914>
- Bodnár, T., Sequeira, A., & Prosi, M. (2011). On the shear-thinning and viscoelastic effects of blood flow under various flow rates. *Applied Mathematics and Computation*, *217*(11), 5055–5067. <https://doi.org/https://doi.org/10.1016/j.amc.2010.07.054>
- Borazjani, I., Ge, L., & Sotiropoulos, F. (2008). Curvilinear Immersed Boundary Method for Simulating Fluid Structure Interaction with Complex 3D Rigid Bodies. *Journal of Computational Physics*, *227*(16), 7587–7620. <https://doi.org/10.1016/j.jcp.2008.04.028>
- Bouaou, K., Bargiotas, I., Dietenbeck, T., Bollache, E., Soulat, G., Craiem, D., Houriez-Gombaud-Saintonge, S., De Cesare, A., Gencer, U., Giron, A., Redheuil, A., Messas, E., Lucor, D., Mousseaux, E., & Kachenoura, N. (2019). Analysis of aortic pressure fields from 4D flow MRI in healthy volunteers: Associations with age and left ventricular remodeling. *Journal of Magnetic Resonance Imaging: JMRI*, *50*(3), 982–993. <https://doi.org/10.1002/jmri.26673>
- Boyd, A. J., Kuhn, D. C. S., Lozowy, R. J., & Kulbisky, G. P. (2016). Low wall shear stress predominates at sites of abdominal aortic aneurysm rupture. *Journal of Vascular Surgery*, *63*(6), 1613–1619. <https://doi.org/https://doi.org/10.1016/j.jvs.2015.01.040>
- Brix, L., Ringgaard, S., Rasmusson, A., Sørensen, T. S., & Kim, W. Y. (2009). Three dimensional three component whole heart cardiovascular magnetic resonance velocity mapping: comparison of flow measurements from 3D and 2D acquisitions. *Journal of Cardiovascular Magnetic Resonance*, *11*(1), 3. <https://doi.org/10.1186/1532-429X-11-3>
- Brown, A. G., Shi, Y., Marzo, A., Staicu, C., Valverde, I., Beerbaum, P., Lawford, P. V., & Hose, D. R. (2012). Accuracy vs. computational time: translating aortic simulations to the clinic. *Journal of Biomechanics*, *45*(3), 516–523. <https://doi.org/10.1016/j.jbiomech.2011.11.041>
- Bürk, J., Blanke, P., Stankovic, Z., Barker, A., Russe, M., Geiger, J.,

- Frydrychowicz, A., Langer, M., & Markl, M. (2012). Evaluation of 3D blood flow patterns and wall shear stress in the normal and dilated thoracic aorta using flow-sensitive 4D CMR. *Journal of Cardiovascular Magnetic Resonance: Official Journal of the Society for Cardiovascular Magnetic Resonance*, *14*(1), 84. <https://doi.org/10.1186/1532-429X-14-84>
- Burris, N. S., & Hope, M. D. (2015). 4D flow MRI applications for aortic disease. *Magnetic Resonance Imaging Clinics of North America*, *23*(1), 15–23. <https://doi.org/10.1016/j.mric.2014.08.006>
- Callaghan, F. M., & Grieve, S. M. (2018). Normal patterns of thoracic aortic wall shear stress measured using four-dimensional flow MRI in a large population. *American Journal of Physiology. Heart and Circulatory Physiology*, *315*(5), H1174–H1181. <https://doi.org/10.1152/ajpheart.00017.2018>
- Caro, C. G., Fitz-Gerald, J. M., & Schroter, R. C. (1971). Atheroma and arterial wall shear. Observation, correlation and proposal of a shear dependent mass transfer mechanism for atherogenesis. *Proceedings of the Royal Society of London. Series B, Biological Sciences*, *177*(1046), 109–159. <https://doi.org/10.1098/rspb.1971.0019>
- Carreau, P. J. (1972). Rheological Equations from Molecular Network Theories. *Transactions of The Society of Rheology*, *16*(1), 99–127. <https://doi.org/10.1122/1.549276>
- CC BY-SA 3.0. (2023). By Wapcaplet - Own work. <https://commons.wikimedia.org/w/index.php?curid=832053>
- Cecchi, E., Giglioli, C., Valente, S., Lazzeri, C., Gensini, G. F., Abbate, R., & Mannini, L. (2011). Role of hemodynamic shear stress in cardiovascular disease. *Atherosclerosis*, *214*(2), 249–256. <https://doi.org/10.1016/j.atherosclerosis.2010.09.008>
- Celis, D., Gomes, B. A. de A., Ibanez, I., Azevedo, P. N., Teixeira, P. S., & Nieckele, A. O. (2020). Predição do Mapa de Estresse em Aorta Ascendente: Otimização da Posição Coaxial no Implante Valvar Aórtico Percutâneo. *Arquivos Brasileiros de Cardiologia*, *115*(4), 680–687. <https://doi.org/10.36660/abc.20190385>
- Celis Torres, D., Ibañez, I., Nieckele, P. A., Nieckele, A. O., Azevedo, B. A. (2017). Numerical investigation of hemodynamics patterns after Transcatheter Aortic Valve Replacement (TAVR). *Proceedings of the Congresso Brasileiro de Engenharia Mecânica (COBEM)*.
- Celis Torres, D. F. (2017). *Numerical study of the influence of tilt valve angle on blood flow in a aortic model*. Masters Dissertation. Pontifícia Universidade

- Católica do Rio de Janeiro.
- Chen, L., Wang, X., Carter, S. A., Shen, Y. H., Bartsch, H. R., Thompson, R. W., Coselli, J. S., Wilcken, D. L., Wang, X. L., & LeMaire, S. A. (2006). A single nucleotide polymorphism in the matrix metalloproteinase 9 gene (-8202A/G) is associated with thoracic aortic aneurysms and thoracic aortic dissection. *The Journal of Thoracic and Cardiovascular Surgery*, *131*(5), 1045–1052. <https://doi.org/10.1016/j.jtcvs.2006.01.003>
- Cherry, M., Khatir, Z., Khan, A., & Bissell, M. (2022). The impact of 4D-Flow MRI spatial resolution on patient-specific CFD simulations of the thoracic aorta. *Scientific Reports*, *12*(1), 15128. <https://doi.org/10.1038/s41598-022-19347-6>
- Chien, S., Usami, S., Dellenback, R. J., & Gregersen, M. I. (1970). Shear-dependent deformation of erythrocytes in rheology of human blood. *The American Journal of Physiology*, *219*(1), 136–142. <https://doi.org/10.1152/ajplegacy.1970.219.1.136>
- Cho, Y., & Kensey, K. (1991). Effects of the non-Newtonian viscosity of blood on flows in a diseased arterial vessel. Part 1: Steady flows. *Biorheology*, *28*, 241–262. <https://doi.org/10.3233/BIR-1991-283-415>
- Cloutier, G., & Shung, K. K. (1993). Study of red cell aggregation in pulsatile flow from ultrasonic Doppler power measurements. *Biorheology*, *30*(5–6), 443–461. <https://doi.org/10.3233/bir-1993-305-615>
- Coady, M A, Rizzo, J. A., Hammond, G. L., Mandapati, D., Darr, U., Kopf, G. S., & Elefteriades, J. A. (1997). What is the appropriate size criterion for resection of thoracic aortic aneurysms? *The Journal of Thoracic and Cardiovascular Surgery*, *113*(3), 476–491. [https://doi.org/10.1016/S0022-5223\(97\)70360-X](https://doi.org/10.1016/S0022-5223(97)70360-X)
- Coady, Michael A, Rizzo, J. A., Hammond, G. L., Kopf, G. S., & Elefteriades, J. A. (1999). Surgical intervention criteria for thoracic aortic aneurysms: a study of growth rates and complications. *The Annals of Thoracic Surgery*, *67*(6), 1922–1926. [https://doi.org/https://doi.org/10.1016/S0003-4975\(99\)00431-2](https://doi.org/https://doi.org/10.1016/S0003-4975(99)00431-2)
- Cosentino, F., Giuseppe, M. D. I., Agnese, V., Gentile, G., Raffa, G. M., Wineski, A., Guccione, J., Pasta, S., & Pilato, M. (2020). On the severity of aortic stenosis in ascending aortic aneurysm: A computational tool to examine ventricular-arterial interaction and aortic wall stress. *Mechanics Research Communications*, *110*, 103621. <https://doi.org/https://doi.org/10.1016/j.mechrescom.2020.103621>
- Courneya, C. A. M., & Parker, M. J. (2011). *Cardiovascular Physiology: A Clinical Approach*. Wolters Kluwer/Lippincott Williams & Wilkins Health. https://books.google.com.br/books?id=mtGi%5C_nM341gC

- Cousins, S., Blencowe, N. S., & Blazeby, J. M. (2019). What is an invasive procedure? A definition to inform study design, evidence synthesis and research tracking. *BMJ Open*, *9*(7), e028576. <https://doi.org/10.1136/bmjopen-2018-028576>
- Criscione, R. (2013). Ascending aorta parametric modeling and fluid dynamics analysis in a child patient with congenital BAV and ascending aorta aneurysm [École Polytechnique de Montréal]. In *PolyPublie*. http://ezproxy.rice.edu/login?url=https://search.proquest.com/docview/1556459930?accountid=7064%0Ahttp://sfxhosted.exlibrisgroup.com/rice?url_ver=Z39.88-2004&rft_val_fmt=info:ofi/fmt:kev:mtx:dissertation&genre=dissertations+%26+theses&sid=ProQ:ProQuest+Di
- Crowley, T. A., & Pizziconi, V. (2005). Isolation of plasma from whole blood using planar microfilters for lab-on-a-chip applications. *Lab on a Chip*, *5*(9), 922–929. <https://doi.org/10.1039/B502930A>
- Davies, P. F., Remuzzi, A., Gordon, E. J., Dewey, C. F. J., & Gimbrone, M. A. J. (1986). Turbulent fluid shear stress induces vascular endothelial cell turnover in vitro. *Proceedings of the National Academy of Sciences of the United States of America*, *83*(7), 2114–2117. <https://doi.org/10.1073/pnas.83.7.2114>
- Davies, R. R., Goldstein, L. J., Coady, M. A., Tittle, S. L., Rizzo, J. A., Kopf, G. S., & Elefteriades, J. A. (2002). Yearly rupture or dissection rates for thoracic aortic aneurysms: simple prediction based on size. *The Annals of Thoracic Surgery*, *73*(1), 17–18. [https://doi.org/10.1016/s0003-4975\(01\)03236-2](https://doi.org/10.1016/s0003-4975(01)03236-2)
- de Azevedo, F. S., Almeida, G. D., Alvares de Azevedo, B., Ibanez Aguilar, I. F., Azevedo, B. N., Teixeira, P. S., Camargo, G. C., Correia, M. G., Nieckele, A. O., & Oliveira, G. M. (2024). Stress Load and Ascending Aortic Aneurysms: An Observational, Longitudinal, Single-Center Study Using Computational Fluid Dynamics. In *Bioengineering* (Vol. 11, Issue 3). <https://doi.org/10.3390/bioengineering11030204>
- de Beaufort, H. W., Shah, D. J., Patel, A. P., Jackson, M. S., Spinelli, D., Yang, E. Y., Ghosn, M. G., Autry, K., Igo, S. R., Lumsden, A. B., Little, S. H., Trimarchi, S., & Bismuth, J. (2019). Four-dimensional flow cardiovascular magnetic resonance in aortic dissection: Assessment in an ex vivo model and preliminary clinical experience. *The Journal of Thoracic and Cardiovascular Surgery*, *157*(2), 467-476.e1. <https://doi.org/10.1016/j.jtcvs.2018.06.022>
- de Leval, M R, Dubini, G., Migliavacca, F., Jalali, H., Camporini, G., Redington, A., & Pietrabissa, R. (1996). Use of computational fluid dynamics in the design of

- surgical procedures: Application to the study of competitive flows in cavopulmonary connections. *The Journal of Thoracic and Cardiovascular Surgery*, 111(3), 502–513. [https://doi.org/https://doi.org/10.1016/S0022-5223\(96\)70302-1](https://doi.org/https://doi.org/10.1016/S0022-5223(96)70302-1)
- de Leval, Marc R, Kilner, P., Gewillig, M., Bull, C., & McGoon, D. C. (1988). Total cavopulmonary connection: A logical alternative to atriopulmonary connection for complex Fontan operations: Experimental studies and early clinical experience. *The Journal of Thoracic and Cardiovascular Surgery*, 96(5), 682–695. [https://doi.org/https://doi.org/10.1016/S0022-5223\(19\)35174-8](https://doi.org/https://doi.org/10.1016/S0022-5223(19)35174-8)
- Deutsch, S., Tarbell, J. M., Manning, K. B., Rosenberg, G., & Fontaine, A. A. (2006). Experimental fluid mechanics of pulsatile artificial blood pumps. *Annual Review of Fluid Mechanics*, 38(December 2013), 65–86. <https://doi.org/10.1146/annurev.fluid.38.050304.092022>
- Deyranlou, A. (2021). *Development a numerical workflow to study effects of atrial fibrillation on cardiovascular circulation*. The University of Manchester.
- Donati, F., Myerson, S., Bissell, M. M., Smith, N. P., Neubauer, S., Monaghan, M. J., Nordsletten, D. A., & Lamata, P. (2017). Beyond Bernoulli: Improving the Accuracy and Precision of Noninvasive Estimation of Peak Pressure Drops. *Circulation. Cardiovascular Imaging*, 10(1), e005207. <https://doi.org/10.1161/CIRCIMAGING.116.005207>
- Duronio, F., & Di Mascio, A. (2023). Blood Flow Simulation of Aneurysmatic and Sane Thoracic Aorta Using OpenFOAM CFD Software. In *Fluids* (Vol. 8, Issue 10). <https://doi.org/10.3390/fluids8100272>
- Ebbers, T., & Farnebäck, G. (2009). Improving computation of cardiovascular relative pressure fields from velocity MRI. *Journal of Magnetic Resonance Imaging : JMRI*, 30(1), 54–61. <https://doi.org/10.1002/jmri.21775>
- Eckstein, H.-H., & Maegdefessel, L. (2020). Linking obesity with abdominal aortic aneurysm development. In *European heart journal* (Vol. 41, Issue 26, pp. 2469–2471). <https://doi.org/10.1093/eurheartj/ehz882>
- Ehrlich, M. P., Ergin, M. A., McCullough, J. N., Lansman, S. L., Galla, J. D., Bodian, C. A., Apaydin, A., & Griepp, R. B. (2000). Results of immediate surgical treatment of all acute type A dissections. *Circulation*, 102(19 Suppl 3), III248-52. https://doi.org/10.1161/01.cir.102.suppl_3.iii-248
- Elefteriades, J. A. (2002). Natural history of thoracic aortic aneurysms: indications for surgery, and surgical versus nonsurgical risks. *The Annals of Thoracic Surgery*, 74(5), S1877-80; discussion S1892-8. [https://doi.org/10.1016/s0003-4975\(02\)04147-4](https://doi.org/10.1016/s0003-4975(02)04147-4)

- Eliathamby, D., Gutierrez, M., Liu, A., Ouzounian, M., Forbes, T. L., Tan, K. T., & Chung, J. (2021). Ascending Aortic Length and Its Association With Type A Aortic Dissection. *Journal of the American Heart Association*, *10*(13), e020140. <https://doi.org/10.1161/JAHA.120.020140>
- Epstein, S., Willemet, M., Chowienczyk, P. J., & Alastruey, J. (2015). Reducing the number of parameters in 1D arterial blood flow modeling: less is more for patient-specific simulations. *American Journal of Physiology-Heart and Circulatory Physiology*, *309*(1), H222–H234. <https://doi.org/10.1152/ajpheart.00857.2014>
- Etli, M., Canbolat, G., Karahan, O., & Koru, M. (2021). Numerical investigation of patient-specific thoracic aortic aneurysms and comparison with normal subject via computational fluid dynamics (CFD). *Medical & Biological Engineering & Computing*, *59*(1), 71–84. <https://doi.org/10.1007/s11517-020-02287-6>
- Eveborn, G. W., Schirmer, H., Lunde, P., Heggelund, G., Hansen, J.-B., & Rasmussen, K. (2014). Assessment of risk factors for developing incident aortic stenosis: the Tromsø Study. *European Journal of Epidemiology*, *29*(8), 567–575. <https://doi.org/10.1007/s10654-014-9936-x>
- Fåhræus, R., & Lindqvist, T. (1931). The viscosity of the blood in narrow capillary tubes. *American Journal of Physiology-Legacy Content*, *96*(3), 562–568. <https://doi.org/10.1152/ajplegacy.1931.96.3.562>
- Faitelson, L. A., & Jakobsons, E. E. (2003). Aggregation of Erythrocytes into Columnar Structures (“Rouleaux”) and the Rheology of Blood. *Journal of Engineering Physics and Thermophysics*, *76*(3), 728–742. <https://doi.org/10.1023/A:1024718308510>
- Feijoo, R. A., & Zouain, N. (1988). Formulations in rates and increments for elastic-plastic analysis. *International Journal for Numerical Methods in Engineering*, *26*(9), 2031–2048.
- Flachskampf, F. A., Weyman, A. E., Guerrero, J. L., & Thomas, J. D. (1990). Influence of orifice geometry and flow rate on effective valve area: an in vitro study. *Journal of the American College of Cardiology*, *15*(5), 1173–1180. [https://doi.org/10.1016/0735-1097\(90\)90260-v](https://doi.org/10.1016/0735-1097(90)90260-v)
- Frank, O. (1899). Die Grundform des arteriellen pulses. Erste Abhandlung. Mathematische Analyse. In *Zeitschrift für Biologie. Offprint TA - TT* -. [publisher not identified] [Place of publication not identified]. <https://doi.org/LK-https://worldcat.org/title/156810337>
- Friedman, M. H., Hutchins, G. M., Barger, C. B., Deters, O. J., & Mark, F. F.

- (1981). Correlation between intimal thickness and fluid shear in human arteries. *Atherosclerosis*, 39(3), 425–436. [https://doi.org/10.1016/0021-9150\(81\)90027-7](https://doi.org/10.1016/0021-9150(81)90027-7)
- Fry, D. (1968). Acute Vascular Endothelial Changes Associated with Increased Blood Velocity Gradients. *Circulation Research*, 22(2), 165–197. <https://doi.org/10.1161/01.RES.22.2.165>
- Frydrychowicz, A., Harloff, A., Jung, B., Zaitsev, M., Weigang, E., Bley, T. A., Langer, M., Hennig, J., & Markl, M. (2007). Time-resolved, 3-dimensional magnetic resonance flow analysis at 3 T: visualization of normal and pathological aortic vascular hemodynamics. *Journal of Computer Assisted Tomography*, 31(1), 9–15. <https://doi.org/10.1097/01.rct.0000232918.45158.c9>
- Garcia, D., Pibarot, P., Landry, C., Allard, A., Chayer, B., Dumesnil, J. G., & Durand, L.-G. (2004). Estimation of aortic valve effective orifice area by Doppler echocardiography: effects of valve inflow shape and flow rate. *Journal of the American Society of Echocardiography*, 17(7), 756–765. <https://doi.org/https://doi.org/10.1016/j.echo.2004.03.030>
- Glagov, S., Zarins, C., Giddens, D. P., & Ku, D. N. (1988). Hemodynamics and atherosclerosis. Insights and perspectives gained from studies of human arteries. *Archives of Pathology & Laboratory Medicine*, 112(10), 1018–1031.
- Gomes, B. A. . (2017). *Simulação in vitro do fluxo sanguíneo em modelo aórtico tridimensional de paciente submetido a implante valvar percutâneo*. Doctoral Thesis [in portuguese]. Universidade Federal do Rio de Janeiro.
- Gomes, B. A. de A., Camargo, G. C., dos Santos, J. R. L., Azevedo, L. F. A., Nieckele, Â. O., Siqueira-Filho, A. G., & de Oliveira, G. M. M. (2017). Influência do ângulo de Inclinação da prótese percutânea aórtica no campo de velocidade e estresse de cisalhamento. *Arquivos Brasileiros de Cardiologia*, 109(3), 231–240. <https://doi.org/10.5935/abc.20170115>
- Goody, P. R., Hosen, M. R., Christmann, D., Niepmann, S. T., Zietzer, A., Adam, M., Bönner, F., Zimmer, S., Nickenig, G., & Jansen, F. (2020). Aortic Valve Stenosis. *Arteriosclerosis, Thrombosis, and Vascular Biology*, 40(4), 885–900. <https://doi.org/10.1161/ATVBAHA.119.313067>
- Gülan, U., Calen, C., Duru, F., & Holzner, M. (2018). Blood flow patterns and pressure loss in the ascending aorta: A comparative study on physiological and aneurysmal conditions. *Journal of Biomechanics*, 76, 152–159. <https://doi.org/https://doi.org/10.1016/j.jbiomech.2018.05.033>
- Gy, V., GyP, S., & Szasz, O. (2016). Non-Newtonian analysis of blood-flow. *Journal*

- of Advances in Physics*, 11, 3470–3481.
- Ha, H., Kim, G. B., Kweon, J., Lee, S. J., Kim, Y.-H., Kim, N., & Yang, D. H. (2016). The influence of the aortic valve angle on the hemodynamic features of the thoracic aorta. *Scientific Reports*, 6, 32316. <https://doi.org/10.1038/srep32316>
- Hagan, P. G., Nienaber, C. A., Isselbacher, E. M., Bruckman, D., Karavite, D. J., Russman, P. L., Evangelista, A., Fattori, R., Suzuki, T., Oh, J. K., Moore, A. G., Malouf, J. F., Pape, L. A., Gaca, C., Sechtem, U., Lenferink, S., Deutsch, H. J., Diedrichs, H., Marcos y Robles, J., ... Eagle, K. A. (2000). The International Registry of Acute Aortic Dissection (IRAD): new insights into an old disease. *JAMA*, 283(7), 897–903. <https://doi.org/10.1001/jama.283.7.897>
- Hallett, J. W. (2009). *Comprehensive Vascular and Endovascular Surgery*. Mosby/Elsevier. <https://books.google.com.br/books?id=x4AmAFc50X0C>
- Hao, Q. (2010). Modeling of Flow in an In Vitro Aneurysm Model : A Fluid-Structure Interaction Approach. In *Open Acces Dissertation*. University of Miami.
- Harlow, F. H.; Nakayama, P. I. (1968). Transport of Turbulence Energy Decay Rate. *United States*. <https://doi.org/doi:10.2172/4556905>
- Hatle, L., Brubfile:///C:/Users/NOTE/Downloads/31326119.nbibakk, A., Tromsdal, A., & Angelsen, B. (1978). Noninvasive assessment of pressure drop in mitral stenosis by Doppler ultrasound. *British Heart Journal*, 40(2), 131–140. <https://doi.org/10.1136/hrt.40.2.131>
- He, X., Avril, S., & Lu, J. (2021). Estimating aortic thoracic aneurysm rupture risk using tension–strain data in physiological pressure range: an in vitro study. *Biomechanics and Modeling in Mechanobiology*, 20(2), 683–699. <https://doi.org/10.1007/s10237-020-01410-8>
- Hellmeier, F., Nordmeyer, S., Yevtushenko, P., Bruening, J., Berger, F., Kuehne, T., Goubergrits, L., & Kelm, M. (2018). Hemodynamic Evaluation of a Biological and Mechanical Aortic Valve Prosthesis Using Patient-Specific MRI-Based CFD. *Artificial Organs*, 42(1), 49–57. <https://doi.org/10.1111/aor.12955>
- Heys, J. J., Holyoak, N., Calleja, A. M., Belohlavek, M., & Chaliki, H. P. (2010). Revisiting the simplified bernoulli equation. *The Open Biomedical Engineering Journal*, 4, 123–128. <https://doi.org/10.2174/1874120701004010123>
- Hoagland, P. M., Cook, E. F., Flatley, M., Walker, C., & Goldman, L. (1985). Case-control analysis of risk factors for presence of aortic stenosis in adults (age 50 years or older). *The American Journal of Cardiology*, 55(6), 744–747. [https://doi.org/10.1016/0002-9149\(85\)90149-3](https://doi.org/10.1016/0002-9149(85)90149-3)

- Homan, Travis D.; Bordes, Stephen J.; Cichowski, E. (2012). *Physiology, Pulse Pressure*. Treasure Island (FL): StatPearls Publishing.
- Hope, M. D., Hope, T. A., Crook, S. E. S., Ordovas, K. G., Urbania, T. H., Alley, M. T., & Higgins, C. B. (2011). 4D flow CMR in assessment of valve-related ascending aortic disease. *JACC. Cardiovascular Imaging*, 4(7), 781–787. <https://doi.org/10.1016/j.jcmg.2011.05.004>
- Hope, T. A., Markl, M., Wigström, L., Alley, M. T., Miller, D. C., & Herfkens, R. J. (2007). Comparison of flow patterns in ascending aortic aneurysms and volunteers using four-dimensional magnetic resonance velocity mapping. *Journal of Magnetic Resonance Imaging*, 26(6), 1471–1479. <https://doi.org/https://doi.org/10.1002/jmri.21082>
- Ibanez, I., de Azevedo Gomes, B. A., & Nieckele, A. O. (2021). Effect of percutaneous aortic valve position on stress map in ascending aorta: A fluid-structure interaction analysis. *Artificial Organs*, 45(7), O195–O206. <https://doi.org/10.1111/aor.13883>
- Ibanez, I. F. (2019). *Estudo numérico da influência da inclinação da prótese valvar aórtica no fluxo sanguíneo em aorta ascendente*. Pontifícia Universidade Católica do Rio de Janeiro.
- Ibanez, I. F., de Azevedo Gomes, B. A., & Nieckele, A. O. (2020). Effect of percutaneous aortic valve position on stress map in ascending aorta: A fluid-structure interaction analysis. In *Artificial Organs*. <https://doi.org/10.1111/aor.13883>
- Isselbacher, E. M. (2005). Thoracic and Abdominal Aortic Aneurysms. *Circulation*, 111(6), 816–828. <https://doi.org/10.1161/01.CIR.0000154569.08857.7A>
- Isselbacher, E. M., Preventza, O., III, J. H. B., Augoustides, J. G., Beck, A. W., Bolen, M. A., Braverman, A. C., Bray, B. E., Brown-Zimmerman, M. M., Chen, E. P., Collins, T. J., DeAnda, A., Fanola, C. L., Girardi, L. N., Hicks, C. W., Hui, D. S., Jones, W. S., Kalahasti, V., Kim, K. M., ... Woo, Y. J. (2022). 2022 ACC/AHA Guideline for the Diagnosis and Management of Aortic Disease. *Journal of the American College of Cardiology*, 80(24), e223–e393. <https://doi.org/10.1016/j.jacc.2022.08.004>
- Itatani, K., Miyazaki, S., Furusawa, T., Numata, S., Yamazaki, S., Morimoto, K., Makino, R., Morichi, H., Nishino, T., & Yaku, H. (2017). New imaging tools in cardiovascular medicine: computational fluid dynamics and 4D flow MRI. *General Thoracic and Cardiovascular Surgery*, 65(11), 611–621. <https://doi.org/10.1007/s11748-017-0834-5>
- Jayendiran, R., Condemi, F., Campisi, S., Viallon, M., Croisille, P., & Avril, S.

- (2020). Computational prediction of hemodynamical and biomechanical alterations induced by aneurysm dilatation in patient-specific ascending thoracic aortas. *International Journal for Numerical Methods in Biomedical Engineering*, 36(6), e3326. <https://doi.org/10.1002/cnm.3326>
- Johnston, B. M., Johnston, P. R., Corney, S., & Kilpatrick, D. (2006). Non-Newtonian blood flow in human right coronary arteries: Transient simulations. *Journal of Biomechanics*, 39(6), 1116–1128. <https://doi.org/https://doi.org/10.1016/j.jbiomech.2005.01.034>
- Jones, W. P., & Launder, B. E. (1972). The prediction of laminarization with a two-equation model of turbulence. *International Journal of Heat and Mass Transfer*, 15(2), 301–314. [https://doi.org/https://doi.org/10.1016/0017-9310\(72\)90076-2](https://doi.org/https://doi.org/10.1016/0017-9310(72)90076-2)
- Kalpakli Vester, A., Örlü, R., & Alfredsson, P. H. (2016). Turbulent Flows in Curved Pipes: Recent Advances in Experiments and Simulations. *Applied Mechanics Reviews*, 68(5). <https://doi.org/10.1115/1.4034135>
- Kato, K., Oguri, M., Kato, N., Hibino, T., Yajima, K., Yoshida, T., Metoki, N., Yoshida, H., Satoh, K., Watanabe, S., Yokoi, K., Murohara, T., & Yamada, Y. (2008). Assessment of genetic risk factors for thoracic aortic aneurysm in hypertensive patients. *American Journal of Hypertension*, 21(9), 1023–1027. <https://doi.org/10.1038/ajh.2008.229>
- Kauhanen, S. P., Liimatainen, T., Kariniemi, E., Korhonen, M., Parkkonen, J., Vienonen, J., Vanninen, R., & Hedman, M. (2020). A smaller heart-aorta-angle associates with ascending aortic dilatation and increases wall shear stress. *European Radiology*, 30(9), 5149–5157. <https://doi.org/10.1007/s00330-020-06852-3>
- Kharawala, A., Barzallo, D., Thankachen, J., & Thachil, R. (2023). Ascending Aortic Aneurysm in an Asymptomatic Young Woman Without Risk Factors. *CASE*. <https://doi.org/10.1016/j.case.2022.11.005>
- Kimura, N., Nakamura, M., Komiya, K., Nishi, S., Yamaguchi, A., Tanaka, O., Misawa, Y., Adachi, H., & Kawahito, K. (2017). Patient-specific assessment of hemodynamics by computational fluid dynamics in patients with bicuspid aortopathy. *The Journal of Thoracic and Cardiovascular Surgery*, 153(4), S52-S62.e3. <https://doi.org/10.1016/j.jtcvs.2016.12.033>
- Kousera, C. A., Wood, N. B., Seed, W. A., Torii, R., O'Regan, D., & Xu, X. Y. (2013). A numerical study of aortic flow stability and comparison with in vivo flow measurements. *Journal of Biomechanical Engineering*, 135(1), 11003. <https://doi.org/10.1115/1.4023132>

- Krams, R., Wentzel, J. J., Oomen, J. A., Vinke, R., Schuurbijs, J. C., de Feyter, P. J., Serruys, P. W., & Slager, C. J. (1997). Evaluation of endothelial shear stress and 3D geometry as factors determining the development of atherosclerosis and remodeling in human coronary arteries in vivo. Combining 3D reconstruction from angiography and IVUS (ANGUS) with computational fluid dyn. *Arteriosclerosis, Thrombosis, and Vascular Biology*, *17*(10), 2061–2065. <https://doi.org/10.1161/01.atv.17.10.2061>
- Krittian, S. B. S., Lamata, P., Michler, C., Nordsletten, D. A., Bock, J., Bradley, C. P., Pitcher, A., Kilner, P. J., Markl, M., & Smith, N. P. (2012). A finite-element approach to the direct computation of relative cardiovascular pressure from time-resolved MR velocity data. *Medical Image Analysis*, *16*(5), 1029–1037. <https://doi.org/https://doi.org/10.1016/j.media.2012.04.003>
- Ku, D. N., Giddens, D. P., Zarins, C. K., & Glagov, S. (1985). Pulsatile flow and atherosclerosis in the human carotid bifurcation. Positive correlation between plaque location and low oscillating shear stress. *Arteriosclerosis (Dallas, Tex.)*, *5*(3), 293–302. <https://doi.org/10.1161/01.atv.5.3.293>
- Kuusisto, J., Räsänen, K., Särkioja, T., Alarakkola, E., & Kosma, V.-M. (2005). Atherosclerosis-like lesions of the aortic valve are common in adults of all ages: a necropsy study. *Heart*, *91*(5), 576–582. <https://doi.org/10.1136/HRT.2004.036848>
- Kuzmik, G. A., Sang, A. X., & Elefteriades, J. A. (2012). Natural history of thoracic aortic aneurysms. *Journal of Vascular Surgery*, *56*(2), 565–571. <https://doi.org/10.1016/j.jvs.2012.04.053>
- Landenhed, M., Engström, G., Gottsäter, A., Caulfield, M. P., Hedblad, B., Newton-Cheh, C., Melander, O., & Smith, J. G. (2015). Risk profiles for aortic dissection and ruptured or surgically treated aneurysms: a prospective cohort study. *Journal of the American Heart Association*, *4*(1), e001513. <https://doi.org/10.1161/JAHA.114.001513>
- Larsson, S. C., Wolk, A., & Bäck, M. (2019). Dietary patterns, food groups, and incidence of aortic valve stenosis: A prospective cohort study. *International Journal of Cardiology*, *283*, 184–188. <https://doi.org/https://doi.org/10.1016/j.ijcard.2018.11.007>
- Lavall, D., Schäfers, H.-J., Böhm, M., & Laufs, U. (2012). Aneurysms of the ascending aorta. *Deutsches Arzteblatt International*, *109*(13), 227–233. <https://doi.org/10.3238/arztebl.2012.0227>
- Lederle, F. A., Johnson, G. R., Wilson, S. E., Chute, E. P., Hye, R. J., Makaroun, M. S., Barone, G. W., Bandyk, D., Moneta, G. L., & Makhoul, R. G. (2000).

- The aneurysm detection and management study screening program: validation cohort and final results. Aneurysm Detection and Management Veterans Affairs Cooperative Study Investigators. *Archives of Internal Medicine*, 160(10), 1425–1430. <https://doi.org/10.1001/archinte.160.10.1425>
- Lee, B.-K. (2011). Computational Fluid Dynamics in Cardiovascular Disease. *Kcj*, 41(8), 423–430. <https://doi.org/10.4070/kcj.2011.41.8.423>
- Lee, C.-A., & Paeng, D.-G. (2021). Numerical simulation of spatiotemporal red blood cell aggregation under sinusoidal pulsatile flow. *Scientific Reports*, 11(1), 9977. <https://doi.org/10.1038/s41598-021-89286-1>
- Lei, H., Fedosov, D. A., Caswell, B., & Karniadakis, G. E. (2013). Blood flow in small tubes: quantifying the transition to the non-continuum regime. *Journal of Fluid Mechanics*, 722. <https://doi.org/10.1017/jfm.2013.91>
- Lerman, D. A., Prasad, S., & Alotti, N. (2015). Calcific Aortic Valve Disease: Molecular Mechanisms and Therapeutic Approaches. *European Cardiology*, 10(2), 108–112. <https://doi.org/10.15420/ecr.2015.10.2.108>
- Li, J. K.-J. (2000). Physiology and Rheology of Arteries. In *The Arterial Circulation: Physical Principles and Clinical Applications* (pp. 13–32). Humana Press. https://doi.org/10.1007/978-1-59259-034-6_2
- Lindman, B. R., Bonow, R. O., & Otto, C. M. (2013). Current management of calcific aortic stenosis. *Circulation Research*, 113(2), 223–237. <https://doi.org/10.1161/CIRCRESAHA.111.300084>
- Lo, E. W. C., Menezes, L. J., & Torii, R. (2019). Impact of Inflow Boundary Conditions on the Calculation of CT-Based FFR. *Fluids*, 4(2). <https://doi.org/10.3390/fluids4020060>
- Long, D. S., Smith, M. L., Pries, A. R., Ley, K., & Damiano, E. R. (2004). Microviscometry reveals reduced blood viscosity and altered shear rate and shear stress profiles in microvessels after hemodilution. *Proceedings of the National Academy of Sciences of the United States of America*, 101(27), 10060–10065.
- Lotz, J., Meier, C., Leppert, A., & Galanski, M. (2002). Cardiovascular Flow Measurement with Phase-Contrast MR Imaging: Basic Facts and Implementation. *RadioGraphics*, 22(3), 651–671. <https://doi.org/10.1148/radiographics.22.3.g02ma11651>
- Malvindi, P. G., Pasta, S., Raffa, G. M., & Livesey, S. (2016). Computational fluid dynamics of the ascending aorta before the onset of type A aortic dissection. *European Journal of Cardio-Thoracic Surgery: Official Journal of the European Association for Cardio-Thoracic Surgery*, 51(3), 597–599.

- <https://doi.org/10.1093/ejcts/ezw306>
- Manchester, E. L., Pirola, S., Salmasi, M. Y., O'Regan, D. P., Athanasiou, T., & Xu, X. Y. (2021). Analysis of Turbulence Effects in a Patient-Specific Aorta with Aortic Valve Stenosis. *Cardiovascular Engineering and Technology*, 12(4), 438–453. <https://doi.org/10.1007/s13239-021-00536-9>
- Marieb, E. N., & Hoehn, K. (2018). *Human Anatomy & Physiology*. Pearson Education, Incorporated. <https://books.google.com.br/books?id=6MrdswEACAAJ>
- Marinov, G., Guidoin, R., Tse, L. W., Ruthrauff, A. A., Yao, T., & King, M. W. (2013). 21 - Endovascular prostheses for aortic aneurysms: a new era for vascular surgery. In M. W. King, B. S. Gupta, & R. B. T.-B. as M. I. Guidoin (Eds.), *Woodhead Publishing Series in Textiles* (pp. 640–675). Woodhead Publishing. <https://doi.org/https://doi.org/10.1533/9780857095602.2.640>
- Mendelson, K., & Schoen, F. J. (2006). Heart valve tissue engineering: concepts, approaches, progress, and challenges. *Annals of Biomedical Engineering*, 34(12), 1799–1819. <https://doi.org/10.1007/s10439-006-9163-z>
- Meng, H., Tutino, V. M., Xiang, J., & Siddiqui, A. (2014). High WSS or low WSS? Complex interactions of hemodynamics with intracranial aneurysm initiation, growth, and rupture: toward a unifying hypothesis. *AJNR. American Journal of Neuroradiology*, 35(7), 1254–1262. <https://doi.org/10.3174/ajnr.A3558>
- Menter, F. R. (1994). Two-equation eddy-viscosity turbulence models for engineering applications. *AIAA Journal*, 32(8), 1598–1605.
- Menter, F. R., Langtry, R. B., Likki, S. R., Suzen, Y. B., Huang, P. G., & Voelker, S. (2004). *A Correlation-Based Transition Model Using Local Variables: Part I — Model Formulation. Volume 4*, 57–67. <https://doi.org/10.1115/GT2004-53452>
- Messika-Zeitoun, D., Bielak, L. F., Peyser, P. A., Sheedy, P. F., Turner, S. T., Nkomo, V. T., Breen, J. F., Maalouf, J., Scott, C., Tajik, A. J., & Enriquez-Sarano, M. (2007). Aortic Valve Calcification. *Arteriosclerosis, Thrombosis, and Vascular Biology*, 27(3), 642–648. <https://doi.org/10.1161/01.ATV.0000255952.47980.c2>
- Milner, J. S., Moore, J. A., Rutt, B. K., & Steinman, D. A. (1998). Hemodynamics of human carotid artery bifurcations: Computational studies with models reconstructed from magnetic resonance imaging of normal subjects. *Journal of Vascular Surgery*, 28(1), 143–156. [https://doi.org/https://doi.org/10.1016/S0741-5214\(98\)70210-1](https://doi.org/https://doi.org/10.1016/S0741-5214(98)70210-1)
- Miyazaki, S., Itatani, K., Furusawa, T., Nishino, T., Sugiyama, M., Takehara, Y., & Yasukochi, S. (2017). Validation of numerical simulation methods in aortic

- arch using 4D Flow MRI. *Heart and Vessels*, 32(8), 1032–1044.
<https://doi.org/10.1007/s00380-017-0979-2>
- Mogensen, M. L. (2011). *A Physiological Mathematical Model of the Respiratory System Mads Lause Mogensen* (Issue October). Aalborg University.
- Mohler, E. R., Sheridan, M. J., Nichols, R., Harvey, W. P., & Waller, B. F. (1991). Development and progression of aortic valve stenosis: atherosclerosis risk factors--a causal relationship? A clinical morphologic study. *Clinical Cardiology*, 14(12), 995–999. <https://doi.org/10.1002/clc.4960141210>
- Morbiducci, U., Ponzini, R., Gallo, D., Bignardi, C., & Rizzo, G. (2013). Inflow boundary conditions for image-based computational hemodynamics: Impact of idealized versus measured velocity profiles in the human aorta. *Journal of Biomechanics*, 46(1), 102–109.
<https://doi.org/https://doi.org/10.1016/j.jbiomech.2012.10.012>
- Morganti, S. (2011). *Finite Element Analysis of Aortic Valve Surgery*. Università degli Studi di Pavia.
- Mynard, J. P., & Nithiarasu, P. (2008). A 1D arterial blood flow model incorporating ventricular pressure, aortic valve and regional coronary flow using the locally conservative Galerkin (LCG) method. *Communications in Numerical Methods in Engineering*, 24(5), 367–417.
<https://doi.org/https://doi.org/10.1002/cnm.1117>
- Nannini, G., Caimi, A., Palumbo, M. C., Saitta, S., Girardi, L. N., Gaudino, M., Roman, M. J., Weinsaft, J. W., & Redaelli, A. (2021). Aortic hemodynamics assessment prior and after valve sparing reconstruction: A patient-specific 4D flow-based FSI model. *Computers in Biology and Medicine*, 135, 104581.
<https://doi.org/10.1016/j.compbimed.2021.104581>
- Neal, M. L., & Kerckhoffs, R. (2009). Current progress in patient-specific modeling. *Briefings in Bioinformatics*, 11(1), 111–126.
<https://doi.org/10.1093/bib/bbp049>
- Nerem, R. M., & Seed, W. A. (1972). An in vivo study of aortic flow disturbances. *Cardiovascular Research*, 6(1), 1–14. <https://doi.org/10.1093/cvr/6.1.1>
- Nolte, D., Urbina, J., Sotelo, J., Sok, L., Montalba, C., Valverde, I., Osses, A., Uribe, S., & Bertoglio, C. (2021). Validation of 4D Flow based relative pressure maps in aortic flows. *Medical Image Analysis*, 74, 102195.
<https://doi.org/https://doi.org/10.1016/j.media.2021.102195>
- Oliveira, G. M. M. de, Brant, L. C. C., Polanczyk, C. A., Malta, D. C., Biolo, A., Nascimento, B. R., Souza, M. de F. M. de, Lorenzo, A. R. De, Júnior, A. A. de P. F., Schaan, B. D., Castilho, F. M. de, Cesena, F. H. Y., Soares, G. P.,

- Junior, G. F. X., Filho, J. A. S. B., Passaglia, L. G., Filho, M. M. P., Machline-Carrion, M. J., Bittencourt, M. S., ... Ribeiro, A. L. P. (2022). Estatística Cardiovascular – Brasil 2021. *Arquivos Brasileiros de Cardiologia*, 118(1), 115–373. <https://doi.org/10.36660/abc.20211012>
- Ong, C. W., Wee, I., Syn, N., Ng, S., Leo, H. L., Richards, A. M., & Choong, A. M. T. L. (2020). Computational Fluid Dynamics Modeling of Hemodynamic Parameters in the Human Diseased Aorta: A Systematic Review. *Annals of Vascular Surgery*, 63, 336–381. <https://doi.org/https://doi.org/10.1016/j.avsg.2019.04.032>
- Otto, C M, Kuusisto, J., Reichenbach, D. D., Gown, A. M., & O'Brien, K. D. (1994). Characterization of the early lesion of “degenerative” valvular aortic stenosis. Histological and immunohistochemical studies. *Circulation*, 90(2), 844–853. <https://doi.org/10.1161/01.CIR.90.2.844>
- Otto, Catherine M. (2008). Calcific aortic stenosis--time to look more closely at the valve. In *The New England journal of medicine* (Vol. 359, Issue 13, pp. 1395–1398). <https://doi.org/10.1056/NEJMe0807001>
- Otto, Catherine M, & Prendergast, B. (2014). Aortic-Valve Stenosis — From Patients at Risk to Severe Valve Obstruction. *New England Journal of Medicine*, 371(8), 744–756. <https://doi.org/10.1056/NEJMra1313875>
- Patankar, S. V. . (1980). *Numerical heat transfer and fluid flow*. Hemisphere Publishing Corporation.
- Patankar, S. V, Pratap, V. S., & Spalding, D. B. (1975). Prediction of turbulent flow in curved pipes. *Journal of Fluid Mechanics*, 67(3), 583–595. <https://doi.org/10.1017/S0022112075000481>
- Pelc, N. J., Bernstein, M. A., Shimakawa, A., & Glover, G. H. (1991). Encoding strategies for three-direction phase-contrast MR imaging of flow. *Journal of Magnetic Resonance Imaging*, 1(4), 405–413. <https://doi.org/https://doi.org/10.1002/jmri.1880010404>
- Pendergraft, B. (2016). *The Effects of Smoking on the Calcification of the Aortic Valve The Effects of Smoking on the Calcification of the Aortic Valve An Honors Thesis submitted in partial fulfillment of the requirements for Honors Studies in Biology Brittany Pendergraft By J .* Doctoral Thesis. University of Arkansas.
- Pirola, S, Jarral, O. A., O'Regan, D. P., Asimakopoulos, G., Anderson, J. R., Pepper, J. R., Athanasiou, T., & Xu, X. Y. (2018). Computational study of aortic hemodynamics for patients with an abnormal aortic valve: The importance of secondary flow at the ascending aorta inlet. *APL*

- Bioengineering*, 2(2). <https://doi.org/10.1063/1.5011960>
- Pirola, Selene, Guo, B., Menichini, C., Saitta, S., Fu, W., Dong, Z., & Xu, X. Y. (2019). 4-D Flow MRI-Based Computational Analysis of Blood Flow in Patient-Specific Aortic Dissection. *IEEE Transactions on Bio-Medical Engineering*, 66(12), 3411–3419. <https://doi.org/10.1109/TBME.2019.2904885>
- Pope, S. B. . (2000). *Turbulent Flows* (C. U. Press (ed.)).
- Pujari, S., & Agasthi, P. (2023). *Aortic Stenosis*. StatPearls [Internet]. <https://www.ncbi.nlm.nih.gov/books/NBK557628/%0A>
- Raghavan, M. L., Vorp, D. A., Federle, M. P., Makaroun, M. S., & Webster, M. W. (2000). Wall stress distribution on three-dimensionally reconstructed models of human abdominal aortic aneurysm. *Journal of Vascular Surgery*, 31(4), 760–769. <https://doi.org/https://doi.org/10.1067/mva.2000.103971>
- Rahmani, S., Li, D., Mao, S. S., Gao, Y., Nakanishi, R., Nezarat, N., Ceponiene, I., Osawa, K., Kanisawa, M., & Budoff, M. (2016). Abstract 18512: Normal Reference Values of Thoracic Aortic Diameter Using Cardiac CT in the Multi-Ethnic Study of Atherosclerosis (MESA). *Circulation*, 134(suppl_1), A18512–A18512. https://doi.org/10.1161/circ.134.suppl_1.18512
- Rajendran, P., Rengarajan, T., Thangavel, J., Nishigaki, Y., Sakthisekaran, D., Sethi, G., & Nishigaki, I. (2013). The vascular endothelium and human diseases. *International Journal of Biological Sciences*, 9(10), 1057–1069. <https://doi.org/10.7150/ijbs.7502>
- Ramaekers, M. J. F. G., Westenberg, J. J. M., Adriaans, B. P., Nijssen, E. C., Wildberger, J. E., Lamb, H. J., & Schalla, S. (2023). A clinician’s guide to understanding aortic 4D flow MRI. *Insights into Imaging*, 14(1), 114. <https://doi.org/10.1186/s13244-023-01458-x>
- Ramlawi, B., Ramchandani, M., & Reardon, M. J. (2014). Surgical Approaches to Aortic Valve Replacement and Repair-Insights and Challenges. *Interventional Cardiology (London, England)*, 9(1), 32–36. <https://doi.org/10.15420/icr.2011.9.1.32>
- Randles, A., Frakes, D. H., & Leopold, J. A. (2017). Computational Fluid Dynamics and Additive Manufacturing to Diagnose and Treat Cardiovascular Disease. *Trends in Biotechnology*, 35(11), 1049–1061. <https://doi.org/https://doi.org/10.1016/j.tibtech.2017.08.008>
- Renapurkar, R. D., Setser, R. M., O’Donnell, T. P., Egger, J., Lieber, M. L., Desai, M. Y., Stillman, A. E., Schoenhagen, P., & Flamm, S. D. (2012). Aortic volume as an indicator of disease progression in patients with untreated infrarenal abdominal aneurysm. *European Journal of Radiology*, 81(2), e87–e93.

- <https://doi.org/https://doi.org/10.1016/j.ejrad.2011.01.077>
- Rengier, F., Delles, M., Eichhorn, J., Azad, Y.-J., von Tengg-Koblighk, H., Ley-Zaporozhan, J., Dillmann, R., Kauczor, H.-U., Unterhinninghofen, R., & Ley, S. (2014). Noninvasive pressure difference mapping derived from 4D flow MRI in patients with unrepaired and repaired aortic coarctation. *Cardiovascular Diagnosis and Therapy*, 4(2), 97–103. <https://doi.org/10.3978/j.issn.2223-3652.2014.03.03>
- Rinaudo, A., & Pasta, S. (2014). Regional variation of wall shear stress in ascending thoracic aortic aneurysms. *Proceedings of the Institution of Mechanical Engineers. Part H, Journal of Engineering in Medicine*, 228.
- Roache, P. J. (1994). Perspective: A Method for Uniform Reporting of Grid Refinement Studies. *Journal of Fluids Engineering*, 116(3), 405–413. <https://doi.org/10.1115/1.2910291>
- Rodkiewicz, C. M. (1983). Arteries and Arterial Blood Flow. In *Arteries and Arterial Blood Flow*. Springer-Verlag Wien GMBH. <https://doi.org/10.1007/978-3-7091-4342-1>
- Rodríguez-Palomares, J. F., Dux-Santoy, L., Guala, A., Kale, R., Maldonado, G., Teixidó-Turà, G., Galian, L., Huguet, M., Valente, F., Gutiérrez, L., González-Alujas, T., Johnson, K. M., Wieben, O., García-Dorado, D., & Evangelista, A. (2018). Aortic flow patterns and wall shear stress maps by 4D-flow cardiovascular magnetic resonance in the assessment of aortic dilatation in bicuspid aortic valve disease. *Journal of Cardiovascular Magnetic Resonance: Official Journal of the Society for Cardiovascular Magnetic Resonance*, 20(1), 28. <https://doi.org/10.1186/s12968-018-0451-1>
- Rose, M. J., Jarvis, K. B., Barker, A. J., Schnell, S., Allen, B. D., Robinson, J. D., Markl, M., & Rigsby, C. K. (2016). Evaluating the disease progression of pediatric bicuspid aortic valve patients using 4D flow MRI data. In *Journal of Cardiovascular Magnetic Resonance* (Vol. 18, Issue Suppl 1). <https://doi.org/10.1186/1532-429X-18-S1-P170>
- Rosencranz, R., & Bogen, S. A. (2006). Clinical laboratory measurement of serum, plasma, and blood viscosity. *American Journal of Clinical Pathology*, 125 Suppl, S78-86. <https://doi.org/10.1309/FFF7U8RRPK26VAPY>
- Roth, G. A., Mensah, G. A., Johnson, C. O., Addolorato, G., Ammirati, E., Baddour, L. M., Barengo, N. C., Beaton, A. Z., Benjamin, E. J., Benziger, C. P., Bonny, A., Brauer, M., Brodmann, M., Cahill, T. J., Carapetis, J., Catapano, A. L., Chugh, S. S., Cooper, L. T., Coresh, J., ... Fuster, V. (2020). Global Burden of Cardiovascular Diseases and Risk Factors, 1990-2019: Update From the

- GBD 2019 Study. *Journal of the American College of Cardiology*, 76(25), 2982–3021. <https://doi.org/10.1016/j.jacc.2020.11.010>
- Saitta, S., Pirola, S., Piatti, F., Votta, E., Lucherini, F., Pluchinotta, F., Carminati, M., Lombardi, M., Geppert, C., Cuomo, F., Figueroa, C. A., Xu, X. Y., & Redaelli, A. (2019). Evaluation of 4D flow MRI-based non-invasive pressure assessment in aortic coarctations. *Journal of Biomechanics*, 94, 13–21. <https://doi.org/10.1016/j.jbiomech.2019.07.004>
- Saliba, E., Sia, Y., Dore, A., & El Hamamsy, I. (2015). The ascending aortic aneurysm: When to intervene? *IJC Heart & Vasculature*, 6, 91–100. <https://doi.org/https://doi.org/10.1016/j.ijcha.2015.01.009>
- Sallam, A. M., & Hwang, N. H. (1984). Human red blood cell hemolysis in a turbulent shear flow: contribution of Reynolds shear stresses. *Biorheology*, 21(6), 783–797. <https://doi.org/10.3233/bir-1984-21605>
- Salmasi, M. Y., Pirola, S., Mahuttanatan, S., Fisichella, S. M., Sengupta, S., Jarral, O. A., Oo, A., O'Regan, D., Xu, X. Y., & Athanasiou, T. (2021). Geometry and flow in ascending aortic aneurysms are influenced by left ventricular outflow tract orientation: Detecting increased wall shear stress on the outer curve of proximal aortic aneurysms. *The Journal of Thoracic and Cardiovascular Surgery*. <https://doi.org/10.1016/j.jtcvs.2021.06.014>
- Saremi, Farhood; Achenbach, Stephan; Arbustini, Eloisa; Narula, J. (2010). *Revisiting Cardiac Anatomy: A Computed-Tomography-Based Atlas and Reference* (Wiley-Blackwell. (ed.); Vol. 4, Issue 1). <https://doi.org/https://doi.org/10.1002/9781444323191>
- Schindelin, J., Arganda-Carreras, I., Frise, E., Kaynig, V., Longair, M., Pietzsch, T., Preibisch, S., Rueden, C., Saalfeld, S., Schmid, B., Tinevez, J.-Y., White, D. J., Hartenstein, V., Eliceiri, K., Tomancak, P., & Cardona, A. (2012). Fiji: an open-source platform for biological-image analysis. *Nature Methods*, 9(7), 676–682. <https://doi.org/10.1038/nmeth.2019>
- Sengupta, S., Yuan, X., Maga, L., Pirola, S., Nienaber, C. A., & Xu, X. Y. (2023). Aortic haemodynamics and wall stress analysis following arch aneurysm repair using a single-branched endograft. *Frontiers in Cardiovascular Medicine*, 10. <https://doi.org/10.3389/fcvm.2023.1125110>
- Sharma, J. (2015). *HEALTH, WELLNESS, FITNESS AND HEALTHY LIFESTYLES*. Horizon Books (A Division of Ignited Minds Edutech P Ltd). <https://books.google.com.br/books?id=T-IIDwAAQBAJ>
- Shi, Y., Valverde, I., Lawford, P. V, Beerbaum, P., & Hose, D. R. (2019). Patient-specific non-invasive estimation of pressure gradient across aortic

- coarctation using magnetic resonance imaging. *Journal of Cardiology*, *73*(6), 544–552. <https://doi.org/10.1016/j.jjcc.2018.12.016>
- Silva, I. A., Corso, R. B., Santos, M. V. N., Souza, H. J. B. de, & Pina, G. K. S. (2019). First Two Brazilian Cases: Correction of Ascending Aortic Aneurysm and Aortic Valve Stenosis with Sutureless/Rapid Deployment Aortic Prosthesis. *Brazilian Journal of Cardiovascular Surgery*, *34*(3), 366–367. <https://doi.org/10.21470/1678-9741-2018-0148>
- Simão, M., Ferreira, J., Tomás, A. C., Fragata, J., & Ramos, H. (2017). Aorta Ascending Aneurysm Analysis Using CFD Models towards Possible Anomalies. *Fluids*, *2*(2). <https://doi.org/10.3390/fluids2020031>
- Snabre, P., Bitbol, M., & Mills, P. (1987). Cell disaggregation behavior in shear flow. *Biophysical Journal*, *51*(5), 795–807. [https://doi.org/https://doi.org/10.1016/S0006-3495\(87\)83406-9](https://doi.org/https://doi.org/10.1016/S0006-3495(87)83406-9)
- Sochi, T. (2013). Non-Newtonian Rheology in Blood Circulation. *ArXiv*, 1–26. <http://arxiv.org/abs/1306.2067>
- Soudah, E., Casacuberta, J., Gamez-Montero, P. J., Pérez, J. S., Rodríguez-Cancio, M., Raush, G., Li, C. H., Carreras, F., & Castilla, R. (2017). Estimation of wall shear stress using 4d flow cardiovascular mri and computational fluid dynamics. *Journal of Mechanics in Medicine and Biology*, *17*(03), 1750046. <https://doi.org/10.1142/S0219519417500464>
- Spartalis, E., Spartalis, M., Athanasiou, A., Paschou, S. A., Patelis, N., Voudris, V., & Iliopoulos, D. C. (2020). Endothelium in Aortic Aneurysm Disease: New Insights. *Current Medicinal Chemistry*, *27*(7), 1081–1088. <https://doi.org/10.2174/0929867326666190923151959>
- Sporschill, G. (2021). *Improved Reynolds-Stress Modeling for Adverse-Pressure-Gradient Turbulent Boundary Layers in Industrial Aeronautical Flow*. Doctoral Thesis. Université de Pau et des Pays de l'Adour.
- Sripathi, V. C., Kumar, R. K., & Balakrishnan, K. R. (2004). Further insights into normal aortic valve function: role of a compliant aortic root on leaflet opening and valve orifice area. *The Annals of Thoracic Surgery*, *77*(3), 844–851. [https://doi.org/https://doi.org/10.1016/S0003-4975\(03\)01518-2](https://doi.org/https://doi.org/10.1016/S0003-4975(03)01518-2)
- Stalder, A. F., Russe, M. F., Frydrychowicz, A., Bock, J., Hennig, J., & Markl, M. (2008). Quantitative 2D and 3D phase contrast MRI: optimized analysis of blood flow and vessel wall parameters. *Magnetic Resonance in Medicine*, *60*(5), 1218–1231. <https://doi.org/10.1002/mrm.21778>
- Stokes, C, Ahmed, D., Lind, N., Haupt, F., Becker, D., Hamilton, J., Muthurangu, V., von Tengg-Kobligh, H., Papadakis, G., Balabani, S., & Díaz-Zuccarini, V.

- (2023). Aneurysmal growth in type-B aortic dissection: assessing the impact of patient-specific inlet conditions on key haemodynamic indices. *Journal of the Royal Society, Interface*, 20(206), 20230281. <https://doi.org/10.1098/rsif.2023.0281>
- Stokes, Catriona, Bonfanti, M., Li, Z., Xiong, J., Chen, D., Balabani, S., & Díaz-Zuccarini, V. (2021). A novel MRI-based data fusion methodology for efficient, personalised, compliant simulations of aortic haemodynamics. *Journal of Biomechanics*, 129, 110793. <https://doi.org/https://doi.org/10.1016/j.jbiomech.2021.110793>
- Stoltz, J. F. (1985). Hemorheology: pathophysiological significance. *Acta Medica Portuguesa*, 6(7–8).
- Stuart, J., & Kenny, M. W. (1980). Blood rheology. *Journal of Clinical Pathology*, 33(5), 417–429. <https://doi.org/10.1136/jcp.33.5.417>
- Sun, L. (2014). *Role of hemodynamic shear stress abnormalities in calcific aortic valve disease* (Issue April) [University of Notre Dame]. <https://doi.org/https://doi.org/10.7274/fb494744f63>
- Swamee, P. (1993). Design of a Submarine Oil Pipeline. *Journal of Transportation Engineering-Asce - J TRANSP ENG-ASCE*, 119. [https://doi.org/10.1061/\(ASCE\)0733-947X\(1993\)119:1\(159\)](https://doi.org/10.1061/(ASCE)0733-947X(1993)119:1(159))
- Takahashi, K., Sekine, T., Ando, T., Ishii, Y., & Kumita, S. (2022). Utility of 4D Flow MRI in Thoracic Aortic Diseases: A Literature Review of Clinical Applications and Current Evidence. *Magnetic Resonance in Medical Sciences : MRMS : An Official Journal of Japan Society of Magnetic Resonance in Medicine*, 21(2), 327–339. <https://doi.org/10.2463/mrms.rev.2021-0046>
- Takehara, Y. (2022). Clinical Application of 4D Flow MR Imaging for the Abdominal Aorta. *Magnetic Resonance in Medical Sciences : MRMS : An Official Journal of Japan Society of Magnetic Resonance in Medicine*, 21(2), 354–364. <https://doi.org/10.2463/mrms.rev.2021-0156>
- Tan, F. P. P., Borghi, A., Mohiaddin, R. H., Wood, N. B., Thom, S., & Xu, X. Y. (2009a). Analysis of flow patterns in a patient-specific thoracic aortic aneurysm model. *Computers & Structures*, 87(11), 680–690. <https://doi.org/https://doi.org/10.1016/j.compstruc.2008.09.007>
- Tan, F. P. P., Torii, R., Borghi, A., Mohiaddin, R. H., Wood, N. B., & Xu, X. Y. (2009b). Fluid-Structure Interaction Analysis of Wall Stress and Flow Patterns in a Thoracic Aortic Aneurysm. *International Journal of Applied Mechanics*, 01(01), 179–199. <https://doi.org/10.1142/S1758825109000095>
- Tanyi, B. A., & Thatcher, R. W. (1996). Iterative Solution Of Incompressible Navier–

- Stokes Equations On The Meiko Computing Surface. *International Journal for Numerical Methods in Fluids*, 22(4), 225–240. [https://doi.org/https://doi.org/10.1002/\(SICI\)1097-0363\(19960229\)22:4<225::AID-FLD313>3.0.CO;2-8](https://doi.org/https://doi.org/10.1002/(SICI)1097-0363(19960229)22:4<225::AID-FLD313>3.0.CO;2-8)
- Taylor, C. A., Draney, M. T., Ku, J. P., Parker, D., Steele, B. N., Wang, K., & Zarins, C. K. (1999). Predictive medicine: computational techniques in therapeutic decision-making. *Computer Aided Surgery: Official Journal of the International Society for Computer Aided Surgery*, 4(5), 231–247. [https://doi.org/10.1002/\(SICI\)1097-0150\(1999\)4:5<231::AID-IGS1>3.0.CO;2-Z](https://doi.org/10.1002/(SICI)1097-0150(1999)4:5<231::AID-IGS1>3.0.CO;2-Z)
- Taylor, C. A., & Figueroa, C. A. (2009). Patient-Specific Modeling of Cardiovascular Mechanics. *Annual Review of Biomedical Engineering*, 11(1), 109–134. <https://doi.org/10.1146/annurev.bioeng.10.061807.160521>
- Thubrikar, M. (2011). *The Aortic Valve* (1st ed.). Routledge. <https://doi.org/https://doi.org/10.4324/9780203737163>
- Ueda, T., Suito, H., Ota, H., & Takase, K. (2018). Computational Fluid Dynamics Modeling in Aortic Diseases. *Cardiovasc Imaging Asia*, 2(2), 58–64. <https://doi.org/10.22468/cvia.2018.00073>
- Vitello, D. J., Ripper, R. M., Fettiplace, M. R., Weinberg, G. L., & Vitello, J. M. (2015). Blood Density Is Nearly Equal to Water Density: A Validation Study of the Gravimetric Method of Measuring Intraoperative Blood Loss. *Journal of Veterinary Medicine*, 2015, 152730. <https://doi.org/10.1155/2015/152730>
- Walburn, F. J., & Schneck, D. J. (1976). A constitutive equation for whole human blood. *Biorheology*, 13(3), 201–210. <https://doi.org/10.3233/bir-1976-13307>
- Weigang, E., Kari, F. A., Beyersdorf, F., Luehr, M., Etz, C. D., Frydrychowicz, A., Harloff, A., & Markl, M. (2008). Flow-sensitive four-dimensional magnetic resonance imaging: flow patterns in ascending aortic aneurysms. *European Journal of Cardio-Thoracic Surgery: Official Journal of the European Association for Cardio-Thoracic Surgery*, 34(1), 11–16. <https://doi.org/10.1016/j.ejcts.2008.03.047>
- Weininger, G., Mori, M., Yousef, S., Hur, D. J., Assi, R., Geirsson, A., & Vallabhajosyula, P. (2022). Growth rate of ascending thoracic aortic aneurysms in a non-referral-based population. *Journal of Cardiothoracic Surgery*, 17(1), 14. <https://doi.org/10.1186/s13019-022-01761-6>
- Westerhof, N., Bosman, F., De Vries, C. J., & Noordergraaf, A. (1969). Analog studies of the human systemic arterial tree. *Journal of Biomechanics*, 2(2), 121–143. [https://doi.org/10.1016/0021-9290\(69\)90024-4](https://doi.org/10.1016/0021-9290(69)90024-4)

- Westerhof, Nico, Lankhaar, J.-W., & Westerhof, B. E. (2009). The arterial Windkessel. *Medical & Biological Engineering & Computing*, *47*(2), 131–141. <https://doi.org/10.1007/s11517-008-0359-2>
- Wigström, L., Sjöqvist, L., & Wranne, B. (1996). Temporally resolved 3D phase-contrast imaging. *Magnetic Resonance in Medicine*, *36*(5), 800–803. <https://doi.org/https://doi.org/10.1002/mrm.1910360521>
- Wilcox, D. C. (1988). Reassessment of the scale-determining equation for advanced turbulence models. *AIAA Journal*, *26*(11), 1299–1310. <https://doi.org/10.2514/3.10041>
- Wootton, D. M., & Ku, D. N. (1999). Fluid mechanics of vascular systems, diseases, and thrombosis. *Annual Review of Biomedical Engineering*, *1*, 299–329. <https://doi.org/10.1146/annurev.bioeng.1.1.299>
- Xiao, M., Wu, J., Chen, D., Wang, C., Wu, Y., Sun, T., & Chen, J. (2023). Ascending aortic volume: A feasible indicator for ascending aortic aneurysm elective surgery? *Acta Biomaterialia*, *167*, 100–108. <https://doi.org/https://doi.org/10.1016/j.actbio.2023.06.026>
- Yamaura, Y., Watanabe, N., Shimaya, M., Tomita, Y., Fukaya, T., & Yoshida, K. (2023). Impact of Cumulative Smoking Exposure on Subclinical Degenerative Aortic Valve Disease in Apparently Healthy Male Workers. *Circulation: Cardiovascular Imaging*, *12*(8), e008901. <https://doi.org/10.1161/CIRCIMAGING.119.008901>
- Yan, A. T., Koh, M., Chan, K. K., Guo, H., Alter, D. A., Austin, P. C., Tu, J. V., Wijeyesundera, H. C., & Ko, D. T. (2017). Association Between Cardiovascular Risk Factors and Aortic Stenosis: The CANHEART Aortic Stenosis Study. *Journal of the American College of Cardiology*, *69*(12), 1523–1532. <https://doi.org/10.1016/j.jacc.2017.01.025>
- Yearwood T L; Misbach G A; Chandran K B; (1989). Experimental fluid dynamics of aortic stenosis in a model of the human aorta. *Clinical Physics and Physiological Measurement*, *10*(1), 11. <https://doi.org/10.1088/0143-0815/10/1/002>
- Yoganathan, A. P., Cape, E. G., Sung, H. W., Williams, F. P., & Jimoh, A. (1988). Review of hydrodynamic principles for the cardiologist: Applications to the study of blood flow and jets by imaging techniques. *Journal of the American College of Cardiology*, *12*(5), 1344–1353. [https://doi.org/10.1016/0735-1097\(88\)92620-4](https://doi.org/10.1016/0735-1097(88)92620-4)
- Youssefi, P., Gomez, A., He, T., Anderson, L., Bunce, N., Sharma, R., Figueroa, C. A., & Jahangiri, M. (2017). Patient-specific computational fluid dynamics-

assessment of aortic hemodynamics in a spectrum of aortic valve pathologies. *The Journal of Thoracic and Cardiovascular Surgery*, 153(1), 8-20.e3. <https://doi.org/10.1016/j.jtcvs.2016.09.040>

A1. Intermittency Transition Model

The turbulent eddy viscosity for the Intermittency Transition $\kappa - \omega$ SST model (Menter et al., 2004) is given by

$$\mu_t = \frac{\rho \kappa}{\omega} \xi \quad (\text{A1.1})$$

where ξ is the blending factor between $\kappa - \varepsilon$ and $\kappa - \omega$ models.

The blending factor is defined as

$$\xi = \frac{1}{\max(1/\alpha^*, S F_2/(a_1 \omega))} \quad (\text{A1.2})$$

where S is the magnitude of the strain rate tensor

$$S = \sqrt{2 S_{ij} S_{ij}} \quad (\text{A1.3})$$

and the empirical function α^* is

$$\alpha^* = \alpha_\infty^* \left(\frac{\beta_i/3 + Re_t/Re_\kappa}{1 + Re_t/Re_\kappa} \right); \quad Re_t = \frac{\rho \kappa}{\mu \omega}; \quad \beta_i = F_1 \beta_{i,1} + (1 - F_1) \beta_{i,2} \quad (\text{A1.4})$$

F_1 and F_2 are damping factors, based on the wall distance y and are used to define which model to use. In this way,

$$F_1 = \tanh(\Phi_1^4); \quad \Phi_1 = \min \left\{ \max \left[\frac{\sqrt{\kappa}}{0.09 \omega y}, \frac{500 \mu}{\rho y^2 \omega}, \frac{4 \rho \kappa}{\sigma_{\omega,2} D_\omega^+ y^2} \right] \right\} \quad (\text{A1.5})$$

$$F_2 = \tanh(\Phi_2^4); \quad \Phi_2 = \max \left[\frac{2 \sqrt{\kappa}}{0.09 \omega y}, \frac{500 \mu}{\rho y^2 \omega} \right] \quad (\text{A1.6})$$

$$D_\omega^+ = \max \left[\frac{2 \rho}{\omega \sigma_{\omega,2}} \frac{\partial \kappa}{\partial x_j} \frac{\partial \omega}{\partial x_j}, 10^{-10} \right] \quad (\text{A1.7})$$

The empirical constants are default suggested by Ansys (2021): $\alpha_\infty^* = 1$; $Re_\kappa = 6$; $a_1 = 0.31$; $\beta_{i,1} = 0.075$; $\beta_{i,2} = 0.0828$; $\sigma_{\omega,2} = 1.168$.

To obtain κ and ω , the following conservation equations must be solved (Menter, 1994),

$$\frac{\partial \rho \kappa}{\partial t} + \frac{\partial \rho u_j \kappa}{\partial x_j} = \frac{\partial}{\partial x_j} \left[\left(\mu + \frac{\mu_t}{\sigma_\kappa} \right) \left(\frac{\partial \kappa}{\partial x_j} \right) \right] + G_\kappa - D_\kappa \quad (\text{A1.8})$$

$$\frac{\partial \rho \omega}{\partial t} + \frac{\partial \rho u_j \omega}{\partial x_j} = \frac{\partial}{\partial x_j} \left[\left(\mu + \frac{\mu_t}{\sigma_\omega} \right) \left(\frac{\partial \omega}{\partial x_j} \right) \right] + G_\omega - D_\omega + 2(1 - F_1) \frac{\rho \sigma_{\omega 2}}{\omega} \frac{\partial \kappa}{\partial x_j} \frac{\partial \omega}{\partial x_j} \quad (\text{A1.9})$$

The generation (G_κ and G_ω) and destruction (D_κ and D_ω) of κ and ω , for the Transition $\kappa - \omega$ SST model are given by

$$G_\kappa = \max(\gamma, \gamma_{sep}) \min(P_\kappa; 10 \rho \beta_i^* \omega \kappa) \quad ; \quad G_\omega = \frac{\rho \alpha}{\mu_t} P_\kappa \quad (\text{A1.10})$$

$$D_\kappa = \min(\max(\max(\gamma, \gamma_{sep}), 0.1), 1.0) \rho \beta_i^* \omega \kappa \quad ; \quad D_\omega = \rho \beta_i \omega^2 \quad (\text{A1.11})$$

where P_κ is defined as

$$P_\kappa = -\rho \overline{u_j' u_i'} \frac{\partial u_i}{\partial x_j} = \mu_t 2 S_{ij} \frac{\partial u_i}{\partial x_j} = \mu_t S^2 \quad (\text{A1.12})$$

with β_i^* and α defined as

$$\beta_i^* = \beta_\infty^* \left(\frac{4/15 + (Re_t/Re_\beta)^4}{1 + (Re_t/Re_\beta)^4} \right) \quad ; \quad \alpha = \frac{\alpha_\infty}{\alpha^*} \left(\frac{\alpha_0 + (Re_t/Re_\omega)}{1 + (Re_t/Re_\omega)} \right) \quad (\text{A1.13})$$

The blended parameters are the κ and ω Prandtl number ($\sigma_\kappa, \sigma_\omega$) and α_∞

$$\sigma_\kappa = [F_1/\sigma_{\kappa,1} + (1 - F_1)/\sigma_{\kappa,2}]^{-1} \quad ; \quad \sigma_\omega = [F_1/\sigma_{\omega,1} + (1 - F_1)/\sigma_{\omega,2}]^{-1} \quad (\text{A1.14})$$

$$\alpha_\infty = F_1 \alpha_{\infty,1} + (1 - F_1) \alpha_{\infty,2} \quad (\text{A1.15})$$

$$\alpha_{\infty,1} = \frac{\beta_{i,1}}{\beta_\infty^*} - \frac{k^2}{\sigma_{\omega,1} \sqrt{\beta_\infty^*}} \quad ; \quad \alpha_{\infty,2} = \frac{\beta_{i,2}}{\beta_\infty^*} - \frac{k^2}{\sigma_{\omega,2} \sqrt{\beta_\infty^*}} \quad (\text{A1.16})$$

where $Re_\beta = 8$; $Re_\omega = 2.95$; $\alpha_0 = \frac{1}{9}$; $\sigma_{\kappa,1} = 1.176$; $\sigma_{\kappa,2} = 1.0$; $\sigma_{\omega,1} = 2.0$; $\sigma_{\omega,2} = 1.168$; $\beta_\infty^* = 0.09$; $k = 0.41$ (Ansys, 2021).

The flow intermittency γ , in Eqs. A1.10 and A1.11, refers to the percentage of time the flow is turbulent (0 = fully laminar, 1 = fully turbulent) and acts on the production of the turbulent kinetic energy transport equation in the SST model to simulate laminar/turbulence flows. γ_{sep} is introduced to improve the predictions of separated flow transition

$$\gamma_{sep} = \min \left(C_{s1} \max \left[\left(\frac{Re_\nu}{3.235 Re_{\theta c}} \right) - 1 \right] F_{reattach}, 2 \right) F_{\theta t} \quad (\text{A1.17})$$

$Re_{\theta c}$ is the critical momentum thickness Reynolds number and can be calculated as

$$Re_{\theta c} = C_{TU1} + C_{TU2} \exp [-C_{TU3} Tu_L F_{PG}(\lambda_{\theta L})] \quad (\text{A1.18})$$

$$Tu_L = \min\left(100 \sqrt{\frac{2\kappa}{3}} \frac{1}{\omega y}, 100\right) \quad (\text{A1.19})$$

$$\lambda_{\theta L} = -0.1111 \frac{dV}{dy} \frac{y^2}{\nu} + 0.1875; \quad \lambda_{\theta L} = \min(\max(\lambda_{\theta L}, -10.0), 10.0) \quad (\text{A1.20})$$

$$F_{PG}(\lambda_{\theta}) = \begin{cases} \min(1 + C_{PG1} \lambda_{\theta}, C_{PG1}^{lim}), & \lambda_{\theta} \geq 0 \\ \min(1 + C_{PG2} \lambda_{\theta} + C_{PG3} \min[\lambda_{\theta} + 1.0, 0], C_{PG2}^{lim}), & \lambda_{\theta} < 0 \end{cases} \quad (\text{A1.21})$$

The others parameters are

$$C_{s1} = 2; \quad Re_V = \frac{\rho y^2 S}{\mu}; \quad F_{reattach} = e^{-\left(\frac{Re_t}{20}\right)^4} \quad (\text{A1.22})$$

$$F_{\theta t} = \min\left(\max\left(F_{wake} e^{\left(\frac{y}{\delta}\right)^4}, 1.0 - \left(\frac{\gamma - 1/50}{1.0 - 1/50}\right)^2\right), 1.0\right) \quad (\text{A1.23})$$

$$F_{wake} = e^{-\left(\frac{Re_{\omega}}{10^5}\right)^2}; \quad Re_{\omega} = \frac{\rho \omega y^2}{\mu}; \quad \delta = \frac{500 \Omega y}{U} \frac{15}{2} \frac{\bar{Re}_{\theta t} \mu}{\rho U} \quad (\text{A1.24})$$

where U is the streamwise velocity:

The intermittency γ transport equation is

$$\frac{\partial \rho \gamma}{\partial t} + \frac{\partial \rho u_j \gamma}{\partial x_j} = P_{\gamma} - E_{\gamma} + \frac{\partial}{\partial x_j} \left[\left(\mu + \frac{\mu_t}{\sigma_{\gamma}} \right) \left(\frac{\partial \gamma}{\partial x_j} \right) \right] \quad (\text{A1.25})$$

where P_{γ} is the transition sources and E_{γ} the destruction/relaminarization source, defined as

$$P_{\gamma} = F_{length} \rho S \gamma (1 - \gamma) F_{onset}; \quad E_{\gamma} = c_{a2} \rho \Omega \gamma F_{turb} (c_{e2} \gamma - 1) \quad (\text{A1.26})$$

being $F_{length} = 10$, $c_{a2} = 0.06$, $c_{e2} = 50$, Ω the magnitude of the absolute vorticity rate and $\Omega \gamma = 1.0$ (Ansys, 2021). The transition onset is controlled by

$$F_{onset1} = \frac{Re_V}{2.2 Re_{\theta c}}; \quad F_{onset2} = \min(F_{onset1}, 2.0) \quad (\text{A1.27})$$

$$F_{onset2} = \max\left(1 - \left(\frac{Re_t}{25}\right)^3, 0\right); \quad F_{onset} = \max(F_{onset2} - F_{onset3}, 0) \quad (\text{A1.28})$$

$$F_{turb} = e^{-\left(\frac{R_T}{2}\right)^4}; \quad R_T = \frac{\rho k}{\mu \omega}; \quad Re_V = \frac{\rho d_{\omega}^2 S}{\mu} \quad (\text{A1.29})$$

where $C_{TU1} = 100$; $C_{TU2} = 1000$; $C_{TU3} = 1$; $C_{PG1} = 1$; $C_{PG2} = -0.5$ and $C_{PG3} = 0$ (Ansys, 2021).

A2. Grid Test

Roache (1994) proposed the Grid Convergence Index (*GCI*) to establish a consistent approach for reporting the outcomes of grid convergence test. Three levels of grid are recommended for a more accurate estimation of the convergence order and to verify if the solutions are within the asymptotic range of convergence.

The *GCI* is defined as

$$GCI = \frac{F_s |\epsilon|}{r^{p-1}} \quad ; \quad |\epsilon| = \left| \frac{\phi_{i+1} - \phi_{2i}}{\phi_{i+1}} \right| \quad ; \quad r = \frac{h_i}{h_{i+1}} \quad (A2.1)$$

where ϕ represents the variable chosen to be examined, the subscript i is the coarse mesh and $i + 1$ is a finer mesh, p is the convergence order of the scheme (defined as 2, corresponding to 2nd order upwind scheme), $|\epsilon|$ the relative error, F_s the safety factor (chosen as 1.25), h the average grid size and r the ratio between the grid sizes.

In this way, three meshes with different refinement levels, (1.87×10^6 , 3.48×10^6 and 7.31×10^6 cells) were created using the Ansys Meshing tool (Ansys, 2021). The meshes were designed employing the tetrahedron method, and near the surface of the aorta, additional refinement was applied to enhance the capture of the boundary layer region, as already shown in Figure 5.5. A first mesh was defined and the subsequent meshes were created by dividing the control volumes by two, imposing restrictions of maximum and minimum control volume size.

The dimensionless wall distance y^+ (Eq. 4.20) was also verified. For all cases, $y^+ < 2.3$, indicating an adequate refinement near the wall for the turbulence model selected.

The representative grid size (h) was estimated based on a tetrahedron edge, with volume given by $\forall_{cell} = h^3 \sqrt{2}/12$. The cell volume \forall_{cell} was determined by simply dividing the total volume \forall by the number of cells, $\forall_{cell} = \forall / N_{cells}$.

The healthy patient's aorta was selected for the mesh convergence test. The total volume of that aorta (\forall) is $3.864 \times 10^{-5} \text{ m}^3$.

To analyse the variables, it was considered the time interval Δt_1 of 0.06s, which is equivalent to 1/5 of the systolic period. This interval contains the most

expressive values of this period, specifically after the systolic peak, as illustrate by Figure A2.1.

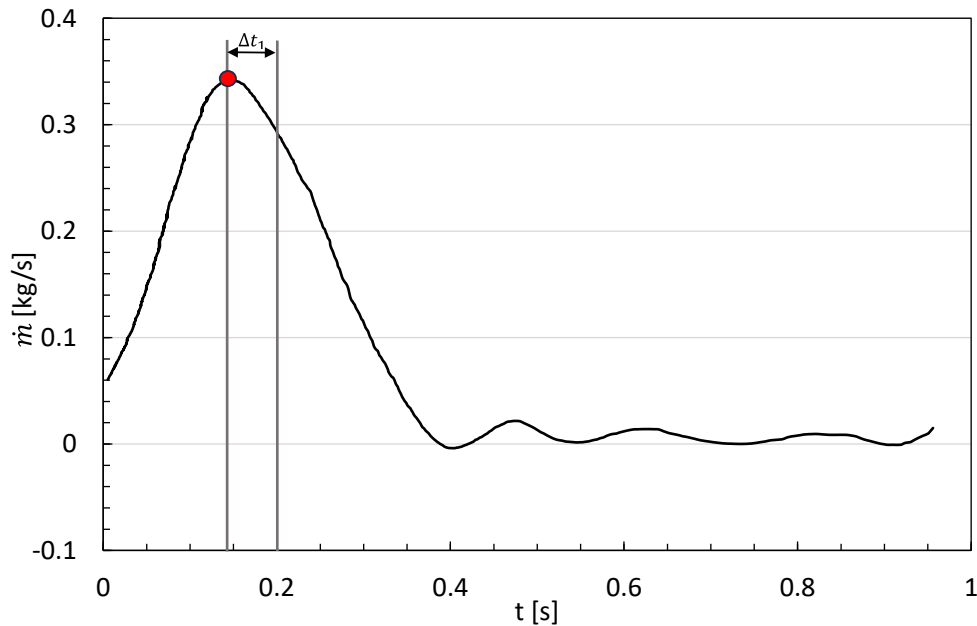


Figure A2.1 – The complete cardiac cycle demarcated by the interval Δt_1 considered to analyze the hemodynamic variables.

First, the grid test was conducted focusing on a defined region of interest at the ascending aortic wall, shown in Figure A2.2, investigating pressure and shear stress as the most significant variables. More precisely, the time average in the interval Δt_1 of the average pressure in the region with pressure above 100 Pa, $\langle \bar{P}_{>100 \text{ Pa}} \rangle$, and the average WSS in the region with WSS above 7 Pa, $\langle \overline{WSS}_{>7 \text{ Pa}} \rangle$. To evaluate the intermittence of the flow, the maximum and the average Oscillatory Shear Index, OSI_{max} and OSI_{ave} , were also determined. Table A2.1 presents these variables. Note that small relative errors between the meshes were obtained. Large GCI was obtained between the coarser and intermediate mesh for the pressure, but it is small between the intermediate and fine mesh. Analysing the average WSS and maximum OSI , a small increase was obtained for both the relative error and GCI , although the differences are very small for. Analysing the flow intermittence through the average OSI , when the mesh is refined, the error and GCI decrease. These results indicate that the intermediate mesh was satisfactory to be employed, considering an accuracy of 0.4% for the pressure, but 5% for WSS and OSI .

Table A2.1 – Variables in the region of interest.

Grid Number [$\times 10^6$]	1.87	3.48	7.31
Grid Size [cm]	0.56	0.46	0.36
$r = \frac{h_i}{h_{i+1}}$		1.2	1.3
$\langle \bar{P}_{>100 Pa} \rangle$ [Pa]	185.75	213.53	213.91
$ \epsilon $ [%]		13.01	0.18
GCI [%]		31.66	0.34
$\langle \overline{WSS}_{>7 Pa} \rangle$ [Pa]	15.29	15.07	15.53
$ \epsilon $ [%]		1.51	2.97
GCI [%]		3.68	5.80
OSI_{max}	0.496	0.497	0.499
$ \epsilon $ [%]		0.17	0.32
GCI [%]		0.43	0.62
OSI_{ave}	0.156	0.277	0.285
$ \epsilon $ [%]		43.58	2.71
GCI [%]		106.03	5.28

To further analyze the mesh impact in the WSS and OSI distribution, the average cycle variables, $TAWSS$ and OSI in the region of interest are shown in Figure A2.2 and Figure A2.3, respectively. Very similar distributions can be seen, indicating a small impact of the mesh in the overall distribution.

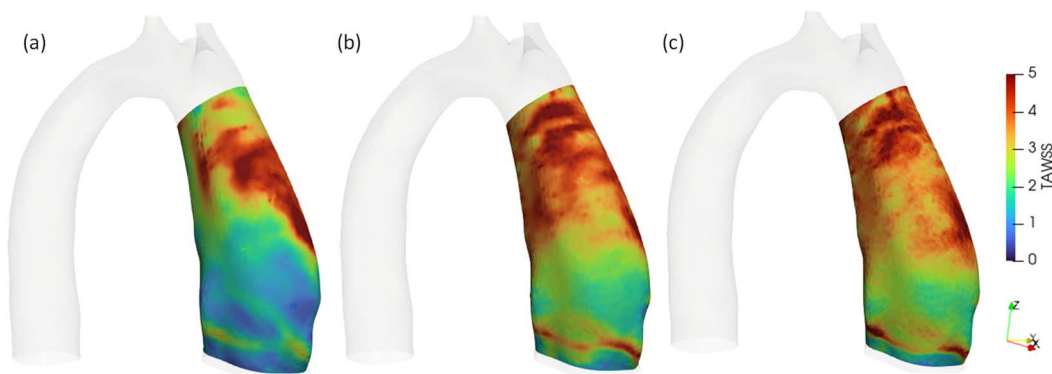


Figure A2.2 – $TAWSS$ field for the three different meshes: (a) 1.87×10^6 cells. (b) 3.48×10^6 cells. (c) 7.31×10^6 cells.

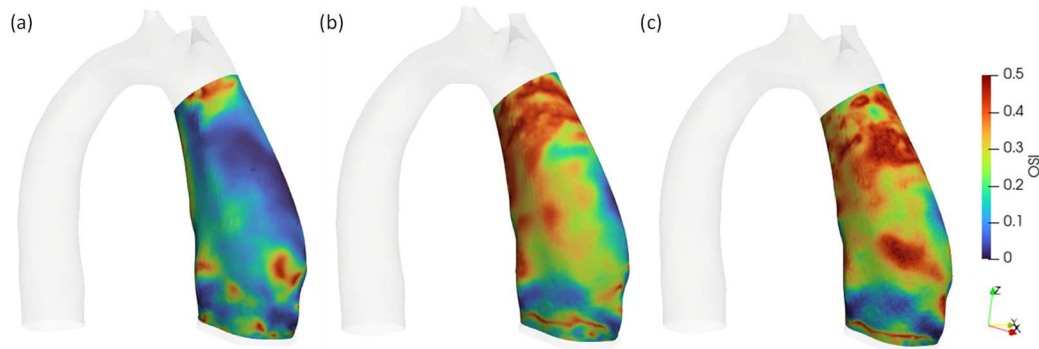


Figure A2.3 - OSI field for the three different meshes: (a) 1.87×10^6 cells. (b) 3.48×10^6 cells. (c) 7.31×10^6 cells.

A second investigation of the impact of mesh size was performed, analysing specific field variables within the interior of the domain. To this end, a z -line was defined, aligned with the axial z -coordinate, in the direction of the inlet flow, as shown in Figure A2.4.



Figure A2.4 – Z-line.

Table A2.2 shows the maximum variables along the z -line and time interval Δt_1 . The selected variables were the time average maximum values of: the velocity magnitude, $\langle \overline{|V|}_{max} \rangle$; the velocity component in y direction, $\langle V_{y_{max}} \rangle$, and the turbulent kinetic energy $\langle \kappa_{max} \rangle$. Note that for all variables, not only the relative error was quite small between the intermediate and fine mesh, but also the GCI . The variation of the velocities in x direction, V_x , and in the z direction, V_z , with the mesh size were negligible and they were not included in the table.

Table A2.2 – Variables in z-line.

Grid Number [$\times 10^6$]	1.87	3.48	7.31
Grid Size [cm]	0.56	0.46	0.36
$r = \frac{h_i}{h_{i+1}}$		1.23	1.28
$\langle \vec{V} _{max} \rangle$ [m/s]	0.958	0.854	0.851
$ \epsilon $ [%]		12.18	0.35
<i>GCI</i> [%]		29.63	0.69
$\langle V_{y_{max}} \rangle$ [cm/s]	5.82	4.91	5.55
$ \epsilon $ [%]		18.48	11.41
<i>GCI</i> [%]		44.96	22.25
$\langle \kappa_{max} \rangle$ [cm ² /s ²]	60.0	31.5	31.9
$ \epsilon $ [%]		90.35	1.30
<i>GCI</i> [%]		219.83	2.54

From the results obtained at the wall as well as at in the interior domain, for selected variables, as the mesh was refined, it is observed a significant reduction in the variables variation, with an acceptable *GCI* between the intermediate and fine mesh. Since the finer mesh requires a significant larger computing effort and does not improve the solution, the most efficient choice is the intermediate mesh of 3.48×10^6 cells.

A3. The Cardiac Cycle Periodicity

In order to guarantee the periodicity of the cardiac cycle, a patient with aneurysm was tested throughout 6 cycles. The variables as the average WSS in the region with WSS above 7 Pa ($\overline{WSS}_{>7 Pa}$) and the average pressure in the region with pressure above 100 Pa ($\overline{P}_{>100 Pa}$) on the wall were evaluated during each complete cardiac cycle. The strain indices $TAWSS_{max}$ and $TAWSS_{ave}$, as well the OSI_{max} , the OSI_{ave} , the TAP_{max} and the TAP_{ave} were also analyzed. Table A3.1 presents the values of the 6th cycle compared to the other cycles to determine the error associated and in Figure A3.1, the average cycle variables, TAP , $TAWSS$ and OSI in the region of interest is presented.

Table A3.1 – Comparison of the cardiac cycles.

Cycle	3rd	4th	5th	6th
$\langle \overline{P}_{>100 Pa} \rangle$ [Pa]	166.08	167.01	167.93	167.03
$ \epsilon $ [%]	0.57	0.01	-0.53	
$\langle \overline{WSS}_{>7 Pa} \rangle$ [Pa]	9.12	9.05	9.01	8.97
$ \epsilon $ [%]	-1.68	-0.95	-0.42	
TAP_{max} [Pa]	8.89e-1	8.80e-1	8.64e-1	8.73e-1
$ \epsilon $ [%]	-1.80	0.78	1.02	
TAP_{ave} [Pa]	2.93e-1	2.96e-1	2.88e-1	2.82e-1
$ \epsilon $ [%]	-3.84	-4.62	-1.95	
$TAWSS_{max}$ [Pa]	4.498	4.427	4.328	4.415
$ \epsilon $ [%]	-1.84	-0.22	2.02	
$TAWSS_{ave}$ [Pa]	1.994	1.999	1.985	1.996
$ \epsilon $ [%]	0.12	-0.15	0.56	
OSI_{max}	4.96e-1	4.97e-1	4.96e-1	4.95e-1
$ \epsilon $ [%]	-0.03	0.32	-0.03	
OSI_{ave}	1.720e-1	1.738e-1	1.742e-1	1.731e-1
$ \epsilon $ [%]	0.60	-0.43	-0.69	

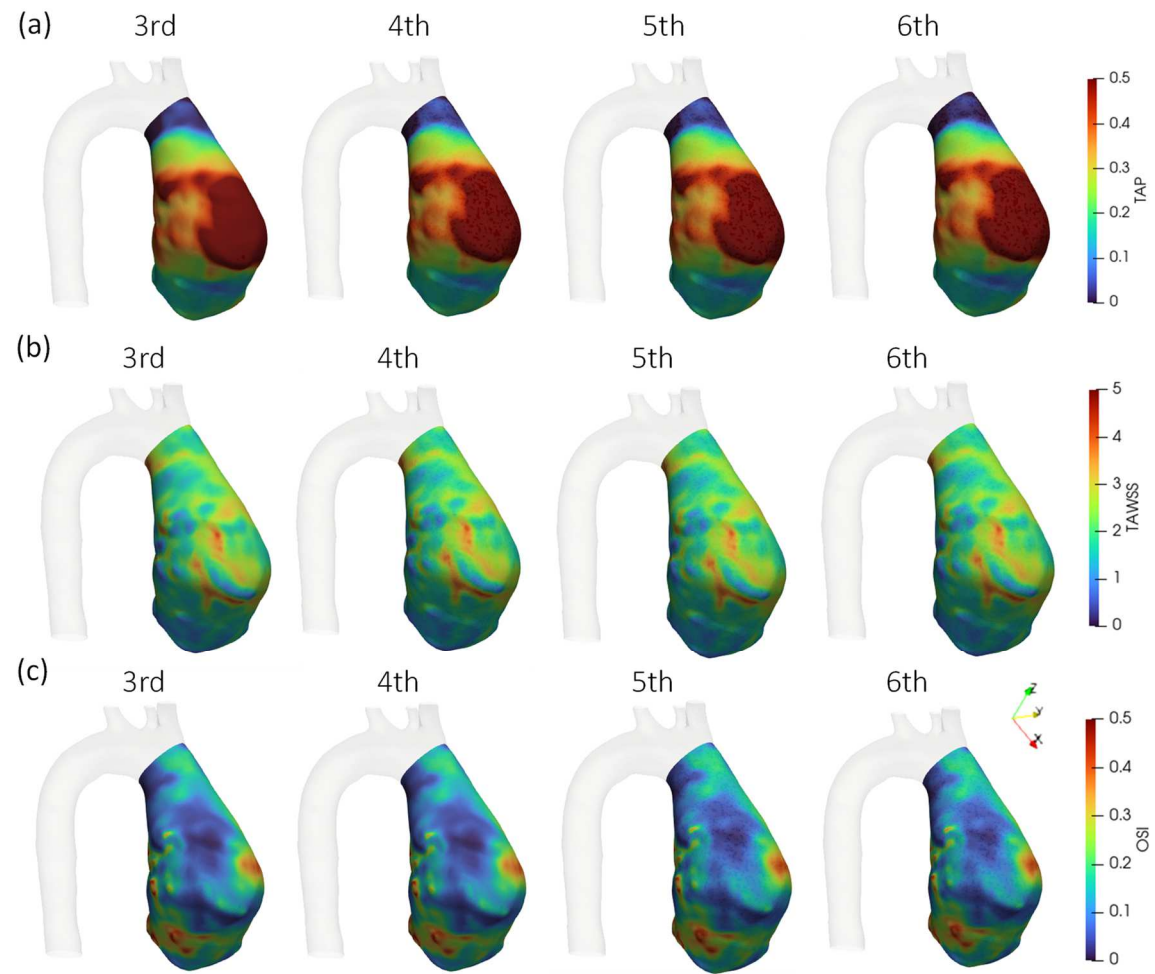


Figure A3.1 – The average cycle variables fields on 4 different cycles: (a) *TAP*. (b) *TAWSS*. (c) *OSI*.

Evaluating the qualitative outcomes illustrated Figure A3.1, is perceived the minimal disparity among the average cycle variables fields between the examined cycles. The quantitative results, presented in Table A3.1, reveal that the 4th cycle, for the most of variables presented, has the smallest errors when it is compared to the 6th cycle. This observation underscores the effectiveness of selecting the 4th cycle, when periodicity is achieved, thereby resulting in minimal variance between the subsequent cycles and consequently saving computational time

A4. Inlet Flow Rate

The data of the mass flow rate input curve presented in Figure 6.3 is detailed in Table A4.1.

Table A4.1 – Mass flow rate input data for healthy patient.

Time [s]	\dot{m}_{in} [kg/s]
0.01	0.056495
0.02	0.071357
0.03	0.087819
0.04	0.107416
0.05	0.128456
0.06	0.154048
0.07	0.183256
0.08	0.215994
0.09	0.24623
0.10	0.272648
0.11	0.299585
0.12	0.320767
0.13	0.342331
0.14	0.353624
0.15	0.360011
0.16	0.361293
0.17	0.356794
0.18	0.347592
0.19	0.335754
0.20	0.323362
0.21	0.309443
0.22	0.294015
0.23	0.278125
0.24	0.260196
0.25	0.246946
0.26	0.221981
0.27	0.20274
0.28	0.177788
0.29	0.158003
0.3	0.137194
0.31	0.120362
0.32	0.10213
0.33	0.085907

0.34	0.069548
0.35	0.054799
0.36	0.0391
0.37	0.026689
0.38	0.014944
0.39	0.005556
0.4	0.000785
0.41	0.004021
0.42	0.003307
0.43	0.000114
0.44	0.004377
0.45	0.009212
0.46	0.01532
0.47	0.01949
0.48	0.022463
0.49	0.022493
0.5	0.018599
0.51	0.013895
0.52	0.009155
0.53	0.005012
0.54	0.002997
0.55	0.001898
0.56	0.001701
0.57	0.002786
0.58	0.004831
0.59	0.008035
0.6	0.010165
0.61	0.012493
0.62	0.01427
0.63	0.014638
0.64	0.01468
0.65	0.014313
0.66	0.011279
0.67	0.009289
0.68	0.007322
0.69	0.005394
0.7	0.003422
0.71	0.002108
0.72	0.001027
0.73	0.000389
0.74	0.000119
0.75	0.000212
0.76	0.000853
0.77	0.002147
0.78	0.003735
0.79	0.004437

0.8	0.006913
0.81	0.008335
0.82	0.009516
0.83	0.009824
0.84	0.009438
0.85	0.009065
0.86	0.009058
0.87	0.008566
0.88	0.006611
0.89	0.003699
0.9	0.001432
0.91	0.000348
0.92	0.000808
0.93	0.000265
0.94	0.001923
0.95	0.006359
0.96	0.010218

The inlet mass flow rate curve showed in Figure 7.7 was made based on the code used in the udf document depicted below:

```

/*****
unsteady.c
UDF for specifying a transient pressure and mass flow rate profile boundaries
conditions
*****/

#include "udf.h"

DEFINE_PROFILE(unsteady_massflow_inlet_Sistole_diastole, thread,
position)
{
    face_t f;
    real t = CURRENT_TIME;
    begin_f_loop(f, thread)
    {
        if(t<=0.86)

            F_PROFILE(f, thread, position) = 0.1136 - 0.05632*cos(t*7.426) +
0.1674*sin(t*7.426) - 0.07484*cos(2*t*7.426) - 0.03332*sin(2*t*7.426) -

```

$$0.0123*\cos(3*t*7.426) - 0.03708*\sin(3*t*7.426) + 0.02886*\cos(4*t*7.426) - \\ 0.01666*\sin(4*t*7.426) + 0.004523*\cos(5*t*7.426) + 0.01195*\sin(5*t*7.426) - \\ 0.0009959*\cos(6*t*7.426) + 0.002558*\sin(6*t*7.426) - 0.001048*\cos(7*t*7.426) - \\ 0.001928*\sin(7*t*7.426) + 0.001602*\cos(8*t*7.426) + 0.001619*\sin(8*t*7.426);$$

else if (0.86<t, t<=1.72)

$$F_PROFILE(f, thread, position) = 0.1136 - 0.05632*\cos((t-0.86)*7.426) + \\ 0.1674*\sin((t-0.86)*7.426) - 0.07484*\cos(2*(t-0.86)*7.426) - 0.03332*\sin(2*(t- \\ 0.86)*7.426) - 0.0123*\cos(3*(t-0.86)*7.426) - 0.03708*\sin(3*(t-0.86)*7.426) + \\ 0.02886*\cos(4*(t-0.86)*7.426) - 0.01666*\sin(4*(t-0.86)*7.426) + 0.004523*\cos(5*(t- \\ 0.86)*7.426) + 0.01195*\sin(5*(t-0.86)*7.426) - 0.0009959*\cos(6*(t-0.86)*7.426) + \\ 0.002558*\sin(6*(t-0.86)*7.426) - 0.001048*\cos(7*(t-0.86)*7.426) - 0.001928*\sin(7*(t- \\ 0.86)*7.426) + 0.001602*\cos(8*(t-0.86)*7.426) + 0.001619*\sin(8*(t-0.86)*7.426);$$

else if (1.72<t, t<=2.58)

$$F_PROFILE(f, thread, position) = 0.1136 - 0.05632*\cos((t-1.72)*7.426) + \\ 0.1674*\sin((t-1.72)*7.426) - 0.07484*\cos(2*(t-1.72)*7.426) - 0.03332*\sin(2*(t- \\ 1.72)*7.426) - 0.0123*\cos(3*(t-1.72)*7.426) - 0.03708*\sin(3*(t-1.72)*7.426) + \\ 0.02886*\cos(4*(t-1.72)*7.426) - 0.01666*\sin(4*(t-1.72)*7.426) + 0.004523*\cos(5*(t- \\ 1.72)*7.426) + 0.01195*\sin(5*(t-1.72)*7.426) - 0.0009959*\cos(6*(t-1.72)*7.426) + \\ 0.002558*\sin(6*(t-1.72)*7.426) - 0.001048*\cos(7*(t-1.72)*7.426) - 0.001928*\sin(7*(t- \\ 1.72)*7.426) + 0.001602*\cos(8*(t-1.72)*7.426) + 0.001619*\sin(8*(t-1.72)*7.426);$$

else if (2.58<t, t<=3.44)

$$F_PROFILE(f, thread, position) = 0.1136 - 0.05632*\cos((t-2.58)*7.426) + \\ 0.1674*\sin((t-2.58)*7.426) - 0.07484*\cos(2*(t-2.58)*7.426) - 0.03332*\sin(2*(t- \\ 2.58)*7.426) - 0.0123*\cos(3*(t-2.58)*7.426) - 0.03708*\sin(3*(t-2.58)*7.426) + \\ 0.02886*\cos(4*(t-2.58)*7.426) - 0.01666*\sin(4*(t-2.58)*7.426) + 0.004523*\cos(5*(t- \\ 2.58)*7.426) + 0.01195*\sin(5*(t-2.58)*7.426) - 0.0009959*\cos(6*(t-2.58)*7.426) + \\ 0.002558*\sin(6*(t-2.58)*7.426) - 0.001048*\cos(7*(t-2.58)*7.426) - 0.001928*\sin(7*(t- \\ 2.58)*7.426) + 0.001602*\cos(8*(t-2.58)*7.426) + 0.001619*\sin(8*(t-2.58)*7.426);$$

}

end_f_loop(f, thread) }

A5. Patients' Information

Table A5.1 – Time between exams, inlet diameter and volume of patients with aneurysm.

Patient	Δt_{scan} [year]	D_{year1} [cm]	D_{year2} [cm]	$\frac{D_{year2}}{D_{year1}}$	V_{year1} [cm ³]	V_{year2} [cm ³]	$\frac{V_{year2}}{V_{year1}}$
				- 1 [%]			1[%]
Y1	1.7	5.5	5.8	5.5	180.8	191.5	5.9
Y2	1.2	5.2	6.3	21.2	165.7	174.5	5.3
Y3	3.6	4.6	4.5	-2.2	82.0	96.2	17.3
Y4	2.1	4.9	4.9	0.0	142.1	168.2	18.4
Y5	1.7	5.5	5.5	0.0	136.7	145.4	6.4
Y6	2.1	5.2	5.6	7.7	178.0	191.0	7.3
Y7	1.7	5.0	5.3	6.0	208.7	246.3	18.0
Y8	1.8	5.2	5.4	3.8	145.5	159.7	9.7
Y9	3.4	5.1	4.9	-3.9	180.8	198.6	9.8
Y10	3.0	5.7	6.2	8.8	153.1	169.2	10.6
Y11	2.4	5.0	5.5	10.0	162.6	186.2	14.5
Y12	2.0	5.2	5.8	11.5	108.9	124.8	14.5
Y13	2.7	4.9	5.1	4.1	164.0	198.0	20.7
Y14	1.3	4.5	5.8	28.9	96.5	115.2	19.4
Y15	1.0	5.0	5.4	8.0	128.4	141.2	10.0
Y16	1.9	5.2	5.4	3.8	126.1	145.7	15.6
N1	2.6	5.0	5.3	5.0	152.0	154.0	1.3
N2	2.7	4.5	4.6	2.9	141.9	119.6	-15.7
N3	1.0	5.2	5.3	1.9	146.8	132.0	-10.0
N4	1.6	5.1	5.1	0.0	118.6	111.4	-6.1
N5	2.6	4.6	4.6	0.0	116.4	110.6	-5.0
N6	1.1	4.7	4.8	2.1	109.9	100.5	-8.6
N7	1.3	6.0	6.2	3.3	293.0	280.0	-4.4
N8	1.9	5.2	5.0	-3.8	174.3	175.2	0.5
N9	0.8	4.9	4.8	-2.0	137.4	139.3	1.4
N10	1.1	5.1	4.5	-11.8	175.5	176.9	0.8
N11	2.2	4.7	4.8	2.1	141.9	119.6	-15.7
N12	0.8	4.6	4.5	-2.2	139.5	133.4	-4.3
N13	2.2	5.2	5.1	-1.9	124.0	122.8	-1.0
N14	1.5	4.8	5.0	4.2	169.0	167.4	-1.0

Table A5.2 – Geometric parameters of patients with aneurysm.

	Patient	D [cm]	θ [°]	θ_I [°]	θ_{II} [°]
WITH GROWTH	Y1	2.33	47.33	135.44	49.82
	Y2	2.27	36.05	121.07	90.11
	Y3	2.27	58.30	115.12	72.45
	Y4	2.15	39.51	148.25	52.66
	Y5	2.03	46.77	119.52	65.26
	Y6	1.96	29.85	137.17	58.16
	Y7	2.63	48.08	138.80	63.56
	Y8	2.63	40.32	117.33	34.79
	Y9	3.11	41.42	126.68	50.56
	Y10	2.77	30.14	124.14	51.71
	Y11	2.80	41.66	101.69	40.82
	Y12	2.55	32.92	135.79	51.30
	Y13	2.77	36.86	129.54	51.37
	Y14	2.31	43.26	123.73	71.68
	Y15	2.92	64.44	116.64	51.34
	Y16	2.77	67.47	116.51	42.61
WITHOUT GROWTH	N1	2.53	47.91	136.91	66.14
	N2	2.77	42.51	120.89	36.99
	N3	2.92	43.72	86.60	89.64
	N4	2.63	33.73	156.42	42.63
	N5	2.72	50.71	119.22	64.07
	N6	2.87	48.76	112.71	71.55
	N7	2.81	40.03	154.29	36.68
	N8	2.55	63.74	155.26	52.81
	N9	3.32	19.06	116.37	67.73
	N10	2.81	62.69	129.21	64.14
	N11	2.23	63.1	139.71	64.17
	N12	2.85	16.83	116.52	65.51
	N13	2.83	21.61	142.48	62.51
	N14	2.24	40.48	135.17	69.21